UNIVERSITAT POLITÈCNICA
DE CATALUNYA
BARCELONATECH

High-fidelity surrogate models for parametric shape design in microfluidics

by
Luca Borchini

High-fidelity surrogate models for parametric shape design in microfluidics

by
Luca Borchini

A thesis submitted in fulfillment of the requirements for the degree of Doctor of Philosophy

in

Simulation in Engineering and Entrepreneurship Development

part of the Marie Skłodowska-Curie ITN-ETN funded by the European Union Horizon 2020 program with grant number 675919

Laboratori de Càlcul Numèric
Universitat Politècnica de Catalunya

in cotutelle with

College of Engineering
Swansea University

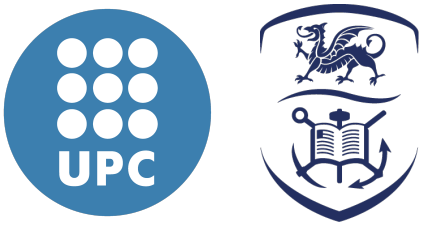

Barcelona, September 2020

Acknowledgements

I would like to express my thankfulness to all my advisors, Prof. Antonio Huerta and Dr. Matteo Giacomini from the Mathematical and Computational Modeling group at the Universitàt Politècnica de Catalunya, and Dr. Rubèn Sevilla from Zienkiewicz Centre for Computational Engineering at Swansea University, for their support and guides during these years.

I am also thankful to all the members of the AdMoRe consortium, both from academic institutions and industrial partners all over Europe. Thanks to all my Early Stage Researchers colleagues. I enjoyed the time spent together working side by side or discussing our progress during the AdMoRe meetings and conferences.

I am grateful to all my friends at UPC and to my office mates, with whom I shared science discussions, but also coffees, lunches, after-work beers and a lot more.

I am also grateful to all my friends at Swansea University, for all the football matches we played in the sunny days and the pints we had in the rainy ones. Thanks to Yvonne and Cliff to make me feel home each moment I stayed in their house.

Thanks to all my friends and flatmates who were, or still are, in Barcelona, and with whom I had the luck to share the beauty of this city.

I am also grateful to all my longtime friends supporting me from all around Europe. Even if living abroad makes everything more complicated, I have always had the feeling old times have never passed.

This four years journey has been much better because of all of you.

Finally, my biggest thanks go to my whole family and Alice for their endless support and encouragement. The strength you transmitted every single day was essential, especially in the hard times. I know without you the path to the finish line would be steeper and more challenging, but at the end, I can finally say we did it!

Abstract

Nowadays, the main computational bottleneck in computer-assisted industrial design procedures is the necessity of testing multiple parameter settings for the same problem. Material properties, boundary conditions or geometry may have a relevant influence on the solution of those problems. Consequently, the effects of changes in these quantities on the numerical solution need to be accurately estimated. That leads to significantly time-consuming multi-query procedures during decision-making processes. Microfluidics is one of the many fields affected by this issue, especially in the context of the design of robotic devices inspired by natural microswimmers. Reduced-order modelling procedures are commonly employed to reduce the computational burden of such parametric studies with multiple parameters. Moreover, high-fidelity simulation techniques play a crucial role in the accurate approximation of the flow features appearing in complex geometries. This thesis proposes a coupled methodology based on the high-order hybridisable discontinuous Galerkin (HDG) method and the proper generalised decomposition (PGD) technique. Geometrically parametrised Stokes equations are solved exploiting the innovative HDG-PGD framework. On the one hand, the parameters describing the geometry of the domain act as extra-coordinates and PGD is employed to construct a separated approximation of the solution. On the other hand, HDG mixed formulation allows separating exactly the terms introduced by the parametric mapping into products of functions depending either on the spatial or on the parametric unknowns. Convergence results validate the methodology and more realistic test cases, inspired by microswimmer devices involving variable geometries, show the potential of the proposed HDG-PGD framework in parametric shape design. The PGD-based surrogate models are also utilised to construct separated response surfaces for the drag force. A comparison between response surfaces obtained through the a priori and the a posteriori PGD is exposed. A critical analysis of the two techniques is presented reporting advantages and drawbacks of both in terms of computational costs and accuracy.

Keywords: Reduced order models, Proper generalised decomposition, Hybridisable discontinuous Galerkin, Parametrised geometry, Response surfaces, Microfluidics.

Contents

List of Figures

Chapter 1

Introduction

1.1 Motivations

Since Richard Feynman's 1959 famous speech "There's Plenty of Room at the Bottom" (Feynman, 1960), representing an invitation to enter new fields of physics, scientists, moved their interests in small-scale phenomena (typically sub-millimetre) rapidly achieving huge technology developments in various fields. Physics, biology, medicine, microelectronics, and among other, microfluidics. Following the definition given by Nguyen et al., (2019), microfluidics is "the science and engineering of systems in which fluid behaviour differs from conventional flow theory primarily due to the small length scale of the system". Today microfluidics is considered a multidisciplinary field that involves engineering, physics, chemistry, biochemistry, nanotechnology, and biotechnology. It has several practical applications in the design of systems that process low volumes of fluids to achieve multiplexing, automation, and high throughput screening (Ashraf et al., 2011; Teh et al., 2008). Microfluidics emerged at the beginning of the 1980s and is employed in the development of inkjet printheads, DNA chips, lab-on-a-chip technology, micro-propulsion, and micro-thermal technologies (Tabeling, 2005; Whitesides, 2006).

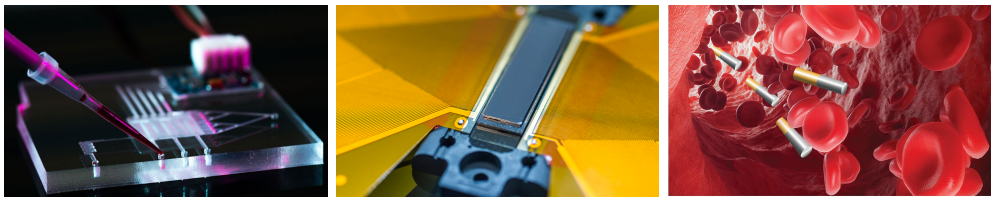

(a) Lab-on-a-chip (b) MEMS inkjet printheads (c) Artificial microswimmer

FIGURE 1.1: Microfluidics applications: Lab-on-a-chip [1], MEMS inkjet printheads [2]and artificial microswimmer [3].

[1]Image downloaded from `https://www.dantecdynamics.com/solutions-applications/applications/microfluidics/`.

[2]Image downloaded from `https://www.innovationservices.philips.com/looking-expertise/mems-micro-devices/mems-applications/inkjet-printheads/`.

[3]Image downloaded on the courtesy of Moran et al., (2019).

As explained by Purcell, (1977) in the work considered the milestone of this studies, at a small scale, everything behaves tremendously different from humans perception of flow phenomena. It is known that at small scale viscous forces dominate inertial ones and the governing equations are the Stokes's one. For an object of characteristic length L and velocity V, the Reynolds number, namely the ratio of inertial forces to the viscous forces is LV/ν, where ν is called the kinematic viscosity. For water, ν assumes the value of 10^{-2} cm^2/s making the Reynolds number for a man swimming in the water around 10^4, for a goldfish 10^2 while for the organisms living at the same microfluidics scale 10^{-4} or 10^{-5}. While fish or men propel themselves by accelerating the surrounding water, these organisms cannot rely on inertia because it is irrelevant for them and their motion is determined entirely by the forces exerted at the exact moment the organism is moving. Clearly, on small swimming organisms or bacteria, no external forces are exerted thus the motion must come from inside them. The only possibility they have to move is thus to deform their body. But it is important to note that not all deformations are useful to move. Several experiments have shown the reversibility of the motion of coloured droplets piped in high viscosity glycerol used to recreate low Reynolds number conditions at a larger scale (Heller, 1960). The sequence of images illustrates in figure 1.2 show the various steps of the experiment.

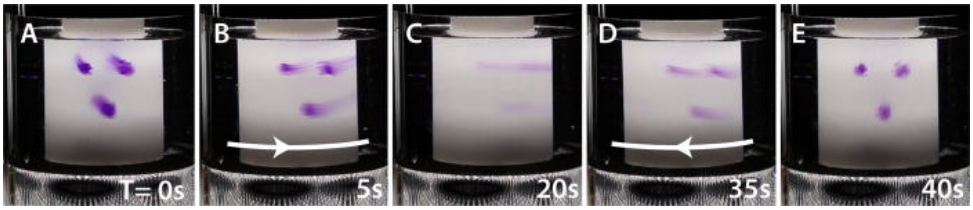

FIGURE 1.2: Time reversibility of Stokes flow: Different steps of the Taylor-Couette flow reversibility demonstration (Fonda et al., 2017).

The only condition at the base of the success of this experiment is the reciprocity of the motion, in this case, a rotation. Other similar examples can be found in nature. The scallop theorem (Lauga, 2011; Purcell, 1977) state that an organism trying to swim by reciprocal motion at low Reynolds number can't go anywhere. The scallop moves opening its shell slowly and closing it fast squirting out water. Its movement only depends on one hinge, and the reversibility of the only degree of freedom prevents it to move when the viscous effects are larger than the inertial. To swim at low Reynolds number an organism needs to perform a non-reciprocal motion that can break the time-reversal symmetry. A minimum of two hinges is thus required to be able to go through a repeated sequence of configurations inducing a net displacement. If the scallop could also rotate upside down as figure 1.3 shows, it would break that symmetry and indeed move in lack of inertia. It is worth noting that for a two hinges organism, the moving cycle is described by a trajectory in the space of coordinates μ_1 and μ_2, representing the two degrees of freedom.

Turning to microfluidics and one of its various applications, this theorem symbolised the beginning of modelling of artificial self-propelled microswimmers inspired by those

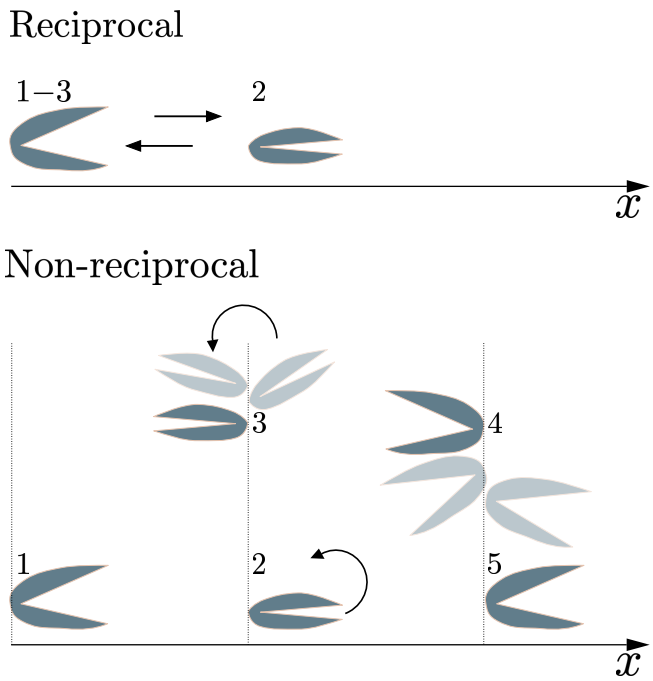

FIGURE 1.3: Scallop theorem: Reciprocal vs non-reciprocal motion characterized by two hinges at low Reynolds number.

existing in nature (Elgeti et al., 2015; Stone et al., 1996). A complete overview about mathematical description of biofluid dynamics and locomotion at low Reynolds can be found in Berg, (1993), Childress, (1981), and Lighthill, (1975). The reason for this increasing interest in understanding optimal swimming strategies for natural and artificial microswimmers hides in the final goal which is to design efficient self-propulsion micro-robots (Gauger et al., 2006) usable for drug delivery applications and minimally invasive surgical procedures.

The first two microswimmers studied were theorised in the pioneering work by Purcell, (1977). The first is Purcell's three-link swimmer (Becker et al., 2003; Tam et al., 2007) made of three-linked segments where the two located at its extremity are free to move independently. A symmetrised version of this swimmer has also been studied (Avron et al., 2008). The second Purcell's microswimmer is a toroidal device powered by surface tank-treading and modelled only several years later by Leshansky et al., (2008). The study of propulsion by a rotating flagellum used by a bacterium such as *Escherichia coli* (Purcell, 1997; Taylor, 1952) inspired different studies. Devices made of a linear chain of colloidal magnetic particles acting as a flexible artificial flagellum (Dreyfus et al., 2005) or helically shaped microswimmers (Keaveny et al., 2013) are some examples. Another mechanical model available in the literature and inspired to Purcell's three-link swimmer is the three-linked-spheres microswimmer introduced by Najafi et al., (2004) and consisting of three hard spheres, connected by two arms of negligible thickness whose length can vary. Similar to this latter and inspired by euglenoid movement, called metaboly and executed by some species of

euglenids (Arroyo et al., 2012; Leander, 2008), is the Push-Me-Pull-You (PMPY) microswimmer proposed by Avron et al., (2005) and further studied by Alouges et al., (2009) and Silverberg et al., (2020). This artificial device is modelled by two spheres also connected by an arm of negligible thickness whose length can vary as can vary the distribution of mass in the two spheres. As shown in figure 1.4, during a stroke, i.e. a periodic closed path in the space of the admissible shapes, large-amplitude deformations causing the rearrangement of mass allows both the euglenids and its artificial reproduction to move. It is worth noting that all this proposed microswimmers respect the rule of the two hinges (two free hinges, two variable distances, variable distance and variable mass). Moreover, for all microswimmer, the shape deformation

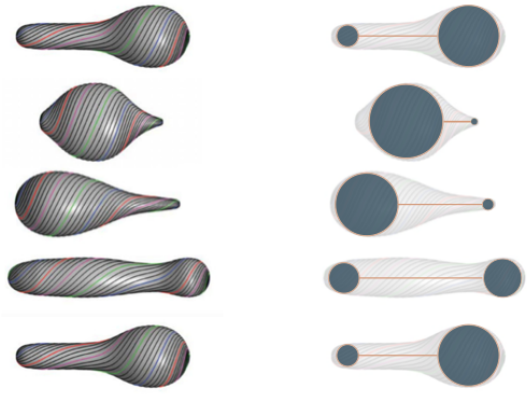

FIGURE 1.4: Metaboly and PMPY stroke: Reconstructions of the euglenoid movement (Arroyo et al., 2012) modelled with the PMPY microswimmer(Avron et al., 2005; Silverberg et al., 2020)

trajectory which allows the motion is not unique. This increases the complexity of the problem as the Stokes governing equations need to be solved for a multitude of different possible configurations of the micro-device. In other words, to find the trajectory that maximizes the movement of the swimmer, a multidimensional parametric problem must be solved. The number of parametric dimensions is exactly the number of hinges characterising each swimmer and describing its shape. In this context, surrogate models represent effective tools to explore the shape configurations of the microswimmers and to devise virtual models of their movement

1.2 State of the art in DG methods for flow problems

Along with many numerical methods, the finite element method (FEM) has been extensively studied in the context of computational fluid dynamics (Zienkiewicz et al., 1967). Despite its ability to handle complicated geometries and its potentiality in going high-order, the oscillatory behaviour of the solution provided by this method in convective-dominated problems, has prompted the CFD community to look for viable alternatives. Finite volume methods (FVM) impose local conservation on a

small volume surrounding each node of the mesh, volume on which the approximation is considered to be constant (LeVeque, 2002). Thanks to their propriety of flux conservation, the amount of fluid entering a given volume is identical to that leaving the adjacent volume, is now a standard approach in CFD. Indeed, FVM is nowadays implemented in many open-source and commercial software, e.g. OpenFOAM, Fluent, FLITE, CFX.

Since approximation is obtained with constant polynomials, the numerical solution found is not the best accurate and one could improve it performing a h-refinement with a consequential increase of the degrees of freedom of the problem and computational cost. For decades, these methods have been wildly studied improving their efficiency and robustness until they became the standard for CFD. Recently, the engineering accuracy that these methods achieve has started to be considered a limit in different fields. For instance, in the aerodynamic performance analysis of flight vehicles, since unsteady vortices are strongly dissipated by first-order and second-order methods, the required mesh resolution for the flow makes such a simulation too costly even on modern supercomputers (Dacles-Mariani et al., 1995; Strawn et al., 2000). High-order methods are therefore needed to accurately resolve unsteady vortices for vortex-dominated flows (Ekaterinaris, 2005). Another research field where a high level of accuracy is required is computational aeroacoustics (CAA) where due to the long-distance propagation of broadband acoustic waves a low-order method would cause significant numerical dissipation or dispersion errors making high-order methods preferable with respect these last one Wagner et al., (2007). Due to the complexity and expensiveness of high order volume scheme based on polynomial reconstructions, e.g. finite volume WENO schemes (Shu, 2003), alternative options related to the FEM framework has started to be considered.

Going back in the years, simultaneously to the development of the FVM to solve convection linked issues experienced by FEM, different strategies were proposed within the FEM framework to circumvent the problem. Several possible stabilisations of the FEM methods were developed, e.g. SUPG (Hughes, 1979), GLS (Hughes et al., 1986), DW (Douglas et al., 1989), and a discontinuous version of the classical continuous Galerkin (CG) method. Discontinuous Galerkin (DG) method first appeared in the study of neutron transport equation, i.e. a time-independent linear hyperbolic equation, by (Reed et al., 1973) and have been further analysed by Johnson et al., (1986) and Lesaint et al., (1974) for the linear advection equation. Successive works resulting in a series of papers (Cockburn et al., 1988, 1989, 1990) devised a high-order accurate total variation bounded (TVB) Runge–Kutta Discontinuous Galerkin (RKDG) method for the solution of non-linear systems of conservation laws. The extension to compressible Navier–Stokes equations proposed by Bassi et al., (1997) resulted in a technique soon after applied to elliptic problems (Brezzi et al., 2000) and whose generalisation for convection-diffusion problems lead to the so-called local discontinuous Galerkin (LDG) method introduced in Cockburn et al., (1998) and further

studied later in (Cockburn et al., 2002, 2004b). The conservative form of the LDG numerical fluxes guarantees the scheme to be conservative and adjoint consistent. By the way, for multidimensional problems, degrees of freedom belonging to elements which are not immediate neighbours can be involved in the same equation making result the stencil involved in LDG discretisation not compact. To circumvent this issue, an improvement of the LDG method was proposed by Peraire et al., (2008) for elliptic problems, the compact discontinuous Galerkin (CDG) which besides all the inherited LDG proprieties uses more compact stencils. Discontinuous finite elements for elliptic and parabolic equations were not a novelty in literature, they have been developed and studied three decades before with the name of interior penalty method (IP). The work done by Arnold et al., (2002) unifies this method in the case of elliptic problems. Later, on the wave of success DG methods have extended to a wide variety of equations tightening up the rivalry with the wide used mixed and continuous Galerkin methods such as the Raviart-Thomas (RT), see (Raviart et al., 1977) and the Brezzi-Douglas-Marini (BDM), see (Brezzi et al., 1985), methods.

The CG method is considered the main numerical technique against which to make both accuracy and computational cost evaluations. It is a method which allows computing a continuous solution of a PDE through piecewise continuous polynomial shape functions. The DG method, which complete overview can be found in Cockburn et al., (2000), contrary relies on the resolution of a PDE using discontinuous shape functions defined element-by-element. That implies a domain decomposition and the consequent duplication of the nodes lying on the internal edges of the elements. This feature represents both the main drawback and the main advantage of DG if compared with CG. On the one hand, the number of degrees of freedom of the problem increases. On the other hand, the problem can be solved independently element-by-element hence it is easily parallelizable (Biswas et al., 1994). Moreover, due to their discontinuity element-by-element nature, DG methods can be considered as generalisations of finite volume methods, inheriting the ideas of numerical fluxes and slope limiters within a finite element framework. They are locally conservative, stable, high-order accurate that can easily handle complex geometries, irregular meshes with hanging nodes, and approximations that have polynomials of different degrees in different elements. Thus, they can easily handle adaptivity strategies which in hyperbolic problems has a particular relevance (Hartmann et al., 2003). That makes them particularly suitable for the resolution of purely convective problems as their ability to capture discontinuities without producing spurious oscillations near them. Increasing the polynomial degree of the shape functions, the number of degrees of freedom in the volumetric interior of an element increases more rapidly than the degrees of freedom on element boundaries. Hence, despite the extra degrees of freedom, the DG methodology becomes more efficient for high-degree polynomial approximations. When the method is pushed to high-order the communication between the element in DG is less demanding than the one needed in CG. That makes DG particularly suitable and natural for high-order approximations. Nevertheless, the increase in cost that both CG and DG have to

face represents the reason for the limited application of these methods outside of the academic context. As a consequence, both CG and DG techniques developed hybridisable counterparts, giving rise to the wave of research in this new topic. See Cockburn, (2016) for an exhaustive overviews. One of the advantages of DG is its capability to easily devise high-order schemes.

In recent years, high-order methods have gained the interest of the Computational Fluid Dynamics (CFD) research community owing to the high accuracy and reliability of their numerical solution. As thoroughly reported in Gassner et al., (2013), applications dealing with transient turbulent flows, such as LES (Nagarajan et al., 2003; Pasquetti, 2005), DNS (Bassi et al., 2016; Chapelier et al., 2014), computational aero-acoustics (Beck et al., 2014; Nguyen et al., 2011a), turbulent combustion and vortex dominated flows (Wang, 2007), all rely on these methods as a solution of the same accuracy based on a low order method would require a computational mesh with a huge number of degrees of freedom and unaffordable computational costs (Lê et al., 2011). The common belief that high order methods are in general more expensive than low order methods has been slowing dismantled by many recent studies (Huerta et al., 2013; Wang et al., 2013, e.g.). High order methods are not only competitive but for a given accuracy are also computationally more convenient than low order ones and their large scale application is only a matter of time (Kroll et al., 2015). As explained by Wang et al., (2013) the most diffuse belief regarding high-order methods is about their higher cost respect their low-order relatives. Comparing the solution of a first-order method with the one obtained employing a high-order method on a given mesh, the latter results to be more CPU time-consuming. This is a matter of fact and it is undeniable. But it is also indisputable that this statement is untrue in terms of accuracy. It is known that for an assigned mesh high-order method delivers higher accuracy respect to low-order methods. A fair question to ask is thus, for a target accuracy which between low and high-order methods are computationally more competitive? Low-order methods will need a finer mesh to obtain a solution able to prevail the high-order ones, which, on their side, can employ a coarser mesh. This rolls the dice to decide a winner, in fact, on these reasons, recent studies have proved that high-order methods are not necessarily expensive (Huerta et al., 2013). By the way, despite their potential and their major accuracy for complex problems, high-order methods are still not used in the design process for several reasons. They are more complicated and hard to implement than low-order methods, less robust because of the much reduced numerical dissipation, they have a high memory requirement if implicit time-stepping is employed and robust high-order mesh generators are not readily available. All of these represents the fields of current research (Wang et al., 2013).

One variation of the CG method contrasting the increase of degrees of freedom is the CG method with static condensation, an implementation technique whose aim is to reduce the size of the stiffness matrix (Guyan, 1965). Partitioning the vector

of degrees of freedom of the approximation into two smaller ones, containing the degrees of freedom associated with the internal and external nodes of the elements, the stiffness matrix can be reorganized in a block structure. This allows obtaining the Schur complement of the block diagonal matrix associated with the internal degrees of freedom. In this way, the latter can be expressed in terms of the boundary ones end removed from the system of equations, thus reducing the dimension of the original system. What static condensation represents for primal methods, for mixed methods takes the name of hybridisation (Veubeke, 1965). The first hybridised techniques appeared in the context of DG are the hybrid DG method (Egger et al., 2010) where hybridisation simply reduces the degrees of freedom (analogously to static condensation) or the hybrid high-order (HHO) method based on an elementwise reconstruction operator (standing for the gradient of the primal solution) and a stabilization terms enforcing the matching between local and hybrid degrees of freedom (Di Pietro et al., 2014, 2015). Given the strong similarities with HDG, HHO has been bridged to the latter in the work done by Cockburn et al., 2016. Differently from the aforementioned

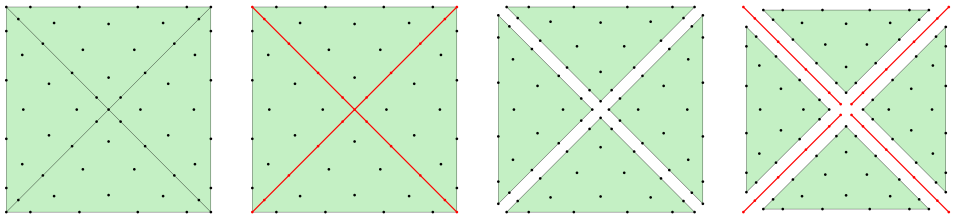

(a) CG (b) CG with s.c. (c) DG (d) HDG

FIGURE 1.5: CG vs CG with static condensation vs DG vs HDG: Degrees of freedom in a mesh of four fifth-order triangles for continuous Galerkin, continuous Galerkin with static condensation, discontinuous Galerkin, and hybridisable discontinuous Galerkin.

methods, a variation of the DG method based on a mixed formulations (Fortin et al., 1991) contrasting the increase of degrees of freedom by hybridisation (Cockburn et al., 2004a) is the hybridisable discontinuous Galerkin (HDG) method. The idea is first proposed in Cockburn et al., (2009c) and then formulated for Stokes flow in Cockburn et al., (2009b). HDG method relies on the definition of a hybrid variable lying on the internal skeleton of the mesh. All the problem variables (i.e. internal and boundary variables) can be expressed in terms of this hybrid variable solving an element-by-element local problem. Then a global problem imposes the interelement continuity of the solution and the normal component of the flux. The number of degrees of freedom, therefore, is significantly reduced as the problem unknowns reduce solely to the trace variable which is defined in a lower-dimensional space (i.e. the edges/faces of the elements) with respect to other variables.

Another particularity of the HDG method follows from the introduction of the mixed variable necessary to obtain a system of first-order PDEs. As all the HDG variables converge with order $k+1$, where k is the degree of the interpolant functions, exploiting

the definition of the mixed variable, an element-by-element local post-process can be obtained for problems at least of the second order (Cockburn et al., 2012). The result of this post-process is the superconvergence of the primal variable with order $k+2$. Moreover, also in HDG as in DG, thanks to the discontinuity of the elements, the degree of the approximating polynomial can be easily changed from one element to the other making possible to implement a p-adaptivity strategy. In elliptic problems, this procedure can be guided in a very natural way by a local a priori error indicator devised from the superconvergence solution (Giorgiani et al., 2012, 2014; Sevilla et al., 2018b). A comparison between CG with static condensation and HDG is proposed in Kirby et al., (2012). This work demonstrates that the HDG approach generates a global system for the approximation on the boundaries of the elements that although larger in rank than the traditional static condensation system in CG, has significantly smaller bandwidth at moderate polynomial degrees.

After their introduction, HDG methods have been extensively studied for convection-diffusion equations in steady and unsteady problems (Nguyen et al., 2009c,d) and second-order symmetric elliptic problems (Nguyen et al., 2010b). In particular, for Stokes flow, several formulations have been proposed. The work produced by Cockburn et al., (2010) compare the velocity-pressure-gradient, velocity-pressure-vorticity and the velocity-pressure-stress formulations showing several shared features of the methods. In terms of accuracy, the gradient-based HDG method provides the most accurate results and a post-processed velocity which converges with order $k+2$ for $k\geq 1$. On the other hand, both the stress-based and the vorticity-based methods yield a loss of superconvergence of the post-processed velocity for low-order approximations. Nevertheless, recent works accomplished in recover optimal orders for the stress-based approach. In Cockburn et al., (2017) the so-called M-decomposition framework is employed to enrich the local discrete space of approximation. This ensures the optimal convergence of the mixed variable and superconvergence of the post-processed one. An additional option consists of the HDG-Voigt approach introduced in Sevilla et al., (2018a) for linear elasticity and then applied to the Stokes flow equations in (Giacomini et al., 2018) recovering, also in this case, the superconvergence of the post-processed primal variable. An extension of the velocity-pressure-gradient formulation to Oseen equations can be found in Cesmelioglu et al., (2013) with particular focus on the stabilization condition applied to preserve the optimal convergence of all variables in convection-dominated problems. A posteriori error analysis of HDG method for this problem is developed in Araya et al., (2019). HDG mixed formulation for the incompressible Navier-Stokes equations was developed by Nguyen et al., (2011b) and Qiu et al., (2016) while the HHO counterpart appeared only a few years later (Di Pietro et al., 2018). Novel studies proposed a relaxed $H(\mathrm{div})$-conforming discretisation of the velocity field (Lederer et al., 2018, 2019). Turning to Stokes flows, HDG application in a microfluidics framework is quite a novelty. Recent works employing a new method inspired by the HDG and FVM frameworks, the face-centred finite volume

(FCFV) method, were developed targeting microfluidics applications with mesh adaptivity (Giacomini et al., 2020a; Vieira et al., 2020). Works involving HDG related to the efficient treatment of the geometry can be found in Sevilla et al., (2018b) where the integration within a CAD environment was proposed and Solano et al., (2019) where a suitable approximation for the Dirichlet boundary data was obtained using a transferring technique based on integrating the extrapolated discrete gradient.

Regarding HDG axisymmetric formulation it is worth to cite the work done by (Sánchez-Vizuet et al., 2019). In this paper an HDG solver for the semi-linear elliptic Grad-Shafranov equation, used to compute the equilibrium magnetic configuration in axisymmetric fusion reactors was developed. Due to the symmetry of the device, the equation can be posed, as usually done in a two-dimensional domain corresponding to a section of the toroidal reactor. As the plasma confinement region does not contain the vertical axis, in this case corresponding with the axis of symmetry, the problem becomes an interior Dirichlet boundary value problem. For that, it does not require any additional hypothesis, as a computational domain containing the symmetry axis would.

Last, it is necessary to recall the novelty of HDG coupling with model order techniques. A combination of HDG with proper orthogonal decomposition (POD) creating the HDG-POD method has been studied recently for the heat equation by Shen et al., (2019). Close to this contribution, but substantially different, lies the work extracted from this thesis which involves the combination of HDG with another model order reduction technique, the proper generalised decomposition (PGD) creating the HDG-PGD method proposed in the published contribution Sevilla et al., (2020a).

1.3 State of the art in ROM

During design processes of many industrial applications, the various viable configurations cause the resolution of the same problem several times. One of the many examples is the design of microswimmers in microfluidics. The variation of the geometry causes the necessity to know the flow solution for each possible shape defined by the parameters of the model. These data are necessary to determine the optimal stroke maximizing the motion of the microswimmer.

Reduced-order models (ROMs) have become commonplace in many areas of computational sciences and engineering (Chinesta et al., 2017; Peherstorfer et al., 2018). They represent the response to the necessity of computing multiple queries of the same problem in design and optimisation processes. Choosing a value of interest for each parameter of the model, the parametric problem is solved for all the required configurations. This is a very time-consuming procedure considering first, the huge amount of parameter settings to be tested and second, that usually, CFD solutions are not calculable instantly. In the best scenario, referring to industrial contexts, they

could take one night, in the worst one, days or weeks. Typical high-tech industries accept simulations of one night run to be able to take decisions the following morning. Anyway, this standard approach results to be the source of the great delays of every decision-making process. A distinct approach consists of considering parameters as extra-coordinates and solve a higher-dimensional problem. Direct resolutions are limited because even for a small number of parameters *curse of dimensionality* arises, making any resolution effort of this type unaffordable for nowadays technology. As computational cost scales exponentially with the discretisation of the mesh, see figure 1.6, a mesh of 1000 nodes for a four-dimensional problem (e.g. a very simple problem with two spatial dimensions plus two additional parametric dimensions) would have 10^{12} unknowns. The necessity of resorting to a reduced model framework

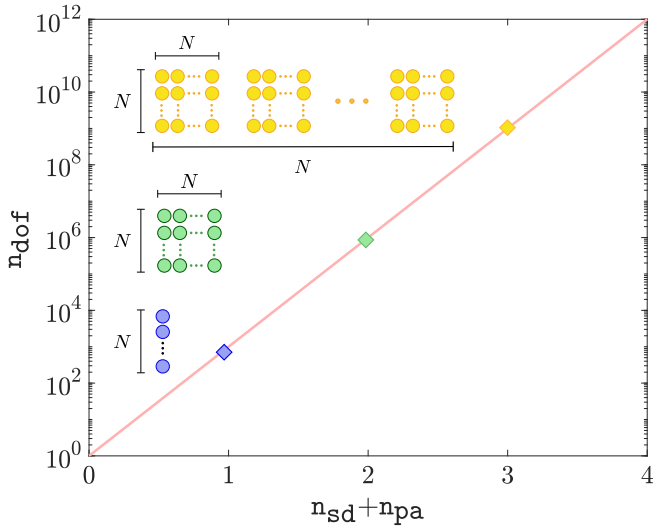

FIGURE 1.6: Curse of dimensionality: Exponential increase of the complexity in function of the number of dimensions considered, assuming N=1000 nodes in each of them.

is straight forward. With one of the various techniques available in the literature, it is possible to solve the high-dimensional problem reducing drastically the computational cost. Once paid the price to calculate the surrogate model at the beginning of the design or optimisation cycle (*off-line phase*), its evaluation can be done real-time during the decision-making procedure (*on-line phase*) not requiring any additional computational effort and thus shortening the whole process.

Model reduction techniques can be classified in *a posteriori* and a *a priori* techniques. The former ones construct the reduced model from an initial collection of information regarding the target problem. Usually, a series of snapshots obtained as full-order solutions of the problem are used. The latter, on the contrary, do not need any prior knowledge about the problem to obtain the surrogate model. The a posteriori MOR techniques are numerous. Among them, the most famous and studied are the proper orthogonal decomposition (POD), see Volkwein, (2011) and the reduced-basis (RB), see Hesthaven et al., (2016), Quarteroni et al., (2015), and Rozza, (2014). In recent years also new ones have been proposed such Hi-POD, a merging between the

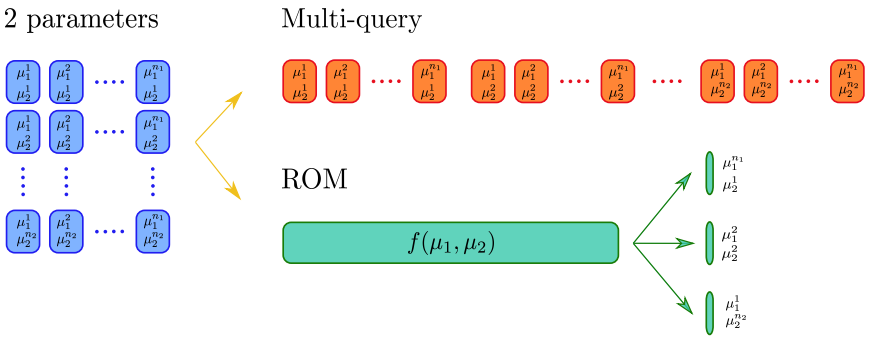

FIGURE 1.7: Multi-query vs ROM approaches: Comparison between a multi-query approach, based on multiple full-order solutions, and a reduced order model approach, split in off-line and on-line phases for a problem with 2 parameters.

hierarchical model reduction, Hi-Mod (Perotto, 2014), with POD introduced by Baroli et al., (2017) and the a posteriori PGD, see Díez et al., (2018, 2019). Among a priori ones in the literature, it is worth to mention the hyperreduction method proposed by Ryckelynck, (2005) and the proper generalised decomposition (PGD) of which a complete overview is given. It is worth noting that all these techniques are not in competition with standard numerical solvers as they are used in combination with these latter, independently from their nature (e.g. SEM, FEM, FDM, FVM).

Introduced by Lumley, (1967) POD is typically applied to build bases for time-dependent problems and is the leading model reduction tool for the unsteady Navier-Stokes equations. It computes basis to represent in a low-dimensional fashion a high-dimensional system introducing a new set of n_m variables known as principal components satisfying the orthogonality relation and with decreasing relevance. Practically, it consists of three phases. First, the n_s snapshots are generated by mean of the full model resolutions. Second, the projection of the full model onto the reduced subspace via singular value decomposition (SVD) of the correlation matrix assembled from the snapshots. Third, the obtained basis are interpolated to reconstruct the parametric dependence of the solution. The first two points form the off-line phase while the third point is the on-line phase where the surrogate model is particularized for required configurations. Recently, a POD-Galerkin framework has been developed (Baiges et al., 2013; Chapelle et al., 2013) based on the combination of POD with Galerkin strategies. This allowed POD to benefit of the robustness of the Galerkin projection making it suitable also for the resolution of parametric variations of time-dependent problems.

Another commonly used a posteriori technique is RB, introduced for non-linear viscous flows (Peterson, 1989). Analogously with the POD method, RB consists first of an off-line phase where a fixed number of snapshots, here named *truth approximations*, are collected using a full order model. A hierarchical Lagrangian reduced space can be thus constructed. Second, the on-line phase consisting of fast and inexpensive evaluations of the reduced model for all required parametric setting is performed via Galerkin projection (Quarteroni et al., 2011). The main critical point of this method

is the choice of the sampling forming the basis. If too few, the sampling may not be representative of the parametric space and the approximation is poor. If too many, the snapshots may be redundant and the following reduced system ill-conditioned. A viable way to check if the approximation is accurate enough is the use of the error estimator, based on the affinity assumptions and provided by the properties of the Galerkin projection (Patera et al., 2007; Rozza et al., 2007). The inexpensive error bounds permit to explore much larger subsets of the parameter domain in search of most representative snapshots, and second, controlling the error, to minimize the computational effort determining when the number of basis functions is enough.

Recently, a new a posteriori technique has been proposed by Baroli et al., (2017), Hi-POD. As anticipated, it takes its name from the combination of two methods, the Hierarchical Model (Hi-Mod) reduction and POD. Hi-Mod has been proposed by Perotto et al., (2010) as a method able to local enrich one-dimensional solutions of problems defined in domains with a geometrically dominant direction. Purely 1D hemodynamic models for instance, completely drop the transversal dynamics which in several cases may be locally important (e.g., in the presence of stenosis or aneurisms). The approach consists of discretizing the main dynamics with a fine finite element mesh while the transversal direction is modelled via spectral elements using a coarse approximation. A key point of this method is the assumption of separability between the main and the transversal directions of the space, a feature that brought to an interesting comparison with another method based on the same hypothesis, the PGD, particularly in its version which considers the separation of space coordinates (Perotto et al., 2018). A comparison between the parametrised PGD and the parametrised version of Hi-Mod, Hi-POD, is also present. This latter is used to solve problem characterised by geometrical or material parametrisation and analogously than POD is based on the calculation of snapshots (via Hi-Mod technique) and computation of the POD basis via singular value decomposition (off-line phase) and interpolation of the basis to compute a particularized solution (on-line phase).

Another newly proposed technique is the a posteriori PGD also known in the literature as least-squares PGD (Modesto et al., 2015), algebraic PGD (Díez et al., 2018) or encapsulated PGD (Díez et al., 2019). The a posteriori PGD framework relies on constructing a reduced basis starting from a series of snapshots obtained with a full model resolution technique. The n_s snapshots are collected in a multidimensional tensor structure counting of one spatial dimension plus one extra dimension for each parameter of the model. The a posteriori PGD computes the separated approximation of the multidimensional tensor in the form of a product of rank-one approximations using, a greedy approach based on an alternate direction scheme.

A critical common aspect for previous techniques to devise competitive and accurate a posteriori numerical strategies is the selection of the snapshots, that is, the sampling procedure in the parametric space. Several techniques were proposed to address this problem, starting from the classical Latin hypercube sampling (McKay et al., 2000)

and centroidal Voronoi tessellation (Du et al., 1999) to greedy approaches, based on a posteriori error estimates (Grepl et al., 2005; Veroy et al., 2005) and model-constrained adaptive sampling (Bui-Thanh et al., 2008). Once the sampling points are selected, the computation of the snapshots is generally performed in parallel, exploiting the independence of each set of parameters to one another, to reduce the computational cost of the off-line phase. Recently, an alternative strategy aiming to reduce the number of required full-order solutions was proposed via an incremental algorithm (Phalippou et al., 2020). The idea is to compute snapshots sequentially and on-the-fly, corresponding to the values of the parameters identified by an appropriate error estimate.

Differently from previously described techniques, a priori PGD automatically determines the number of terms of the reduced basis and do not require any prior knowledge about the problem, circumventing the sampling step. Conceptually, PGD has been developed independently by Ladevèze, (1999) and Ammar et al., (2006, 2007). Similarly to a posteriori PGD, it relies on a greedy algorithm which sequentially computes the terms of the reduced solution projecting the high-dimensional problem on a selected dimension, obtaining a lower-dimensional problem much cheaper to solve (Chinesta et al., 2013b). This projection is made possible by an important assumption on which the whole PGD technique depends, the *separability* of the solution. Separated representations were introduced by Ladevèze, (1991) for the resolution of transient problems in strongly non-linear models. The innovative approach consisted of a non-incremental integration procedure to avoid the enormous computational costs that those problem required. Using a standard incremental strategy, a transient problem defined in 3D physical space would require the resolution of as many 3D problems as the number of time steps selected, which could be millions. By contrast, using the space-time separated representation the number of spatial resolutions, i.e. the number of bases computed times the number of non-linear iterations needed to compute each one, was much smaller (order of hundreds). The computational saving was considerable. Later, separated representations were extended to stochastic modelling (Nouy, 2010) and for solving kinetic theory multidimensional models suffering the so-called curse of dimensionality (Ammar et al., 2006, 2007). Since its introduction PGD has been widely investigated and been proposed to circumvent computational issues in different cases: multidimensional models, efficient transient non-incremental solutions, space separation in degenerated domains, data-driven application systems (DDDAS), inverse identification and parametric solutions which pave the way to efficient optimisation and real-time simulations through computational vademecums (Chinesta et al., 2011). In recent years, there has been an increase in non-intrusive implementations of the PGD integrating commercial codes to solve multi-dimensional problems. Parametric stochastic equations (Giraldi et al., 2015), biomechanics problems (Zou et al., 2018), production of multi-component systems (Quaranta et al., 2020), incompressible flow problems (Tsiolakis et al., 2020a) also extended to fully-developed turbulent flow (Tsiolakis et al., 2020b) are some examples of involved applications. However,

intrusive implementations have also been explored for different fields. Among them, Navier-Stokes equations (Dumon et al., 2011), design of 3D-printed architectured materials (Sibileau et al., 2018), coupled magneto-mechanical problems addressed to MRI scanner applications (Barroso et al., 2020a,b), harbour agitation (Modesto et al., 2020) or crack propagation (Garikapati et al., 2020).

Among parametric problems, the case of geometrically parametrised PDEs has often been considered a challenge for both a priori and a posteriori frameworks. Among a posteriori techniques, RB have been widely used to solve flow problems in parametric domains (Manzoni et al., 2017). Viscous internal flow problems (Negri et al., 2013, 2015; Rozza, 2011; Rozza et al., 2013) or Navier-Stokes problems with haemodynamics applications (Manzoni, 2014; Manzoni et al., 2012a,b; Quarteroni et al., 2007) are some examples. Targeted to the same applications are several recent works exploiting the POD-Galerkin framework (Ballarin et al., 2015, 2016a,b, 2017, 2019). Turning to a priori PGD, in terms of geometrically parametrised problems, early works focused on solutions tailored to specific problems (Bognet et al., 2012; Chinesta et al., 2013a; Heuzé et al., 2016; Leygue et al., 2010) or strategies only applicable in a context of low order approximations (Ammar et al., 2014; Zlotnik et al., 2015). Similar to these works where piecewise linear geometric parametrisations are used, other PGD approaches that employ piecewise NURBS parametrisations have been proposed (Chamoin et al., 2019). More recently, a general approach to deal with geometrically parametrised problems in a CAD environment was proposed (Sevilla et al., 2020b). This work focuses on PGD algorithms based on high-fidelity spatial solvers.

Starting from the reduced solution obtained using either a priori or a posteriori approaches, parametric response surfaces can also be efficiently devised. In this context, a critical aspect is represented by the interpolation strategy used to evaluate the quantities of interest depending on the solution manifold constructed using the ROMs. The difficulty of effectively interpolating the reduced solution in a multidimensional manifold was first addressed in Amsallem et al., (2008). Since then, different strategies were proposed to reduce the dimensionality of the input space, e.g. via kernel principal component analysis (González et al., 2018) and manifold learning (Millán et al., 2013). Recently, manifold learning techniques and collocation methods inspired by sparse grids have been coupled with PGD-based separated representations of functions of interest (Ibañez et al., 2017; Ibanez et al., 2018). The resulting methodologies, including sparse subspace learning and sparse PGD (Ibáñez et al., 2018), allow to concurrently devise low-dimensional descriptions of the parameter space and functional approximation of the solution manifold, leading to the so-called *hybrid twins* paradigm (Chinesta et al., 2020). Although both a priori and a posteriori ROMs have been utilised to solve parametrised PDEs and to devise parametric response surfaces, it is not possible to know a priori which reduction approach will perform better for a given problem and, to the best of the author's knowledge, a comparison is presented for the first time in Giacomini et al., (2020b).

1.4 Objectives of the thesis

The primary objective of this thesis is to develop a new methodology combining high-order method and model order reduction to solve multidimensional geometrically parametrised problem. The reasons of using a high-order method such as hybridisable discontinuous Galerkin (HDG) within a geometrically parametrised Stokes flow framework are different. First, the use of HDG for the spatial discretisation guarantees that equal order of approximation can be used for all the variables circumventing the so-called Ladyzhenskaya-Babuška-Brezzi (LBB) condition. This is of special importance in this work, where geometrically parametrised domains are considered with curved boundaries. The use of the same degree of approximation for all the variables means that standard isoparametric elements can be used. In contrast, the work in Sevilla et al., 2020b, employing standard FEs, required the use of sub-parametric or super-parametric formulations in the presence of curved boundaries due to the different degree of approximation used for the velocity and pressure, as required to satisfy the LBB condition. Second, the HDG mixed formulation allows separating exactly the terms introduced by the parametric mapping. Different approaches, as the classical FEM used in Sevilla et al., (2020b), leads to the need to use numerical separation techniques to obtain such approximations. Third, the proposed HDG-PGD approach facilitates the imposition of the Dirichlet boundary conditions as in the HDG context all boundary conditions are weakly imposed. Last, looking to future perspectives and applications, this new methodology is designed to face more complex problems exploiting all the features of high-order techniques. For that reason, a digression about the Oseen equation is also presented showing an application of the method to a different problem, in particular, to flow problems defined in fluids with parametrised viscosity. This is useful also to highlight the major challenge of operating in a parametrised geometry respect to parametrised physical proprieties. Moreover, the merger of the HDG-PGD solver for a geometrically parametrised Stokes equation with the one for the Oseen equation with parametrised viscosity paves the way for the future development of an HDG-PGD solver for Navier-Stokes equations with coupled parametrised viscosity (i.e. Reynolds number) and parametrised domain. Between all the possible model order reduction techniques that literature offers, the proper generalised decomposition (PGD) have been chosen, mainly in its a priori framework. This coupling shapes the so-called HDG-PGD methodology, formulated for the steady Stokes equation in geometrically parametrised domains. The a posteriori framework of the PGD is also developed to devise a critical comparison between the two techniques coupled with the HDG solver.

In particular, the following contributions have been realized:

1. **Development and implementation of HDG formulation for axisymmetric Stokes flow**. Considering the Stokes equation, the classical HDG formulation is obtained showing the proprieties of convergence of the method.

Through a change of coordinates, the axisymmetric formulation is devised for a three-dimensional problem. Introducing a suitable hypothesis it is shown how the implementation of the axisymmetric formulation reduces to a classical bi-dimensional problem accounting for one extra variable. The proposed formulation is validated showing optimal rates of convergence for two academic problems equipped with analytical solutions. No published contribution has been extracted from this work.

2. **Development and implementation of HDG-PGD formulation for geometrically parametrised Stokes flow**. Starting from the Stokes equation, the weak form of the multidimensional parametrised Stokes problem is devised. Affine geometrical mapping is applied to operate on a reference parameter-independent domain. Separability hypothesis is introduced and the HDG-PGD Separability hypothesis is introduced and the HDG-PGD algorithm is described. The multidimensional Stokes problem is thus solved with the proposed HDG-PGD technique. First, the solver is validated for different scenarios using academic problems equipped with analytical solutions. Then, the method is exploited to solve problems of physical interest in microfluidics. This work outlined the published paper "Hybridisable discontinuous Galerkin solution of geometrically parametrised Stokes flows" (Sevilla, Borchini, Giacomini, and Huerta, 2020a).

3. **Comparison between a priori and a posteriori PGD**. The proposed a priori solver is compared with an a posteriori PGD technique. Accuracy and cost, calculated in terms of total calls to the spatial solver, are examined. In particular, both techniques are used to devise response surfaces in context of microfluidics applications. This work outlined the submitted paper "Separated response surfaces for flows in parametrised domains: comparison of a priori and a posteriori PGD algorithms" (Giacomini, Borchini, Sevilla, and Huerta, 2020b).

4. **Development and implementation of HDG-PGD formulation for Oseen equations with parametrised viscosity**. Considering the Oseen equation, obtained from a linearisation of the steady Navier-Stokes equation, the HDG formulation is devised. Exploiting the HDG-PGD framework defined, the proposed HDG-PGD solver is used to solve the multidimensional Oseen equations with parametrised viscosity. No published contribution has been extracted from this work.

1.5 Chapters overview

This section outlines the structure of the thesis detailing, in particular, the contents of each one of the chapters.

Chapter 2 is dedicated to the first contribution of the thesis and aims to devise the HDG axisymmetric formulation for the Stokes equation. Two possible cases are analysed, whether the axis of symmetry intersects the computational domain or not. Regarding domains intersecting the axis of symmetry, a new boundary condition needs to be introduced. A comparison between the resolution of a three-dimensional problem via a classical three-dimensional HDG formulation and via the proposed axisymmetric formulation is made focusing on the number of degrees of freedom used.

Chapter 3 is dedicated to the central contribution of this thesis, the formulation and development of the HDG-PGD methodology for the Stokes equation in a geometrically parametrised domain. The multidimensional problem is solved with the proposed HDG-PGD technique exploiting a projection on a lower-dimensional space defined by either space or parameters. Each term of the recursively computed reduced basis is obtained solving a non-linear problem through an alternate direction algorithm. The proposed solver is validated for different scenarios using academic problems equipped with analytical solutions. Bi-dimensional, axisymmetric and three-dimensional problems are studied. Then, the method is employed to solve problems of physical interest in microfluidics.

Chapter 4 presents the second main contribution of this thesis and develops a comparison between two conceptually different model order reduction techniques in coupling with the high-order solver HDG. The proposed a priori HDG-PGD solver is compared with the a posteriori PGD technique introduced by Modesto et al., (2015) and Díez et al., (2018, 2019). A critical comparison of the two reduction techniques is performed stating attractive properties and drawbacks of both and extensive numerical experiments are presented to validate this comparison. Both the influence of the number of parameters affecting the shape of the geometry and the influence of their range of variation on the reduced solution is investigated. Costs, calculated in terms of total calls to the spatial solver, are examined and reported for both approaches. The two techniques are applied to compute separate response surfaces to evaluate real-time quantities of interest, e.g. the drag force, in the context of microfluidics applications.

Chapter 5 summarises the results presented and presents possible future perspectives and developments starting from the work done in this thesis.

Appendix A develops one of the possible extensions presented in chapter 5 consisting of the application of the HDG-PGD methodology to a different parametric problem. Considering a linearisation of the convective term of the steady Navier-Stokes equation, the Oseen equations are obtained. Their parametric counterpart is discussed for the case of parametrised material parameters. Preliminary numerical results for diffusion-dominated and convection-dominated flows are presented using an academic test case with parametrised viscosity.

Chapter 2

HDG solution of Stokes flow problems

2.1 Problem statement

Let us consider a domain $\Omega \subset \mathbb{R}^{\mathtt{n_{sd}}}$, where $\mathtt{n_{sd}}$ is the number of spatial dimensions. The strong form of the stationary Stokes problem is obtained by neglecting the transient and convective effects in the full incompressible Navier–Stokes equations (Donea et al., 2003). The so-called velocity-pressure formulation is so obtained and reads

$$\begin{cases} -\boldsymbol{\nabla}\cdot(\nu\boldsymbol{\nabla}\boldsymbol{u} - p\mathbf{I}_{\mathtt{n_{sd}}}) = \boldsymbol{s} & \text{in } \Omega, \\ \boldsymbol{\nabla}\cdot\boldsymbol{u} = 0 & \text{in } \Omega, \\ \boldsymbol{u} = \boldsymbol{u}_D & \text{on } \Gamma_D, \\ \boldsymbol{n}\cdot\left(\nu\boldsymbol{\nabla}\boldsymbol{u} - p\mathbf{I}_{\mathtt{n_{sd}}}\right) = \boldsymbol{g}_N & \text{on } \Gamma_N, \\ \boldsymbol{u}\cdot\boldsymbol{D} + \boldsymbol{n}\cdot\left(\nu\boldsymbol{\nabla}\boldsymbol{u} - p\mathbf{I}_{\mathtt{n_{sd}}}\right)\boldsymbol{E} = \mathbf{0} & \text{on } \Gamma_S. \end{cases} \tag{2.1}$$

where unknowns $\boldsymbol{u}$ and p denote the velocity and the dynamic pressure, respectively, $\nu{>}0$ is the kinematic viscosity, $\boldsymbol{s}$ is the volumetric source and $\boldsymbol{n}$ is the outward unit normal vector to $\partial\Omega$. The boundary of the domain, $\partial\Omega$, is partitioned into the non-overlapping Dirichlet, Γ_D, Neumann, Γ_N, and slip, Γ_S, boundaries such that $\overline{\partial\Omega}{=}\overline{\Gamma}_D \cup \overline{\Gamma}_N \cup \overline{\Gamma}_S$. On the Dirichlet boundary the velocity is given by $\boldsymbol{u}_D$. On the Neumann boundary the *pseudo-traction* is given by $\boldsymbol{g}_N$. Finally, on the slip boundary, the matrices $\boldsymbol{D}$ and $\boldsymbol{E}$ are given by $\boldsymbol{D}{=}[\boldsymbol{n}, \mathbf{0}_{\mathtt{n_{sd}}\times(\mathtt{n_{sd}}-1)}]$ and $\boldsymbol{E}{=}[\mathbf{0}, \boldsymbol{t}_1, ..., \boldsymbol{t}_{\mathtt{n_{sd}}-1}]$, as detailed in Giacomini et al., (2020c). The tangential vectors $\boldsymbol{t}_k$, for $k{=}1, \ldots \mathtt{n_{sd}} - 1$ are such that $\{\boldsymbol{n}, \boldsymbol{t}_1, ..., \boldsymbol{t}_{\mathtt{n_{sd}}-1}\}$ form an orthonormal system of vectors.

Remark 1. *As noted by Donea et al., (2003), a velocity-pressure formulation enforces a pseudo-traction. To enforce a boundary traction an alternative formulation must be considered, the so-called Cauchy-stress formulation (Giacomini et al., 2020c).*

The free divergence condition in equation (2.1) induces the compatibility condition

$$\langle 1, \boldsymbol{u}_D\cdot\boldsymbol{n}\rangle_{\Gamma_D} + \langle 1, \boldsymbol{u}\cdot\boldsymbol{n}\rangle_{\partial\Omega\setminus\Gamma_D} = 0, \tag{2.2}$$

where $\langle\cdot,\cdot\rangle_S$ denotes the standard $\mathcal{L}_2$ scalar product in any domain $S \subset \partial\Omega$.

Besides, it is worth noting that, if $\Gamma_N{=}\emptyset$, an additional constraint to avoid the indeterminacy of the pressure is required. One common option (Cockburn et al., 2009b, 2014; Giacomini et al., 2018; Nguyen et al., 2010b) that is considered here, consists of imposing the mean pressure on the boundary of the domain, namely

$$\Big\langle \frac{1}{|\partial\Omega|} p, 1 \Big\rangle_{\partial\Omega} = 0. \tag{2.3}$$

2.2 HDG formulation

This section briefly presents the HDG formulation for the Stokes problem. The presentation is based on previous work on HDG methods found in Cockburn et al., (2009b, 2011, 2014) and Giacomini et al., (2018, 2020c).

2.2.1 Mixed formulation

Let us consider a subdivision of the domain Ω in $\mathtt{n_{el}}$ disjoint subdomains Ω_e such that

$$\overline{\Omega} = \bigcup_{e=1}^{\mathtt{n_{el}}} \overline{\Omega}_e. \tag{2.4}$$

The interior boundaries of the subdomains define the so-called mesh skeleton or internal interface Γ as

$$\Gamma := \left[\bigcup_{e=1}^{\mathtt{n_{el}}} \partial\Omega_e \right] \setminus \partial\Omega. \tag{2.5}$$

Introducing the so-called *mixed variable* $\boldsymbol{L}{=}-\nu\boldsymbol{\nabla}\boldsymbol{u}$, the Stokes problem can be written as a first-order system of equations in the broken computational domain, namely

$$\begin{cases} \boldsymbol{L}_e + \nu\boldsymbol{\nabla}\boldsymbol{u}_e = \boldsymbol{0} & \text{in } \Omega_e, \text{ and for } e = 1,\dots,\mathtt{n_{el}}, \\ \boldsymbol{\nabla}\cdot\big(\boldsymbol{L}_e + p_e\mathbf{I}_{\mathtt{n_{sd}}}\big) = \boldsymbol{s} & \text{in } \Omega_e, \text{ and for } e = 1,\dots,\mathtt{n_{el}}, \\ \boldsymbol{\nabla}\cdot\boldsymbol{u}_e = 0 & \text{in } \Omega_e, \text{ and for } e = 1,\dots,\mathtt{n_{el}}, \\ \boldsymbol{u}_e = \boldsymbol{u}_D & \text{on } \partial\Omega_e \cap \Gamma_D, \\ \boldsymbol{n}\cdot\big(\boldsymbol{L}_e + p_e\mathbf{I}_{\mathtt{n_{sd}}}\big) = -\boldsymbol{g}_N & \text{on } \partial\Omega_e \cap \Gamma_N, \\ \boldsymbol{u}_e\cdot\boldsymbol{D} - \boldsymbol{n}\cdot\big(\boldsymbol{L}_e + p_e\mathbf{I}_{\mathtt{n_{sd}}}\big)\boldsymbol{E} = \boldsymbol{0} & \text{on } \partial\Omega_e \cap \Gamma_S, \\ [\![\boldsymbol{u}\otimes\boldsymbol{n}]\!] = \boldsymbol{0} & \text{on } \Gamma, \\ [\![\boldsymbol{n}\cdot\big(\boldsymbol{L} + p\mathbf{I}_{\mathtt{n_{sd}}}\big)]\!] = \boldsymbol{0} & \text{on } \Gamma, \end{cases} \tag{2.6}$$

where the last two equations, known as *transmission conditions*, impose the continuity of the velocity and the normal flux on the mesh skeleton. Following Montlaur et al., (2008), the *jump* operator $[\![\cdot]\!]$ is defined as the sum from the left, Ω_l, and right, Ω_r,

elements of a given portion of the interface Γ, that is

$$[\![\odot]\!] = \odot_l + \odot_r. \tag{2.7}$$

2.2.2 Strong form of the local and global problems

The HDG method solves the mixed problem of equation (2.6) in two steps. First, the so-called *local problems* are considered

$$\begin{cases} \boldsymbol{L}_e + \nu \boldsymbol{\nabla} \boldsymbol{u}_e = \boldsymbol{0} & \text{in } \Omega_e, \text{ and for } e = 1, \dots, \mathtt{n_{el}}, \\ \boldsymbol{\nabla} \cdot \left(\boldsymbol{L}_e + p_e \mathbf{I}_{\mathtt{n_{sd}}} \right) = \boldsymbol{s} & \text{in } \Omega_e, \text{ and for } e = 1, \dots, \mathtt{n_{el}}, \\ \boldsymbol{\nabla} \cdot \boldsymbol{u}_e = 0 & \text{in } \Omega_e, \text{ and for } e = 1, \dots, \mathtt{n_{el}}, \\ \boldsymbol{u}_e = \boldsymbol{u}_D & \text{on } \partial\Omega_e \cap \Gamma_D, \\ \boldsymbol{u}_e = \hat{\boldsymbol{u}} & \text{on } \partial\Omega_e \setminus \Gamma_D, \\ \left\langle \dfrac{1}{|\partial\Omega_e|} p_e, 1 \right\rangle_{\partial\Omega_e} = \rho_e, & \text{for } e = 1, \dots, \mathtt{n_{el}}, \end{cases} \tag{2.8}$$

where $\hat{\boldsymbol{u}}$ is the so-called hybrid variable, which is an independent variable representing the trace of the solution on the element faces, and ρ_e is the mean value of the pressure on the boundary $\partial\Omega_e$. It is worth noting that the local problem is a pure Dirichlet problem and therefore, the last condition in equation (2.8) is introduced to ensure the uniqueness of the pressure. The local problems can be solved independently, element by element, to write $\boldsymbol{L}_e$, $\boldsymbol{u}_e$ and p_e in terms of $\hat{\boldsymbol{u}}$ and ρ_e along the interface $\Gamma \cup \Gamma_N \cup \Gamma_S$.

Second, the so-called *global problem* is defined to impose the continuity of the normal flux on the inter-element faces and the Neumann and slip boundary conditions, namely

$$\begin{cases} [\![\boldsymbol{n} \cdot \left(\boldsymbol{L} + p \mathbf{I}_{\mathtt{n_{sd}}} \right)]\!] = \boldsymbol{0} & \text{on } \Gamma, \\ \boldsymbol{n} \cdot \left(\boldsymbol{L}_e + p_e \mathbf{I}_{\mathtt{n_{sd}}} \right) = -\boldsymbol{g}_N & \text{on } \partial\Omega_e \cap \Gamma_N, \\ \boldsymbol{u}_e \cdot \boldsymbol{D} - \boldsymbol{n} \cdot \left(\boldsymbol{L}_e + p_e \mathbf{I}_{\mathtt{n_{sd}}} \right) \boldsymbol{E} = \boldsymbol{0} & \text{on } \partial\Omega_e \cap \Gamma_S. \end{cases} \tag{2.9}$$

It is worth noting that, due to the unique definition of the hybrid variable on each face and the Dirichlet boundary condition in the local problems, there is no need to enforce the continuity of the solution in the global problem.

The constraint of equation (2.2), induced by the incompressibility condition, is also considered in the global problem and written in terms of the hybrid variable as

$$\langle 1, \boldsymbol{u}_D \cdot \boldsymbol{n} \rangle_{\Gamma_D} + \langle 1, \hat{\boldsymbol{u}} \cdot \boldsymbol{n} \rangle_{(\partial\Omega \setminus \Gamma_D)} = 0. \tag{2.10}$$

2.2.3 Weak form of the local and global problems

The following discrete functional spaces are introduced:

$$\begin{aligned}
\mathcal{V}^h(\Omega) &:= \{v \in \mathcal{L}_2(\Omega) : v|_{\Omega_e} \in \mathcal{P}^k(\Omega_e)\ \forall \Omega_e\,,\ e = 1, \ldots, \mathtt{n_{el}}\},\\
\widehat{\mathcal{V}}^h(S) &:= \{\hat{v} \in \mathcal{L}_2(S) : \hat{v}|_{\Gamma_i} \in \mathcal{P}^k(\Gamma_i)\ \forall \Gamma_i \subset S \subseteq \Gamma \cup \partial\Omega\},\\
\widehat{\boldsymbol{\mathcal{V}}}^h &:= \left[\widehat{\mathcal{V}}^h(\Gamma \cup \Gamma_N \cup \Gamma_S)\right]^{\mathtt{n_{sd}}},\\
\boldsymbol{\mathcal{V}}^h &:= \left[\mathcal{V}^h(\Omega)\right]^{\mathtt{n_{sd}}},\\
\boldsymbol{\mathcal{W}}^h &:= \left[\mathcal{V}^h(\Omega)\right]^{\mathtt{n_{sd}}\times\mathtt{n_{sd}}},
\end{aligned}$$

where $\mathcal{P}^k(\Omega_e)$ and $\mathcal{P}^k(\Gamma_i)$ stand for the spaces of polynomial functions of complete degree at most k in Ω_e and on Γ_i respectively.

The weak form of the local problems, for e=1, ..., $\mathtt{n_{el}}$, reads: given $\boldsymbol{u}_D$ on Γ_D and $\hat{\boldsymbol{u}}^h$ on $\Gamma \cup \Gamma_N \cup \Gamma_S$, find $(\boldsymbol{L}_e^h, \boldsymbol{u}_e^h, p_e^h) \in \boldsymbol{\mathcal{W}}^h \times \boldsymbol{\mathcal{V}}^h \times \mathcal{V}^h$ that satisfy

$$\begin{aligned}
A_{LL}(\boldsymbol{W}, \boldsymbol{L}_e^h) + A_{Lu}(\boldsymbol{W}, \boldsymbol{u}_e^h) &= L_L(\boldsymbol{W}) + A_{L\hat{u}}(\boldsymbol{W}, \hat{\boldsymbol{u}}^h),\\
A_{uL}(\boldsymbol{v}, \boldsymbol{L}_e^h) + A_{uu}(\boldsymbol{v}, \boldsymbol{u}_e^h) + A_{up}(\boldsymbol{v}, p_e^h) &= L_u(\boldsymbol{v}) + A_{u\hat{u}}(\boldsymbol{v}, \hat{\boldsymbol{u}}^h),\\
A_{pu}(v, \boldsymbol{u}_e^h) &= L_p(v) + A_{p\hat{u}}(v, \hat{\boldsymbol{u}}^h),\\
A_{\rho p}(1, p_e^h) &= A_{\rho\rho}(1, \rho_e^h),
\end{aligned} \tag{2.11}$$

for all $(\boldsymbol{W}, \boldsymbol{v}, v) \in \boldsymbol{\mathcal{W}}^h \times \boldsymbol{\mathcal{V}}^h \times \mathcal{V}^h$, where the bilinear and linear forms of the local problem are given by

$$\begin{aligned}
A_{LL}(\boldsymbol{W}, \boldsymbol{L}) &:= -\big(\boldsymbol{W}, \nu^{-1}\boldsymbol{L}\big)_{\Omega_e}, & A_{Lu}(\boldsymbol{W}, \boldsymbol{u}) &:= \big(\boldsymbol{\nabla}\cdot \boldsymbol{W}, \boldsymbol{u}\big)_{\Omega_e},\\
A_{L\hat{u}}(\boldsymbol{W}, \hat{\boldsymbol{u}}) &:= \langle \boldsymbol{n}\cdot\boldsymbol{W}, \hat{\boldsymbol{u}}\rangle_{\partial\Omega_e\setminus\Gamma_D}, & A_{uL}(\boldsymbol{v}, \boldsymbol{L}) &:= \big(\boldsymbol{v}, \boldsymbol{\nabla}\cdot\boldsymbol{L}\big)_{\Omega_e},\\
A_{uu}(\boldsymbol{v}, \boldsymbol{u}) &:= \langle \boldsymbol{v}, \boldsymbol{\tau}\boldsymbol{u}\rangle_{\partial\Omega_e}, & A_{up}(\boldsymbol{v}, p) &:= \big(\boldsymbol{v}, \boldsymbol{\nabla}p\big)_{\Omega_e},\\
A_{u\hat{u}}(\boldsymbol{v}, \hat{\boldsymbol{u}}) &:= \langle \boldsymbol{v}, \boldsymbol{\tau}\hat{\boldsymbol{u}}\rangle_{\partial\Omega_e\setminus\Gamma_D}, & A_{pu}(v, \boldsymbol{u}) &:= \big(\boldsymbol{\nabla}v, \boldsymbol{u}\big)_{\Omega_e},\\
A_{p\hat{u}}(v, \hat{\boldsymbol{u}}) &:= \langle v, \hat{\boldsymbol{u}}\cdot\boldsymbol{n}\rangle_{\partial\Omega_e\setminus\Gamma_D}, & A_{\rho p}(w, p) &:= \langle w, |\partial\Omega_e|^{-1}p\rangle_{\partial\Omega_e},\\
A_{\rho\rho}(w, \rho) &:= w\rho,
\end{aligned} \tag{2.12}$$

and

$$\begin{aligned}
L_L(\boldsymbol{W}) &:= \langle \boldsymbol{n}\cdot\boldsymbol{W}, \boldsymbol{u}_D\rangle_{\partial\Omega_e\cap\Gamma_D},\\
L_u(\boldsymbol{v}) &:= \big(\boldsymbol{v}, \boldsymbol{s}\big)_{\Omega_e} + \langle \boldsymbol{v}, \boldsymbol{\tau}\boldsymbol{u}_D\rangle_{\partial\Omega_e\cap\Gamma_D},\\
L_p(v) &:= \langle v, \boldsymbol{u}_D\cdot\boldsymbol{n}\rangle_{\partial\Omega_e\cap\Gamma_D},
\end{aligned} \tag{2.13}$$

respectively, where $(\cdot,\cdot)_D$ denotes the standard $\mathcal{L}_2$ scalar product in a generic subdomain D and $\boldsymbol{\tau}$ is the stabilisation tensor, whose selection has an important influence on the accuracy, stability and convergence properties of the resulting HDG method (Cockburn et al., 2009c; Nguyen et al., 2009c,d, 2010b).

Similarly, the weak form of the global problem is: find $\hat{\boldsymbol{u}}^h \in \widehat{\boldsymbol{\mathcal{V}}}^h$ and $\rho^h \in \mathbb{R}^{\mathtt{n_{el}}}$ that satisfies

$$\begin{aligned}\sum_{e=1}^{\mathtt{n_{el}}} \left\{ A_{\hat{u}L}(\hat{\boldsymbol{v}}, \boldsymbol{L}_e^h) + A_{\hat{u}u}(\hat{\boldsymbol{v}}, \boldsymbol{u}_e^h) + A_{\hat{u}p}(\hat{\boldsymbol{v}}, p_e^h) + A_{\hat{u}\hat{u}}(\hat{\boldsymbol{v}}, \hat{\boldsymbol{u}}^h) \right\} &= \sum_{e=1}^{\mathtt{n_{el}}} \left\{ L_{\hat{u}}(\hat{\boldsymbol{v}}) \right\}, \\ A_{p\hat{u}}(1, \hat{\boldsymbol{u}}^h) &= -L_p(1),\end{aligned} \tag{2.14}$$

for all $\hat{\boldsymbol{v}} \in \widehat{\boldsymbol{\mathcal{V}}}^h$, where the multi-dimensional bilinear and linear forms of the global problem are given by

$$\begin{aligned} A_{\hat{u}L}(\hat{\boldsymbol{v}}, \boldsymbol{L}) :=& \langle \hat{\boldsymbol{v}}, \boldsymbol{n} \cdot \boldsymbol{L} \rangle_{\partial\Omega_e \setminus (\Gamma_D \cup \Gamma_S)} - \langle \hat{\boldsymbol{v}}, \boldsymbol{n} \cdot \boldsymbol{L}\boldsymbol{E} \rangle_{\partial\Omega_e \cap \Gamma_S} \\ A_{\hat{u}u}(\hat{\boldsymbol{v}}, \boldsymbol{u}) :=& \langle \hat{\boldsymbol{v}}, \boldsymbol{\tau}\boldsymbol{u} \rangle_{\partial\Omega_e \setminus (\Gamma_D \cup \Gamma_S)} - \langle \hat{\boldsymbol{v}}, (\boldsymbol{\tau}\boldsymbol{u}) \cdot \boldsymbol{E} \rangle_{\partial\Omega_e \cap \Gamma_S} \\ A_{\hat{u}p}(\hat{\boldsymbol{v}}, p) :=& \langle \hat{\boldsymbol{v}}, p\boldsymbol{n} \rangle_{\partial\Omega_e \setminus (\Gamma_D \cup \Gamma_S)} \\ A_{\hat{u}\hat{u}}(\hat{\boldsymbol{v}}, \hat{\boldsymbol{u}}) :=& -\langle \hat{\boldsymbol{v}}, \boldsymbol{\tau}\hat{\boldsymbol{u}} \rangle_{\partial\Omega_e \setminus (\Gamma_D \cup \Gamma_S)} + \langle \hat{\boldsymbol{v}}, \hat{\boldsymbol{u}} \cdot \boldsymbol{D} + (\boldsymbol{\tau}\hat{\boldsymbol{u}}) \cdot \boldsymbol{E} \rangle_{\partial\Omega_e \cap \Gamma_S} \end{aligned} \tag{2.15}$$

and

$$L_{\hat{u}}(\hat{\boldsymbol{v}}) := -\langle \hat{\boldsymbol{v}}, \boldsymbol{g}_N \rangle_{\partial\Omega_e \cap \Gamma_N}, \tag{2.16}$$

respectively.

2.2.4 Discretisation

Introducing an isoparametric formulation with equal interpolation for all the local and global variables (Sevilla et al., 2016b, 2018a,b), the discretisation of the weak form of the local and global problems given by (2.11) and (2.14), respectively, can be obtained. Local problem, leads to a system of equations for each element with the following structure:

$$\begin{bmatrix} \mathbf{A}_{LL} & \mathbf{A}_{Lu} & \mathbf{0} & \mathbf{0} \\ \mathbf{A}_{Lu}^T & \mathbf{A}_{uu} & \mathbf{A}_{up} & \mathbf{0} \\ \mathbf{0} & \mathbf{A}_{up}^T & \mathbf{0} & \boldsymbol{a}_{\rho p}^T \\ \mathbf{0} & \mathbf{0} & \boldsymbol{a}_{\rho p} & 0 \end{bmatrix}_e \begin{Bmatrix} \mathbf{L} \\ \mathbf{u} \\ \mathbf{p} \\ \zeta \end{Bmatrix}_e = \begin{Bmatrix} \mathbf{f}_L \\ \mathbf{f}_u \\ \mathbf{f}_p \\ 0 \end{Bmatrix}_e + \begin{bmatrix} \mathbf{A}_{L\hat{u}} \\ \mathbf{A}_{u\hat{u}} \\ \mathbf{A}_{p\hat{u}} \\ \mathbf{0} \end{bmatrix}_e \hat{\mathbf{u}} + \begin{Bmatrix} \mathbf{0} \\ \mathbf{0} \\ \mathbf{0} \\ 1 \end{Bmatrix}_e \rho_e, \tag{2.17}$$

where $\mathbf{L}$, $\mathbf{u}$, $\mathbf{p}$ and $\hat{\mathbf{u}}$ denote the nodal values of $\boldsymbol{L}$, $\boldsymbol{u}$, p and $\hat{\boldsymbol{u}}$ respectively and the constraint on the mean value ρ of the pressure on the element boundaries is enforced using the Lagrange multiplier ζ.

Similarly, the discretisation of the global problem leads to a system of equations for the trace of the velocity on the element boundaries and the mean value of the pressure

in each element, namely

$$\sum_{e=1}^{\mathtt{n_{el}}} \left\{ \begin{bmatrix} \mathbf{A}_{\hat{u}L} & \mathbf{A}_{\hat{u}u} & \mathbf{A}_{\hat{u}p} \end{bmatrix}_e \begin{Bmatrix} \mathbf{L} \\ \mathbf{u} \\ \mathbf{p} \end{Bmatrix}_e + [\mathbf{A}_{\hat{u}\hat{u}}]_e \, \hat{\mathbf{u}} \right\} = \sum_{e=1}^{\mathtt{n_{el}}} [\mathbf{f}_{\hat{u}}]_e, \tag{2.18}$$

$$\mathbf{1}^T [\mathbf{A}_{p\hat{u}}]_e \hat{\mathbf{u}} = -\mathbf{1}^T [\mathbf{f}_p]_e.$$

As usual in an HDG context, the local problem of equation (2.17) is used to express the gradient of the velocity, the velocity and the pressure in terms of the trace of the velocity and the mean pressure. Introducing these expressions into the global problem leads to the global system

$$\begin{bmatrix} \widehat{\mathbf{K}} & \mathbf{G} \\ \mathbf{G}^T & \mathbf{0} \end{bmatrix} \begin{Bmatrix} \hat{\mathbf{u}} \\ \boldsymbol{\rho} \end{Bmatrix} = \begin{Bmatrix} \hat{\mathbf{f}}_{\hat{u}} \\ \hat{\mathbf{f}}_{\rho} \end{Bmatrix}, \tag{2.19}$$

where the only unknowns are the trace of the velocity and the mean pressure and

$$\widehat{\mathbf{K}} = \mathop{\mathbf{A}}_{e=1}^{\mathtt{n_{el}}} \begin{bmatrix} \mathbf{A}_{\hat{u}L} & \mathbf{A}_{\hat{u}u} & \mathbf{A}_{\hat{u}p} & \mathbf{0} \end{bmatrix}_e \begin{bmatrix} \mathbf{A}_{LL} & \mathbf{A}_{Lu} & \mathbf{0} & \mathbf{0} \\ \mathbf{A}_{Lu}^T & \mathbf{A}_{uu} & \mathbf{A}_{up} & \mathbf{0} \\ \mathbf{0} & \mathbf{A}_{up}^T & \mathbf{0} & \boldsymbol{a}_{\rho p}^T \\ \mathbf{0} & \mathbf{0} & \boldsymbol{a}_{\rho p} & 0 \end{bmatrix}_e^{-1} \begin{bmatrix} \mathbf{A}_{L\hat{u}} \\ \mathbf{A}_{u\hat{u}} \\ \mathbf{A}_{p\hat{u}} \\ \mathbf{0} \end{bmatrix}_e + [\mathbf{A}_{\hat{u}\hat{u}}]_e,$$

$$\mathbf{G}^T = \begin{bmatrix} \mathbf{1}^T[\mathbf{A}_{p\hat{u}}]_1 \\ \mathbf{1}^T[\mathbf{A}_{p\hat{u}}]_2 \\ \vdots \\ \mathbf{1}^T[\mathbf{A}_{p\hat{u}}]_{\mathtt{n_{el}}} \end{bmatrix}_e,$$

$$\hat{\mathbf{f}}_{\hat{u}} = \mathop{\mathbf{A}}_{e=1}^{\mathtt{n_{el}}} [\hat{\mathbf{f}}_{\hat{\boldsymbol{u}}}]_e - \begin{bmatrix} \mathbf{A}_{\hat{u}L} & \mathbf{A}_{\hat{u}u} & \mathbf{A}_{\hat{u}p} & \mathbf{0} \end{bmatrix}_e \begin{bmatrix} \mathbf{A}_{LL} & \mathbf{A}_{Lu} & \mathbf{0} & \mathbf{0} \\ \mathbf{A}_{Lu}^T & \mathbf{A}_{uu} & \mathbf{A}_{up} & \mathbf{0} \\ \mathbf{0} & \mathbf{A}_{up}^T & \mathbf{0} & \boldsymbol{a}_{\rho p}^T \\ \mathbf{0} & \mathbf{0} & \boldsymbol{a}_{\rho p} & 0 \end{bmatrix}_e^{-1} \begin{Bmatrix} \mathbf{f}_L \\ \mathbf{f}_u \\ \mathbf{f}_p \\ 0 \end{Bmatrix}_e,$$

$$\hat{\mathbf{f}}_{\rho} = -\begin{bmatrix} \mathbf{1}^T[\mathbf{f}_p]_1 \\ \mathbf{1}^T[\mathbf{f}_p]_2 \\ \vdots \\ \mathbf{1}^T[\mathbf{f}_p]_{\mathtt{n_{el}}} \end{bmatrix}_e.$$

2.2.5 Implementation details

Following Giacomini et al., (2020c) and Sevilla et al., (2016b), the matrices and vectors appearing in the discrete form of the HDG can be particularized. The local elemental variables $\boldsymbol{u}$,p,$\boldsymbol{L}$ are defined in a reference element $\widetilde{\Omega}(\boldsymbol{\xi}), \boldsymbol{\xi}=(\xi_1, \ldots, \xi_{\mathtt{n_{sd}}})$ whereas the

hybrid variable $\hat{\boldsymbol{u}}$, is defined on a reference face $\widetilde{\Gamma}(\boldsymbol{\eta}), \boldsymbol{\eta}{=}(\eta_1, \ldots, \eta_{\mathtt{n_{sd}}})$ as

$$\begin{aligned} \boldsymbol{u}(\boldsymbol{\xi}) &\simeq \sum_{j=1}^{\mathtt{n_{en}}} \mathbf{u}_j N_j(\boldsymbol{\xi}), \qquad p(\boldsymbol{\xi}) \simeq \sum_{j=1}^{\mathtt{n_{en}}} \mathbf{p}_j N_j(\boldsymbol{\xi}), \\ \boldsymbol{L}(\boldsymbol{\xi}) &\simeq \sum_{j=1}^{\mathtt{n_{en}}} \mathbf{L}_j N_j(\boldsymbol{\xi}), \qquad \hat{\boldsymbol{u}}(\boldsymbol{\eta}) \simeq \sum_{j=1}^{\mathtt{n_{fn}}} \hat{\mathbf{u}}_j \hat{N}_j(\boldsymbol{\eta}), \end{aligned}$$

where $\mathbf{u}_j, \mathbf{p}_j, \mathbf{L}_j$ and $\hat{\mathbf{u}}_j$ are the nodal value of the approximation, $\mathtt{n_{en}}$ and $\mathtt{n_{fn}}$ the number of nodes in the element and face, respectively, and N_j and $\hat{N}_j$ the polynomial shape functions in the reference element and face, respectively. An isoparametric transformation is used to map reference and local coordinates

$$\boldsymbol{x}(\boldsymbol{\xi}) = \sum_{i=1}^{\mathtt{n_{en}}} \mathbf{x}_i N_i(\boldsymbol{\xi}),$$

where vector $\boldsymbol{x}_i$, with $i = 1, \ldots, \mathtt{n_{en}}$ denotes the elemental nodal coordinates.

Following Sevilla et al., (2016b), the compact form of the interpolation functions are introduced

$$\begin{aligned} \mathbf{N} &= [N_1 \quad N_2 \quad \ldots \quad N_{\mathtt{n_{en}}}]^T, \qquad \mathbf{N}_{\boldsymbol{n}} = [N_1\boldsymbol{n} \quad N_2\boldsymbol{n} \quad \ldots \quad N_{\mathtt{n_{en}}}\boldsymbol{n}]^T, \\ \hat{\mathbf{N}} &= [\hat{N}_1 \quad \hat{N}_2 \quad \ldots \quad \hat{N}_{\mathtt{n_{fn}}}]^T, \qquad \hat{\mathbf{N}}_{\boldsymbol{n}} = [\hat{N}_1\boldsymbol{n} \quad \hat{N}_2\boldsymbol{n} \quad \ldots \quad \hat{N}_{\mathtt{n_{fn}}}\boldsymbol{n}]^T, \\ \boldsymbol{\nabla}\mathbf{N} &= [(\boldsymbol{J}^{-1}\boldsymbol{\nabla}N_1)^T \quad (\boldsymbol{J}^{-1}\boldsymbol{\nabla}N_2)^T \quad \ldots \quad (\boldsymbol{J}^{-1}\boldsymbol{\nabla}N_{\mathtt{n_{en}}})^T]^T, \\ \mathbf{N}_{\mathtt{n_{sd}}} &= [N_1\mathbf{I}_{\mathtt{n_{sd}}} \quad N_2\mathbf{I}_{\mathtt{n_{sd}}} \quad \ldots \quad N_{\mathtt{n_{en}}}\mathbf{I}_{\mathtt{n_{sd}}}]^T, \\ \mathbf{N}_{\mathtt{n_{sd}^2}} &= [N_1\mathbf{I}_{\mathtt{n_{sd}^2}} \quad N_2\mathbf{I}_{\mathtt{n_{sd}^2}} \quad \ldots \quad N_{\mathtt{n_{en}}}\mathbf{I}_{\mathtt{n_{sd}^2}}]^T, \end{aligned}$$

where $\boldsymbol{n}{=}(n_1, \ldots, n_{\mathtt{n_{sd}}})$ represents the outward unit normal vector to an edge or face, $\boldsymbol{J}$ is the Jacobian of the isoparametric transformation and $\mathbf{I}_{\mathtt{n_{sd}}}$ and $\mathbf{I}_{\mathtt{n_{sd}^2}}$ is the identity matrix of dimension $\mathtt{n_{sd}}$ and $\mathtt{n_{sd}^2}$, respectively.

The different matrices appearing in equation (2.17), computed for each element $e{=}1, \ldots, \mathtt{n_{el}}$, can be expresses as

$$\begin{aligned} [\mathbf{A}_{LL}]_e &= -\sum_{g=1}^{\mathtt{n_{ip}^e}} \nu^{-1}\mathbf{N}_{\mathtt{n_{sd}^2}}(\boldsymbol{\xi}_g^e)\mathbf{N}_{\mathtt{n_{sd}^2}}^T(\boldsymbol{\xi}_g^e)w_g^e, \quad [\mathbf{A}_{Lu}]_e = \sum_{g=1}^{\mathtt{n_{ip}^e}} \boldsymbol{\nabla}\mathbf{N}(\boldsymbol{\xi}_g^e)\mathbf{N}^T(\boldsymbol{\xi}_g^e)w_g^e, \\ [\mathbf{A}_{L\hat{u}}]_e &= \sum_{\partial\Omega_e\backslash\Gamma_D}\sum_{g=1}^{\mathtt{n_{ip}^f}} \mathbf{N}_{\boldsymbol{n}}(\boldsymbol{\xi}_g^f)\hat{\mathbf{N}}^T(\boldsymbol{\xi}_g^f)w_g^f, \quad [\mathbf{A}_{uu}]_e = \sum_{\partial\Omega_e}\sum_{g=1}^{\mathtt{n_{ip}^f}} \mathbf{N}(\boldsymbol{\xi}_g^f)(\boldsymbol{\tau}\mathbf{N}(\boldsymbol{\xi}_g^f))^T w_g^f, \\ [\mathbf{A}_{up}]_e &= \sum_{g=1}^{\mathtt{n_{ip}^e}} \mathbf{N}(\boldsymbol{\xi}_g^e)\boldsymbol{\nabla}\mathbf{N}^T(\boldsymbol{\xi}_g^e)w_g^e, \qquad [\mathbf{A}_{u\hat{u}}]_e = \sum_{\partial\Omega_e\backslash\Gamma_D}\sum_{g=1}^{\mathtt{n_{ip}^f}} \mathbf{N}(\boldsymbol{\xi}_g^f)(\boldsymbol{\tau}\hat{\mathbf{N}}(\boldsymbol{\xi}_g^f))^T w_g^f, \\ [\mathbf{A}_{p\hat{u}}]_e &= \sum_{\partial\Omega_e\backslash\Gamma_D}\sum_{g=1}^{\mathtt{n_{ip}^f}} \mathbf{N}(\boldsymbol{\xi}_g^f)\hat{\mathbf{N}}_{\boldsymbol{n}}^T(\boldsymbol{\xi}_g^f)w_g^f, \qquad [\mathbf{A}_{\rho p}]_e = \sum_{\partial\Omega_e}\sum_{g=1}^{\mathtt{n_{ip}^f}} \mathbf{N}^T(\boldsymbol{\xi}_g^f)w_g^f, \end{aligned}$$

$$[\mathbf{f}_L]_e = \sum_{\partial\Omega_e\cap\Gamma_D}\sum_{g=1}^{\mathtt{n}^{\mathtt{f}}_{\mathtt{ip}}} \mathbf{N}_{\boldsymbol{n}}(\boldsymbol{\xi}^f_g)\boldsymbol{u}^T_D(\boldsymbol{x}^{\boldsymbol{\mu}}(\boldsymbol{\xi}^f_g))w^f_g,$$

$$[\mathbf{f}_u]_e = \sum_{g=1}^{\mathtt{n}^{\mathtt{e}}_{\mathtt{ip}}} \mathbf{N}_{\mathtt{n}_{\mathtt{sd}}}(\boldsymbol{\xi}^e_g)\boldsymbol{s}^T(\boldsymbol{x}^{\boldsymbol{\mu}}(\boldsymbol{\xi}^f_g))w^e_g + \sum_{\partial\Omega_e\cap\Gamma_D}\sum_{g=1}^{\mathtt{n}^{\mathtt{f}}_{\mathtt{ip}}} \mathbf{N}_{\mathtt{n}_{\mathtt{sd}}}(\boldsymbol{\xi}^f_g)(\boldsymbol{\tau}\boldsymbol{u}_D(\boldsymbol{x}^{\boldsymbol{\mu}}(\boldsymbol{\xi}^f_g)))^T w^f_g,$$

$$[\mathbf{f}_p]_e = \sum_{\partial\Omega_e\cap\Gamma_D}\sum_{g=1}^{\mathtt{n}^{\mathtt{f}}_{\mathtt{ip}}} \mathbf{N}_{\boldsymbol{n}}(\boldsymbol{\xi}^f_g)\boldsymbol{u}^T_D(\boldsymbol{x}^{\boldsymbol{\mu}}(\boldsymbol{\xi}^f_g))w^f_g.$$

Analogously the different matrices appearing in equation (2.18), computed for each element e=1, ..., $\mathtt{n}_{\mathtt{el}}$, can be expresses as

$$[\mathbf{A}_{\hat{u}L}]_e = \sum_{\partial\Omega_e\setminus(\Gamma_D\cup\Gamma_S)}\sum_{g=1}^{\mathtt{n}^{\mathtt{f}}_{\mathtt{ip}}} \hat{\mathbf{N}}(\boldsymbol{\xi}^f_g)\mathbf{N}^T_{\boldsymbol{n}}(\boldsymbol{\xi}^f_g)w^f_g - \sum_{\partial\Omega_e\cap\Gamma_S}\sum_{g=1}^{\mathtt{n}^{\mathtt{f}}_{\mathtt{ip}}} \hat{\mathbf{N}}(\boldsymbol{\xi}^f_g)(\mathbf{N}_{\boldsymbol{n}}(\boldsymbol{\xi}^f_g)\boldsymbol{E})^T w^f_g,$$

$$[\mathbf{A}_{\hat{u}u}]_e = \sum_{\partial\Omega_e\setminus(\Gamma_D\cup\Gamma_S)}\sum_{g=1}^{\mathtt{n}^{\mathtt{f}}_{\mathtt{ip}}} \hat{\mathbf{N}}(\boldsymbol{\xi}^f_g)(\boldsymbol{\tau}\mathbf{N}(\boldsymbol{\xi}^f_g))^T w^f_g - \sum_{\partial\Omega_e\cap\Gamma_S}\sum_{g=1}^{\mathtt{n}^{\mathtt{f}}_{\mathtt{ip}}} \hat{\mathbf{N}}(\boldsymbol{\xi}^f_g)(\boldsymbol{\tau}\mathbf{N}(\boldsymbol{\xi}^f_g)\boldsymbol{E})^T w^f_g,$$

$$[\mathbf{A}_{\hat{u}p}]_e = \sum_{\partial\Omega_e\setminus(\Gamma_D\cup\Gamma_S)}\sum_{g=1}^{\mathtt{n}^{\mathtt{f}}_{\mathtt{ip}}} \hat{\mathbf{N}}(\boldsymbol{\xi}^f_g)\mathbf{N}^T(\boldsymbol{\xi}^f_g)w^f_g,$$

$$\begin{aligned}[\mathbf{A}_{\hat{u}\hat{u}}]_e = &- \sum_{\partial\Omega_e\setminus(\Gamma_D\cup\Gamma_S)}\sum_{g=1}^{\mathtt{n}^{\mathtt{f}}_{\mathtt{ip}}} \hat{\mathbf{N}}(\boldsymbol{\xi}^f_g)(\boldsymbol{\tau}\hat{\mathbf{N}}(\boldsymbol{\xi}^f_g))^T w^f_g + \sum_{\partial\Omega_e\cap\Gamma_S}\sum_{g=1}^{\mathtt{n}^{\mathtt{f}}_{\mathtt{ip}}} \hat{\mathbf{N}}(\boldsymbol{\xi}^f_g)(\hat{\mathbf{N}}(\boldsymbol{\xi}^f_g)\boldsymbol{D})^T w^f_g \\ &+ \sum_{\partial\Omega_e\cap\Gamma_S}\sum_{g=1}^{\mathtt{n}^{\mathtt{f}}_{\mathtt{ip}}} \hat{\mathbf{N}}(\boldsymbol{\xi}^f_g)(\boldsymbol{\tau}\hat{\mathbf{N}}(\boldsymbol{\xi}^f_g)\boldsymbol{E})^T w^f_g,\end{aligned}$$

$$[\mathbf{f}_{\hat{u}}]_e = - \sum_{\partial\Omega_e\cap\Gamma_N}\sum_{g=1}^{\mathtt{n}^{\mathtt{f}}_{\mathtt{ip}}} \hat{\mathbf{N}}(\boldsymbol{\xi}^f_g)\boldsymbol{g}^T_N(\boldsymbol{x}^{\boldsymbol{\mu}}(\boldsymbol{\xi}^f_g))w^f_g.$$

In the above expressions, $\boldsymbol{\xi}^e_g$ and w^e_g are the $\mathtt{n}^{\mathtt{e}}_{\mathtt{ip}}$ integration points and weights defined on the reference element and $\boldsymbol{\xi}^f_g$ and w^f_g are the $\mathtt{n}^{\mathtt{f}}_{\mathtt{ip}}$ integration points and weights defined on the reference edge/face.

2.2.6 Local postprocess of the primal variable

As wildly explained in the literature in Sevilla et al., (2016b) and Giacomini et al., (2020c), the solution of the HDG problem obtained solving (2.19) computes the optimal solution for both $\boldsymbol{u}$, p and $\boldsymbol{L}$ with optimal rate of convergence k+1 in $\mathcal{L}_2$ norm, as the polynomial used to approximate these variables are of the same degree. From this, follows that $\boldsymbol{L}$, which is the gradient of the velocity, will be one degree lower than $\boldsymbol{u}$. This allows to develop the concept of superconvergence using local postprocessing (Cockburn et al., 2008). Local postprocessing, thus, can be used to obtain a superconvergent solution for primal variable, i.e. the velocity, called $\boldsymbol{u}^*$, converging

with order $k+2$ in $\mathcal{L}_2$ norm (Cockburn et al., 2008, 2009a). This is achieved by solving the following equations element-by-element:

$$\begin{cases} \boldsymbol{\nabla}\cdot\boldsymbol{\nabla}\boldsymbol{u}^* = -\boldsymbol{\nabla}\cdot\boldsymbol{L} & \text{in } \Omega_e, \\ \boldsymbol{n}\cdot\boldsymbol{\nabla}\boldsymbol{u}^* = -\boldsymbol{n}\cdot\boldsymbol{L} & \text{on } \partial\Omega_e, \end{cases} \tag{2.20}$$

with the additional constraint:

$$\int_{\Omega_e} \boldsymbol{u}^* \, \mathrm{d}\Omega = \int_{\Omega_e} \boldsymbol{u} \, \mathrm{d}\Omega, \tag{2.21}$$

where $\boldsymbol{u}^* \in \mathcal{P}^{k+1}(\Omega_e)$ and k is the polynomial degree of approximation. The week form of the problem can be written as:

$$(\boldsymbol{\nabla}\boldsymbol{v}, \boldsymbol{\nabla}\boldsymbol{u}^*)_{\Omega_e} = -(\boldsymbol{\nabla}\boldsymbol{v}, \boldsymbol{L})_{\Omega_e} \tag{2.22}$$

$$(\boldsymbol{u}^*, 1)_{\Omega_e} = -(\boldsymbol{u}, 1)_{\Omega_e}, \tag{2.23}$$

for all $\boldsymbol{v} \in \mathcal{P}^{k+1}(\Omega_e)$ and the solution $\boldsymbol{u}^*$ converges asymptotically at a faster rate of $k+2$ in $\mathcal{L}_2$ norm for uniform degree of the approximation polynomial k.

2.2.7 Numerical validation

The first example studied to validate the method is the so-called Wang flow (Wang, 1991) in $\Omega=[0,1]^2 \in \mathbb{R}^2$. The analytical solution of the velocity (whose magnitude is shown in figure 2.1) and pressure is given by

$$\begin{aligned} u_x &= 2ay - b\lambda \exp(-\lambda y)\cos(\lambda x), \\ u_y &= b\lambda \exp(-\lambda y)\sin(\lambda x), \\ p &= 0, \end{aligned} \tag{2.24}$$

with parameters selected as a=b=1, λ=10 and kinematic viscosity ν=1.

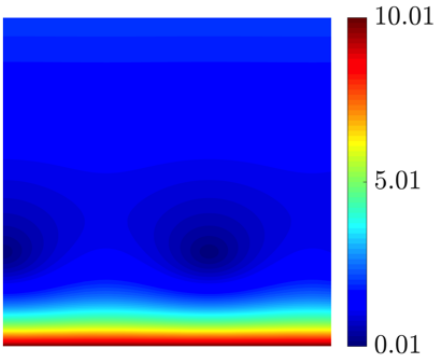

FIGURE 2.1: Wang flow: Analytical solution of the norm of the velocity field.

Neumann boundary conditions are imposed on the bottom part of the domain, defined as $\Gamma_N=\{(x,y) \in \Omega \mid y=0\}$, whereas Dirichlet boundary conditions are imposed on $\Gamma_D=\partial\Omega \setminus \Gamma_N$. A consecutive refinement of uniform triangular meshes with $\mathtt{n_{el}}=\{16, 64, 256, 1024\}$ is used to obtain convergence rates for different degrees of polynomial functions, in particular $k=\{1,2,3,4\}$. Results are shown in figure 2.2. Optimal convergence rates of at least order $k+1$ are obtained for all the variables and $k+2$ for the postprocessed variable, respectively.

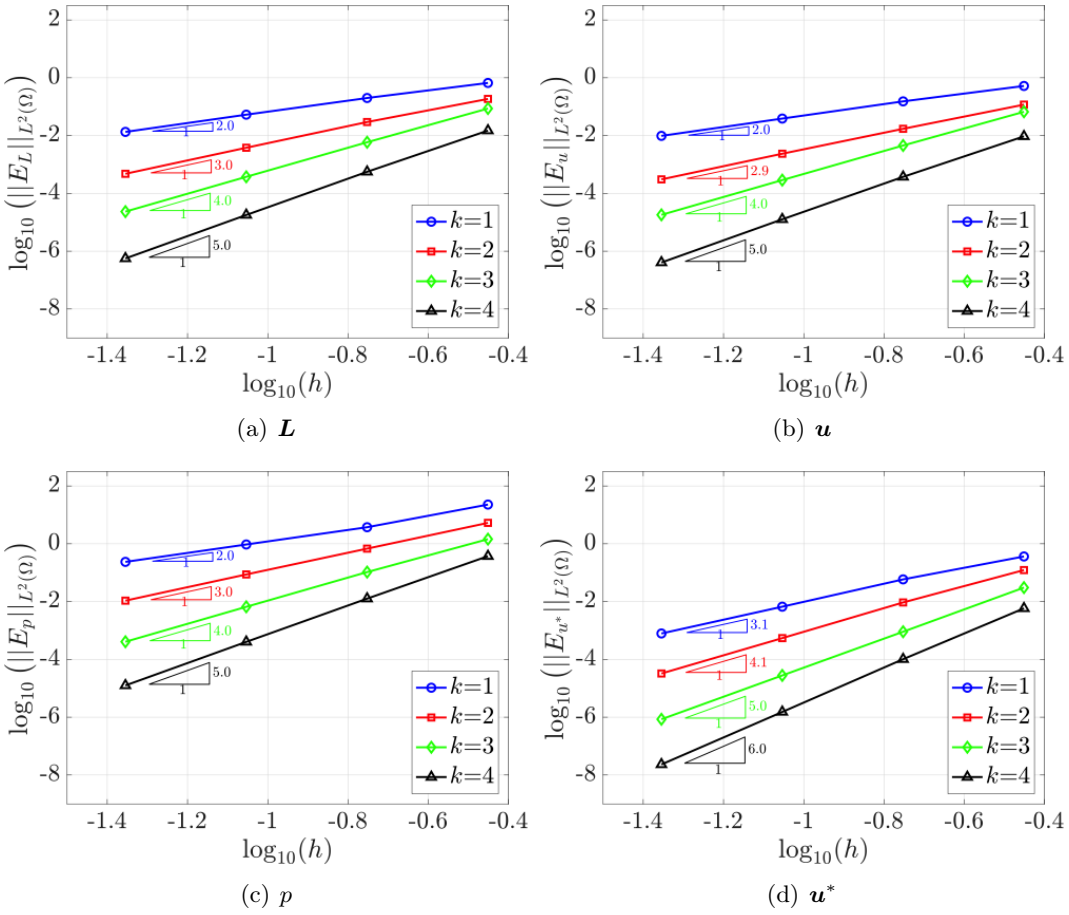

(a) $\boldsymbol{L}$ (b) $\boldsymbol{u}$

(c) p (d) $\boldsymbol{u}^*$

FIGURE 2.2: Wang flow: mesh convergence of the $\mathcal{L}_2$ norm of the error for $\boldsymbol{L}$, $\boldsymbol{u}$, p and $\boldsymbol{u}^*$.

2.3 HDG formulation in axisymmetric problems

This section is dedicated to the derivation and implementation of the HDG formulation for Stokes problems under the hypothesis of axial symmetry. This derivation has not been found anywhere in literature and does not appear in any publications extracted from this thesis. Initially, the three-dimensional case of problem statement presented in section 2.1 is written in cylindrical coordinates. Then, under proper assumptions of axial symmetry and non-rotative flow, it is shown how a 3D axisymmetric problem can be reduced to a 2D problem with one extra unknown.

2.3.1 Cylindrical coordinates

A *cylindrical-Cartesian* transformation allows to rewrite whatever problem from a three-dimensional Cartesian reference system $\boldsymbol{x}=(x,y,z)^T$ to cylindrical coordinates $\boldsymbol{r}=(r,\theta,z)^T$, where r is the radial distance from the z-axis and the angle θ, called azimuth or angular position, defining a two-dimensional polar coordinate system in the reference plane, which is an arbitrary plane orthogonal to the z-axis. To write the Stokes problem in cylindrical coordinates let us previously recall some scholastic relations. Cartesian coordinates $\boldsymbol{x}=(x,y,z)^T$ and cylindrical coordinates $\boldsymbol{r}=(r,\theta,z)^T$ are related by

$$\begin{cases} x = r\cos\theta, \\ y = r\sin\theta, \\ z = z, \end{cases} \qquad \begin{cases} r = \sqrt{x^2+y^2}, \\ \theta = \text{atan2}(y,x), \\ z = z, \end{cases} \tag{2.25}$$

where atan2 is the four-quadrant inverse tangent, which is a usual variation of the arctangent function than produces azimuths such that $\theta \in [-\pi,\pi]$ and is defined as

$$\text{atan2}(y,x) = \begin{cases} \arctan(y/x) & \text{if } x>0 \\ \arctan(y/x)+\pi & \text{if } x<0 \text{ and } y\geq 0 \\ \arctan(y/x)+\pi & \text{if } x<0 \text{ and } y<0 \\ \pi/2 & \text{if } x=0 \text{ and } y>0 \\ -\pi/2 & \text{if } x=0 \text{ and } y<0 \\ \text{undefined} & \text{if } x=0 \text{ and } y=0. \end{cases} \tag{2.26}$$

The Jacobian for cylindrical to Cartesian and Cartesian to cylindrical mappings are respectively

$$\frac{\partial \boldsymbol{x}}{\partial \boldsymbol{r}} := \begin{pmatrix} \cos\theta & -r\sin\theta & 0 \\ \sin\theta & r\cos\theta & 0 \\ 0 & 0 & 1 \end{pmatrix} \quad \frac{\partial \boldsymbol{r}}{\partial \boldsymbol{x}} := \begin{pmatrix} \cos\theta & \sin\theta & 0 \\ -(\sin\theta)/r & (\cos\theta)/r & 0 \\ 0 & 0 & 1 \end{pmatrix} \tag{2.27}$$

with the range of variation $0 \leq r<\infty$, $-\pi\leq\theta<\pi$, and $-\infty<z<\infty$. It is worth noting that $\det(\partial\boldsymbol{x}/\partial\boldsymbol{r})=r$, which is needed for the change of variables in the weak forms.

The cylindrical basis vectors $(\mathbf{e}_r,\mathbf{e}_\theta,\mathbf{e}_z)$ can be written in terms of Cartesian ones $(\mathbf{e}_x,\mathbf{e}_y,\mathbf{e}_z)$ and viceversa

$$\begin{cases} \mathbf{e}_r = \cos\theta\mathbf{e}_x + \sin\theta\mathbf{e}_y, \\ \mathbf{e}_\theta = -\sin\theta\mathbf{e}_x + \cos\theta\mathbf{e}_y, \\ \mathbf{e}_z = \mathbf{e}_z, \end{cases} \qquad \begin{cases} \mathbf{e}_x = \cos\theta\mathbf{e}_r - \sin\theta\mathbf{e}_\theta, \\ \mathbf{e}_y = \sin\theta\mathbf{e}_r + \cos\theta\mathbf{e}_\theta, \\ \mathbf{e}_z = \mathbf{e}_z. \end{cases} \tag{2.28}$$

which are clearly orthonormal as $\mathbf{e}_r \times \mathbf{e}_\theta \cdot \mathbf{e}_z = 1$. Moreover, a Cartesian vector field $\boldsymbol{u}$ may be resolved in this basis

$$\boldsymbol{u} = \mathbf{e}_r u_r + \mathbf{e}_\theta u_\theta + \mathbf{e}_z u_z,$$

where

$$u_r = \boldsymbol{u} \cdot \mathbf{e}_r, \qquad u_\theta = \boldsymbol{u} \cdot \mathbf{e}_\theta, \qquad u_z = \boldsymbol{u} \cdot \mathbf{e}_z.$$

Using the chain rule and relations (2.28), the expression of the gradient operator in cylindrical coordinates can be determined from its Cartesian counterpart

$$\boldsymbol{\nabla}^{\boldsymbol{r}} = \frac{\partial}{\partial x}\mathbf{e}_x + \frac{\partial}{\partial y}\mathbf{e}_y + \frac{\partial}{\partial z}\mathbf{e}_z = \frac{\partial}{\partial r}\mathbf{e}_r + \frac{1}{r}\frac{\partial}{\partial \theta}\mathbf{e}_\theta + \frac{\partial}{\partial z}\mathbf{e}_z. \tag{2.29}$$

Thus, it is straightforward to apply this operator to scalar functions as in the Cartesian case, namely

$$\boldsymbol{\nabla}^{\boldsymbol{r}} v = \frac{\partial v}{\partial r}\mathbf{e}_r + \frac{1}{r}\frac{\partial v}{\partial \theta}\mathbf{e}_\theta + \frac{\partial v}{\partial z}\mathbf{e}_z. \tag{2.30}$$

However, contrary to Cartesian coordinates where $\partial e_i/\partial x_j = 0$ for $i, j = x, y, z$, in cylindrical coordinates it is important to recall that, not all derivatives are zero. In particular, from (2.25) follows that

$$\frac{\partial \mathbf{e}_r}{\partial \theta} = \mathbf{e}_\theta, \qquad \frac{\partial \mathbf{e}_\theta}{\partial \theta} = -\mathbf{e}_r \tag{2.31}$$

while the other derivatives are zero. These properties are crucial when computing derivatives of vectors or tensors. For instance, the gradient of a vector in cylindrical coordinates is

$$\begin{aligned}
\boldsymbol{\nabla}^{\boldsymbol{r}} \boldsymbol{v} = \boldsymbol{u} \otimes \boldsymbol{\nabla}^{\boldsymbol{r}} &= (v_r \mathbf{e}_r + v_\theta \mathbf{e}_\theta + v_z \mathbf{e}_z) \otimes \left(\mathbf{e}_r \frac{\partial}{\partial r} + \mathbf{e}_\theta \frac{1}{r}\frac{\partial}{\partial \theta} + \mathbf{e}_z \frac{\partial}{\partial z} \right) \\
&= \begin{pmatrix} \dfrac{\partial v_r}{\partial r} & \dfrac{1}{r}\dfrac{\partial v_r}{\partial \theta} & \dfrac{\partial v_r}{\partial z} \\ \dfrac{\partial v_\theta}{\partial r} & \dfrac{1}{r}\dfrac{\partial v_\theta}{\partial \theta} & \dfrac{\partial v_\theta}{\partial z} \\ \dfrac{\partial v_z}{\partial r} & \dfrac{1}{r}\dfrac{\partial v_z}{\partial \theta} & \dfrac{\partial v_z}{\partial z} \end{pmatrix} + \frac{v_r}{r}\frac{\partial \mathbf{e}_r}{\partial \theta} \otimes \mathbf{e}_\theta + \frac{v_\theta}{r}\frac{\partial \mathbf{e}_\theta}{\partial \theta} \otimes \mathbf{e}_\theta \\
&= \begin{pmatrix} \dfrac{\partial v_r}{\partial r} & \dfrac{1}{r}\dfrac{\partial v_r}{\partial \theta} - \dfrac{v_\theta}{r} & \dfrac{\partial v_r}{\partial z} \\ \dfrac{\partial v_\theta}{\partial r} & \dfrac{1}{r}\dfrac{\partial v_\theta}{\partial \theta} + \dfrac{v_r}{r} & \dfrac{\partial v_\theta}{\partial z} \\ \dfrac{\partial v_z}{\partial r} & \dfrac{1}{r}\dfrac{\partial v_z}{\partial \theta} & \dfrac{\partial v_z}{\partial z} \end{pmatrix},
\end{aligned} \tag{2.32a}$$

while the divergence of a vector is

$$\begin{aligned}\boldsymbol{\nabla}^{\boldsymbol{r}}\cdot\boldsymbol{v} &= \Big(\frac{\partial}{\partial r}\mathbf{e}_r+\frac{\partial}{\partial\theta}\mathbf{e}_\theta+\frac{\partial}{\partial z}\mathbf{e}_z\Big)\cdot(v_r\mathbf{e}_r+v_\theta\mathbf{e}_\theta+v_z\mathbf{e}_z)\\ &= \frac{\partial v_r}{\partial r}+\frac{1}{r}\frac{\partial v_\theta}{\partial\theta}+\frac{\partial v_z}{\partial z}+\frac{v_r}{r}\mathbf{e}_\theta\cdot\frac{\partial\mathbf{e}_r}{\partial\theta}+\frac{v_\theta}{r}\mathbf{e}_\theta\cdot\frac{\partial\mathbf{e}_\theta}{\partial\theta} \qquad (2.33a)\\ &= \frac{1}{r}\frac{\partial(rv_r)}{\partial r}+\frac{1}{r}\frac{\partial v_\theta}{\partial\theta}+\frac{\partial v_z}{\partial z}.\end{aligned}$$

Previous expressions are used together with relations (2.31) to compute the divergence of a gradient of a vector

$$\boldsymbol{\nabla}^{\boldsymbol{r}}\cdot\boldsymbol{\nabla}^{\boldsymbol{r}}\boldsymbol{v} = \begin{pmatrix}\dfrac{\partial^2 v_r}{\partial r^2}+\dfrac{1}{r}\dfrac{\partial v_r}{\partial r}+\dfrac{1}{r^2}\dfrac{\partial^2 v_r}{\partial\theta^2}-\dfrac{2}{r^2}\dfrac{\partial v_\theta}{\partial\theta}-\dfrac{v_r}{r^2}+\dfrac{\partial^2 v_r}{\partial z^2}\\ \dfrac{\partial^2 v_\theta}{\partial r^2}+\dfrac{1}{r}\dfrac{\partial v_\theta}{\partial r}+\dfrac{1}{r^2}\dfrac{\partial^2 v_\theta}{\partial\theta^2}+\dfrac{2}{r^2}\dfrac{\partial v_r}{\partial\theta}-\dfrac{v_\theta}{r^2}+\dfrac{\partial^2 v_\theta}{\partial z^2}\\ \dfrac{\partial^2 v_z}{\partial r^2}+\dfrac{1}{r}\dfrac{\partial v_z}{\partial r}+\dfrac{1}{r^2}\dfrac{\partial^2 v_z}{\partial\theta^2}+\dfrac{\partial^2 v_r}{\partial z^2},\end{pmatrix}, \qquad (2.34)$$

and analogously the divergence of a second-order tensor

$$\boldsymbol{\nabla}^{\boldsymbol{r}}\cdot\boldsymbol{W} = \begin{pmatrix}\dfrac{\partial W_{rr}}{\partial r}+\dfrac{1}{r}W_{rr}+\dfrac{1}{r}\dfrac{W_{r\theta}}{\partial\theta}+\dfrac{\partial W_{rz}}{\partial z}-\dfrac{1}{r}W_{\theta\theta}\\ \dfrac{\partial W_{\theta r}}{\partial r}+\dfrac{1}{r}W_{\theta r}+\dfrac{1}{r}\dfrac{W_{\theta\theta}}{\partial\theta}+\dfrac{\partial W_{\theta z}}{\partial z}+\dfrac{1}{r}W_{r\theta}\\ \dfrac{\partial W_{zr}}{\partial r}+\dfrac{1}{r}W_{zr}+\dfrac{1}{r}\dfrac{W_{z\theta}}{\partial\theta}+\dfrac{\partial W_{zz}}{\partial z}\end{pmatrix}. \qquad (2.35)$$

2.3.2 Problem statement and axisymmetric hypothesis

Let us consider problem statement (2.1) defined in domain $\Omega_0\in\mathbb{R}^{\mathtt{n_{sd}}}$ with $\mathtt{n_{sd}}$=3. Let us also assume that domain Ω_0 is the results of a full rotation around the z-axis of a 2D generator domain $\Omega\subset\mathbb{R}^2$. By mean of a change of coordinates (2.1) can be rewritten in cylindrical coordinates. The goal is still to find the velocity and pressure fields as functions in a multidimensional space, namely $\boldsymbol{u}(\boldsymbol{x})$ and $p(\boldsymbol{x})$:

$$\begin{cases}-\boldsymbol{\nabla}^{\boldsymbol{r}}\cdot(\nu\boldsymbol{\nabla}^{\boldsymbol{r}}\boldsymbol{u}-p\mathbf{I}_{\mathtt{n_{sd}}})=\boldsymbol{s} & \text{in } \Omega\times[-\pi,\pi),\\ \boldsymbol{\nabla}^{\boldsymbol{r}}\cdot\boldsymbol{u}=0 & \text{in } \Omega\times[-\pi,\pi),\\ \boldsymbol{u}=\boldsymbol{u}_D & \text{on } \Gamma_D\times[-\pi,\pi),\\ \boldsymbol{n}\cdot\big(\nu\boldsymbol{\nabla}^{\boldsymbol{r}}\boldsymbol{u}-p\mathbf{I}_{\mathtt{n_{sd}}}\big)=\boldsymbol{g}_N & \text{on } \Gamma_N\times[-\pi,\pi),\\ \boldsymbol{u}\cdot\boldsymbol{D}+\boldsymbol{n}\cdot\big(\nu\boldsymbol{\nabla}^{\boldsymbol{r}}\boldsymbol{u}-p\mathbf{I}_{\mathtt{n_{sd}}}\big)\boldsymbol{E}=\mathbf{0} & \text{on } \Gamma_S\times[-\pi,\pi).\end{cases} \qquad (2.36)$$

where $\boldsymbol{\nabla}^{\boldsymbol{r}}$ is the nabla operator defined in cylindrical coordinates.

By definition, in axisymmetric problems, all variables are independent of the angular coordinate θ. This allows reducing the dimension of the problem solving the equations

only in the generator plane Ω. Under this hypothesis two different scenarios are possible: the z-axis intersects or does not intersect the generator domain Ω. As it is shown in the following, this small difference has a huge impact on the axisymmetric HDG formulation as for one of the two cases a new boundary conditions must be introduced.

Case 1: The z-axis does not intersect Ω If z-axis does not intersects Ω (e.g. a hollow cylinder), no further hypothesis is required and the resolution of the problem follows the classical HDG approach presented in section 2.2. In this case, the axisymmetric hypothesis simply helps to reduce the dimension of the integration domain. A three-dimensional Cartesian integral can be computed exploiting a 2π-rotation of a two dimensional integral around the axis of symmetry, simply accounting of the differential terms arising from the Cartesian-cylindrical change of coordinates. In other words, the whole rotation of each element Ω_e of the generator domain $\Omega \in \mathbb{R}^2$ produces a toroidal prism, and the union of all these prisms reconstructs $\Omega_0 \in \mathbb{R}^3$. In this case, the axisymmetric problem statement reads

$$\begin{cases} -\boldsymbol{\nabla}^{\boldsymbol{r}} \cdot (\nu \boldsymbol{\nabla}^{\boldsymbol{r}} \boldsymbol{u} - p\mathbf{I}_{\mathtt{n_{sd}}}) = \boldsymbol{s} & \text{in } \Omega \times [-\pi, \pi), \\ \boldsymbol{\nabla}^{\boldsymbol{r}} \cdot \boldsymbol{u} = 0 & \text{in } \Omega \times [-\pi, \pi), \\ \boldsymbol{u} = \boldsymbol{u}_D & \text{on } \Gamma_D \times [-\pi, \pi), \\ \boldsymbol{n} \cdot \left(\nu \boldsymbol{\nabla}^{\boldsymbol{r}} \boldsymbol{u} - p\mathbf{I}_{\mathtt{n_{sd}}}\right) = \boldsymbol{g}_N & \text{on } \Gamma_N \times [-\pi, \pi), \\ \boldsymbol{u} \cdot \boldsymbol{D} + \boldsymbol{n} \cdot \left(\nu \boldsymbol{\nabla}^{\boldsymbol{r}} \boldsymbol{u} - p\mathbf{I}_{\mathtt{n_{sd}}}\right) \boldsymbol{E} = \mathbf{0} & \text{on } \Gamma_S \times [-\pi, \pi), \end{cases} \tag{2.37}$$

where θ-dimension is simply integrated resulting in a scaling term 2π for all variables.

Case 2: The z-axis intersects Ω A completely different and more complex scenario appears when the axis of symmetry intersects the domain Ω (i.e. coincides with one of its boundaries). In this case, an extra artificial boundary must be accounted for apart from the Dirichlet, Neumann and Slip. Conceptually, while the behaviour of the elements which do not intersect the new boundary Γ_A is univariate respect the previous case, those having one of their faces in contact with it must be treated differently. The idea of exploiting rotation to reduce the integration dimension still holds, but as a new boundary is introduced, a new boundary condition is required. The Axisymmetric boundary Γ_A is thus defined such that $\partial\Omega = \overline{\Gamma}_D \cup \overline{\Gamma}_N \cup \overline{\Gamma}_S \cup \overline{\Gamma}_A$. Being a boundary with a physical symmetry imposed, boundary conditions on Γ_A are identical to those imposed for free slip condition on Γ_S, $\boldsymbol{u} \cdot \boldsymbol{n} = 0$ and $\boldsymbol{n} \cdot \boldsymbol{\nabla}^{\boldsymbol{r}} \boldsymbol{u}\, \boldsymbol{t}_k = 0$ for

k=1, ... $\mathtt{n_{sd}} - 1$. In this case, the axisymmetric problem statement reads

$$\begin{cases} -\boldsymbol{\nabla}^{\boldsymbol{r}}\cdot(\nu\boldsymbol{\nabla}^{\boldsymbol{r}}\boldsymbol{u} - p\mathbf{I}_{\mathtt{n_{sd}}}) = \boldsymbol{s} & \text{in } \Omega\times[-\pi,\pi), \\ \boldsymbol{\nabla}^{\boldsymbol{r}}\cdot\boldsymbol{u} = 0 & \text{in } \Omega\times[-\pi,\pi), \\ \boldsymbol{u} = \boldsymbol{u}_D & \text{on } \Gamma_D\times[-\pi,\pi), \\ \boldsymbol{n}\cdot\left(\nu\boldsymbol{\nabla}^{\boldsymbol{r}}\boldsymbol{u} - p\mathbf{I}_{\mathtt{n_{sd}}}\right) = \boldsymbol{g}_N & \text{on } \Gamma_N\times[-\pi,\pi), \\ \boldsymbol{u}\cdot\boldsymbol{D} + \boldsymbol{n}\cdot\left(\nu\boldsymbol{\nabla}^{\boldsymbol{r}}\boldsymbol{u} - p\mathbf{I}_{\mathtt{n_{sd}}}\right)\boldsymbol{E} = \mathbf{0} & \text{on } \Gamma_S\times[-\pi,\pi), \\ \boldsymbol{u}\cdot\boldsymbol{D} + \boldsymbol{n}\cdot\nu\boldsymbol{\nabla}^{\boldsymbol{r}}\boldsymbol{u}\boldsymbol{E} = \mathbf{0} & \text{on } \Gamma_A. \end{cases} \tag{2.38}$$

It is worth noting that the last equation is defined only on the artificial axisymmetric boundary Γ_A which physically does not represent any three-dimensional surface as other boundaries do. The only aim of this condition is to close the problem without which the final HDG system of equations would results indeterminate, leaving the degrees of freedom of $\hat{\boldsymbol{u}}$ lying on Γ_A unconstrained. Analogously to Case 1, where involved (i.e. except in last equation of system (2.38)), θ-dimension is simply integrated resulting in a scaling term 2π for all variables.

In the following, HDG formulation is developed only for the second case where z-axis intersects Ω as (2.37) is a particular case of (2.38) where Γ_A=$\emptyset$.

2.3.3 Strong form of the local and global problems

Following HDG rationale (2.38) is solved in two steps. First local problems are solved element by element

$$\begin{cases} \boldsymbol{L}_e + \nu\boldsymbol{\nabla}^{\boldsymbol{r}}\boldsymbol{u}_e = \mathbf{0} & \text{in } \Omega_e\times[-\pi,\pi), \text{ and for } e = 1,\dots,\mathtt{n_{el}}, \\ \boldsymbol{\nabla}^{\boldsymbol{r}}\cdot\left(\boldsymbol{L}_e + p_e\mathbf{I}_{\mathtt{n_{sd}}}\right) = \boldsymbol{s} & \text{in } \Omega_e\times[-\pi,\pi), \text{ and for } e = 1,\dots,\mathtt{n_{el}}, \\ \boldsymbol{\nabla}^{\boldsymbol{r}}\cdot\boldsymbol{u}_e = 0 & \text{in } \Omega_e\times[-\pi,\pi), \text{ and for } e = 1,\dots,\mathtt{n_{el}}, \\ \boldsymbol{u}_e = \boldsymbol{u}_D & \text{on } (\partial\Omega_e\cap\Gamma_D)\times[-\pi,\pi), \\ \boldsymbol{u}_e = \hat{\boldsymbol{u}} & \text{on } (\partial\Omega_e\setminus\Gamma_D)\times[-\pi,\pi), \\ \left\langle\dfrac{1}{|\partial\Omega_e|}p_e, 2\pi\right\rangle_{\partial\Omega_e} = \rho_e, & \text{for } e = 1,\dots,\mathtt{n_{el}}. \end{cases} \tag{2.39}$$

Note that the hybrid variable $\hat{\boldsymbol{u}}$ beside on the Neumann and Slip boundaries is also defined on the artificial Axisymmetric boundary. This guarantees that all local problems are still pure Dirichlet problems and that each of them can be solved independently, element by element, to write $\boldsymbol{L}_e$, $\boldsymbol{u}_e$ and p_e in terms of $\hat{\boldsymbol{u}}$ and ρ_e along the interface $\Gamma\cup\Gamma_N\cup\Gamma_S\cup\Gamma_A$. Moreover, it is worth to notice that being pure Dirichlet problem, each local problem fall in the class of problems whose boundary does not intersect Γ_A thus its resolution only requires to account some small changes in the differential of integration arising from the change of coordinates (i.e. it behaves exactly as problems belonging to Case 1).

Second, the so-called *global problem* is defined accounting also of the extra condition on Γ_A, namely

$$\begin{cases} [\![\boldsymbol{n}\cdot\big(\boldsymbol{L}+p\mathbf{I}_{\mathtt{n_{sd}}}\big)]\!]=\mathbf{0} & \text{on } \Gamma\times[-\pi,\pi), \\ \boldsymbol{n}\cdot(\boldsymbol{L}_e+p_e\mathbf{I}_{\mathtt{n_{sd}}})=-\boldsymbol{g}_N & \text{on } (\partial\Omega_e\cap\Gamma_N)\times[-\pi,\pi), \\ \boldsymbol{u}_e\cdot\boldsymbol{D}-\boldsymbol{n}\cdot(\boldsymbol{L}_e+p_e\mathbf{I}_{\mathtt{n_{sd}}})\,\boldsymbol{E}=\mathbf{0} & \text{on } (\partial\Omega_e\cap\Gamma_S)\times[-\pi,\pi), \\ \boldsymbol{u}_e\cdot\boldsymbol{D}-\boldsymbol{n}\cdot\boldsymbol{L}_e\boldsymbol{E}=\mathbf{0} & \text{on } (\partial\Omega_e\cap\Gamma_A). \end{cases} \tag{2.40}$$

2.3.4 3D weak form of the local and global problems

Exploiting the functional spaces defined in section 2.2.3 the weak form of the local problems, for e=1,...,$\mathtt{n_{el}}$, reads: given $\boldsymbol{u}_D$ on Γ_D and $\hat{\boldsymbol{u}}^h$ on $\Gamma\cup\Gamma_N\cup\Gamma_S\cup\Gamma_A$, find $(\boldsymbol{L}_e^h,\boldsymbol{u}_e^h,p_e^h)\in\boldsymbol{\mathcal{W}}^h\times\boldsymbol{\mathcal{V}}^h\times\mathcal{V}^h$ that satisfy

$$\begin{aligned} A^r_{LL}(\boldsymbol{W},\boldsymbol{L}_e^h)+A^r_{Lu}(\boldsymbol{W},\boldsymbol{u}_e^h)&=L^r_L(\boldsymbol{W})+A^r_{L\hat{u}}(\boldsymbol{W},\hat{\boldsymbol{u}}^h),\\ A^r_{uL}(\boldsymbol{v},\boldsymbol{L}_e^h)+A^r_{uu}(\boldsymbol{v},\boldsymbol{u}_e^h)+A^r_{up}(\boldsymbol{v},p_e^h)&=L^r_u(\boldsymbol{v})+A^r_{u\hat{u}}(\boldsymbol{v},\hat{\boldsymbol{u}}^h),\\ A^r_{pu}(v,\boldsymbol{u}_e^h)&=L^r_p(v)+A^r_{p\hat{u}}(v,\hat{\boldsymbol{u}}^h),\\ A^r_{\rho p}(1,p_e^h)&=A^r_{\rho\rho}(1,\rho_e^h), \end{aligned} \tag{2.41}$$

for all $(\boldsymbol{W},\boldsymbol{v},v)\in\boldsymbol{\mathcal{W}}^h\times\boldsymbol{\mathcal{V}}^h\times\mathcal{V}^h$, where the multi-dimensional bilinear and linear forms of the local problem are given by

$$\begin{aligned} A^r_{LL}(\boldsymbol{W},\boldsymbol{L})&:=-\big(\boldsymbol{W},\nu^{-1}\boldsymbol{L}\,2\pi r\big)_{\Omega_e},\\ A^r_{Lu}(\boldsymbol{W},\boldsymbol{u})&:=\big(\boldsymbol{\nabla}^{\boldsymbol{r}}\cdot\boldsymbol{W},\boldsymbol{u}\,2\pi r\big)_{\Omega_e},\\ A^r_{L\hat{u}}(\boldsymbol{W},\hat{\boldsymbol{u}})&:=\langle\boldsymbol{n}\cdot\boldsymbol{W},\hat{\boldsymbol{u}}\,2\pi r\rangle_{\partial\Omega_e\setminus\Gamma_D},\\ A^r_{uL}(\boldsymbol{v},\boldsymbol{L})&:=\big(\boldsymbol{v},\boldsymbol{\nabla}^{\boldsymbol{r}}\cdot\boldsymbol{L}\,2\pi r\big)_{\Omega_e},\\ A^r_{uu}(\boldsymbol{v},\boldsymbol{u})&:=\langle\boldsymbol{v},\boldsymbol{\tau}\boldsymbol{u}\,2\pi r\rangle_{\partial\Omega_e},\\ A^r_{up}(\boldsymbol{v},p)&:=\big(\boldsymbol{v},\boldsymbol{\nabla}^{\boldsymbol{r}}p\,2\pi r\big)_{\Omega_e},\\ A^r_{u\hat{u}}(\boldsymbol{v},\hat{\boldsymbol{u}})&:=\langle\boldsymbol{v},\boldsymbol{\tau}\hat{\boldsymbol{u}}\,2\pi r\rangle_{\partial\Omega_e\setminus\Gamma_D},\\ A^r_{pu}(v,\boldsymbol{u})&:=\big(\boldsymbol{\nabla}^{\boldsymbol{r}}v,\boldsymbol{u}\,2\pi r\big)_{\Omega_e},\\ A^r_{p\hat{u}}(v,\hat{\boldsymbol{u}})&:=\langle v,\hat{\boldsymbol{u}}\cdot\boldsymbol{n}\,2\pi r\rangle_{\partial\Omega_e\setminus\Gamma_D},\\ A^r_{\rho p}(w,p)&:=\langle w,|\partial\Omega_e|^{-1}p\,2\pi r\rangle_{\partial\Omega_e},\\ A^r_{\rho\rho}(w,\rho)&:=w\rho\,2\pi, \end{aligned} \tag{2.42}$$

and

$$\begin{aligned} L^r_L(\boldsymbol{W})&:=\langle\boldsymbol{n}\cdot\boldsymbol{W},\boldsymbol{u}_D\,2\pi r\rangle_{\partial\Omega_e\cap\Gamma_D},\\ L^r_u(\boldsymbol{v})&:=\big(\boldsymbol{v},\boldsymbol{s}\,2\pi r\big)_{\Omega_e}+\langle\boldsymbol{v},\boldsymbol{\tau}\boldsymbol{u}_D\,2\pi r\rangle_{\partial\Omega_e\cap\Gamma_D},\\ L^r_p(v)&:=\langle v,\boldsymbol{u}_D\cdot\boldsymbol{n}\,2\pi r\rangle_{\partial\Omega_e\cap\Gamma_D}, \end{aligned} \tag{2.43}$$

respectively.

Similarly, the weak form of the global problem is: find $\hat{\boldsymbol{u}}^h \in \widehat{\boldsymbol{\mathcal{V}}}^h$ and $\rho^h \in \mathbb{R}^{\mathtt{n_{el}}}$ that satisfies

$$\begin{aligned}\sum_{e=1}^{\mathtt{n_{el}}} \left\{ A^r_{\hat{u}L}(\hat{\boldsymbol{v}}, \boldsymbol{L}^h_e) + A^r_{\hat{u}u}(\hat{\boldsymbol{v}}, \boldsymbol{u}^h_e) + A^r_{\hat{u}p}(\hat{\boldsymbol{v}}, p^h_e) + A^r_{\hat{u}\hat{u}}(\hat{\boldsymbol{v}}, \hat{\boldsymbol{u}}^h) \right\} &= \sum_{e=1}^{\mathtt{n_{el}}} \left\{ L^r_{\hat{u}}(\hat{\boldsymbol{v}}) \right\}, \\ A^r_{p\hat{u}}(1, \hat{\boldsymbol{u}}^h) &= -L_p(1),\end{aligned} \tag{2.44}$$

for all $\hat{\boldsymbol{v}} \in \widehat{\boldsymbol{\mathcal{V}}}^h$, where the multi-dimensional bilinear and linear forms of the global problem are given by

$$\begin{aligned}A^r_{\hat{u}L}(\hat{\boldsymbol{v}}, \boldsymbol{L}) :=& \langle \hat{\boldsymbol{v}}, \boldsymbol{n} \cdot \boldsymbol{L}\, 2\pi r \rangle_{\partial\Omega_e \setminus (\Gamma_D \cup \Gamma_S \cup \Gamma_A)} \\ &- \langle \hat{\boldsymbol{v}}, \boldsymbol{n} \cdot \boldsymbol{LE}\, 2\pi r \rangle_{\partial\Omega_e \cap \Gamma_S} \\ &- \langle \hat{\boldsymbol{v}}, \boldsymbol{n} \cdot \boldsymbol{LE} \rangle_{\partial\Omega_e \cap \Gamma_A} \\ A^r_{\hat{u}u}(\hat{\boldsymbol{v}}, \boldsymbol{u}) :=& \langle \hat{\boldsymbol{v}}, \boldsymbol{\tau u}\, 2\pi r \rangle_{\partial\Omega_e \setminus (\Gamma_D \cup \Gamma_S \cup \Gamma_A)} \\ &- \langle \hat{\boldsymbol{v}}, (\boldsymbol{\tau u}) \cdot \boldsymbol{E}\, 2\pi r \rangle_{\partial\Omega_e \cap \Gamma_S} \\ &- \langle \hat{\boldsymbol{v}}, (\boldsymbol{\tau u}) \cdot \boldsymbol{E} \rangle_{\partial\Omega_e \cap \Gamma_A} \\ A^r_{\hat{u}p}(\hat{\boldsymbol{v}}, p) :=& \langle \hat{\boldsymbol{v}}, p\boldsymbol{n}\, 2\pi r \rangle_{\partial\Omega_e \setminus (\Gamma_D \cup \Gamma_S \cup \Gamma_A)} \\ A^r_{\hat{u}\hat{u}}(\hat{\boldsymbol{v}}, \hat{\boldsymbol{u}}) :=& - \langle \hat{\boldsymbol{v}}, \boldsymbol{\tau}\hat{\boldsymbol{u}}\, 2\pi r \rangle_{\partial\Omega_e \setminus (\Gamma_D \cup \Gamma_S \cup \Gamma_A)} \\ &+ \langle \hat{\boldsymbol{v}}, (\hat{\boldsymbol{u}} \cdot \boldsymbol{D} + (\boldsymbol{\tau}\hat{\boldsymbol{u}}) \cdot \boldsymbol{E})\, 2\pi r \rangle_{\partial\Omega_e \cap \Gamma_S} \\ &+ \langle \hat{\boldsymbol{v}}, \hat{\boldsymbol{u}} \cdot \boldsymbol{D} + (\boldsymbol{\tau}\hat{\boldsymbol{u}}) \cdot \boldsymbol{E} \rangle_{\partial\Omega_e \cap \Gamma_A}\end{aligned} \tag{2.45}$$

and

$$L^r_{\hat{u}}(\hat{\boldsymbol{v}}) := -\langle \hat{\boldsymbol{v}}, \boldsymbol{g}_N\, 2\pi r \rangle_{\partial\Omega_e \cap \Gamma_N}, \tag{2.46}$$

respectively. It is worth noting that the only differences between forms of section 2.2.3 and those defined here are the scaling term 2π, following from the integration of θ-dimension, the extra term r appearing in the differential after the Cartesian-cylindrical change of coordinates, and the bi-dimensional integrations on Γ_A appearing only in global problem forms.

2.3.5 Axysimmetric formulation as extension of the bi-dimensional formulation

Beside the new boundary, another difference between equations (2.39)-(2.40) and equations (2.8)-(2.9) hides in the nabla operator. When applied to vectors or tensors in cylindrical coordinates, extra terms arise. Accordingly to the definition of the gradient of a vector in cylindrical coordinates defined in (2.32), under axisymmetrical

hypothesis component $L_{z\theta}$ of the mixed variable vanishes

$$\boldsymbol{L} = \begin{pmatrix} L_{rr} & L_{r\theta} & L_{rz} \\ L_{\theta r} & L_{\theta\theta} & L_{\theta z} \\ L_{zr} & 0 & L_{zz} \end{pmatrix}, \tag{2.47}$$

meanwhile the velocity vector remains $\boldsymbol{u}=(u_r, u_\theta, u_z)^T$. Note that the assumption of axisymmetric motion does not imply that circumferential velocities u_θ are zero. There are many examples of axisymmetric flows involving swirl or rotation such as a rotating flow in a cylindrical cavity or the swirling flow in a gas. By the way, under the additional hypothesis of non-rotative flow u_θ is null. Consequentially, also components $L_{r\theta}$, $L_{\theta r}$,$L_{\theta z}$ of $\boldsymbol{L}$ vanish and mixed variable tensor reads

$$\boldsymbol{L} = \begin{pmatrix} L_{rr} & 0 & L_{rz} \\ 0 & L_{\theta\theta} & 0 \\ L_{zr} & 0 & L_{zz} \end{pmatrix}. \tag{2.48}$$

In agreement with the dimension of $\boldsymbol{L}$, outward unit normal vector $\boldsymbol{n}$ is defined in $\mathbb{R}^{\mathtt{n_{sd}}}$ with $\mathtt{n_{sd}}$=3. In particular given the axisymmetric nature of the problem follows that $\boldsymbol{n}=(n_r, 0, n_z)^T$ as the outward normal is always orthogonal to the plane r-z.

That, with the simplification of $\boldsymbol{u}$ and $\boldsymbol{L}$, allows seeing a three-dimensional non-rotative axisymmetric problem as a two-dimensional problem defined in the generator domain accounting of one extra variable. It is worth noting that the axisymmetric mixed variable can be seen as the classic mixed variable associated to space (z, r) plus an extra component due to the axisymmetric nature of the problem, $L_{\theta\theta}$. For that purpose, a new variable Λ is introduced representing this fifth component of $\boldsymbol{L}$ and associated to a scalar test function λ representing the fifth component of $\boldsymbol{W}$, namely $W_{\theta\theta}$. This implies

$$\boldsymbol{n} = \begin{pmatrix} n_r \\ n_z \end{pmatrix}, \quad \boldsymbol{u} = \begin{pmatrix} u_r \\ u_z \end{pmatrix}, \quad \boldsymbol{L} = \begin{pmatrix} L_{rr} & L_{rz} \\ L_{zr} & L_{zz} \end{pmatrix}. \tag{2.49}$$

It is important to clarify the significance of Λ. As previously said it represents component $L_{\theta\theta}$ of the three-dimensional mixed variable tensor. Its definition follows from the attempt to preserve as much as possible the bi-dimensional structure of the 2D formulation and seeing axial symmetry as a possible extension. Moreover, in this fashion, it is also possible to consider shape functions living in functional space generated by $\mathtt{n_{sd}}$=2, instead of $\mathtt{n_{sd}}$=3 as from a theoretical point of view is needed. This brings enormous advantages from an implementation perspective as it allows to re-use entirely the 2D formulation. For that reason, here, Λ has not been included inside $\boldsymbol{L}$, while, in all respect, it is a part of it. By the way, out of this chapter, principally used

to introduce axisymmetric HDG formulation, when one refers to $\boldsymbol{L}$ in the axisymmetric case (e.g. error computation, rate of convergence), always refers to matrix (2.48), thus accounting of term $L_{\theta\theta}$, i.e. Λ. In other words, the axisymmetric mixed variable $\boldsymbol{L}$ incorporates Λ, becoming $\mathbf{L}_{\texttt{Axi}}$=$[\mathbf{L}_{\texttt{2D}}, \boldsymbol{\Lambda}]$.

2.3.6 2D weak form of the local and global problems

Weak forms of local (2.41) and global problems (2.44) can thus be rewritten accounting of previous considerations, thus using shape functions properly defined for a Cartesian domain with $\texttt{n}_{\texttt{sd}}$=2 where $(z, r) \in \Omega \subset \mathbb{R}^2$.

The weak form of the local problems, for e=$1, \dots, \texttt{n}_{\texttt{el}}$, reads: given $\boldsymbol{u}_D$ on Γ_D and $\hat{\boldsymbol{u}}^h$ on $\Gamma \cup \Gamma_N \cup \Gamma_S \cup \Gamma_A$, find $(\boldsymbol{L}_e^h, \boldsymbol{u}_e^h, p_e^h, \Lambda_e^h) \in \boldsymbol{\mathcal{W}}^h \times \boldsymbol{\mathcal{V}}^h \times \mathcal{V}^h \times \mathcal{V}^h$ that satisfy

$$\begin{aligned}
A^r_{LL}(\boldsymbol{W}, \boldsymbol{L}_e^h) + A^\theta_{Lu}(\boldsymbol{W}, \boldsymbol{u}_e^h) &= L^r_L(\boldsymbol{W}) + A^r_{L\hat{u}}(\boldsymbol{W}, \hat{\boldsymbol{u}}^h),\\
A^\theta_{\Lambda\Lambda}(\lambda, \Lambda_e^h) + A^\theta_{\Lambda u}(\lambda, \boldsymbol{u}_e^h) &= 0,\\
A^\theta_{uL}(\boldsymbol{v}, \boldsymbol{L}_e^h) + A^\theta_{u\Lambda}(\boldsymbol{v}, \Lambda_e^h) + A^r_{uu}(\boldsymbol{v}, \boldsymbol{u}_e^h) + A^\theta_{up}(\boldsymbol{v}, p_e^h)&\\
= L^r_u(\boldsymbol{v}) + A^r_{u\hat{u}}(\boldsymbol{v}, \hat{\boldsymbol{u}}^h),&\\
A^\theta_{pu}(v, \boldsymbol{u}_e^h) = L^r_p(v) + A^r_{p\hat{u}}(v, \hat{\boldsymbol{u}}^h),&\\
A^r_{\rho p}(1, p_e^h) = A^r_{\rho\rho}(1, \rho_e^h),&
\end{aligned} \tag{2.50}$$

for all $(\boldsymbol{W}, \boldsymbol{v}, v, \lambda) \in \boldsymbol{\mathcal{W}}^h \times \boldsymbol{\mathcal{V}}^h \times \mathcal{V}^h \times \mathcal{V}^h$, where forms equipped with the superindex ^{r} are those defined in (2.42) neglecting θ dimension, while the ones equipped with the superindex $^\theta$ are defined in the following

$$\begin{aligned}
A^\theta_{Lu}(\boldsymbol{W}, \boldsymbol{u}) &:= \big(\boldsymbol{\nabla}\cdot \boldsymbol{W}, \boldsymbol{u}\, 2\pi r\big)_{\Omega_e} + \big(\mathbf{e}_r/r \cdot \boldsymbol{W}, \boldsymbol{u}\, 2\pi r\big)_{\Omega_e},\\
A^\theta_{\Lambda\Lambda}(\lambda, \Lambda) &:= -\big(\lambda, \nu^{-1}\Lambda\, 2\pi r\big)_{\Omega_e},\\
A^\theta_{\Lambda u}(\lambda, \boldsymbol{u}) &:= -\big(\lambda, \mathbf{e}_r/r \cdot \boldsymbol{u}\, 2\pi r\big)_{\Omega_e},\\
A^\theta_{uL}(\boldsymbol{v}, \boldsymbol{L}) &:= \big(\boldsymbol{v}, \boldsymbol{\nabla}\cdot \boldsymbol{L}\, 2\pi r\big)_{\Omega_e} + \big(\boldsymbol{v}, \mathbf{e}_r/r \cdot \boldsymbol{L}\, 2\pi r\big)_{\Omega_e},\\
A^\theta_{u\Lambda}(\boldsymbol{v}, \Lambda) &:= -\big(\boldsymbol{v}, \mathbf{e}_r/r\Lambda\, 2\pi r\big)_{\Omega_e},\\
A^\theta_{up}(\boldsymbol{v}, p) &:= \big(\boldsymbol{v}, \boldsymbol{\nabla} p\, 2\pi r\big)_{\Omega_e},\\
A^\theta_{pu}(v, \boldsymbol{u}) &:= \big(\boldsymbol{\nabla} v, \boldsymbol{u}\, 2\pi r\big)_{\Omega_e} + \big(\mathbf{e}_r/r\, p, \boldsymbol{u}\, 2\pi r\big)_{\Omega_e}.
\end{aligned} \tag{2.51}$$

It is worth noting that nabla operator is now the operator associated to the bi-dimensional Cartesian space (z, r), i.e. $\boldsymbol{\nabla}$=$[\partial/\partial z, \partial/\partial r]^T$.

Similarly, the weak form of the global problem is: find $\hat{\boldsymbol{u}}^h \in \widehat{\boldsymbol{\mathcal{V}}}^h$ and $\rho^h \in \mathbb{R}^{\texttt{n}_{\texttt{el}}}$ that satisfies

$$\begin{aligned}
\sum_{e=1}^{\texttt{n}_{\texttt{el}}} \Big\{ A^r_{\hat{u}L}(\hat{\boldsymbol{v}}, \boldsymbol{L}_e^h) + A^r_{\hat{u}u}(\hat{\boldsymbol{v}}, \boldsymbol{u}_e^h) + A^r_{\hat{u}p}(\hat{\boldsymbol{v}}, p_e^h) + A^r_{\hat{u}\hat{u}}(\hat{\boldsymbol{v}}, \hat{\boldsymbol{u}}^h) \Big\} &= \sum_{e=1}^{\texttt{n}_{\texttt{el}}} \left\{ L^r_{\hat{u}}(\hat{\boldsymbol{v}}) \right\},\\
A^r_{p\hat{u}}(1, \hat{\boldsymbol{u}}^h) &= -L^r_p(1),
\end{aligned} \tag{2.52}$$

for all $\hat{\boldsymbol{v}} \in \widehat{\boldsymbol{\mathcal{V}}}^h$, where the multi-dimensional bilinear and linear forms of the global problem are the same ones defined in (2.45).

Remark 2. *As it is observable from previous definitions, axisymmetric extra contributions just affect the volumetric terms of the l.h.s. of the equations, where nabla operator is applied. In fact, it is easy to see, developing a 3D formulation in cylindrical coordinates, that all boundary terms related to the θ-dimension vanish because of axisymmetric and non rotative flow hypothesis ($\partial/\partial\theta$=0, u_θ=0, n_θ=0).*

2.3.7 Discretisation

Analogously to section 2.2.4, introducing an isoparametric formulation with equal interpolation for all the local and global variables, the discretisation of the weak form of the local and global problems given by (2.41) and (2.44), respectively, can be obtained. Owning one extra unknown respect to (2.11), local problem, leads to a system of equations similar to 2.17 but owning one extra rows and one extra column

$$\begin{bmatrix} \mathbf{A}_{LL} & \mathbf{0} & \mathbf{A}_{Lu} & \mathbf{0} & \mathbf{0} \\ \mathbf{0} & \mathbf{A}_{\Lambda\Lambda} & \mathbf{A}_{\Lambda u} & \mathbf{0} & \mathbf{0} \\ \mathbf{A}_{uL} & \mathbf{A}_{u\Lambda} & \mathbf{A}_{uu} & \mathbf{A}_{up} & \mathbf{0} \\ \mathbf{0} & \mathbf{0} & \mathbf{A}_{pu} & \mathbf{0} & \boldsymbol{a}_{\rho p}^T \\ \mathbf{0} & \mathbf{0} & \mathbf{0} & \boldsymbol{a}_{\rho p} & 0 \end{bmatrix}_e \begin{Bmatrix} \mathbf{L} \\ \mathbf{\Lambda} \\ \mathbf{u} \\ \mathbf{p} \\ \zeta \end{Bmatrix}_e = \begin{Bmatrix} \mathbf{f}_L \\ \mathbf{0} \\ \mathbf{f}_u \\ \mathbf{f}_p \\ 0 \end{Bmatrix}_e + \begin{bmatrix} \mathbf{A}_{L\hat{u}} \\ \mathbf{0} \\ \mathbf{A}_{u\hat{u}} \\ \mathbf{A}_{p\hat{u}} \\ \mathbf{0} \end{bmatrix}_e \hat{\mathbf{u}} + \begin{Bmatrix} \mathbf{0} \\ \mathbf{0} \\ \mathbf{0} \\ \mathbf{0} \\ 1 \end{Bmatrix}_e \rho_e, \tag{2.53}$$

where $\mathbf{L}$, $\mathbf{\Lambda}$, $\mathbf{u}$, $\mathbf{p}$ and $\hat{\mathbf{u}}$ denote the nodal values of the unknown spatial functions $\boldsymbol{L}$, Λ, $\boldsymbol{u}$, p and $\hat{\boldsymbol{u}}$ respectively and the constraint on the mean value ρ of the pressure on the element boundaries is enforced using the Lagrange multiplier ζ.

Analogously, the discretisation of the global problem of the spatial iteration leads to a system of equations identical to the one defined in (2.54), namely

$$\begin{aligned} \sum_{e=1}^{\mathtt{nel}} \left\{ \begin{bmatrix} \mathbf{A}_{\hat{u}L} & \mathbf{A}_{\hat{u}u} & \mathbf{A}_{\hat{u}p} \end{bmatrix}_e \begin{Bmatrix} \mathbf{L} \\ \mathbf{u} \\ \mathbf{p} \end{Bmatrix}_e + [\mathbf{A}_{\hat{u}\hat{u}}]_e \, \hat{\mathbf{u}} \right\} &= \sum_{e=1}^{\mathtt{nel}} [\mathbf{f}_{\hat{u}}]_e, \\ \mathbf{1}^T [\mathbf{A}_{p\hat{u}}]_e \hat{\mathbf{u}} &= -\mathbf{1}^T [\mathbf{f}_p]_e. \end{aligned} \tag{2.54}$$

since Λ does not appear in the global problem.

Finally, exploiting the same strategy of section 2.2.4, i.e. expressing local variables in terms of the global ones, the final global system is obtained

$$\begin{bmatrix} \widehat{\mathbf{K}} & \mathbf{G} \\ \mathbf{G}^T & \mathbf{0} \end{bmatrix} \begin{Bmatrix} \hat{\mathbf{u}} \\ \boldsymbol{\rho} \end{Bmatrix} = \begin{Bmatrix} \hat{\mathbf{f}}_{\hat{u}} \\ \hat{\mathbf{f}}_{\rho} \end{Bmatrix}, \tag{2.55}$$

which once solved, returns the value of the global variables required to obtained the elemental value of all local variables, $\boldsymbol{L}$, $\boldsymbol{u}$, p and Λ.

2.3.8 Numerical validation

To validate the HDG axisymmetric formulation developed in the previous sections, two academic examples with a known analytical solution are proposed. The first one consists of the Poiseuille flow insides a channel solved for both bi-dimensional and axisymmetric cases while the second consists in the axisymmetric flow past a sphere.

Plane Poiseuille flow

In the first example considered, the fully developed plane Poiseuille flow, the domain of interest is the rectangle $\Omega{=}[0, L] \times [-R, R] \in \mathbb{R}^2$, with $L{=}3$ and $R{=}1$, and the analytical solution in Cartesian coordinates, shown in figure 2.3 is given by the following velocity and pressure fields where V is the maximum value of the velocity magnitude

$$\begin{aligned} u_x &= \mathrm{V}\Big(1 - \frac{y^2}{R^2}\Big) \\ u_y &= 0 \\ p &= -\frac{2\mathrm{V}}{R^2} z + \text{const} \end{aligned} \tag{2.56}$$

Numerical experiments are performed on a sequence of structured triangular meshes,

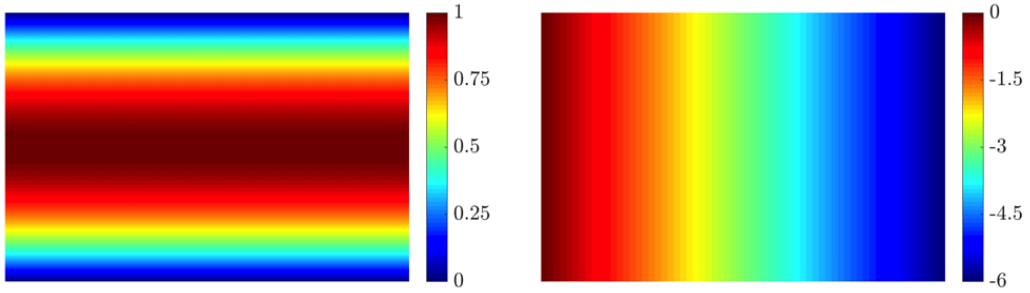

(a) $\boldsymbol{u}$ (b) p

FIGURE 2.3: Plane Poiseuille flow: analytical solution of velocity magnitude and pressure for the plane Poiseuille flow.

where the coarsest is formed of 32 elements. Dirichlet boundary conditions are imposed on all the boundaries of the domain. In figure 2.4, optimal rates of convergence are shown for variables $\boldsymbol{L}$, $\boldsymbol{u}$, p, $\hat{\boldsymbol{u}}$ and $\boldsymbol{u}^*$ only for degree $k{=}1$.

Being the analytical solution a quadratic polynomial, interpolation functions of degree $k{=}2$ solve the problem exactly. Optimal rates of convergence are obtained for all variables.

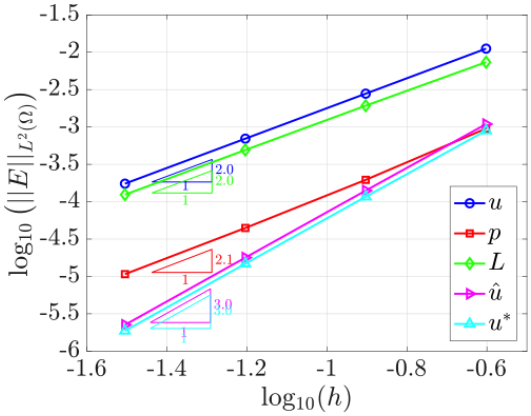

FIGURE 2.4: Plane Poiseuille flow: mesh convergence of the $\mathcal{L}_2$ norm of the error for $\boldsymbol{L}$, $\boldsymbol{u}$, p, $\hat{\boldsymbol{u}}$ and $\boldsymbol{u}^*$.

Axysimmetric Poiseuille flow

In the axysimmetric version of the Poiseuille flow, the considered domain is a full rotation of the plane case half-domain Ω=$[0, L] \times [0, R] \in \mathbb{R}^2$, with L=3 and R=1, around the z-axis, such that Ω_0=$\Omega \times [-\pi, \pi]$ and the analytical solution in cylindrical coordinates, shown in figure 2.5, is given by the following velocity and pressure fields where again V is the maximum value of the velocity magnitude

$$\begin{aligned} u_r &= 0, \\ u_\theta &= 0, \\ u_z &= \mathrm{V}\Big(1 - \frac{r^2}{R^2}\Big) \\ p &= -\frac{4\mathrm{V}}{R^2} z + \text{const} \end{aligned} \tag{2.57}$$

Note that the only change between the two analytical solutions of equations (2.56)

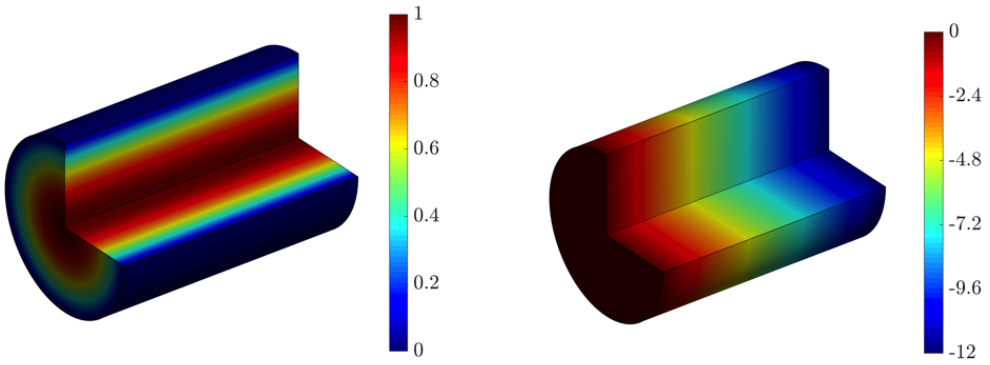

(a) $\boldsymbol{u}$ (b) p

FIGURE 2.5: Axysimmetric Poiseuille flow: analytical solution of velocity magnitude and pressure for the axysimmetric Poiseuille flow.

and (2.57) is in the definition of the pressure, while the velocity in the flow direction

(x and z, respectively) is equal, as it is the velocity in other directions, i.e. null.

Numerical experiments are performed on the same set of meshes used for the previous example. In figure 2.6, optimal rates of convergence are shown only for degree k=1,

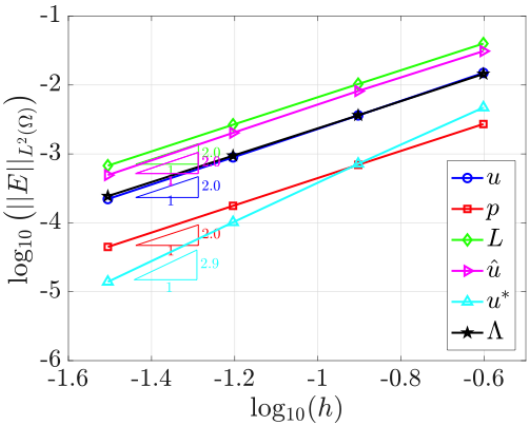

FIGURE 2.6: Axysimmetric Poiseuille flow: mesh convergence of the $\mathcal{L}_2$ norm of the error for $\boldsymbol{L}$, $\boldsymbol{u}$, p, $\hat{\boldsymbol{u}}$, Λ and $\boldsymbol{u}^*$.

owing to the same reasons for the plane case.

Axisymmetric Stokes flow past a sphere

The second validation example, as anticipated, considers the Stokes flow past a sphere. The domain of interest is selected as the region confined by two concentric spheres with radius R_{in} and R_{out} respectively, with $R_{\text{in}}<R_{\text{out}}$. The domain considered the axial symmetry of the problem is defined as $\Omega=\{\boldsymbol{r} \in \mathbb{R}^2 \mid r \geq 0 \text{ and } R_{\text{in}} \leq \rho \leq R_{\text{out}}\}$, with $\rho=\sqrt{r^2+z^2}$, R_{in}=1 and R_{out}=5. The analytical solution, shown in figure 2.7, is given by the following velocity and pressure fields in polar coordinates

$$\begin{aligned} u_\rho &= \frac{v_\infty}{2\rho^3}\left(2\rho^3 - 3R_{\text{in}}\rho^2 + R_{\text{in}}^3\right)\cos\phi, \\ u_\theta &= 0, \\ u_\phi &= -\frac{v_\infty}{4\rho^3}\left(4\rho^3 - 3R_{\text{in}}\rho^2 + R_{\text{in}}^3\right)\sin\phi, \\ p &= p_\infty - \frac{3}{2\rho^2}\nu v_\infty R_{\text{in}}\cos\phi, \end{aligned} \tag{2.58}$$

where v_∞ and p_∞ are the magnitude of the velocity and the pressure of the undisturbed flow, far away from the obstacle. It is worth noting that in other to avoid misunderstandings, being variable r the distance from the z-axis in cylindrical coordinates, variable ρ has been introduced to describe the Cartesian radius in polar coordinates, which is consistently defined as $\rho=\sqrt{x^2+y^2+z^2}=\sqrt{r^2+z^2}$. The analogous

equations in cylindrical coordinates are easily obtainable with few extra computations

$$\begin{aligned} u_r &= u_\rho \cos\phi - u_\phi \sin\phi, \\ u_\theta &= u_\theta, \\ u_z &= u_\rho \sin\phi + u_\phi \cos\phi, \\ p &= p_\infty - \frac{3}{2r^3}\nu v_\infty R_{\text{in}} z, \end{aligned} \tag{2.59}$$

where $z{=}\rho\cos\phi$ and $r{=}\rho\sin\phi$ following from the mapping between polar and cylindrical coordinates. Note that in literature (Childs, 2010; White et al., 2006), in the majority of the cases, equation (2.58) is presented with the two angles θ and ϕ inverted. The choice here has been made in agreement with the definition of axisymmetry made in this work ($\partial/\partial\theta{=}0$).

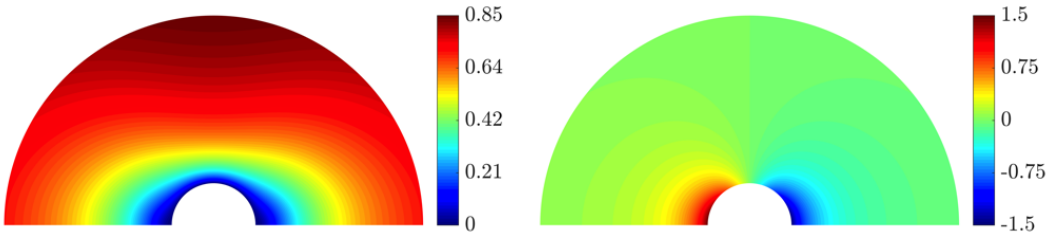

(a) $\boldsymbol{u}$ (b) p

FIGURE 2.7: Axisymmetric flow past a sphere: analytical solution of velocity magnitude and pressure for a sphere of unitary radius.

To qualitatively compare the 2D axisymmetric formulation with the corresponding 3D, figure 2.8 shows the 3D reconstruction of the axisymmetric flow past a sphere computed on a triangular mesh of 1024 elements and using degree $k = 4$ while 2.9 shows the HDG solution obtained solving the three-dimensional problem in Cartesian

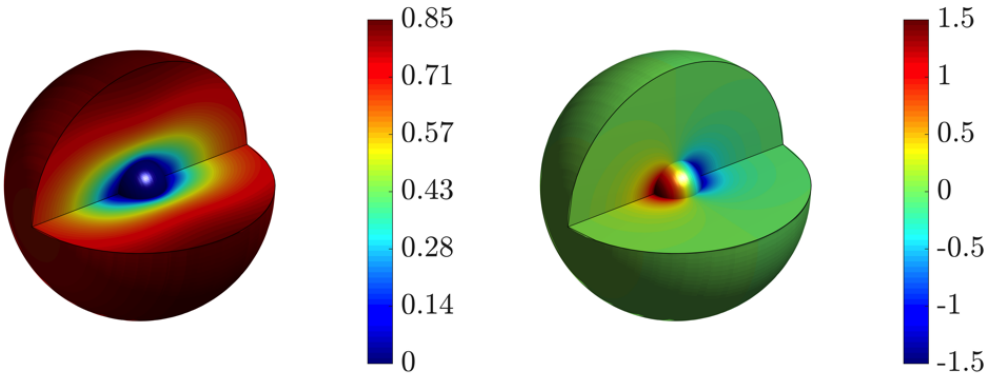

(a) $\boldsymbol{u}$ (b) p

FIGURE 2.8: Axisymmetric flow past a sphere: 3D reconstruction of the HDG solution of velocity magnitude and pressure for a sphere of unitary radius.

coordinates on a tetrahedral mesh of 747 elements using degree $k = 4$. The size of the HDG global problems associated with both cases are 15680 and 71190, respectively.

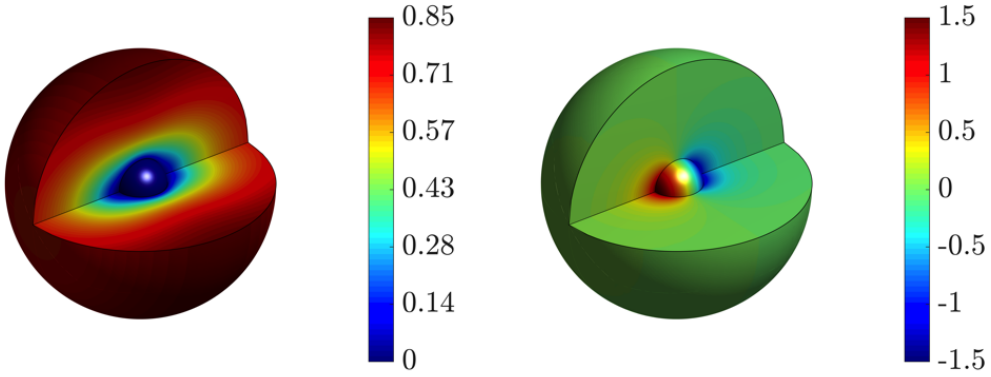

(a) $\boldsymbol{u}$ (b) p

FIGURE 2.9: Flow past a sphere: HDG solution of velocity magnitude and pressure for a sphere of unitary radius.

To prove the advantages of the axisymmetric formulation, a study on a physical quantity of interest is performed. A typical quantity of interest in this problem is the drag force, whose exact value is given by $F_D{=}6\pi\nu v_\infty R_{\text{in}}$.

The computation was performed using four triangular meshes where the coarsest counts of 64 elements end others are obtained by a sequential refinement. Analogous refinement is also considered for the tetrahedral mesh, where computations are bounded by memory limits. Figure 2.10 shows the numerical error of the drag force as a function of the degrees of freedom of the global problem. In all cases, convergence

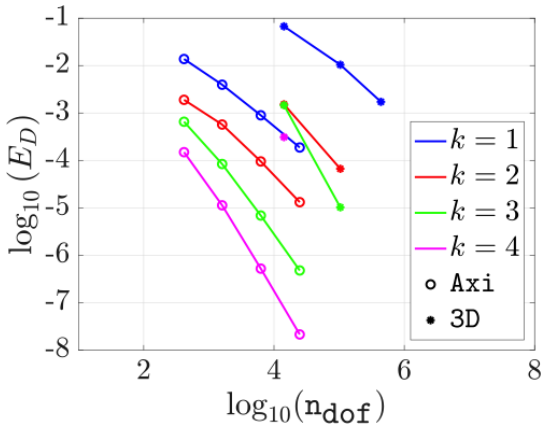

FIGURE 2.10: Axisymmetric and 3D flow past a sphere: evolution of the error in the drag of a sphere of unitary radius for different degrees of approximations.

to exact value is observed, and the superiority of using high-order approximations is appreciated. Moreover, it is visible the enormous saving in terms of degrees of freedom that an axisymmetric strategy provides.

To further validate the methodology figure 2.11 shows rates of convergence of the local variables, the trace of the velocity and the postprocessed velocity for the axisymmetric problem.

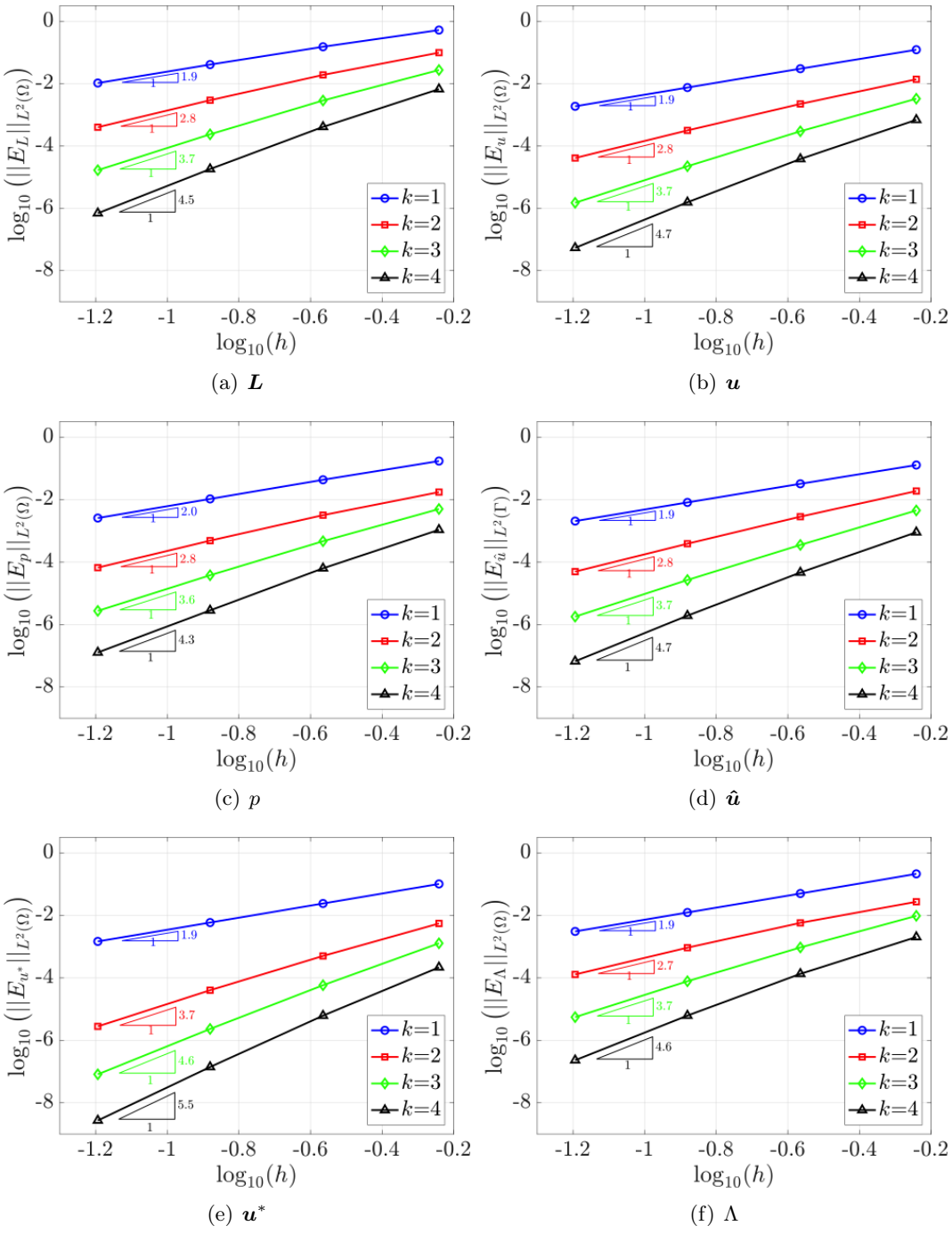

(a) $\boldsymbol{L}$ (b) $\boldsymbol{u}$

(c) p (d) $\hat{\boldsymbol{u}}$

(e) $\boldsymbol{u}^*$ (f) Λ

FIGURE 2.11: Axisymmetric flow past a sphere: mesh convergence of the $\mathcal{L}_2$ norm of the error for $\boldsymbol{L}$, $\boldsymbol{u}$, p, $\hat{\boldsymbol{u}}$, $\boldsymbol{u}^*$ and Λ for a sphere of unitary radius.

It is worth noting that optimal rates are obtained for all the numerical variables except $\boldsymbol{u}^*$ where a sub-optimal rate of convergence is observed for degree k=1. As explained in Sevilla et al., (2018b), the sub-optimal rate of convergence is due to the polygonal

approximation of the boundary, which in this case is done using an isoparametric approach, i.e. using k=1 a linear approximation is performed. As the geometric error converges with order k=2, it prevents the error of the numerical solution to converge faster. A possible way to circumvent this issue is proposed in Sevilla et al., (2018b) by mean of NEFEM elements where an exact description of the geometry boundary is used.

Chapter 3

HDG-PGD solution of geometrically parametrised Stokes flows

In this chapter[1], HDG formulation for the Stokes equations derived in chapter 2 is extended to parametrized problem, in particular to those defined on a parametrised domain. The full-order resolution of these multi-dimensional parametric problems is quickly tied by the so-called *curse of dimensionality*, thus a proper generalised decomposition framework is introduced.

3.1 Problem statement

3.1.1 The Stokes problem on a parametrised domain

Let us consider a parametrised domain $\Omega^{\boldsymbol{\mu}} \subset \mathbb{R}^{\mathtt{n_{sd}}}$, where $\mathtt{n_{sd}}$ is the number of spatial dimensions and $\boldsymbol{\mu} \in \boldsymbol{\mathcal{I}} \subset \mathbb{R}^{\mathtt{n_{pa}}}$ is a set of geometric parameters that controls the boundary representation of the domain, with $\mathtt{n_{pa}}$ being the number of geometric parameters. It is worth noting that the set of geometric parameters can be written as $\boldsymbol{\mathcal{I}} := \mathcal{I}^1 \times \mathcal{I}^2 \times \cdots \times \mathcal{I}^{\mathtt{n_{pa}}}$ with $\mu_j \in \mathcal{I}^j$ for $j{=}1, \ldots, \mathtt{n_{pa}}$.

For any set of parameters $\boldsymbol{\mu}$, the goal is to find the parametric velocity, $\boldsymbol{u}(\boldsymbol{x}^{\boldsymbol{\mu}})$, and pressure, $p(\boldsymbol{x}^{\boldsymbol{\mu}})$, fields that satisfy the Stokes problem given by

$$
\begin{cases}
-\boldsymbol{\nabla}\cdot\left(\nu\boldsymbol{\nabla}\boldsymbol{u} - p\mathbf{I}_{\mathtt{n_{sd}}}\right) = \boldsymbol{s} & \text{in } \Omega^{\boldsymbol{\mu}}, \\
\boldsymbol{\nabla}\cdot\boldsymbol{u} = 0 & \text{in } \Omega^{\boldsymbol{\mu}}, \\
\boldsymbol{u} = \boldsymbol{u}_D & \text{on } \Gamma_D^{\boldsymbol{\mu}}, \\
\boldsymbol{n}^{\boldsymbol{\mu}}\cdot\left(\nu\boldsymbol{\nabla}\boldsymbol{u} - p\mathbf{I}_{\mathtt{n_{sd}}}\right) = \boldsymbol{g}_N & \text{on } \Gamma_N^{\boldsymbol{\mu}}, \\
\boldsymbol{u}\cdot\boldsymbol{D}^{\boldsymbol{\mu}} + \boldsymbol{n}^{\boldsymbol{\mu}}\cdot\left(\nu\boldsymbol{\nabla}\boldsymbol{u} - p\mathbf{I}_{\mathtt{n_{sd}}}\right)\boldsymbol{E}^{\boldsymbol{\mu}} = \mathbf{0} & \text{on } \Gamma_S^{\boldsymbol{\mu}},
\end{cases}
\tag{3.1}
$$

[1]This chapter is a modified version of the published article "Hybridisable discontinuous Galerkin solution of geometrically parametrised Stokes flows" (Sevilla, Borchini, Giacomini, and Huerta, 2020a).

where $\nu>0$ is the kinematic viscosity, $\boldsymbol{s}$ is the volumetric source and $\boldsymbol{n}^{\boldsymbol{\mu}}$ is the outward unit normal vector to $\partial\Omega^{\boldsymbol{\mu}}$. The boundary of the domain, $\partial\Omega^{\boldsymbol{\mu}}$, is partitioned into the non-overlapping Dirichlet, $\Gamma_D^{\boldsymbol{\mu}}$, Neumann, $\Gamma_N^{\boldsymbol{\mu}}$, and slip, $\Gamma_S^{\boldsymbol{\mu}}$, boundaries such that $\overline{\partial\Omega}^{\boldsymbol{\mu}} = \overline{\Gamma}_D^{\boldsymbol{\mu}} \cup \overline{\Gamma}_N^{\boldsymbol{\mu}} \cup \overline{\Gamma}_S^{\boldsymbol{\mu}}$. On the Dirichlet boundary the velocity is given by $\boldsymbol{u}_D$. On the Neumann boundary the *pseudo-traction* is given by $\boldsymbol{g}_N$. Finally, on the slip boundary, the matrices $\boldsymbol{D}^{\boldsymbol{\mu}}$ and $\boldsymbol{E}^{\boldsymbol{\mu}}$ are given by $\boldsymbol{D}^{\boldsymbol{\mu}}=[\boldsymbol{n}^{\boldsymbol{\mu}}, \boldsymbol{0}_{\mathtt{n_{sd}}\times(\mathtt{n_{sd}}-1)}]$ and $\boldsymbol{E}^{\boldsymbol{\mu}}=[\boldsymbol{0}, \boldsymbol{t}_1^{\boldsymbol{\mu}}, ..., \boldsymbol{t}_{\mathtt{n_{sd}}-1}^{\boldsymbol{\mu}}]$, as detailed in Giacomini et al., (2020c). The tangential vectors $\boldsymbol{t}_k^{\boldsymbol{\mu}}$, for $k=1,\dots \mathtt{n_{sd}}-1$ are such that $\{\boldsymbol{n}^{\boldsymbol{\mu}}, \boldsymbol{t}_1^{\boldsymbol{\mu}}, ..., \boldsymbol{t}_{\mathtt{n_{sd}}-1}^{\boldsymbol{\mu}}\}$ form an orthonormal system of vectors.

The free divergence condition in equation (3.1) induces the compatibility condition

$$\langle 1, \boldsymbol{u}_D \cdot \boldsymbol{n}^{\boldsymbol{\mu}} \rangle_{\Gamma_D^{\boldsymbol{\mu}}} + \langle 1, \boldsymbol{u} \cdot \boldsymbol{n}^{\boldsymbol{\mu}} \rangle_{\partial\Omega^{\boldsymbol{\mu}}\setminus\Gamma_D^{\boldsymbol{\mu}}} = 0, \tag{3.2}$$

where $\langle\cdot,\cdot\rangle_S$ denotes the standard $\mathcal{L}_2$ scalar product in any domain $S \subset \partial\Omega^{\boldsymbol{\mu}}$.

In addition, it is worth noting that, if $\Gamma_N^{\boldsymbol{\mu}}=\emptyset$, an additional constraint to avoid the indeterminacy of the pressure is required. One common option (Cockburn et al., 2009b, 2014; Giacomini et al., 2018; Nguyen et al., 2010b) that is considered here, consists of imposing the mean pressure on the boundary of the domain, namely

$$\Big\langle \frac{1}{|\partial\Omega^{\boldsymbol{\mu}}|} p, 1 \Big\rangle_{\partial\Omega^{\boldsymbol{\mu}}} = 0. \tag{3.3}$$

3.1.2 The multi-dimensional parametric Stokes problem

The classical strategy to solve the parametric Stokes problem is to solve equation (3.1) for every set of parameters $\boldsymbol{\mu}\in\boldsymbol{\mathcal{I}}$. However, this strategy is not well suited when fast queries are required.

Reduced order models have demonstrated to be a viable alternative to compute multi-dimensional parametric solutions in an offline phase. Once the offline solution is available, the computation of the solution for a given set of parameters has a very small computational cost, being very well suited for applications where fast queries are required.

The multi-dimensional parametric problem arises from interpreting $\boldsymbol{\mu}$ as additional parametric coordinates, rather than parameters of the problem. In the context of the Stokes problem considered here, the strategy is to consider the velocity and pressure fields as functions in a multidimensional space, namely $\boldsymbol{u}(\boldsymbol{x}^{\boldsymbol{\mu}}, \boldsymbol{\mu})$ and $p(\boldsymbol{x}^{\boldsymbol{\mu}}, \boldsymbol{\mu})$. The

multi-dimensional parametric Stokes problem can be written as

$$\begin{cases} -\boldsymbol{\nabla}_{\boldsymbol{\mu}}\cdot(\nu\boldsymbol{\nabla}_{\boldsymbol{\mu}}\boldsymbol{u}-p\mathbf{I}_{\mathtt{n_{sd}}}) = \boldsymbol{s} & \text{in } \Omega^{\boldsymbol{\mu}}\times\boldsymbol{\mathcal{I}}, \\ \boldsymbol{\nabla}_{\boldsymbol{\mu}}\cdot\boldsymbol{u} = 0 & \text{in } \Omega^{\boldsymbol{\mu}}\times\boldsymbol{\mathcal{I}}, \\ \boldsymbol{u} = \boldsymbol{u}_D & \text{on } \Gamma_D^{\boldsymbol{\mu}}\times\boldsymbol{\mathcal{I}}, \\ \boldsymbol{n}^{\boldsymbol{\mu}}\cdot\big(\nu\boldsymbol{\nabla}_{\boldsymbol{\mu}}\boldsymbol{u}-p\mathbf{I}_{\mathtt{n_{sd}}}\big) = \boldsymbol{g}_N & \text{on } \Gamma_N^{\boldsymbol{\mu}}\times\boldsymbol{\mathcal{I}}, \\ \boldsymbol{u}\cdot\boldsymbol{D}^{\boldsymbol{\mu}}+\boldsymbol{n}^{\boldsymbol{\mu}}\cdot\big(\nu\boldsymbol{\nabla}_{\boldsymbol{\mu}}\boldsymbol{u}-p\mathbf{I}_{\mathtt{n_{sd}}}\big)\boldsymbol{E}^{\boldsymbol{\mu}} = \mathbf{0} & \text{on } \Gamma_S^{\boldsymbol{\mu}}\times\boldsymbol{\mathcal{I}}. \end{cases} \tag{3.4}$$

For the multi-dimensional problem, the compatibility condition induced by the free divergence condition can be written as

$$\langle 1, \boldsymbol{u}_D\cdot\boldsymbol{n}^{\boldsymbol{\mu}}\rangle_{\Gamma_D^{\boldsymbol{\mu}}\times\boldsymbol{\mathcal{I}}} + \langle 1, \boldsymbol{u}\cdot\boldsymbol{n}^{\boldsymbol{\mu}}\rangle_{(\partial\Omega^{\boldsymbol{\mu}}\setminus\Gamma_D^{\boldsymbol{\mu}})\times\boldsymbol{\mathcal{I}}} = 0 \tag{3.5}$$

and the additional constraint to avoid the indeterminacy of the pressure, required when $\Gamma_N^{\boldsymbol{\mu}}=\emptyset$, becomes

$$\Big\langle \frac{1}{|\partial\Omega^{\boldsymbol{\mu}}|}p, 1\Big\rangle_{\partial\Omega^{\boldsymbol{\mu}}\times\boldsymbol{\mathcal{I}}} = 0. \tag{3.6}$$

3.2 Hybridisable discontinuous Galerkin formulation

Let us consider a subdivision of the domain $\Omega^{\boldsymbol{\mu}}$ in $\mathtt{n_{el}}$ disjoint subdomains $\Omega_e^{\boldsymbol{\mu}}$ such that

$$\overline{\Omega}^{\boldsymbol{\mu}} = \bigcup_{e=1}^{\mathtt{n_{el}}} \overline{\Omega}_e^{\boldsymbol{\mu}}. \tag{3.7}$$

The interior boundaries of the subdomains define the so-called mesh skeleton or internal interface $\Gamma^{\boldsymbol{\mu}}$ as

$$\Gamma^{\boldsymbol{\mu}} := \left[\bigcup_{e=1}^{\mathtt{n_{el}}} \partial\Omega_e^{\boldsymbol{\mu}}\right] \setminus \partial\Omega^{\boldsymbol{\mu}}. \tag{3.8}$$

A partition of the parametric domains $\mathcal{I}^j$, for $j=1,\ldots,\mathtt{n_{pa}}$, in $\mathtt{n}_{\mathtt{el}}^j$ disjoint subdomains $\mathcal{I}_e^j$ such that

$$\overline{\mathcal{I}}^j = \bigcup_{e=1}^{\mathtt{n}_{\mathtt{el}}^j} \overline{\mathcal{I}}_e^j, \tag{3.9}$$

is also considered to use a Galerkin approach for the parametric problems. This is in contrast with other approaches that use collocation for the parametric problems.

3.2.1 Mixed formulation

Introducing the so-called *mixed variable* $\boldsymbol{L}=-\nu\boldsymbol{\nabla}_{\boldsymbol{\mu}}\boldsymbol{u}$, the Stokes problem can be written as a first-order system of equations in the broken computational domain,

namely

$$\begin{cases} \boldsymbol{L}_e + \nu \boldsymbol{\nabla}_{\boldsymbol{\mu}} \boldsymbol{u}_e = \boldsymbol{0} & \text{in } \Omega_e^{\boldsymbol{\mu}} \times \boldsymbol{\mathcal{I}}, \text{ and for } e = 1, \dots, \mathtt{n_{el}}, \\ \boldsymbol{\nabla}_{\boldsymbol{\mu}} \cdot \left(\boldsymbol{L}_e + p_e \mathbf{I}_{\mathtt{n_{sd}}} \right) = \boldsymbol{s} & \text{in } \Omega_e^{\boldsymbol{\mu}} \times \boldsymbol{\mathcal{I}}, \text{ and for } e = 1, \dots, \mathtt{n_{el}}, \\ \boldsymbol{\nabla}_{\boldsymbol{\mu}} \cdot \boldsymbol{u}_e = 0 & \text{in } \Omega_e^{\boldsymbol{\mu}} \times \boldsymbol{\mathcal{I}}, \text{ and for } e = 1, \dots, \mathtt{n_{el}}, \\ \boldsymbol{u}_e = \boldsymbol{u}_D & \text{on } \left(\partial \Omega_e^{\boldsymbol{\mu}} \cap \Gamma_D^{\boldsymbol{\mu}} \right) \times \boldsymbol{\mathcal{I}}, \\ \boldsymbol{n}^{\boldsymbol{\mu}} \cdot \left(\boldsymbol{L}_e + p_e \mathbf{I}_{\mathtt{n_{sd}}} \right) = -\boldsymbol{g}_N & \text{on } \left(\partial \Omega_e^{\boldsymbol{\mu}} \cap \Gamma_N^{\boldsymbol{\mu}} \right) \times \boldsymbol{\mathcal{I}}, \\ \boldsymbol{u}_e \cdot \boldsymbol{D}^{\boldsymbol{\mu}} - \boldsymbol{n}^{\boldsymbol{\mu}} \cdot \left(\boldsymbol{L}_e + p_e \mathbf{I}_{\mathtt{n_{sd}}} \right) \boldsymbol{E}^{\boldsymbol{\mu}} = \boldsymbol{0} & \text{on } \left(\partial \Omega_e^{\boldsymbol{\mu}} \cap \Gamma_S^{\boldsymbol{\mu}} \right) \times \boldsymbol{\mathcal{I}}, \\ [\![\boldsymbol{u} \otimes \boldsymbol{n}^{\boldsymbol{\mu}}]\!] = \boldsymbol{0} & \text{on } \Gamma^{\boldsymbol{\mu}} \times \boldsymbol{\mathcal{I}}, \\ [\![\boldsymbol{n}^{\boldsymbol{\mu}} \cdot \left(\boldsymbol{L} + p \mathbf{I}_{\mathtt{n_{sd}}} \right)]\!] = \boldsymbol{0} & \text{on } \Gamma^{\boldsymbol{\mu}} \times \boldsymbol{\mathcal{I}}, \end{cases} \tag{3.10}$$

where the last two equations, known as *transmission conditions*, impose the continuity of the velocity and the normal flux on the mesh skeleton. Following Montlaur et al., (2008), the *jump* operator $[\![\cdot]\!]$ is defined as the sum from the left, Ω_l, and right, Ω_r, elements of a given portion of the interface $\Gamma^{\mu} \times \boldsymbol{\mathcal{I}}$, that is

$$[\![\odot]\!] = \odot_l + \odot_r. \tag{3.11}$$

3.2.2 Strong form of the local and global problems

The HDG method solves the mixed problem of equation (3.10) in two steps. First, the so-called *local problems* are considered

$$\begin{cases} \boldsymbol{L}_e + \nu \boldsymbol{\nabla}_{\boldsymbol{\mu}} \boldsymbol{u}_e = \boldsymbol{0} & \text{in } \Omega_e^{\boldsymbol{\mu}} \times \boldsymbol{\mathcal{I}}, \text{ and for } e = 1, \dots, \mathtt{n_{el}}, \\ \boldsymbol{\nabla}_{\boldsymbol{\mu}} \cdot \left(\boldsymbol{L}_e + p_e \mathbf{I}_{\mathtt{n_{sd}}} \right) = \boldsymbol{s} & \text{in } \Omega_e^{\boldsymbol{\mu}} \times \boldsymbol{\mathcal{I}}, \text{ and for } e = 1, \dots, \mathtt{n_{el}}, \\ \boldsymbol{\nabla}_{\boldsymbol{\mu}} \cdot \boldsymbol{u}_e = 0 & \text{in } \Omega_e^{\boldsymbol{\mu}} \times \boldsymbol{\mathcal{I}}, \text{ and for } e = 1, \dots, \mathtt{n_{el}}, \\ \boldsymbol{u}_e = \boldsymbol{u}_D & \text{on } \left(\partial \Omega_e^{\boldsymbol{\mu}} \cap \Gamma_D^{\boldsymbol{\mu}} \right) \times \boldsymbol{\mathcal{I}}, \\ \boldsymbol{u}_e = \hat{\boldsymbol{u}} & \text{on } \left(\partial \Omega_e^{\boldsymbol{\mu}} \setminus \Gamma_D^{\boldsymbol{\mu}} \right) \times \boldsymbol{\mathcal{I}}, \\ \left\langle \dfrac{1}{|\partial \Omega_e^{\boldsymbol{\mu}}|} p_e, 1 \right\rangle_{\partial \Omega_e^{\boldsymbol{\mu}} \times \boldsymbol{\mathcal{I}}} = \rho_e, & \text{for } e = 1, \dots, \mathtt{n_{el}}, \end{cases} \tag{3.12}$$

where $\hat{\boldsymbol{u}}$ is the so-called hybrid variable, which is an independent variable representing the trace of the solution on the element faces, and ρ_e is the mean value of the pressure on the boundary $\partial \Omega_e$. It is worth noting that the local problem is a pure Dirichlet problem and therefore, the last condition in equation (3.12) is introduced to ensure the uniqueness of the pressure. The local problems can be solved independently, element by element, to write $\boldsymbol{L}_e$, $\boldsymbol{u}_e$ and p_e in terms of $\hat{\boldsymbol{u}}$ and ρ_e along the interface $\Gamma^{\boldsymbol{\mu}} \cup \Gamma_N^{\boldsymbol{\mu}} \cup \Gamma_S^{\boldsymbol{\mu}}$.

Second, the so-called *global problem* is defined to impose the continuity of the normal flux on the inter-element faces and the Neumann and slip boundary conditions, namely

$$\begin{cases} [\![\boldsymbol{n}^{\boldsymbol{\mu}} \cdot \left(\boldsymbol{L} + p\mathbf{I}_{\mathtt{n_{sd}}}\right)]\!] = \mathbf{0} & \text{on } \Gamma^{\boldsymbol{\mu}} \times \boldsymbol{\mathcal{I}}, \\ \boldsymbol{n}^{\boldsymbol{\mu}} \cdot (\boldsymbol{L}_e + p_e \mathbf{I}_{\mathtt{n_{sd}}}) = -\boldsymbol{g}_N & \text{on } \left(\partial\Omega_e^{\boldsymbol{\mu}} \cap \Gamma_N^{\boldsymbol{\mu}}\right) \times \boldsymbol{\mathcal{I}}, \\ \boldsymbol{u}_e \cdot \boldsymbol{D}^{\boldsymbol{\mu}} - \boldsymbol{n}^{\boldsymbol{\mu}} \cdot (\boldsymbol{L}_e + p_e \mathbf{I}_{\mathtt{n_{sd}}})\, \boldsymbol{E}^{\boldsymbol{\mu}} = \mathbf{0} & \text{on } \left(\partial\Omega_e^{\boldsymbol{\mu}} \cap \Gamma_S^{\boldsymbol{\mu}}\right) \times \boldsymbol{\mathcal{I}}. \end{cases} \tag{3.13}$$

It is worth noting that, due to the unique definition of the hybrid variable on each face and the Dirichlet boundary condition in the local problems, there is no need to enforce the continuity of the solution in the global problem.

The constraint of equation (3.5), induced by the incompressibility condition, is also considered in the global problem and written in terms of the hybrid variable as

$$\langle 1, \boldsymbol{u}_D \cdot \boldsymbol{n}^{\boldsymbol{\mu}} \rangle_{\Gamma_D^{\boldsymbol{\mu}} \times \boldsymbol{\mathcal{I}}} + \langle 1, \hat{\boldsymbol{u}} \cdot \boldsymbol{n}^{\boldsymbol{\mu}} \rangle_{(\partial\Omega^{\boldsymbol{\mu}} \setminus \Gamma_D^{\boldsymbol{\mu}}) \times \boldsymbol{\mathcal{I}}} = 0. \tag{3.14}$$

3.2.3 Weak form of the local and global problems

The following discrete functional spaces are introduced:

$$\begin{aligned} \mathcal{V}^h(\Omega^{\boldsymbol{\mu}}) &:= \{v \in \mathcal{L}_2(\Omega^{\boldsymbol{\mu}}) : v|_{\Omega_e^{\boldsymbol{\mu}}} \in \mathcal{P}^k(\Omega_e^{\boldsymbol{\mu}})\ \forall \Omega_e^{\boldsymbol{\mu}}\,,\ e = 1, \dots, \mathtt{n_{el}}\}, \\ \widehat{\mathcal{V}}^h(S) &:= \{\hat{v} \in \mathcal{L}_2(S) : \hat{v}|_{\Gamma_i^{\boldsymbol{\mu}}} \in \mathcal{P}^k(\Gamma_i^{\boldsymbol{\mu}})\ \forall \Gamma_i^{\boldsymbol{\mu}} \subset S \subseteq \Gamma^{\boldsymbol{\mu}} \cup \partial\Omega^{\boldsymbol{\mu}}\}, \\ \mathcal{L}^h(\mathcal{I}^j) &:= \{v \in \mathcal{L}_2(\mathcal{I}^j) : v|_{\mathcal{I}_e^j} \in \mathcal{P}^k(\mathcal{I}_e^j)\ \forall \mathcal{I}_e^j\,,\ e = 1, \dots, \mathtt{n}_{\mathtt{el}}^j\}, \\ \boldsymbol{\mathcal{L}}^h(\boldsymbol{\mathcal{I}}) &:= \mathcal{L}^h(\mathcal{I}^1) \otimes \cdots \otimes \mathcal{L}^h(\mathcal{I}^{\mathtt{n_{pa}}}), \\ \mathcal{V}_{\boldsymbol{\mu}}^h &:= \mathcal{V}^h(\Omega^{\boldsymbol{\mu}}) \otimes \boldsymbol{\mathcal{L}}^h(\boldsymbol{\mathcal{I}}), \\ \widehat{\boldsymbol{\mathcal{V}}}_{\boldsymbol{\mu}}^h &:= \left[\widehat{\mathcal{V}}^h(\Gamma^{\boldsymbol{\mu}} \cup \Gamma_N^{\boldsymbol{\mu}} \cup \Gamma_S^{\boldsymbol{\mu}}) \otimes \boldsymbol{\mathcal{L}}^h(\boldsymbol{\mathcal{I}})\right]^{\mathtt{n_{sd}}}, \\ \boldsymbol{\mathcal{V}}_{\boldsymbol{\mu}}^h &:= \left[\mathcal{V}^h(\Omega^{\boldsymbol{\mu}}) \otimes \boldsymbol{\mathcal{L}}^h(\boldsymbol{\mathcal{I}})\right]^{\mathtt{n_{sd}}}, \\ \boldsymbol{\mathcal{W}}_{\boldsymbol{\mu}}^h &:= \left[\mathcal{V}^h(\Omega^{\boldsymbol{\mu}}) \otimes \boldsymbol{\mathcal{L}}^h(\boldsymbol{\mathcal{I}})\right]^{\mathtt{n_{sd}} \times \mathtt{n_{sd}}}, \end{aligned}$$

where $\mathcal{P}^k(\Omega_e^{\boldsymbol{\mu}})$, $\mathcal{P}^k(\Gamma_i^{\boldsymbol{\mu}})$ and $\mathcal{P}^k(\mathcal{I}_e^j)$ stand for the spaces of polynomial functions of complete degree at most k in $\Omega_e^{\boldsymbol{\mu}}$, on $\Gamma_i^{\boldsymbol{\mu}}$ and in $\mathcal{I}_e^j$ respectively.

The weak form of the local problems, for e=$1, \dots, \mathtt{n_{el}}$, reads: given $\boldsymbol{u}_D$ on $\Gamma_D^{\boldsymbol{\mu}}$ and $\hat{\boldsymbol{u}}^h$ on $\Gamma^{\boldsymbol{\mu}} \cup \Gamma_N^{\boldsymbol{\mu}} \cup \Gamma_S^{\boldsymbol{\mu}}$, find $(\boldsymbol{L}_e^h, \boldsymbol{u}_e^h, p_e^h) \in \boldsymbol{\mathcal{W}}_{\boldsymbol{\mu}}^h \times \boldsymbol{\mathcal{V}}_{\boldsymbol{\mu}}^h \times \mathcal{V}_{\boldsymbol{\mu}}^h$ that satisfy

$$\begin{aligned} A_{LL}(\boldsymbol{W}, \boldsymbol{L}_e^h) + A_{Lu}(\boldsymbol{W}, \boldsymbol{u}_e^h) &= L_L(\boldsymbol{W}) + A_{L\hat{u}}(\boldsymbol{W}, \hat{\boldsymbol{u}}^h), \\ A_{uL}(\boldsymbol{v}, \boldsymbol{L}_e^h) + A_{uu}(\boldsymbol{v}, \boldsymbol{u}_e^h) + A_{up}(\boldsymbol{v}, p_e^h) &= L_u(\boldsymbol{v}) + A_{u\hat{u}}(\boldsymbol{v}, \hat{\boldsymbol{u}}^h), \\ A_{pu}(v, \boldsymbol{u}_e^h) &= L_p(v) + A_{p\hat{u}}(v, \hat{\boldsymbol{u}}^h), \\ A_{\rho p}(1, p_e^h) &= A_{\rho\rho}(1, \rho_e^h), \end{aligned} \tag{3.15}$$

for all $(\boldsymbol{W}, \boldsymbol{v}, v) \in \boldsymbol{\mathcal{W}}_{\boldsymbol{\mu}}^h \times \boldsymbol{\mathcal{V}}_{\boldsymbol{\mu}}^h \times \mathcal{V}_{\boldsymbol{\mu}}^h$, where the multi-dimensional bilinear and linear forms of the local problem are given by

$$\begin{aligned}
A_{LL}(\boldsymbol{W}, \boldsymbol{L}) &:= -\big(\boldsymbol{W}, \nu^{-1}\boldsymbol{L}\big)_{\Omega_e^{\boldsymbol{\mu}} \times \boldsymbol{\mathcal{I}}}, & A_{Lu}(\boldsymbol{W}, \boldsymbol{u}) &:= \big(\boldsymbol{\nabla}_{\boldsymbol{\mu}} \cdot \boldsymbol{W}, \boldsymbol{u}\big)_{\Omega_e^{\boldsymbol{\mu}} \times \boldsymbol{\mathcal{I}}}, \\
A_{L\hat{u}}(\boldsymbol{W}, \hat{\boldsymbol{u}}) &:= \langle \boldsymbol{n}^{\boldsymbol{\mu}} \cdot \boldsymbol{W}, \hat{\boldsymbol{u}} \rangle_{(\partial\Omega_e^{\boldsymbol{\mu}} \setminus \Gamma_D^{\boldsymbol{\mu}}) \times \boldsymbol{\mathcal{I}}}, & A_{uL}(\boldsymbol{v}, \boldsymbol{L}) &:= \big(\boldsymbol{v}, \boldsymbol{\nabla}_{\boldsymbol{\mu}} \cdot \boldsymbol{L}\big)_{\Omega_e^{\boldsymbol{\mu}} \times \boldsymbol{\mathcal{I}}}, \\
A_{uu}(\boldsymbol{v}, \boldsymbol{u}) &:= \langle \boldsymbol{v}, \boldsymbol{\tau}^{\boldsymbol{\mu}} \boldsymbol{u} \rangle_{\partial\Omega_e^{\boldsymbol{\mu}} \times \boldsymbol{\mathcal{I}}}, & A_{up}(\boldsymbol{v}, p) &:= \big(\boldsymbol{v}, \boldsymbol{\nabla}_{\boldsymbol{\mu}} p\big)_{\Omega_e^{\boldsymbol{\mu}} \times \boldsymbol{\mathcal{I}}}, \\
A_{u\hat{u}}(\boldsymbol{v}, \hat{\boldsymbol{u}}) &:= \langle \boldsymbol{v}, \boldsymbol{\tau}^{\boldsymbol{\mu}} \hat{\boldsymbol{u}} \rangle_{(\partial\Omega_e^{\boldsymbol{\mu}} \setminus \Gamma_D^{\boldsymbol{\mu}}) \times \boldsymbol{\mathcal{I}}}, & A_{pu}(v, \boldsymbol{u}) &:= \big(\boldsymbol{\nabla}_{\boldsymbol{\mu}} v, \boldsymbol{u}\big)_{\Omega_e^{\boldsymbol{\mu}} \times \boldsymbol{\mathcal{I}}}, \\
A_{p\hat{u}}(v, \hat{\boldsymbol{u}}) &:= \langle v, \hat{\boldsymbol{u}} \cdot \boldsymbol{n}^{\boldsymbol{\mu}} \rangle_{(\partial\Omega_e^{\boldsymbol{\mu}} \setminus \Gamma_D^{\boldsymbol{\mu}}) \times \boldsymbol{\mathcal{I}}}, & A_{\rho p}(w, p) &:= \langle w, |\partial\Omega_e^{\boldsymbol{\mu}}|^{-1} p \rangle_{\partial\Omega_e^{\boldsymbol{\mu}} \times \boldsymbol{\mathcal{I}}}, \\
A_{\rho\rho}(w, \rho) &:= \big(w, \rho\big)_{\boldsymbol{\mathcal{I}}}, &&
\end{aligned} \tag{3.16}$$

and

$$\begin{aligned}
L_L(\boldsymbol{W}) &:= \langle \boldsymbol{n}^{\boldsymbol{\mu}} \cdot \boldsymbol{W}, \boldsymbol{u}_D \rangle_{(\partial\Omega_e^{\boldsymbol{\mu}} \cap \Gamma_D^{\boldsymbol{\mu}}) \times \boldsymbol{\mathcal{I}}}, \\
L_u(\boldsymbol{v}) &:= \big(\boldsymbol{v}, \boldsymbol{s}\big)_{\Omega_e^{\boldsymbol{\mu}} \times \boldsymbol{\mathcal{I}}} + \langle \boldsymbol{v}, \boldsymbol{\tau}^{\boldsymbol{\mu}} \boldsymbol{u}_D \rangle_{(\partial\Omega_e^{\boldsymbol{\mu}} \cap \Gamma_D^{\boldsymbol{\mu}}) \times \boldsymbol{\mathcal{I}}}, \\
L_p(v) &:= \langle v, \boldsymbol{u}_D \cdot \boldsymbol{n}^{\boldsymbol{\mu}} \rangle_{(\partial\Omega_e^{\boldsymbol{\mu}} \cap \Gamma_D^{\boldsymbol{\mu}}) \times \boldsymbol{\mathcal{I}}},
\end{aligned} \tag{3.17}$$

respectively, where $(\cdot, \cdot)_D$ denotes the standard $\mathcal{L}_2$ scalar product in a generic subdomain D and $\boldsymbol{\tau}^{\boldsymbol{\mu}}$ is the stabilisation tensor, whose selection has an important influence on the accuracy, stability and convergence properties of the resulting HDG method (Cockburn et al., 2009c; Nguyen et al., 2009c,d, 2010b). The choice of the stabilisation tensor for geometrically parametrised problems will be discussed in the next section.

Similarly, the weak form of the global problem is: find $\hat{\boldsymbol{u}}^h \in \widehat{\boldsymbol{\mathcal{V}}}_{\boldsymbol{\mu}}^h$ and $\rho^h \in \mathbb{R}^{\mathtt{n_{el}}} \otimes \boldsymbol{\mathcal{L}}^h(\boldsymbol{\mathcal{I}})$ that satisfies

$$\begin{aligned}
\sum_{e=1}^{\mathtt{n_{el}}} \Big\{ A_{\hat{u}L}(\hat{\boldsymbol{v}}, \boldsymbol{L}_e^h) + A_{\hat{u}u}(\hat{\boldsymbol{v}}, \boldsymbol{u}_e^h) + A_{\hat{u}p}(\hat{\boldsymbol{v}}, p_e^h) + A_{\hat{u}\hat{u}}(\hat{\boldsymbol{v}}, \hat{\boldsymbol{u}}^h) \Big\} &= \sum_{e=1}^{\mathtt{n_{el}}} \left\{ L_{\hat{u}}(\hat{\boldsymbol{v}}) \right\}, \\
A_{p\hat{u}}(1, \hat{\boldsymbol{u}}^h) &= -L_p(1),
\end{aligned} \tag{3.18}$$

for all $\hat{\boldsymbol{v}} \in \widehat{\boldsymbol{\mathcal{V}}}_{\boldsymbol{\mu}}^h$, where the multi-dimensional bilinear and linear forms of the global problem are given by

$$\begin{aligned}
A_{\hat{u}L}(\hat{\boldsymbol{v}}, \boldsymbol{L}) :=& \langle \hat{\boldsymbol{v}}, \boldsymbol{n}^{\boldsymbol{\mu}} \cdot \boldsymbol{L} \rangle_{(\partial\Omega_e^{\boldsymbol{\mu}} \setminus (\Gamma_D^{\boldsymbol{\mu}} \cup \Gamma_S^{\boldsymbol{\mu}})) \times \boldsymbol{\mathcal{I}}} - \langle \hat{\boldsymbol{v}}, \boldsymbol{n}^{\boldsymbol{\mu}} \cdot \boldsymbol{L}\boldsymbol{E}^{\boldsymbol{\mu}} \rangle_{(\partial\Omega_e^{\boldsymbol{\mu}} \cap \Gamma_S^{\boldsymbol{\mu}}) \times \boldsymbol{\mathcal{I}}} \\
A_{\hat{u}u}(\hat{\boldsymbol{v}}, \boldsymbol{u}) :=& \langle \hat{\boldsymbol{v}}, \boldsymbol{\tau}^{\boldsymbol{\mu}} \boldsymbol{u} \rangle_{(\partial\Omega_e^{\boldsymbol{\mu}} \setminus (\Gamma_D^{\boldsymbol{\mu}} \cup \Gamma_S^{\boldsymbol{\mu}})) \times \boldsymbol{\mathcal{I}}} - \langle \hat{\boldsymbol{v}}, (\boldsymbol{\tau}^{\boldsymbol{\mu}} \boldsymbol{u}) \cdot \boldsymbol{E}^{\boldsymbol{\mu}} \rangle_{(\partial\Omega_e^{\boldsymbol{\mu}} \cap \Gamma_S^{\boldsymbol{\mu}}) \times \boldsymbol{\mathcal{I}}} \\
A_{\hat{u}p}(\hat{\boldsymbol{v}}, p) :=& \langle \hat{\boldsymbol{v}}, p\boldsymbol{n}^{\boldsymbol{\mu}} \rangle_{(\partial\Omega_e^{\boldsymbol{\mu}} \setminus (\Gamma_D^{\boldsymbol{\mu}} \cup \Gamma_S^{\boldsymbol{\mu}})) \times \boldsymbol{\mathcal{I}}} \\
A_{\hat{u}\hat{u}}(\hat{\boldsymbol{v}}, \hat{\boldsymbol{u}}) :=& - \langle \hat{\boldsymbol{v}}, \boldsymbol{\tau}^{\boldsymbol{\mu}} \hat{\boldsymbol{u}} \rangle_{(\partial\Omega_e^{\boldsymbol{\mu}} \setminus (\Gamma_D^{\boldsymbol{\mu}} \cup \Gamma_S^{\boldsymbol{\mu}})) \times \boldsymbol{\mathcal{I}}} \\
&+ \langle \hat{\boldsymbol{v}}, \hat{\boldsymbol{u}} \cdot \boldsymbol{D}^{\boldsymbol{\mu}} + (\boldsymbol{\tau}^{\boldsymbol{\mu}} \hat{\boldsymbol{u}}) \cdot \boldsymbol{E}^{\boldsymbol{\mu}} \rangle_{(\partial\Omega_e^{\boldsymbol{\mu}} \cap \Gamma_S^{\boldsymbol{\mu}}) \times \boldsymbol{\mathcal{I}}}
\end{aligned} \tag{3.19}$$

and

$$L_{\hat{u}}(\hat{\boldsymbol{v}}) := -\langle \hat{\boldsymbol{v}}, \boldsymbol{g}_N \rangle_{(\partial\Omega_e^{\boldsymbol{\mu}} \cap \Gamma_N^{\boldsymbol{\mu}}) \times \boldsymbol{\mathcal{I}}}, \tag{3.20}$$

respectively.

The local problem of equation (3.15) is used to write the velocity, $\boldsymbol{u}_e$, pressure, p_e, and gradient of the velocity $\boldsymbol{L}_e$, as a function of the hybrid variable, $\hat{u}$, and the mean value of the pressure in each element, ρ_e. Inserting these expressions in the global problem of equation (3.18) leads to a global problem with $\hat{u}$, and ρ being the only unknowns. Once the global problem is solved, the local problem can be solved, element-by-element, to retrieve the velocity, pressure and the gradient of the velocity in each element.

3.3 The proper generalised decomposition strategy

The solution of the parametric problem of dimension $\mathtt{n_{sd}}+\mathtt{n_{pa}}$, presented in the previous section, with the standard HDG approach is usually not affordable, even for a relatively small number of parameters. To circumvent the *curse of dimensionality*, this section proposes the use of the PGD framework. As it will be shown in this section, the use of an HDG formulation has important advantages compared to other formulations such as standard finite elements (Sevilla et al., 2020b).

To simplify the presentation, the subindex $_e$ and the superindex ^{h} used in the previous section to specify the element and the discrete approximations will be omitted here, unless they are needed to follow the development.

3.3.1 Separated spatial mapping to obtain generalised solutions

As discussed in detail in Patera et al., (2007), Rozza, (2014), and Sevilla et al., (2020b), the solution of the parametric problem described in section 3.2 requires that the bilinear and linear forms in the weak form can be expressed, or well approximated, by a sum of products of parametric functions and operators that are parameter-independent. To enforce the affine parameter dependence, the integrals appearing in the weak form must involve domains that are not dependent upon the parameters. Following the work of Ammar et al., (2014), Sevilla et al., (2020b), and Zlotnik et al., (2015), a mapping between a parameter-independent reference domain, Ω, and the geometrically parametrised domain is considered, namely

$$\begin{aligned} \boldsymbol{\mathcal{M}}_{\boldsymbol{\mu}} \; &: \Omega \times \boldsymbol{\mathcal{I}} \longrightarrow \Omega^{\boldsymbol{\mu}} \\ &(\boldsymbol{x}, \boldsymbol{\mu}) \longmapsto \boldsymbol{x}^{\boldsymbol{\mu}} = \boldsymbol{\mathcal{M}}_{\boldsymbol{\mu}}(\boldsymbol{x}, \boldsymbol{\mu}). \end{aligned} \tag{3.21}$$

The coordinates of the reference, or *undeformed*, domain are denoted by $\boldsymbol{x}$ whereas the coordinates of the parametric, or *deformed*, domain are denoted by $\boldsymbol{x}^{\boldsymbol{\mu}}$. To ensure the affine parameter dependence, the mapping is assumed to be given in separated form as

$$\boldsymbol{\mathcal{M}}_{\boldsymbol{\mu}}(\boldsymbol{x}, \boldsymbol{\mu}) = \sum_{k=1}^{\mathtt{n_M}} \mathbf{M}^k(\boldsymbol{x}) \phi^k(\boldsymbol{\mu}), \tag{3.22}$$

where $\mathtt{n_M}$ is the number of terms required to express the mapping in a separable form.

Remark 3. *To simplify the presentation here, it is assumed that the separated representation of the mapping is given analytically. As mentioned earlier, a general strategy to construct a separable mapping was described in Sevilla et al., (2020b) using an exact boundary description of the computational domain by means of NURBS.*

The separated representation of the mapping leads to the following separated representation of its Jacobian

$$\mathbf{J}_{\boldsymbol{\mu}}(\boldsymbol{x},\boldsymbol{\mu}) = \frac{\partial \boldsymbol{x}^{\boldsymbol{\mu}}}{\partial \boldsymbol{x}}(\boldsymbol{x},\boldsymbol{\mu}) = \sum_{k=1}^{\mathtt{n_M}} \mathbf{J}^k(\boldsymbol{x})\phi^k(\boldsymbol{\mu}). \tag{3.23}$$

The separated description of the mapping is used to obtain a separated expression of the determinant and the adjoint of the Jacobian.

Using the Leibniz formula, a separated representation of the determinant is obtained, namely

$$\det(\mathbf{J}_{\boldsymbol{\mu}}) = \Big(\sum_{k=1}^{\mathtt{n_M}} \phi^k J_{11}^k\Big)\Big(\sum_{k=1}^{\mathtt{n_M}} \phi^k J_{22}^k\Big) - \Big(\sum_{k=1}^{\mathtt{n_M}} \phi^k J_{12}^k\Big)\Big(\sum_{k=1}^{\mathtt{n_M}} \phi^k J_{21}^k\Big)$$

in two dimensions and

$$\det(\mathbf{J}_{\boldsymbol{\mu}}) = \sum_{\sigma\in\mathcal{S}_3} \operatorname{sgn}(\sigma) \prod_{l=1}^{3}\Big(\sum_{k=1}^{\mathtt{n_M}} \phi^k \mathbf{J}_{l\sigma(l)}^k\Big),$$

in three dimensions, where $\mathcal{S}_3$ denotes the set of permutations of the integers $\{1,2,3\}$, with $\sigma(l)$ being the element in position l after the reordering, $\operatorname{sgn}(\sigma)$ is the signature of σ (i.e. $+1$ for even σ and -1 for odd σ) and $\delta_{i\sigma(i)}$ is the classical Kronecker delta.

Similarly, using the Leverrier's algorithm, a separated representation of the adjoint is obtained, namely

$$\operatorname{adj}(\mathbf{J}_{\boldsymbol{\mu}}) = \sum_{k=1}^{\mathtt{n_M}} \phi^k \Big(\operatorname{tr}(\mathbf{J}^k)\mathbf{I}_2 - \mathbf{J}^k\Big)$$

and

$$\begin{aligned}\operatorname{adj}(\mathbf{J}_{\boldsymbol{\mu}}) = &\sum_{k=1}^{\mathtt{n_M}} \phi^k \Big(\operatorname{tr}(\mathbf{J}^k)\mathbf{I}_3 - \mathbf{J}^k\Big) \\ &+ \sum_{k=1}^{\mathtt{n_M}}\sum_{l=1}^{\mathtt{n_M}} \phi^k\phi_l \Big(\frac{1}{2}\big(\operatorname{tr}(\mathbf{J}^k)\,\operatorname{tr}(\mathbf{J}^l) - \operatorname{tr}(\mathbf{J}^k\mathbf{J}^l)\big)\mathbf{I}_3 - \operatorname{tr}(\mathbf{J}^k)\,\mathbf{J}^l + \mathbf{J}^k\mathbf{J}^l\Big)\end{aligned}$$

in three dimensions.

The separated expression of the determinant of the Jacobian and its adjoint are written in compact form as

$$\det(\mathbf{J}_{\boldsymbol{\mu}})(\boldsymbol{x},\boldsymbol{\mu}) = \sum_{k=1}^{\mathtt{n_d}} D^k(\boldsymbol{x})\theta^k(\boldsymbol{\mu}) \tag{3.24}$$

and

$$\operatorname{adj}(\mathbf{J}_{\boldsymbol{\mu}})(\boldsymbol{x},\boldsymbol{\mu}) = \sum_{k=1}^{\mathtt{n_a}} \mathbf{A}^k(\boldsymbol{x})\vartheta^k(\boldsymbol{\mu}), \tag{3.25}$$

respectively.

It is worth noting that the number of terms required to write the determinant and the adjoint in a separated form, $\mathtt{n_d}$ and $\mathtt{n_a}$ respectively, is higher than the number of terms required to describe the mapping in a separated form $\mathtt{n_M}$.

3.3.2 Affine parameter dependence of the HDG bilinear and linear forms

Introducing the mapping $\boldsymbol{\mathcal{M}}_{\boldsymbol{\mu}}$ of equation (3.21) into the weak form of the local and global problems, it is possible to write the integrals over the reference domain, Ω, and its boundary, $\partial\Omega$, not dependent on the parameters $\boldsymbol{\mu}$. The bilinear and linear forms for the local problems can be written as

$$\begin{aligned}
A_{LL}(\boldsymbol{W},\boldsymbol{L}) &= -\big(\boldsymbol{W}, \nu^{-1}\det(\mathbf{J}_{\boldsymbol{\mu}})\boldsymbol{L}\big)_{\Omega_e\times\boldsymbol{\mathcal{I}}},\\
A_{Lu}(\boldsymbol{W},\boldsymbol{u}) &= \big(\operatorname{adj}(\mathbf{J}_{\boldsymbol{\mu}})\boldsymbol{\nabla}\cdot\boldsymbol{W}, \boldsymbol{u}\big)_{\Omega_e\times\boldsymbol{\mathcal{I}}},\\
A_{L\hat{u}}(\boldsymbol{W},\hat{\boldsymbol{u}}) &= \langle\operatorname{adj}(\mathbf{J}_{\boldsymbol{\mu}})\boldsymbol{n}\cdot\boldsymbol{W}, \hat{\boldsymbol{u}}\rangle_{(\partial\Omega_e\setminus\Gamma_D)\times\boldsymbol{\mathcal{I}}},\\
A_{uL}(\boldsymbol{v},\boldsymbol{L}) &= \big(\boldsymbol{v}, \operatorname{adj}(\mathbf{J}_{\boldsymbol{\mu}})\boldsymbol{\nabla}\cdot\boldsymbol{L}\big)_{\Omega_e\times\boldsymbol{\mathcal{I}}},\\
A_{uu}(\boldsymbol{v},\boldsymbol{u}) &= \langle\boldsymbol{v}, \boldsymbol{\tau}\boldsymbol{u}\rangle_{\partial\Omega_e\times\boldsymbol{\mathcal{I}}},\\
A_{up}(\boldsymbol{v},p) &= \big(\boldsymbol{v}, \operatorname{adj}(\mathbf{J}_{\boldsymbol{\mu}})\boldsymbol{\nabla}p\big)_{\Omega_e\times\boldsymbol{\mathcal{I}}},\\
A_{u\hat{u}}(\boldsymbol{v},\hat{\boldsymbol{u}}) &= \langle\boldsymbol{v}, \boldsymbol{\tau}\hat{\boldsymbol{u}}\rangle_{(\partial\Omega_e\setminus\Gamma_D)\times\boldsymbol{\mathcal{I}}},\\
A_{pu}(v,\boldsymbol{u}) &= \big(\operatorname{adj}(\mathbf{J}_{\boldsymbol{\mu}})\boldsymbol{\nabla}v, \boldsymbol{u}\big)_{\Omega_e\times\boldsymbol{\mathcal{I}}},\\
A_{p\hat{u}}(v,\hat{\boldsymbol{u}}) &= \langle v, \hat{\boldsymbol{u}}\cdot\operatorname{adj}(\mathbf{J}_{\boldsymbol{\mu}})\boldsymbol{n}\rangle_{(\partial\Omega_e\setminus\Gamma_D)\times\boldsymbol{\mathcal{I}}},\\
A_{\rho p}(w,p) &= \langle w, |\partial\Omega_e|^{-1}p\rangle_{\partial\Omega_e\times\boldsymbol{\mathcal{I}}},\\
A_{\rho\rho}(w,\rho) &= \big(w,\rho\big)_{\boldsymbol{\mathcal{I}}},
\end{aligned} \tag{3.26}$$

and

$$\begin{aligned}
L_L(\boldsymbol{W}) &= \langle\operatorname{adj}(\mathbf{J}_{\boldsymbol{\mu}})\boldsymbol{n}\cdot\boldsymbol{W}, \boldsymbol{u}_D\rangle_{(\partial\Omega_e\cap\Gamma_D)\times\boldsymbol{\mathcal{I}}},\\
L_u(\boldsymbol{v}) &= \big(\boldsymbol{v}, \det(\mathbf{J}_{\boldsymbol{\mu}})\boldsymbol{s}\big)_{\Omega_e\times\boldsymbol{\mathcal{I}}} + \langle\boldsymbol{v}, \boldsymbol{\tau}\boldsymbol{u}_D\rangle_{(\partial\Omega_e\cap\Gamma_D)\times\boldsymbol{\mathcal{I}}},\\
L_p(v) &= \langle v, \boldsymbol{u}_D\cdot\operatorname{adj}(\mathbf{J}_{\boldsymbol{\mu}})\boldsymbol{n}\rangle_{(\partial\Omega_e\cap\Gamma_D)\times\boldsymbol{\mathcal{I}}},
\end{aligned} \tag{3.27}$$

respectively, where the adjoint operator is defined as $\text{adj}(\boldsymbol{A}) = \det(\boldsymbol{A})\,\boldsymbol{A}^{-1}$ and the stabilisation parameter in the deformed domain is chosen as

$$\boldsymbol{\tau}^{\boldsymbol{\mu}} := \frac{1}{\|\,\text{adj}(\mathbf{J}_{\boldsymbol{\mu}})\boldsymbol{n}\|}\boldsymbol{\tau}. \tag{3.28}$$

The scaling factor $\|\text{adj}(\mathbf{J}_{\boldsymbol{\mu}})\boldsymbol{n}\|$ in equation (3.28) accounts for the increased or decreased area of the deformed face, $\partial\Omega_e^{\boldsymbol{\mu}}$, with respect to the reference one, $\partial\Omega_e$. This definition, inspired by the expression of the penalty coefficient in classical interior penalty DG methods (Arnold, 1982), ensures that the larger the deformation of the face, the smaller the value of $\boldsymbol{\tau}^{\boldsymbol{\mu}}$ is. This ensures that a weaker continuity is imposed for large deformations and it is justified by the expected loss of accuracy in the hybrid variable when the mapping introduces a large deformation.

Following previous work on HDG methods for Stokes problems (Giacomini et al., 2018), the stabilisation parameter in the reference domain is selected as $\boldsymbol{\tau} = (\tau\nu/\ell)\mathbf{I}_{\mathtt{n_{sd}}}$, where τ is a numerical parameter, selected as $\tau = 10$ in this work, and ℓ is a characteristic length of the domain.

Remark 4. *As mentioned above, it holds that* $\|\,\text{adj}(\mathbf{J}_{\boldsymbol{\mu}})\boldsymbol{n}\| = |\partial\Omega_e^{\boldsymbol{\mu}}|/|\partial\Omega_e|$. *Hence, no parametric dependence appears in the arguments of the bilinear form* $A_{\rho p}$.

Analogously, the bilinear and linear forms for the global problem can be written as

$$\begin{aligned}
A_{\hat{u}L}(\hat{\boldsymbol{v}}, \boldsymbol{L}) =& \langle \hat{\boldsymbol{v}}, \text{adj}\,(\mathbf{J}_{\boldsymbol{\mu}})\boldsymbol{n} \cdot \boldsymbol{L}\rangle_{(\partial\Omega_e \setminus (\Gamma_D \cup \Gamma_S))\times\boldsymbol{\mathcal{I}}} \\
&- \langle \hat{\boldsymbol{v}}, \text{adj}\,(\mathbf{J}_{\boldsymbol{\mu}})\boldsymbol{n} \cdot \boldsymbol{L}\boldsymbol{E}\rangle_{(\partial\Omega_e \cap \Gamma_S)\times\boldsymbol{\mathcal{I}}} \\
A_{\hat{u}u}(\hat{\boldsymbol{v}}, \boldsymbol{u}) =& \langle \hat{\boldsymbol{v}}, \boldsymbol{\tau}\boldsymbol{u}\rangle_{(\partial\Omega_e \setminus (\Gamma_D \cup \Gamma_S))\times\boldsymbol{\mathcal{I}}} - \langle \hat{\boldsymbol{v}}, (\boldsymbol{\tau}\boldsymbol{u})\cdot\boldsymbol{E}\rangle_{(\partial\Omega_e \cap \Gamma_S)\times\boldsymbol{\mathcal{I}}} \\
A_{\hat{u}p}(\hat{\boldsymbol{v}}, p) =& \langle \hat{\boldsymbol{v}}, p\,\text{adj}\,(\mathbf{J}_{\boldsymbol{\mu}})\boldsymbol{n}\rangle_{(\partial\Omega_e \setminus (\Gamma_D \cup \Gamma_S))\times\boldsymbol{\mathcal{I}}} \\
A_{\hat{u}\hat{u}}(\hat{\boldsymbol{v}}, \hat{\boldsymbol{u}}) =& - \langle \hat{\boldsymbol{v}}, \boldsymbol{\tau}\hat{\boldsymbol{u}}\rangle_{(\partial\Omega_e \setminus (\Gamma_D \cup \Gamma_S))\times\boldsymbol{\mathcal{I}}} \\
&+ \langle \hat{\boldsymbol{v}}, \hat{\boldsymbol{u}}\cdot\text{adj}\,(\mathbf{J}_{\boldsymbol{\mu}})\boldsymbol{D} + (\boldsymbol{\tau}\hat{\boldsymbol{u}})\cdot\boldsymbol{E}\rangle_{(\partial\Omega_e \cap \Gamma_S)\times\boldsymbol{\mathcal{I}}}
\end{aligned} \tag{3.29}$$

and

$$L_{\hat{u}}(\hat{\boldsymbol{v}}) = -\langle \hat{\boldsymbol{v}}, \boldsymbol{g}_N\rangle_{(\partial\Omega_e \cap \Gamma_N)\times\boldsymbol{\mathcal{I}}}, \tag{3.30}$$

respectively.

Remark 5. *The derivation of the terms on the slip boundary in* (3.29) *follows from the relationship* $\langle \hat{\boldsymbol{v}}, \boldsymbol{n}^{\boldsymbol{\mu}} \cdot \boldsymbol{H}\rangle_{(\partial\Omega_e^{\boldsymbol{\mu}} \cap \Gamma_S^{\boldsymbol{\mu}})\times\boldsymbol{\mathcal{I}}} = \langle \hat{\boldsymbol{v}}, \text{adj}\,(\mathbf{J}_{\boldsymbol{\mu}})\boldsymbol{n} \cdot \boldsymbol{H}\rangle_{(\partial\Omega_e \cap \Gamma_S)\times\boldsymbol{\mathcal{I}}}$ *and the definition* (3.28). *The slip boundary condition is used here to enforce a symmetry condition and therefore, it is assumed that the orientation of the vectors* $\{\boldsymbol{n}^{\boldsymbol{\mu}}, \boldsymbol{t}_1^{\boldsymbol{\mu}}, ..., \boldsymbol{t}_{\mathtt{n_{sd}}-1}^{\boldsymbol{\mu}}\}$ *is preserved by the mapping* $\boldsymbol{\mathcal{M}}_{\boldsymbol{\mu}}$. *It is worth noting that this does not imply that* $\Gamma_S^{\boldsymbol{\mu}} = \Gamma_S$ *as it will be shown with numerical examples.*

Remark 6. *As is typical in the context of shape optimisation (Allaire et al., 2007), in* (3.30) *it is assumed that Neumann boundaries, where a traction (or pseudo-traction)*

is imposed, are fixed, that is, $\Gamma_N^{\boldsymbol{\mu}}=\Gamma_N$*. On the contrary, deformable Neumann boundaries, also known as free boundaries, are traction-free, whence* $\boldsymbol{g}_N$ *is null.*

3.3.3 Separated representation of the data

As usual in a PGD context, the data is assumed to be given in separated form. For the Stokes problem under consideration, this means that the Dirichlet and Neumann data and the source term can be written as

$$\begin{aligned}\boldsymbol{u}_D &= \sum_{l=1}^{\mathtt{n_D}} \boldsymbol{g}_D^l(\boldsymbol{x})\lambda_D^l(\boldsymbol{\mu}),\\ \boldsymbol{g}_N &= \sum_{l=1}^{\mathtt{n_N}} \boldsymbol{g}_N^l(\boldsymbol{x})\lambda_N^l(\boldsymbol{\mu}),\\ \boldsymbol{s} &= \sum_{l=1}^{\mathtt{n_S}} \boldsymbol{g}_S^l(\boldsymbol{x})\lambda_S^l(\boldsymbol{\mu}).\end{aligned} \tag{3.31}$$

Even if the data is not directly given in this form, it is possible to obtain a good approximation in a separated form, see Chinesta et al., (2013b).

3.3.4 Separated representation of the primal, mixed and hybrid variables

The standard PGD approach consists of assuming a separated representation of all the variables. For instance, for the velocity field, it is assumed that its PGD approximation can be written as

$$\boldsymbol{u}_{\mathtt{PGD}}^m(\boldsymbol{x},\boldsymbol{\mu}) = \sum_{k=1}^{m} \tilde{\boldsymbol{f}}_u^{\,k}(\boldsymbol{x})\,\tilde{\psi}^k(\boldsymbol{\mu}),$$

where $\tilde{\boldsymbol{f}}_u^{\,k}$ and $\tilde{\psi}^k$ are the k-th spatial and parametric modes respectively and the total number of modes is a priori unknown and automatically determined by the algorithm based on a user-defined tolerance, as described in the next section.

In practice, it is advantageous (Sevilla et al., 2020b) to write the separated approximation as

$$\boldsymbol{u}_{\mathtt{PGD}}^m(\boldsymbol{x},\boldsymbol{\mu}) = \sigma_u^m \boldsymbol{f}_u^m(\boldsymbol{x})\,\psi^m(\boldsymbol{\mu}) + \boldsymbol{u}_{\mathtt{PGD}}^{m-1}(\boldsymbol{x},\boldsymbol{\mu}),$$

where $\boldsymbol{f}_u^m$ and ψ^m are the normalised m-th spatial and parametric modes, respectively, and σ_u^m is the amplitude of the m-th mode, namely $\boldsymbol{f}_u^m := \tilde{\boldsymbol{f}}_u^{\,m}/\|\tilde{\boldsymbol{f}}_u^{\,m}\|$, $\psi^m := \tilde{\psi}^m/\|\tilde{\psi}^m\|$ and $\sigma_u^m := \|\tilde{\boldsymbol{f}}_u^{\,m}\|\|\tilde{\psi}^m\|$.

This alternative expression enables to directly use the amplitude of the modes, σ_u^m, to determine when it is feasible to stop adding new modes. In addition, as explained in detail in the next section, the expression of equation (3.3.4) suggests that the modes

are computed sequentially. So, assuming that the first $m-1$ modes are known, the next section will focus on detailing how the new mode m is computed.

In this work, the implementation follows the *predictor-corrector* PGD rationale, which has been shown (Tsiolakis et al., 2020a) to improve the original algorithm, because it applies the alternating direction method to the Jacobian of the high-dimensional nonlinear problem. This improves the convergence for each mode because it is easier to select the initial prediction and provides a faster convergence.

Each variable of the HDG formulation, presented in section 3.2, is written as a rank-m separable approximation, that is

$$\begin{aligned}
\boldsymbol{L}^m_{\texttt{PGD}}(\boldsymbol{x},\boldsymbol{\mu}) &= \sigma^m_L[\boldsymbol{F}^m_L(\boldsymbol{x})\,\psi^m(\boldsymbol{\mu}) + \Delta\boldsymbol{L}^m_{\texttt{PGD}}(\boldsymbol{x},\boldsymbol{\mu})] + \boldsymbol{L}^{m-1}_{\texttt{PGD}}(\boldsymbol{x},\boldsymbol{\mu}),\\
\boldsymbol{u}^m_{\texttt{PGD}}(\boldsymbol{x},\boldsymbol{\mu}) &= \sigma^m_u[\boldsymbol{f}^m_u(\boldsymbol{x})\,\psi^m(\boldsymbol{\mu}) + \Delta\boldsymbol{u}^m_{\texttt{PGD}}(\boldsymbol{x},\boldsymbol{\mu})] + \boldsymbol{u}^{m-1}_{\texttt{PGD}}(\boldsymbol{x},\boldsymbol{\mu}),\\
p^m_{\texttt{PGD}}(\boldsymbol{x},\boldsymbol{\mu}) &= \sigma^m_p[f^m_p(\boldsymbol{x})\,\psi^m(\boldsymbol{\mu}) + \Delta p^m_{\texttt{PGD}}(\boldsymbol{x},\boldsymbol{\mu})] + p^{m-1}_{\texttt{PGD}}(\boldsymbol{x},\boldsymbol{\mu}),\\
\hat{\boldsymbol{u}}^m_{\texttt{PGD}}(\boldsymbol{x},\boldsymbol{\mu}) &= \sigma^m_{\hat{u}}[\boldsymbol{f}^m_{\hat{u}}(\boldsymbol{x})\,\psi^m(\boldsymbol{\mu}) + \Delta\hat{\boldsymbol{u}}^m_{\texttt{PGD}}(\boldsymbol{x},\boldsymbol{\mu})] + \hat{\boldsymbol{u}}^{m-1}_{\texttt{PGD}}(\boldsymbol{x},\boldsymbol{\mu}),\\
\rho^m_{\texttt{PGD}}(\boldsymbol{x},\boldsymbol{\mu}) &= \sigma^m_\rho[f^m_\rho(\boldsymbol{x})\,\psi^m(\boldsymbol{\mu}) + \Delta\rho^m_{\texttt{PGD}}(\boldsymbol{x},\boldsymbol{\mu})] + \rho^{m-1}_{\texttt{PGD}}(\boldsymbol{x},\boldsymbol{\mu}),
\end{aligned} \tag{3.32}$$

where $\sigma^m_L\boldsymbol{F}^m_L\psi^m$, $\sigma^m_u\boldsymbol{f}^m_u\psi^m$, $\sigma^m_p f^m_p\psi^m$, $\sigma^m_{\hat{u}}\boldsymbol{f}^m_{\hat{u}}\psi^m$ and $\sigma^m_\rho f^m_\rho\psi^m$ are the predictors of the m-th mode in the PGD expansion, whereas $\sigma^m_L\Delta\boldsymbol{L}^m_{\texttt{PGD}}$, $\sigma^m_u\Delta\boldsymbol{u}^m_{\texttt{PGD}}$, $\sigma^m_p\Delta p^m_{\texttt{PGD}}$, $\sigma^m_{\hat{u}}\Delta\hat{\boldsymbol{u}}^m_{\texttt{PGD}}$ and $\sigma^m_\rho\Delta\rho^m_{\texttt{PGD}}$ are the corresponding correction terms. Introducing the variation Δ, the correctors are defined as

$$\begin{aligned}
\Delta\boldsymbol{L}^m_{\texttt{PGD}}(\boldsymbol{x},\boldsymbol{\mu}) &:= \Delta\boldsymbol{F}_L(\boldsymbol{x})\,\psi^m(\boldsymbol{\mu}) + \boldsymbol{F}^m_L(\boldsymbol{x})\,\Delta\psi(\boldsymbol{\mu}) + \Delta\boldsymbol{F}_L(\boldsymbol{x})\,\Delta\psi(\boldsymbol{\mu}),\\
\Delta\boldsymbol{u}^m_{\texttt{PGD}}(\boldsymbol{x},\boldsymbol{\mu}) &:= \Delta\boldsymbol{f}_u(\boldsymbol{x})\,\psi^m(\boldsymbol{\mu}) + \boldsymbol{f}^m_u(\boldsymbol{x})\,\Delta\psi(\boldsymbol{\mu}) + \Delta\boldsymbol{f}_u(\boldsymbol{x})\,\Delta\psi(\boldsymbol{\mu}),\\
\Delta p^m_{\texttt{PGD}}(\boldsymbol{x},\boldsymbol{\mu}) &:= \Delta f_p(\boldsymbol{x})\,\psi^m(\boldsymbol{\mu}) + f^m_p(\boldsymbol{x})\,\Delta\psi(\boldsymbol{\mu}) + \Delta f_p(\boldsymbol{x})\,\Delta\psi(\boldsymbol{\mu}),\\
\Delta\hat{\boldsymbol{u}}^m_{\texttt{PGD}}(\boldsymbol{x},\boldsymbol{\mu}) &:= \Delta\boldsymbol{f}_{\hat{u}}(\boldsymbol{x})\,\psi^m(\boldsymbol{\mu}) + \boldsymbol{f}^m_{\hat{u}}(\boldsymbol{x})\,\Delta\psi(\boldsymbol{\mu}) + \Delta\boldsymbol{f}_{\hat{u}}(\boldsymbol{x})\,\Delta\psi(\boldsymbol{\mu}),\\
\Delta\rho^m_{\texttt{PGD}}(\boldsymbol{x},\boldsymbol{\mu}) &:= \Delta f_\rho(\boldsymbol{x})\,\psi^m(\boldsymbol{\mu}) + f^m_\rho(\boldsymbol{x})\,\Delta\psi(\boldsymbol{\mu}) + \Delta f_\rho(\boldsymbol{x})\,\Delta\psi(\boldsymbol{\mu}),
\end{aligned} \tag{3.33}$$

where the last term denotes a high-order variation and it is henceforth neglected.

Each term, or *mode*, of the PGD approximation is the product of a function that depends upon the spatial coordinates and a function that depends upon the parameters. In addition, the parametric functions are assumed to be the product of functions that depend upon a single parameter, namely

$$\psi^m(\boldsymbol{\mu}) = \prod_{j=1}^{\texttt{n}_{\texttt{pa}}} \psi^m_j(\mu_j). \tag{3.34}$$

Remark 7. *This work considers the so-called single-parameter approach, where the parametric function of the m-th mode, ψ^m, is the same for all the variables. Other approaches, including a different parametric function for each variable or even the use of vector-valued parametric functions in the approximation of vector fields are discussed in Díez et al., (2017). It is worth noting that using the same parametric*

function for all the variables is particularly beneficial in the context of HDG due to the large number of functions involved, not only velocity and pressure but also the trace of the velocity, the velocity gradient and the mean value of the pressure.

The tangent manifold for $\boldsymbol{L}$ is characterised by choosing $\boldsymbol{W}$ as variations of $\boldsymbol{F}_L\psi$, that is

$$\boldsymbol{W} = \delta\boldsymbol{F}_L\psi^m + \sigma_L^m\boldsymbol{F}_L^m\delta\psi, \tag{3.35}$$

for $\delta\boldsymbol{F}_L \in \boldsymbol{\mathcal{W}}^h$ and $\delta\psi \in \boldsymbol{\mathcal{L}}^h(\boldsymbol{\mathcal{I}})$. Similarly, the tangent manifolds for $\boldsymbol{u}$, p, $\hat{\boldsymbol{u}}$ and ρ are characterised by choosing

$$\begin{aligned} \boldsymbol{v} &= \delta\boldsymbol{f}_u\psi^m + \sigma_u^m\boldsymbol{f}_u^m\delta\psi, \quad v = \delta f_p\psi^m + \sigma_p^m f_p^m\delta\psi, \\ \hat{\boldsymbol{v}} &= \delta\boldsymbol{f}_{\hat{u}}\psi^m + \sigma_{\hat{u}}^m\boldsymbol{f}_{\hat{u}}^m\delta\psi, \quad w = \delta f_\rho\psi^m + \sigma_\rho^m f_\rho^m\delta\psi, \end{aligned} \tag{3.36}$$

for $\delta\boldsymbol{f}_u \in \boldsymbol{\mathcal{V}}^h$, $\delta f_p \in \mathcal{V}^h$, $\delta\boldsymbol{f}_{\hat{u}} \in \widehat{\boldsymbol{\mathcal{V}}}^h$ and $\delta f_\rho \in \mathbb{R}^{\mathtt{n_{el}}}$. Note that the functional spaces $\boldsymbol{\mathcal{W}}^h, \boldsymbol{\mathcal{V}}^h, \mathcal{V}^h, \widehat{\boldsymbol{\mathcal{V}}}^h$ are those defined in section 2.2.3 for a spatial problem.

3.3.5 Alternating direction scheme

With the separated structure of the PGD approximations, the weighting functions and the bilinear and linear HDG forms described in the previous sections, it is possible to drastically reduce the complexity of the problem. The PGD uses a fixed-point iteration scheme for the high-dimensional nonlinear problem solved with an alternating direction strategy to reduce the computational cost (iterating along low-dimensional problems).

First, in the so-called *spatial iteration*, the parametric function of the m-th mode is assumed known and the spatial functions are determined. As it will be shown, this step requires to solve a system of equations with a very similar structure to the non-parametric HDG problem. Second, in the so-called *parametric iteration*, the parametric function is computed using the spatial functions determined in the first step. This process is repeated until convergence is achieved. It is worth noting that the order of the spatial and parametric iterations can be swapped without affecting the alternating direction algorithm.

Let us assume that we have computed the first $m-1$ modes and it is of interest to compute the m-th mode. In the next two sections, the alternating direction strategy to compute the spatial and parametric modes is detailed.

The spatial iteration

In the spatial iteration, it is assumed that the parametric function ψ^m and the spatial predictions $\sigma_L^m\boldsymbol{F}_L^m$, $\sigma_u^m\boldsymbol{f}_u^m$, $\sigma_p^m f_p^m$, $\sigma_{\hat{u}}^m\boldsymbol{f}_{\hat{u}}^m$ and $\sigma_\rho^m f_\rho^m$ are known and the goal is to compute the corresponding corrections $\sigma_L^m\Delta\boldsymbol{F}_L$, $\sigma_u^m\Delta\boldsymbol{f}_u$, $\sigma_p^m\Delta f_p$, $\sigma_{\hat{u}}^m\Delta\boldsymbol{f}_{\hat{u}}$ and $\sigma_\rho^m\Delta f_\rho$.

As usual in a PGD context, it is assumed that no previous knowledge of the solution is available and therefore, the trivial initial guess of ψ^m=1 is employed for the parametric function.

Taking into account that $\delta\psi$=0 when ψ^m is known and introducing the expression of the PGD approximations and the weighting functions in the weak form of the HDG local problems, the following weak form of the local problem for the spatial iteration is obtained: find $(\sigma_L^m \Delta \boldsymbol{F}_L, \sigma_u^m \Delta \boldsymbol{f}_u, \sigma_p^m \Delta f_p) \in \boldsymbol{\mathcal{W}}^h \times \boldsymbol{\mathcal{V}}^h \times \mathcal{V}^h$ that satisfy

$$
\begin{aligned}
\sum_{k=1}^{\mathtt{n_d}} \beta_\theta^k \mathcal{A}_{LL}^k(\delta \boldsymbol{F}_L, \sigma_L^m \Delta \boldsymbol{F}_L) + \sum_{k=1}^{\mathtt{n_a}} \beta_\vartheta^k \mathcal{A}_{Lu}^k(\delta \boldsymbol{F}_L, \sigma_u^m \Delta \boldsymbol{f}_u) & \\
= \mathcal{R}_L^m(\delta \boldsymbol{F}_L \psi^m) + \sum_{k=1}^{\mathtt{n_a}} \beta_\vartheta^k \mathcal{A}_{L\hat{u}}^k(\delta \boldsymbol{F}_L, \sigma_{\hat{u}}^m \Delta \boldsymbol{f}_{\hat{u}}), & \\
\sum_{k=1}^{\mathtt{n_a}} \beta_\vartheta^k \mathcal{A}_{uL}^k(\delta \boldsymbol{f}_u, \sigma_L^m \Delta \boldsymbol{F}_L) + \beta \mathcal{A}_{uu}(\delta \boldsymbol{f}_u, \sigma_u^m \Delta \boldsymbol{f}_u) & \\
+ \sum_{k=1}^{\mathtt{n_a}} \beta_\vartheta^k \mathcal{A}_{up}^k(\delta \boldsymbol{f}_u, \sigma_p^m \Delta f_p) = \mathcal{R}_u^m(\delta \boldsymbol{f}_u \psi^m) + \beta \mathcal{A}_{u\hat{u}}(\delta \boldsymbol{f}_u, \sigma_{\hat{u}}^m \Delta \boldsymbol{f}_{\hat{u}}), & \\
\sum_{k=1}^{\mathtt{n_a}} \beta_\vartheta^k \mathcal{A}_{pu}^k(\delta f_p, \sigma_u^m \Delta \boldsymbol{f}_u) = \mathcal{R}_p^m(\delta f_p \psi^m) + \sum_{k=1}^{\mathtt{n_a}} \beta_\vartheta^k \mathcal{A}_{p\hat{u}}^k(\delta f_p, \sigma_{\hat{u}}^m \Delta \boldsymbol{f}_{\hat{u}}) & \\
\beta \mathcal{A}_{\rho p}^k(1, \sigma_p^m \Delta f_p) = \mathcal{R}_{\overline{p}}^m(\psi^m) + \beta \mathcal{A}_{\rho\rho}(1, \sigma_\rho^m \Delta f_\rho), &
\end{aligned}
\tag{3.37}
$$

for all $(\delta \boldsymbol{F}_L, \delta \boldsymbol{f}_u, \delta f_p) \in \boldsymbol{\mathcal{W}}^h \times \boldsymbol{\mathcal{V}}^h \times \mathcal{V}^h$.

The bilinear and linear forms of the local problem are detailed in equation (3.38)

$$
\begin{aligned}
\mathcal{A}_{LL}^k(\delta \boldsymbol{F}_L, \boldsymbol{F}_L) &:= -\left(\delta \boldsymbol{F}_L, \nu^{-1} D^k \boldsymbol{F}_L\right)_{\Omega_e}, \\
\mathcal{A}_{Lu}^k(\delta \boldsymbol{F}_L, \boldsymbol{f}_u) &:= \left(\mathbf{A}^k \boldsymbol{\nabla} \cdot \delta \boldsymbol{F}_L, \boldsymbol{f}_u\right)_{\Omega_e}, \\
\mathcal{A}_{L\hat{u}}^k(\delta \boldsymbol{F}_L, \boldsymbol{f}_{\hat{u}}) &:= \langle \mathbf{A}^k \boldsymbol{n} \cdot \delta \boldsymbol{F}_L, \boldsymbol{f}_{\hat{u}} \rangle_{\partial\Omega_e \setminus \Gamma_D}, \\
\mathcal{A}_{uL}^k(\delta \boldsymbol{f}_u, \boldsymbol{F}_L) &:= \left(\delta \boldsymbol{f}_u, \mathbf{A}^k \boldsymbol{\nabla} \cdot \boldsymbol{F}_L\right)_{\Omega_e}, \\
\mathcal{A}_{uu}(\delta \boldsymbol{f}_u, \boldsymbol{f}_u) &:= \langle \delta \boldsymbol{f}_u, \boldsymbol{\tau} \boldsymbol{f}_u \rangle_{\partial\Omega_e}, \\
\mathcal{A}_{up}^k(\delta \boldsymbol{f}_u, f_p) &:= \left(\delta \boldsymbol{f}_u, \mathbf{A}^k \boldsymbol{\nabla} f_p\right)_{\Omega_e}, \\
\mathcal{A}_{u\hat{u}}(\delta \boldsymbol{f}_u, \boldsymbol{f}_{\hat{u}}) &:= \langle \delta \boldsymbol{f}_u, \boldsymbol{\tau} \boldsymbol{f}_{\hat{u}} \rangle_{\partial\Omega_e \setminus \Gamma_D} \\
\mathcal{A}_{pu}^k(\delta f_p, \boldsymbol{f}_u) &:= \left(\mathbf{A}^k \boldsymbol{\nabla} \delta f_p, \boldsymbol{f}_u\right)_{\Omega_e}, \\
\mathcal{A}_{p\hat{u}}^k(\delta f_p, \boldsymbol{f}_{\hat{u}}) &:= \langle \delta f_p, \boldsymbol{f}_{\hat{u}} \cdot \mathbf{A}^k \boldsymbol{n} \rangle_{\partial\Omega_e \setminus \Gamma_D}, \\
\mathcal{A}_{\rho p}(\delta f_\rho, f_p) &:= \langle \delta f_\rho, |\partial\Omega_e|^{-1} f_p \rangle_{\partial\Omega_e}, \\
\mathcal{A}_{\rho\rho}(\delta f_\rho, f_\rho) &:= \delta f_\rho \, f_\rho,
\end{aligned}
\tag{3.38}
$$

and equation (3.39), respectively

$$
\begin{aligned}
\mathcal{R}_L^m(\delta\boldsymbol{F}_L\psi) :=& \sum_{k=1}^{\mathtt{n_a}}\sum_{l=1}^{\mathtt{n_D}}\langle \mathbf{A}^k\boldsymbol{n}\cdot\delta\boldsymbol{F}_L, \boldsymbol{g}_D^l\rangle_{\partial\Omega_e\cap\Gamma_D}\mathcal{A}_\vartheta^k(\psi,\lambda_D^l)\\
&-\sum_{i=1}^{m}\sum_{k=1}^{\mathtt{n_d}}\mathcal{A}_{LL}^k(\delta\boldsymbol{F}_L,\sigma_L^i\boldsymbol{F}_L^i)\mathcal{A}_\theta^k(\psi,\psi^i)\\
&-\sum_{i=1}^{m}\sum_{k=1}^{\mathtt{n_a}}\left\{\mathcal{A}_{Lu}^k(\delta\boldsymbol{F}_L,\sigma_u^i\boldsymbol{f}_u^i)-\mathcal{A}_{L\hat{u}}^k(\delta\boldsymbol{F}_L,\sigma_{\hat{u}}^i\boldsymbol{f}_{\hat{u}}^i)\right\}\mathcal{A}_\vartheta^k(\psi,\psi^i)\\
\mathcal{R}_u^m(\delta\boldsymbol{f}_u\psi) :=& \sum_{k=1}^{\mathtt{n_d}}\sum_{l=1}^{\mathtt{n_S}}\left(\delta\boldsymbol{f}_u, D^k\boldsymbol{g}_S^l\right)_{\Omega_e}\mathcal{A}_\theta^k(\psi,\lambda_S^l)\\
&+\sum_{l=1}^{\mathtt{n_D}}\langle\delta\boldsymbol{f}_u,\boldsymbol{\tau}\boldsymbol{g}_D^l\rangle_{\partial\Omega_e\cap\Gamma_D}\mathcal{A}(\psi,\lambda_D^l)\\
&-\sum_{i=1}^{m}\sum_{k=1}^{\mathtt{n_a}}\left\{\mathcal{A}_{uL}^k(\delta\boldsymbol{f}_u,\sigma_L^i\boldsymbol{F}_L^i)+\mathcal{A}_{up}^k(\delta\boldsymbol{f}_u,\sigma_p^i f_p^i)\right\}\mathcal{A}_\vartheta^k(\psi,\psi^i)\\
&-\sum_{i=1}^{m}\left\{\mathcal{A}_{uu}(\delta\boldsymbol{f}_u,\sigma_u^i\boldsymbol{f}_u^i)-\mathcal{A}_{u\hat{u}}(\delta\boldsymbol{f}_u,\sigma_{\hat{u}}^i\boldsymbol{f}_{\hat{u}}^i)\right\}\mathcal{A}(\psi,\psi^i)\\
\mathcal{R}_p^m(\delta f_p\psi) :=& \sum_{k=1}^{\mathtt{n_a}}\sum_{l=1}^{\mathtt{n_D}}\langle\delta f_p,\boldsymbol{g}_D^l\cdot\mathbf{A}^k\boldsymbol{n}\rangle_{\partial\Omega_e\cap\Gamma_D}\mathcal{A}_\vartheta^k(\psi,\lambda_D^l)\\
&-\sum_{i=1}^{m}\sum_{k=1}^{\mathtt{n_a}}\left\{\mathcal{A}_{pu}^k(\delta f_p,\sigma_u^i\boldsymbol{f}_u^i)-\mathcal{A}_{p\hat{u}}^k(\delta f_p,\sigma_{\hat{u}}^i\boldsymbol{f}_{\hat{u}}^i)\right\}\mathcal{A}_\vartheta^k(\psi,\psi^i)\\
\mathcal{R}_{\overline{p}}^m(\delta f_\rho\psi) :=& -\sum_{i=1}^{m}\left\{\mathcal{A}_{\rho p}(\delta f_\rho,\sigma_p^i f_p^i)-\mathcal{A}_{\rho\rho}(\delta f_\rho,\sigma_\rho^i f_\rho^i)\right\}\mathcal{A}(\psi,\psi^i).
\end{aligned}
\tag{3.39}
$$

The constants in equation (3.37) are given by

$$
\beta_\theta^k := \mathcal{A}_\theta^k(\psi^m,\psi^m)\qquad \beta_\vartheta^k := \mathcal{A}_\vartheta^k(\psi^m,\psi^m),\qquad \beta := \mathcal{A}(\psi^m,\psi^m),
\tag{3.40}
$$

where the bilinear forms involved in the definitions of these constants are introduced in equation (3.41)

$$
\begin{aligned}
\mathcal{A}_\theta^k(\delta\psi,\psi) &:= \left(\delta\psi,\theta^k\psi\right)_{\boldsymbol{\mathcal{I}}},\\
\mathcal{A}_\vartheta^k(\delta\psi,\psi) &:= \left(\delta\psi,\vartheta^k\psi\right)_{\boldsymbol{\mathcal{I}}},\\
\mathcal{A}(\delta\psi,\psi) &:= \left(\delta\psi,\psi\right)_{\boldsymbol{\mathcal{I}}}.
\end{aligned}
\tag{3.41}
$$

As mentioned earlier, in remark 7, this work considers the same parametric function for all the variables. It is worth noting that this choice reduces the number of different constants in equation (3.37).

Similarly, the weak form of the global problem is: find $\sigma_{\hat{u}}^m \Delta \boldsymbol{f}_{\hat{u}} \in \widehat{\boldsymbol{\mathcal{V}}}^h$ and $\sigma_\rho^m \Delta f_\rho \in \mathbb{R}^{\mathtt{n_{el}}}$ that satisfy

$$\begin{aligned}\sum_{e=1}^{\mathtt{n_{el}}}\Bigg\{\sum_{k=1}^{\mathtt{n_a}}\beta_\vartheta^k\mathcal{A}_{\hat{u}L}^k(\delta\boldsymbol{f}_{\hat{u}},\sigma_L^m\Delta\boldsymbol{F}_L)+\beta\mathcal{A}_{\hat{u}u}(\delta\boldsymbol{f}_{\hat{u}},\sigma_u^m\Delta\boldsymbol{f}_u)\\ +\sum_{k=1}^{\mathtt{n_a}}\beta_\vartheta^k\mathcal{A}_{\hat{u}p}^k(\delta\boldsymbol{f}_{\hat{u}},\sigma_p^m\Delta f_p)+\beta\mathcal{A}_{\hat{u}\hat{u}}(\delta\boldsymbol{f}_{\hat{u}},\sigma_{\hat{u}}^m\Delta\boldsymbol{f}_{\hat{u}})\\ +\sum_{k=1}^{\mathtt{n_a}}\beta_\vartheta^k\mathcal{A}_{\hat{u}\hat{u}}^k(\delta\boldsymbol{f}_{\hat{u}},\sigma_{\hat{u}}^m\Delta\boldsymbol{f}_{\hat{u}})\Bigg\}=\sum_{e=1}^{\mathtt{n_{el}}}\mathcal{R}_{\hat{u}}^m(\delta\boldsymbol{f}_{\hat{u}}\psi^m),\end{aligned}\tag{3.42a}$$

for all $\delta\boldsymbol{f}_{\hat{u}} \in \widehat{\boldsymbol{\mathcal{V}}}^h$, with the incompressibility constraint

$$\sum_{k=1}^{\mathtt{n_a}}\beta_\vartheta^k\mathcal{A}_{p\hat{u}}^k(1,\sigma_{\hat{u}}^m\Delta\boldsymbol{f}_{\hat{u}})=\mathcal{R}_\rho^m(\psi^m),\quad e=1,\dots,\mathtt{n_{el}}.\tag{3.42b}$$

The bilinear and linear forms of the global problem are detailed in equation (3.43)

$$\begin{aligned}\mathcal{A}_{\hat{u}L}^k(\delta\boldsymbol{f}_{\hat{u}},\boldsymbol{F}_L)&:=\langle\delta\boldsymbol{f}_{\hat{u}},\mathbf{A}^k\boldsymbol{n}\cdot\boldsymbol{F}_L\rangle_{\partial\Omega_e\setminus(\Gamma_D\cup\Gamma_S)}-\langle\delta\boldsymbol{f}_{\hat{u}},\mathbf{A}^k\boldsymbol{n}\cdot\boldsymbol{F}_L\boldsymbol{E}\rangle_{\partial\Omega_e\cap\Gamma_S},\\ \mathcal{A}_{\hat{u}u}(\delta\boldsymbol{f}_{\hat{u}},\boldsymbol{f}_u)&:=\langle\delta\boldsymbol{f}_{\hat{u}},\boldsymbol{\tau}\boldsymbol{f}_u\rangle_{\partial\Omega_e\setminus(\Gamma_D\cup\Gamma_S)}-\langle\delta\boldsymbol{f}_{\hat{u}},(\boldsymbol{\tau}\boldsymbol{f}_u)\cdot\boldsymbol{E}\rangle_{\partial\Omega_e\cap\Gamma_S},\\ \mathcal{A}_{\hat{u}p}^k(\delta\boldsymbol{f}_{\hat{u}},f_p)&:=\langle\delta\boldsymbol{f}_{\hat{u}},f_p\mathbf{A}^k\boldsymbol{n}\rangle_{\partial\Omega_e\setminus(\Gamma_D\cup\Gamma_S)},\\ \mathcal{A}_{\hat{u}\hat{u}}(\delta\boldsymbol{f}_{\hat{u}},\boldsymbol{f}_{\hat{u}})&:=-\langle\delta\boldsymbol{f}_{\hat{u}},\boldsymbol{\tau}\boldsymbol{f}_{\hat{u}}\rangle_{\partial\Omega_e\setminus(\Gamma_D\cup\Gamma_S)}+\langle\delta\boldsymbol{f}_{\hat{u}},(\boldsymbol{\tau}\boldsymbol{f}_{\hat{u}})\cdot\boldsymbol{E}\rangle_{\partial\Omega_e\cap\Gamma_S},\\ \mathcal{A}_{\hat{u}\hat{u}}^k(\delta\boldsymbol{f}_{\hat{u}},\boldsymbol{f}_{\hat{u}})&:=\langle\delta\boldsymbol{f}_{\hat{u}},\boldsymbol{f}_{\hat{u}}\cdot\mathbf{A}^k\boldsymbol{D}\rangle_{\partial\Omega_e\cap\Gamma_S},\end{aligned}\tag{3.43}$$

and equation (3.44), respectively

$$\begin{aligned}\mathcal{R}_{\hat{u}}^m(\delta\boldsymbol{f}_{\hat{u}}\psi):=&-\sum_{l=1}^{\mathtt{n_N}}\langle\delta\boldsymbol{f}_{\hat{u}},\boldsymbol{g}_N^l\rangle_{\partial\Omega_e\cap\Gamma_N}\mathcal{A}(\psi,\lambda_N^l)\\ &-\sum_{i=1}^{m}\left\{\mathcal{A}_{\hat{u}u}(\delta\boldsymbol{f}_{\hat{u}},\sigma_u^i\boldsymbol{f}_u^i)+\mathcal{A}_{\hat{u}\hat{u}}(\delta\boldsymbol{f}_{\hat{u}},\sigma_{\hat{u}}^i\boldsymbol{f}_{\hat{u}}^i)\right\}\mathcal{A}(\psi,\psi^i)\\ &-\sum_{i=1}^{m}\sum_{k=1}^{\mathtt{n_a}}\Big\{\mathcal{A}_{\hat{u}L}^k(\delta\boldsymbol{f}_{\hat{u}},\sigma_L^i\boldsymbol{F}_L^i)\mathcal{A}_\vartheta^k(\psi,\psi^i)\\ &+\left[\mathcal{A}_{\hat{u}p}^k(\delta\boldsymbol{f}_{\hat{u}},\sigma_p^i f_p^i)+\mathcal{A}_{\hat{u}\hat{u}}^k(\delta\boldsymbol{f}_{\hat{u}},\sigma_{\hat{u}}^i\boldsymbol{f}_{\hat{u}}^i)\right]\mathcal{A}_\vartheta^k(\psi,\psi^i)\Big\},\\ \mathcal{R}_\rho^m(\delta f_\rho\psi):=&-\sum_{k=1}^{\mathtt{n_a}}\sum_{l=1}^{\mathtt{n_D}}\langle\delta f_\rho,\boldsymbol{g}_D^l\cdot\mathbf{A}^k\boldsymbol{n}\rangle_{\partial\Omega_e\cap\Gamma_D}\mathcal{A}_\vartheta^k(\psi,\lambda_D^l)\\ &-\sum_{i=1}^{m}\sum_{k=1}^{\mathtt{n_a}}\mathcal{A}_{p\hat{u}}^k(\delta f_\rho,\sigma_{\hat{u}}^i\boldsymbol{f}_{\hat{u}}^i)\mathcal{A}_\vartheta^k(\psi,\psi^i).\end{aligned}\tag{3.44}$$

The parametric iteration

After computing the spatial corrections following the procedure described in the previous section, the spatial modes are updated, namely

$$\begin{aligned}
\sigma_L^m \boldsymbol{F}_L^m &\leftarrow \sigma_L^m \boldsymbol{F}_L^m + \sigma_L^m \Delta \boldsymbol{F}_L, \\
\sigma_u^m \boldsymbol{f}_u^m &\leftarrow \sigma_u^m \boldsymbol{f}_u^m + \sigma_u^m \Delta \boldsymbol{f}_u, \\
\sigma_p^m f_p^m &\leftarrow \sigma_p^m f_p^m + \sigma_p^m \Delta f_p, \\
\sigma_{\hat{u}}^m \boldsymbol{f}_{\hat{u}}^m &\leftarrow \sigma_{\hat{u}}^m \boldsymbol{f}_{\hat{u}}^m + \sigma_{\hat{u}}^m \Delta \boldsymbol{f}_{\hat{u}}, \\
\sigma_\rho^m f_\rho^m &\leftarrow \sigma_\rho^m f_\rho^m + \sigma_\rho^m \Delta f_\rho,
\end{aligned} \tag{3.45}$$

where the constant $\sigma_\diamond^m$ on the left hand side denotes the amplitude of the newly computed m-th mode of the function $\diamond$, e.g. $\sigma_p^m \leftarrow \|\sigma_p^m f_p^m + \sigma_p^m \Delta f_p\|$.

In the parametric iteration, the goal is to compute the parametric correction $\Delta\psi$ given the prediction ψ^m and the known spatial functions in (3.45). Following the assumption that such functions are known, it holds that $\delta\boldsymbol{F}_L = \delta\boldsymbol{f}_u = \delta f_p = \delta\boldsymbol{f}_{\hat{u}} = \delta f_\rho = 0$. Introducing the expression of the PGD approximations and the weighting functions in the weak form of the HDG local problems, the following weak form of the local problem for the spatial iteration is obtained: find $\Delta\psi \in \boldsymbol{\mathcal{L}}^h(\boldsymbol{\mathcal{I}})$ such that

$$\begin{aligned}
&\sum_{k=1}^{\mathtt{n_d}} \gamma_{LL}^k \mathcal{A}_\theta^k(\delta\psi, \Delta\psi) + \sum_{k=1}^{\mathtt{n_a}} \gamma_{Lu}^k \mathcal{A}_\vartheta^k(\delta\psi, \Delta\psi) \\
&\qquad = \mathcal{R}_L^m(\sigma_L^m \boldsymbol{F}_L^m \delta\psi) + \sum_{k=1}^{\mathtt{n_a}} \gamma_{L\hat{u}}^k \mathcal{A}_\vartheta^k(\delta\psi, \Delta\psi), \\
&\sum_{k=1}^{\mathtt{n_a}} \gamma_{uL}^k \mathcal{A}_\vartheta^k(\delta\psi, \Delta\psi) + \gamma_{uu} \mathcal{A}(\delta\psi, \Delta\psi) \\
&\quad + \sum_{k=1}^{\mathtt{n_a}} \gamma_{up}^k \mathcal{A}_\vartheta^k(\delta\psi, \Delta\psi) = \mathcal{R}_u^m(\sigma_u^m \boldsymbol{f}_u^m \delta\psi) + \gamma_{u\hat{u}} \mathcal{A}(\delta\psi, \psi^m), \\
&\quad \sum_{k=1}^{\mathtt{n_a}} \gamma_{pu}^k \mathcal{A}_\vartheta^k(\delta\psi, \Delta\psi) = \mathcal{R}_p^m(\sigma_p^m f_p^m \delta\psi) + \sum_{k=1}^{\mathtt{n_a}} \gamma_{p\hat{u}}^k \mathcal{A}_\vartheta^k(\delta\psi, \Delta\psi), \\
&\qquad \gamma_{\rho p} \mathcal{A}(\delta\psi, \Delta\psi) = \mathcal{R}_{\overline{p}}^m(\delta\psi) + \gamma_{\rho\rho} \mathcal{A}(\delta\psi, \Delta\psi),
\end{aligned} \tag{3.46}$$

for all $\delta\psi \in \boldsymbol{\mathcal{L}}^h(\boldsymbol{\mathcal{I}})$.

Similarly, the weak form of the global problem is: find $\Delta\psi \in \boldsymbol{\mathcal{L}}^h(\boldsymbol{\mathcal{I}})$ that satisfies

$$\begin{aligned}\sum_{e=1}^{\mathtt{n_{el}}}\Bigg\{\sum_{k=1}^{\mathtt{n_a}}\gamma_{\hat{u}L}^k\mathcal{A}_\vartheta^k(\delta\psi,\Delta\psi)+\gamma_{\hat{u}u}\mathcal{A}(\delta\psi,\Delta\psi)+\sum_{k=1}^{\mathtt{n_a}}\gamma_{\hat{u}p}^k\mathcal{A}_\vartheta^k(\delta\psi,\Delta\psi)\\ +\gamma_{\hat{u}\hat{u}}\mathcal{A}(\delta\psi,\Delta\psi)+\sum_{k=1}^{\mathtt{n_a}}\gamma_{\hat{u}\hat{u}}^k\mathcal{A}_\vartheta^k(\delta\psi,\Delta\psi)\Bigg\}=\sum_{e=1}^{\mathtt{n_{el}}}\mathcal{R}_{\hat{u}}^m(\sigma_{\hat{u}}^m\boldsymbol{f}_{\hat{u}}^m\delta\psi),\\ \sum_{k=1}^{\mathtt{n_a}}\gamma_{\rho\hat{u}}^k\mathcal{A}_\vartheta^k(\delta\psi,\psi^m)=\mathcal{R}_\rho^m(\delta\psi),\end{aligned}\tag{3.47}$$

for all $\delta\psi \in \boldsymbol{\mathcal{L}}^h(\boldsymbol{\mathcal{I}})$.

The constants in equations (3.46) and (3.47) are defined as

$$\begin{aligned}\gamma_{LL}^k&:=\mathcal{A}_{LL}^k(\sigma_L^m\boldsymbol{F}_L^m,\sigma_L^m\boldsymbol{F}_L^m),&\gamma_{Lu}^k&:=\mathcal{A}_{Lu}^k(\sigma_L^m\boldsymbol{F}_L^m,\sigma_u^m\boldsymbol{f}_u^m),\\ \gamma_{L\hat{u}}^k&:=\mathcal{A}_{L\hat{u}}^k(\sigma_L^m\boldsymbol{F}_L^m,\sigma_{\hat{u}}^m\boldsymbol{f}_{\hat{u}}^m),&\gamma_{uL}^k&:=\mathcal{A}_{uL}^k(\sigma_u^m\boldsymbol{f}_u^m,\sigma_L^m\boldsymbol{F}_L^m),\\ \gamma_{uu}&:=\mathcal{A}_{uu}(\sigma_u^m\boldsymbol{f}_u^m,\sigma_u^m\boldsymbol{f}_u^m),&\gamma_{up}^k&:=\mathcal{A}_{up}^k(\sigma_u^m\boldsymbol{f}_u^m,\sigma_p^m f_p^m),\\ \gamma_{u\hat{u}}&:=\mathcal{A}_{u\hat{u}}(\sigma_u^m\boldsymbol{f}_u^m,\sigma_{\hat{u}}^m\boldsymbol{f}_{\hat{u}}^m),&\gamma_{pu}^k&:=\mathcal{A}_{pu}^k(\sigma_p^m f_p^m,\sigma_u^m\boldsymbol{f}_u^m),\\ \gamma_{p\hat{u}}^k&:=\mathcal{A}_{p\hat{u}}^k(\sigma_p^m f_p^m,\sigma_{\hat{u}}^m\boldsymbol{f}_{\hat{u}}^m),&\gamma_{\rho p}&:=\mathcal{A}_{\rho p}(1,\sigma_p^m f_p^m),\\ \gamma_{\rho\rho}&:=\mathcal{A}_{\rho\rho}(1,\sigma_\rho^m f_\rho^m),&&\\ \gamma_{\hat{u}L}^k&:=\mathcal{A}_{\hat{u}L}^k(\sigma_{\hat{u}}^m\boldsymbol{f}_{\hat{u}}^m,\sigma_L^m\boldsymbol{F}_L^m),&\gamma_{\hat{u}u}&:=\mathcal{A}_{\hat{u}u}(\sigma_{\hat{u}}^m\boldsymbol{f}_{\hat{u}}^m,\sigma_u^m\boldsymbol{f}_u^m),\\ \gamma_{\hat{u}p}^k&:=\mathcal{A}_{\hat{u}p}^k(\sigma_{\hat{u}}^m\boldsymbol{f}_{\hat{u}}^m,\sigma_p^m f_p^m),&\gamma_{\hat{u}\hat{u}}&:=\mathcal{A}_{\hat{u}\hat{u}}(\sigma_{\hat{u}}^m\boldsymbol{f}_{\hat{u}}^m,\sigma_{\hat{u}}^m\boldsymbol{f}_{\hat{u}}^m),\\ \gamma_{\hat{u}\hat{u}}^k&:=\mathcal{A}_{\hat{u}\hat{u}}^k(\sigma_{\hat{u}}^m\boldsymbol{f}_{\hat{u}}^m,\sigma_{\hat{u}}^m\boldsymbol{f}_{\hat{u}}^m),&\gamma_{\rho\hat{u}}^k&:=\mathcal{A}_{p\hat{u}}^k(1,\sigma_{\hat{u}}^m\boldsymbol{f}_{\hat{u}}^m).\end{aligned}\tag{3.48}$$

The choice of a single parameter approximation implies that we can combine equations (3.46) and (3.47) to obtain the following parametric problem: find $\Delta\psi \in \boldsymbol{\mathcal{L}}^h(\boldsymbol{\mathcal{I}})$ that satisfies

$$\sum_{k=1}^{\mathtt{n_d}}\gamma_{LL}^k\mathcal{A}_\theta^k(\delta\psi,\Delta\psi)+\sum_{k=1}^{\mathtt{n_a}}\gamma_\vartheta^k\mathcal{A}_\vartheta^k(\delta\psi,\Delta\psi)+\gamma\mathcal{A}(\delta\psi,\Delta\psi)=\mathcal{R}^m(\delta\psi),\tag{3.49}$$

for all $\delta\psi \in \boldsymbol{\mathcal{L}}^h(\boldsymbol{\mathcal{I}})$, where

$$\begin{aligned}\gamma_\vartheta^k:=&\gamma_{Lu}^k-\gamma_{L\hat{u}}^k+\gamma_{uL}^k+\gamma_{up}^k+\gamma_{pu}^k-\gamma_{p\hat{u}}^k+\gamma_{\hat{u}L}^k+\gamma_{\hat{u}p}^k+\gamma_{\hat{u}\hat{u}}^k+\gamma_{\rho\hat{u}}^k,\\ \gamma:=&\gamma_{uu}-\gamma_{u\hat{u}}+\gamma_{\rho p}-\gamma_{\rho\rho}+\gamma_{\hat{u}u}+\gamma_{\hat{u}\hat{u}},\\ \mathcal{R}^m(\delta\psi):=&\mathcal{R}_L^m(\sigma_L^m\boldsymbol{F}_L^m\delta\psi)+\mathcal{R}_u^m(\sigma_u^m\boldsymbol{f}_u^m\delta\psi)+\mathcal{R}_p^m(\sigma_p^m f_p^m\delta\psi)\\ &+\mathcal{R}_{\overline{p}}^m(\delta\psi)+\mathcal{R}_{\hat{u}}^m(\sigma_{\hat{u}}^m\boldsymbol{f}_{\hat{u}}^m\delta\psi)+\mathcal{R}_\rho^m(\delta\psi).\end{aligned}\tag{3.50}$$

Remark 8. *Alternative formulations of the parametric problem may be devised, e.g. by considering only equation* (3.46) *or* (3.47)*. In this work, equation* (3.57) *has been considered in the parametric iteration in order to account for the information of both the local and the global HDG problems.*

As detailed in equation (3.34), the parametric iteration involves $\mathtt{n}_{\mathtt{pa}}$ geometric parameters. To reduce the size of the problem of the parametric iteration, $\mathtt{n}_{\mathtt{pa}}$ one-dimensional problems are solved sequentially, as commonly done in a PGD framework (Chinesta et al., 2014).

An important implementation detail

The resolution of the parametric problem is a linearisation of a non-linear problem. In the computation of PGD modes of minor relevance, thus associated with smaller amplitudes, if the ADA does not converge the maximum number of non-linear iteration is reached. That signifies including in the PGD reduced basis a mode which has not converged. Nevertheless, that is not an issue. Due to the nature of the PGD algorithm, with the next computed mode, usually, the error introduced into the approximation by the term not converging is lightened. In these circumstances, where the ADA does not converge, numerical experiments have shown the appearance of peaks in the computed parametric modes. This phenomenon results in creating oscillations and causing the PGD algorithm to stuck or diverge. Additional analyses showed that this issue appears when the algebraic matrix associated with the parametric problem is indefinite, i.e. accounts of both positive and negative eigenvalues.

In this work, to avoid this issue, a check on the parametric algebraic matrix associated with the mode computed, when the number of iterations performed has reached the maximum value, is done. In the case the matrix results indefinite, some extra iterations are performed, usually one or two, until the resulting not converging mode is smooth. Other possibilities, such as discarding the computed m-th mode and changing the initial parametric guess of the ADA or applying the PGD compression on the reduced basis before restarting the computation of the m-th mode are some other attempted strategies. Increasing the maximum number of iterations and refining the parametric mesh are also investigated options. All of them do not circumvent the problem but only delays it providing, sometimes, the convergence of the considered m-th mode but causing to experience the same issue in the computation of the successive one.

3.3.6 The HDG-PGD algorithm

The HDG solver for geometrically parametrised Stokes equation is described in algorithm 1. Differently from traditional PGD strategies relying on continuous Galerkin approximations, Dirichlet boundary conditions do not require a special treatment in the context of HDG-PGD. More precisely, Dirichlet conditions are imposed in a weak sense and appear in the linear forms (3.17) of the HDG local problem.

Algorithm 1 The HDG-PGD implementation

Require: For the greedy enrichment loop, the value $\eta^\star$ of the tolerance. For the alternating direction iterations, the values $\eta_{\hat{u}}$ and $\eta^r_\circ$ of the tolerances for the mode amplitude $\sigma_{\hat{u}}$ and the residuals $r_\circ$ obtained from the linear forms in 3.39 and 3.44, respectively. For the spatial and parametric problems, the typical values $\text{typ}_\circ$ of the residuals. $\circ = \hat{u}, \psi$.

1: Set $m \leftarrow 1$ and initialise the amplitude of the spatial mode $\sigma^1_{\hat{u}} \leftarrow 1$.
2: **while** $\sigma^m_{\hat{u}} > \eta^\star \, \sigma^1_{\hat{u}}$ **do**
3: Set $q \leftarrow 1$ and initialise the parametric predictor $\psi^m \leftarrow 1$.
4: Compute the spatial constants (3.40).
5: Solve the HDG global (3.42a)-(3.42b) and local problems (3.37).
6: Initialise $\varepsilon_{\hat{u}} \leftarrow 1$, $\varepsilon^r_\circ \leftarrow \text{typ}_\circ$.
7: **while** $\varepsilon_{\hat{u}} > \eta_{\hat{u}}$ or $\varepsilon^r_\circ > \eta^r_\circ$ **do**
8: Compute the parametric constants (3.48).
9: Solve the parametric linear system (3.57).
10: Update the parametric predictor $\psi^m \leftarrow (\psi^m + \Delta\psi)/\|\psi^m + \Delta\psi\|$.
11: Compute the spatial constants (3.40).
12: Solve the HDG global (3.42a)-(3.42b) and local problems (3.37).
13: Normalise the spatial predictor $\sigma^m_{\hat{u}} \leftarrow \|\sigma^m_{\hat{u}} \boldsymbol{f}^m_{\hat{u}} + \sigma^m_{\hat{u}} \Delta \boldsymbol{f}_{\hat{u}}\|$.
14: Update the spatial predictor $\sigma^m_{\hat{u}} \boldsymbol{f}^m_{\hat{u}} \leftarrow \sigma^m_{\hat{u}} \boldsymbol{f}^m_{\hat{u}} + \sigma^m_{\hat{u}} \Delta \boldsymbol{f}_{\hat{u}}$.
15: Update the stopping criteria for the mode amplitude $\varepsilon_{\hat{u}} \leftarrow \|\sigma^m_{\hat{u}} \Delta \boldsymbol{f}_{\hat{u}}\|/\sigma^m_{\hat{u}}$ and the residuals $\varepsilon^r_\circ \leftarrow \|r_\circ\|$.
16: Increase the counter of the alternating direction iterations $q \leftarrow q+1$.
17: **end while**
18: Increase the mode counter $m \leftarrow m+1$.
19: **end while**

In the greedy enrichment loop, first a predictor of the spatial mode is computed as the solution of the HDG global and local problems using a guess for the parametric mode (Algorithm 1 - Steps 3-5). Then, the alternating direction scheme computes the corrections of the parametric (Algorithm 1 - Steps 8-10) and spatial mode (Algorithm 1 - Steps 11-14) solving a parametric linear system and the HDG global and local problems, respectively. As susual when solving a nonlinear system of equations, the nonlinear iterations of the alternating direction scheme stop when the amplitude $\sigma^m_{\hat{u}} \Delta \boldsymbol{f}_{\hat{u}}$ of the correction is negligible with respect to the amplitude $\sigma^m_{\hat{u}}$ of the current mode and the residuals of the spatial and parametric problems are below a given tolerance (Algorithm 1 - Steps 7 and 15). The stopping criterion for the greedy enrichment algorithm relies on the relative amplitude $\sigma^m_{\hat{u}}$ of the current mode being negligible with respect to the first mode $\sigma^1_{\hat{u}}$ (Algorithm 1 - Step 2).

Alternative stopping criteria based on normalising the amplitude of the current mode with respect to the cumulative amplitudes of the previous modes have also been considered in the literature, see e.g. Tsiolakis et al., (2020a). Note that for the purpose of normalisation (Algorithm 1 - Step 14), an appropriate norm needs to be defined and the $\mathcal{L}_\infty$ norm has been utilised for the simulations in section 3.4.

Discretisation of the spatial and parametric problems

The discretisation of the local problems of the spatial iteration using an isoparametric formulation with equal interpolation for all the variables (Sevilla et al., 2016b, 2018a,b), leads to a system of equations for each element with the following structure:

$$\begin{bmatrix} \mathbf{A}_{LL} & \mathbf{A}_{Lu} & \mathbf{0} & \mathbf{0} \\ \mathbf{A}_{Lu}^T & \mathbf{A}_{uu} & \mathbf{A}_{up} & \mathbf{0} \\ \mathbf{0} & \mathbf{A}_{up}^T & \mathbf{0} & \boldsymbol{a}_{\rho p}^T \\ \mathbf{0} & \mathbf{0} & \boldsymbol{a}_{\rho p} & 0 \end{bmatrix}_e \begin{Bmatrix} \mathbf{F}_L \\ \mathbf{F}_u \\ \mathbf{F}_p \\ \mathrm{F}_\zeta \end{Bmatrix}_e = \begin{Bmatrix} \mathbf{f}_L \\ \mathbf{f}_u \\ \mathbf{f}_p \\ 0 \end{Bmatrix}_e + \begin{bmatrix} \mathbf{A}_{L\hat{u}} \\ \mathbf{A}_{u\hat{u}} \\ \mathbf{A}_{p\hat{u}} \\ \mathbf{0} \end{bmatrix}_e \mathbf{F}_{\hat{u}} + \begin{Bmatrix} \mathbf{0} \\ \mathbf{0} \\ \mathbf{0} \\ 1 \end{Bmatrix}_e \mathrm{F}_\rho, \tag{3.51}$$

where $\mathbf{F}_L$, $\mathbf{F}_u$, $\mathbf{F}_p$ and $\mathbf{F}_{\hat{u}}$ denote the nodal values of the unknown spatial functions $\sigma_L^m \boldsymbol{\Delta F}_L$, $\sigma_u^m \boldsymbol{\Delta f}_u$, $\sigma_p^m \Delta f_p$ and $\sigma_{\hat{u}}^m \boldsymbol{\Delta f}_{\hat{u}}$ respectively and the constraint on the mean value F_ρ of the pressure on the element boundaries is enforced using the Lagrange multiplier F_ζ.

The only difference between the local system obtained in the spatial iteration of the proposed HDG-PGD approach and the local system of a standard HDG method (Sevilla et al., 2018a,b) lies in the construction of the blocks forming the matrices $\mathbf{A}_{\odot\circledcirc}$ and vectors $\mathbf{f}_\odot$. As an example, let us consider the matrix $\mathbf{A}_{LL}$. In the proposed HDG-PGD framework, this matrix is defined as

$$(\mathbf{A}_{LL})_{IJ} = -\sum_{k=1}^{\mathtt{n_d}} \beta_\theta^k \big(N_I, \nu^{-1} D^k N_J\big)_{\Omega_e} \mathbf{I}_{\mathtt{n}_{\mathtt{sd}}^2} \tag{3.52}$$

whereas in a standard HDG approach, the corresponding matrix is defined as

$$(\mathbf{A}_{LL})_{IJ} = -\big(N_I, \nu^{-1} N_J\big)_{\Omega_e} \mathbf{I}_{\mathtt{n}_{\mathtt{sd}}^2}. \tag{3.53}$$

In the above expressions $\{N_I\}$ denotes the set of shape functions used to define the spatial approximation of the mixed variable.

Similarly, the discretisation of the global problem of the spatial iteration leads to a system of equations for the trace of the velocity on the element boundaries and the

mean value of the pressure in each element, namely

$$\sum_{e=1}^{\mathtt{n_{el}}}\left\{\begin{bmatrix}\mathbf{A}_{\hat{u}L} & \mathbf{A}_{\hat{u}u} & \mathbf{A}_{\hat{u}p}\end{bmatrix}_e\begin{Bmatrix}\mathbf{F}_L\\ \mathbf{F}_u\\ \mathbf{F}_p\end{Bmatrix}_e+\left[\mathbf{A}_{\hat{u}\hat{u}}\right]_e\mathbf{F}_{\hat{u}}\right\}=\sum_{e=1}^{\mathtt{n_{el}}}[\mathbf{f}_{\hat{u}}]_e,\qquad \mathbf{1}^T\left[\mathbf{A}_{p\hat{u}}\right]_e\mathbf{F}_{\hat{u}}=-\mathbf{1}^T\left[\mathbf{f}_p\right]_e. \tag{3.54}$$

As usual in an HDG context, the local problem of equation (3.51) is used to express the spatial part of the gradient of the velocity, the velocity and the pressure in terms of the spatial part of the trace of the velocity and the mean pressure. Introducing these expressions into the global problem, leads to the global system

$$\begin{bmatrix}\widehat{\mathbf{K}} & \mathbf{G}\\ \mathbf{G}^T & \mathbf{0}\end{bmatrix}\begin{Bmatrix}\mathbf{F}_{\hat{u}}\\ \mathbf{F}_\rho\end{Bmatrix}=\begin{Bmatrix}\hat{\mathbf{f}}_{\hat{u}}\\ \hat{\mathbf{f}}_\rho\end{Bmatrix}, \tag{3.55}$$

where the only unknowns are the spatial parts of the trace of the velocity and the mean pressure.

In a similar fashion, the discretisation of the parametric problem (3.57) using Lagrange shape functions leads to an algebraic system of equations

$$\mathbf{M}\mathbf{F}_\psi=\mathbf{f}_\psi, \tag{3.56}$$

whose unknowns $\mathbf{F}_\psi$ denotes the nodal values of the unknown parametric function $\Delta\psi$ and the weighted matrix $\mathbf{M}$ is the sum of different contributions

$$\mathbf{M}=\sum_{k=1}^{\mathtt{n_d}}\gamma_{LL}^k\big(N_I,\theta^kN_J\big)_{\boldsymbol{\mathcal{I}}}+\sum_{k=1}^{\mathtt{n_a}}\gamma_\vartheta^k\big(N_I,\vartheta^kN_J\big)_{\boldsymbol{\mathcal{I}}}+\gamma\big(N_I,N_J\big)_{\boldsymbol{\mathcal{I}}}, \tag{3.57}$$

and $\{N_I\}$ in this case denotes the set of shape functions used to define approximation of the parametric variable.

A remark for a computationally efficient implementation

The evaluation of the right hand sides of the PGD spatial and parametric iterations tends to become computationally expensive when approximations with a large number of modes are considered. Indeed, the number of terms involved in such computation experiences a geometric growth rate during the iterations of the greedy algorithm.

In order to ease the computational burden of the overall algorithm, the number of terms in the modal approximations $\boldsymbol{u}^m_{\mathtt{PGD}}, p^m_{\mathtt{PGD}}, \boldsymbol{L}^m_{\mathtt{PGD}}, \hat{\boldsymbol{u}}^m_{\mathtt{PGD}}$ and $\rho^m_{\mathtt{PGD}}$ is reduced. It is well known that the terms in the PGD reduced basis are not orthogonal to each other and repeated information may appear. Hence, orthogonal separable approximations featuring $\widetilde{m} < m$ modes are constructed via the PGD compression (Díez et al., 2019; Modesto et al., 2015), that is, a least-squares higher-order projection minimising the

$\mathcal{L}_2$ norm of the difference between target and test functions, namely

$$\begin{aligned}
\boldsymbol{L}_{\texttt{PGD}}^{\widetilde{m}} &= \underset{\boldsymbol{W}\in\boldsymbol{\mathcal{W}}^h}{\arg\min} \|\boldsymbol{W} - \boldsymbol{L}_{\texttt{PGD}}^{m}\|_{\mathcal{L}_2(\Omega\times\boldsymbol{\mathcal{I}})},\\
\boldsymbol{u}_{\texttt{PGD}}^{\widetilde{m}} &= \underset{\boldsymbol{v}\in\boldsymbol{\mathcal{V}}^h}{\arg\min} \|\boldsymbol{v} - \boldsymbol{u}_{\texttt{PGD}}^{m}\|_{\mathcal{L}_2(\Omega\times\boldsymbol{\mathcal{I}})},\\
p_{\texttt{PGD}}^{\widetilde{m}} &= \underset{v\in\mathcal{V}^h}{\arg\min} \|v - p_{\texttt{PGD}}^{m}\|_{\mathcal{L}_2(\Omega\times\boldsymbol{\mathcal{I}})},\\
\hat{\boldsymbol{u}}_{\texttt{PGD}}^{\widetilde{m}} &= \underset{\hat{\boldsymbol{v}}\in\widehat{\boldsymbol{\mathcal{V}}}^h}{\arg\min} \|\hat{\boldsymbol{v}} - \hat{\boldsymbol{u}}_{\texttt{PGD}}^{m}\|_{\mathcal{L}_2(\Gamma\cup\Gamma_N\cup\Gamma_S\times\boldsymbol{\mathcal{I}})},\\
\rho_{\texttt{PGD}}^{\widetilde{m}} &= \underset{q\in\mathbb{R}^{\texttt{n}_{\texttt{el}}}\otimes\boldsymbol{\mathcal{L}}^h(\boldsymbol{\mathcal{I}})}{\arg\min} \|q - \rho_{\texttt{PGD}}^{m}\|_{\mathcal{L}_2(\mathbb{R}^{\texttt{n}_{\texttt{el}}}\times\boldsymbol{\mathcal{I}})}.
\end{aligned}$$

From a practical point of view, the PGD compression is applied during the enrichment strategy described in algorithm 1. A trade-off between the cost of performing the greedy iterations with a larger number of modes and the extra cost required by the PGD compression needs to be achieved. For the simulations in section 3.4, PGD compression is applied every ten new computed modes for the analytical examples and every five for the microfluidics test cases.

3.3.7 Local postprocess of the primal variable

For a multi-dimensional geometrically parametrised problem, the local postprocess necessary to obtain the superconvergent solution $\boldsymbol{u}^*$ analogous to system of equations (2.22) reads: given $\boldsymbol{u}\in\boldsymbol{\mathcal{V}}_{\boldsymbol{\mu}}^h$ and $\boldsymbol{L}\in\boldsymbol{\mathcal{W}}_{\boldsymbol{\mu}}^h$ find $\boldsymbol{u}^*\in\boldsymbol{\mathcal{U}}_{\boldsymbol{\mu}}^h$ that satisfies

$$\begin{aligned}
\big(\boldsymbol{\nabla}_{\boldsymbol{\mu}}\boldsymbol{v}, \boldsymbol{\nabla}_{\boldsymbol{\mu}}\boldsymbol{u}^*\big)_{\Omega_e^{\boldsymbol{\mu}}\times\boldsymbol{\mathcal{I}}} &= -\big(\boldsymbol{\nabla}_{\boldsymbol{\mu}}\boldsymbol{v}, \nu^{-1}\boldsymbol{L}\big)_{\Omega_e^{\boldsymbol{\mu}}\times\boldsymbol{\mathcal{I}}}\\
\big(w, \boldsymbol{u}^*\big)_{\Omega_e^{\boldsymbol{\mu}}\times\boldsymbol{\mathcal{I}}} &= \big(w, \boldsymbol{u}\big)_{\Omega_e^{\boldsymbol{\mu}}\times\boldsymbol{\mathcal{I}}},
\end{aligned}\tag{3.58}$$

where the tangent manifolds for $\boldsymbol{u}$ is equal to $\boldsymbol{v}\in\boldsymbol{\mathcal{U}}_{\boldsymbol{\mu}}^h$, defined as

$$\begin{aligned}
\mathcal{U}^h(\Omega^{\boldsymbol{\mu}}) &:= \{v\in\mathcal{L}_2(\Omega^{\boldsymbol{\mu}}) : v|_{\Omega_e^{\boldsymbol{\mu}}}\in\mathcal{P}^{k+1}(\Omega_e^{\boldsymbol{\mu}})\ \forall\Omega_e^{\boldsymbol{\mu}}\ ,\ e=1,\dots,\texttt{n}_{\texttt{el}}\},\\
\boldsymbol{\mathcal{U}}^h &:= \Big[\mathcal{U}^h(\Omega)\Big]^{\texttt{n}_{\texttt{sd}}},\\
\boldsymbol{\mathcal{U}}_{\boldsymbol{\mu}}^h &:= \Big[\mathcal{U}^h(\Omega^{\boldsymbol{\mu}})\otimes\boldsymbol{\mathcal{L}}^h(\boldsymbol{\mathcal{I}})\Big]^{\texttt{n}_{\texttt{sd}}},
\end{aligned}$$

and $w\in\boldsymbol{\mathcal{L}}^h(\boldsymbol{\mathcal{I}})$, with $\boldsymbol{\mathcal{L}}^h(\boldsymbol{\mathcal{I}})$ defined in section 3.2.3.

Analogously to section 3.3.1 a separable mapping between a parameter-independent domain and the geometrically parametrised domain allows to rewrite system (3.58) as

$$\begin{aligned}
\big(\operatorname{adj}(\mathbf{J}_{\boldsymbol{\mu}})\boldsymbol{\nabla}\boldsymbol{v}, \operatorname{adj}(\mathbf{J}_{\boldsymbol{\mu}})\det(\mathbf{J}_{\boldsymbol{\mu}})^{-1}\boldsymbol{\nabla}\boldsymbol{u}^*\big)_{\Omega_e\times\boldsymbol{\mathcal{I}}} &= -\big(\operatorname{adj}(\mathbf{J}_{\boldsymbol{\mu}})\boldsymbol{\nabla}\boldsymbol{v}, \nu^{-1}\boldsymbol{L}\big)_{\Omega_e\times\boldsymbol{\mathcal{I}}}\\
\big(w, \det(\mathbf{J}_{\boldsymbol{\mu}})\boldsymbol{u}^*\big)_{\Omega_e\times\boldsymbol{\mathcal{I}}} &= -\big(w, \det(\mathbf{J}_{\boldsymbol{\mu}})\boldsymbol{u}\big)_{\Omega_e\times\boldsymbol{\mathcal{I}}}.
\end{aligned}\tag{3.59}$$

for all $\boldsymbol{v}\in\boldsymbol{\mathcal{U}}_{\boldsymbol{\mu}}^h$.

Within an HDG-PGD framework, where *single-parameter* approach is considered, a rank-m separable approximation assumed for all the variables of equation (3.32) is also extended to $\boldsymbol{u}^*$, namely

$$\boldsymbol{u}^{*,m}_{\texttt{PGD}}(\boldsymbol{x},\boldsymbol{\mu}) = \sigma^{*,m}_u \boldsymbol{f}^{*,m}_u(\boldsymbol{x})\,\psi^m(\boldsymbol{\mu}) + \boldsymbol{u}^{*,m-1}_{\texttt{PGD}}(\boldsymbol{x},\boldsymbol{\mu}). \tag{3.60}$$

It is worth noting that unlike other variables, $\boldsymbol{u}^*$ is approximated introducing only predictors $\sigma^{*,m}_u \boldsymbol{f}^{*,m}_u \psi^m$ of the m-th mode in the PGD expansion whereas the corresponding correction terms are not necessary. This is because the postprocessed velocity mode is computed only when the alternating direction algorithm of the m-enrichment is ended. In other words, for each enrichment, given the final values of the prediction of $\sigma^m_u \boldsymbol{f}^m_u \psi^m$ and $\sigma^m_L \boldsymbol{F}^m_L \psi^m$ it is easy to obtain $\sigma^{*,m}_u \boldsymbol{f}^{*,m}_u \psi^m$.

Introducing equation 3.60 in (3.59) and restricting the problem to the computation of the m-th mode of the postprocessed velocity, weak form 3.59 becomes: given $\sigma^m_u \boldsymbol{f}^m_u \in \boldsymbol{\mathcal{V}}^h$ and $\sigma^m_L \boldsymbol{F}^m_L \in \boldsymbol{\mathcal{W}}^h$ find $\sigma^{*,m}_u \boldsymbol{f}^{*,m}_u \in \boldsymbol{\mathcal{U}}^h$ that satisfies

$$\begin{aligned}
&\big(\operatorname{adj}(\mathbf{J}_{\boldsymbol{\mu}})\boldsymbol{\nabla}\boldsymbol{v}, \operatorname{adj}(\mathbf{J}_{\boldsymbol{\mu}})\det(\mathbf{J}_{\boldsymbol{\mu}})^{-1}\boldsymbol{\nabla}\sigma^{*,m}_u \boldsymbol{f}^{*,m}_u \psi^m\big)_{\Omega_e\times\boldsymbol{\mathcal{I}}} \\
&\qquad = -\big(\operatorname{adj}(\mathbf{J}_{\boldsymbol{\mu}})\boldsymbol{\nabla}\boldsymbol{v}, \nu^{-1}\sigma^m_L \boldsymbol{F}^m_L \psi^m\big)_{\Omega_e\times\boldsymbol{\mathcal{I}}} \\
&\big(\det(\mathbf{J}_{\boldsymbol{\mu}})\sigma^{*,m}_u \boldsymbol{f}^{*,m}_u \psi^m, \psi^m\big)_{\Omega_e\times\boldsymbol{\mathcal{I}}} \\
&\qquad = -\big(\det(\mathbf{J}_{\boldsymbol{\mu}})\sigma^m_u \boldsymbol{f}^m_u \psi^m, \psi^m\big)_{\Omega_e\times\boldsymbol{\mathcal{I}}},
\end{aligned} \tag{3.61}$$

with $\boldsymbol{v}{=}\delta\boldsymbol{f}_u\psi^m$ tangent manifolds for $\boldsymbol{u}^*$. The separated expression of the determinant of the Jacobian and its adjoint defined in equations (3.24) and (3.25) only partly allow to rewrite weak form (3.61) in a separable form

$$\begin{aligned}
&\big(\operatorname{adj}(\mathbf{J}_{\boldsymbol{\mu}})\boldsymbol{\nabla}\boldsymbol{v}, \operatorname{adj}(\mathbf{J}_{\boldsymbol{\mu}})\det(\mathbf{J}_{\boldsymbol{\mu}})^{-1}\boldsymbol{\nabla}\sigma^{*,m}_u \boldsymbol{f}^{*,m}_u \psi^m\big)_{\Omega_e\times\boldsymbol{\mathcal{I}}} \\
&\qquad = -\sum_{k=1}^{\mathtt{n_a}} \beta^k_\vartheta \big(\boldsymbol{\nabla}\delta\boldsymbol{f}_u, \mathbf{A}^k \sigma^m_L \boldsymbol{F}^m_L\big)_{\Omega_e} \\
&\sum_{k=1}^{\mathtt{n_d}} \beta^k_\theta \big(D^k \sigma^{*,m}_u \boldsymbol{f}^{*,m}_u, 1\big)_{\Omega_e} = -\sum_{k=1}^{\mathtt{n_d}} \beta^k_\theta \big(D^k \sigma^m_u \boldsymbol{f}^m_u, 1\big)_{\Omega_e}.
\end{aligned} \tag{3.62}$$

As there is not any analytical result ensuring the separability of the inverse of the determinant of the Jacobian, in a general framework it is not separable and it can not be represented in an exact separable form.

To overcome this issue and be able to create a vademecum also for the postprocess velocity in a parametrized geometrical framework it is necessary to approximate this term by mean of the higher-order PGD projection as done in Sevilla et al., (2020b). Due to the high computational cost of this procedure, this relevant feature of the HDG method is not investigated further for geometrically parametrised problems.

3.4 Numerical examples

This section presents six numerical examples. The first three examples are used to validate the implementation of the proposed approach as well as to study a number of properties of the proposed ROM. The last three examples are inspired from two applications taken from the biomechanics community and involve the Stokes flow around two cylinders, a microswimmer formed by two spheres and the flow around a sphere in a corrugated channel. All the examples consider geometric parameters as extra coordinates within the proposed PGD approach.

3.4.1 Coaxial Couette flow

The first example considers the well known coaxial Couette flow problem (Childs, 2010), consisting of the flow confined within two infinite coaxial circular cylinders with radius R_{in} and R_{out} respectively, with $R_{\text{in}}<R_{\text{out}}$. The boundary conditions introduce the known angular velocities, Ω_{in} and Ω_{out}, at R_{in} and R_{out}, respectively. The problem has analytical solution, given by the azimuthal component of the velocity as

$$v_\phi = \frac{R_{\text{out}}^2\Omega_{\text{out}} - R_{\text{in}}^2\Omega_{\text{in}}}{R_{\text{out}}^2 - R_{\text{in}}^2} r + \frac{(\Omega_{\text{in}} - \Omega_{\text{out}})R_{\text{out}}^2 R_{\text{in}}^2}{R_{\text{out}}^2 - R_{\text{in}}^2}\frac{1}{r} \tag{3.63}$$

where r is the distance to the axis of the cylinders.

Geometric mapping To demonstrate the applicability of the proposed ROM the problem is considered in two dimensions, with $\Omega^\mu=\{\boldsymbol{x}^{\boldsymbol{\mu}} \in \mathbb{R}^2 \mid \mu_1 \leq r^\mu \leq R_{\text{out}}\}$, with $R_{\text{out}}=5$ and $\mu_1 \in \boldsymbol{\mathcal{I}}=\mathcal{I}^1=[1,3]$ and where $r^\mu = \sqrt{(x^\mu)^2 + (y^\mu)^2}$. The reference domain is chosen to be $\Omega=\{\boldsymbol{x} \in \mathbb{R}^2 \mid 1 \leq r \leq R_{\text{out}}\}$ and the mapping between the reference and the geometrically parametrised domains is defined by the general separable expression of equation (3.21) with the mapping of equation (3.22) given by

$$\begin{aligned} \mathbf{M}^1(\boldsymbol{x}) &= \frac{1}{r}\boldsymbol{x} \qquad & \psi^1(\mu) &= \frac{R_{\text{out}}(\mu-1)}{R_{\text{out}}-1}, \\ \mathbf{M}^2(\boldsymbol{x}) &= \boldsymbol{x} \qquad & \psi^2(\mu) &= \frac{R_{\text{out}}-\mu}{R_{\text{out}}-1}, \end{aligned} \tag{3.64}$$

and the Jacobian of the mapping is also written in the general separated form of equation (3.23), with

$$\mathbf{J}^1(\boldsymbol{x}) = \frac{1}{r^3}\begin{bmatrix} y^2 & -xy \\ -xy & x^2 \end{bmatrix}, \qquad \mathbf{J}^2(\boldsymbol{x}) = \mathbf{I}_2. \tag{3.65}$$

where $r = \sqrt{x^2+y^2}$.

Off-line phase For the numerical experiments in this section, four triangular meshes of the reference domain are generated, as shown in figure 3.1. The meshes have 128, 512, 2,048 and 8,192 elements respectively. The proposed HDG-PGD framework

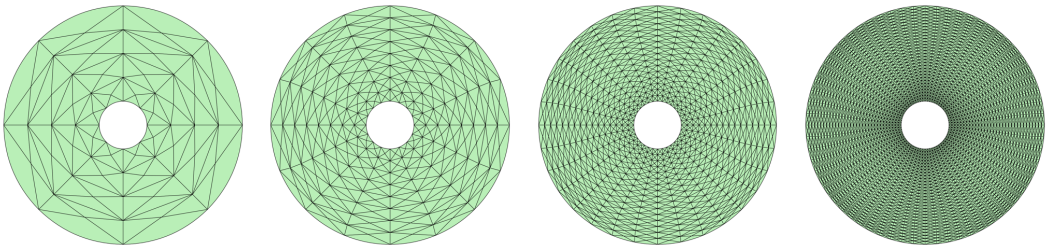

(a) Mesh 1 (b) Mesh 2 (c) Mesh 3 (d) Mesh 4

FIGURE 3.1: Coaxial Couette flow: Four triangular meshes of the reference domain.

is used to obtain the generalised solution of the parametric Stokes problem. The computation was performed using the second mesh shown in figure 3.1 with a degree of approximation k=4 for all the variables and with a mesh of 1,000 elements in the parametric dimension with also k=4.

The first eight normalised modes of the magnitude of the velocity field are displayed in figure 3.2. As usual in a the context of ROMs, the first modes capture the most relevant and global features of the solution whereas the features captured for the next modes only introduce localised features.

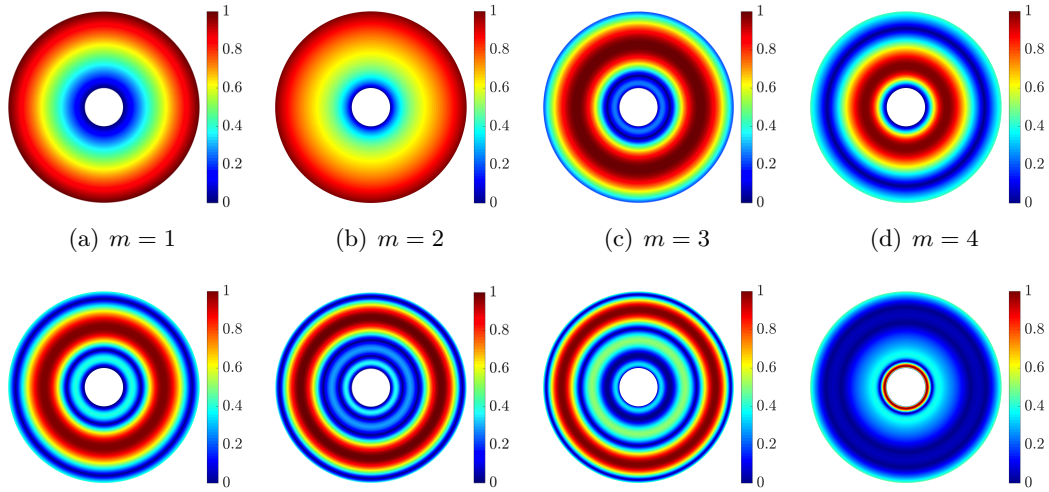

(a) $m = 1$ (b) $m = 2$ (c) $m = 3$ (d) $m = 4$

(e) $m = 5$ (f) $m = 6$ (g) $m = 7$ (h) $m = 8$

FIGURE 3.2: Coaxial Couette flow: First eight normalised spatial modes of the velocity field.

Figure 3.3 shows the first eight normalised parametric modes computed. It can be observed that the first three modes are smooth, whereas the next modes, that have a less relevant contribution to the generalised solution, show a more oscillatory character.

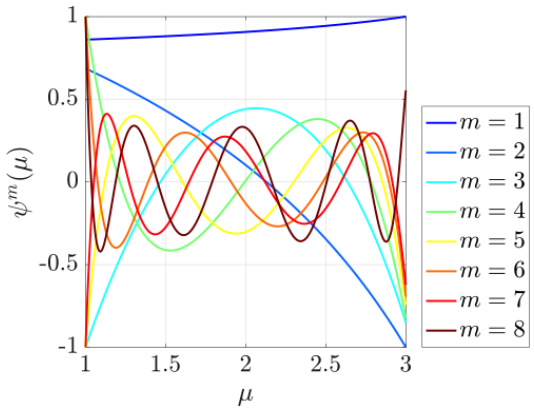

FIGURE 3.3: Coaxial Couette flow: First eight normalised parametric modes.

To quantify the importance of the modes on the generalised solution, figure 3.4 shows the relative amplitudes of the modes with respect to the amplitude of the first mode for all the variables. It can be clearly observed that the fourth mode has an amplitude

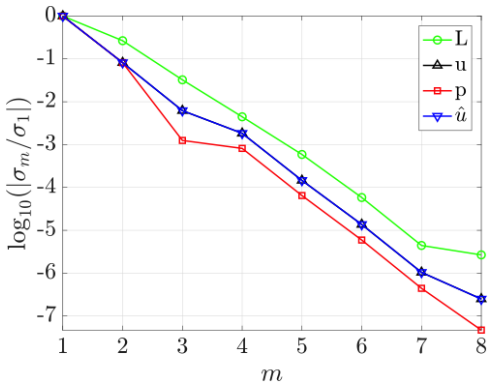

FIGURE 3.4: Coaxial Couette flow: Convergence of the mode amplitudes.

that is already more than 100 times smaller than the amplitude of the first mode. After computing only nine modes the relative amplitude is already of the order of 10^{-6}. It is worth noting that in practice it is not required to add modes with such a lower relative amplitude with respect to the first mode, but in this first example nine modes are computed to show the rapid decrease in their amplitudes.

On-line phase Once the generalised solution is computed, it is of interest to quantify its accuracy.

Figure 3.5 shows the absolute value of the error of the velocity magnitude using as the number of modes is increased for three relevant configurations corresponding to the parameter μ_1=1, μ_1=2 and μ_1=3. The results show that with only one PGD mode an absolute error below 10^{-1} is already obtained for all three configurations, with more accurate results for the case with μ_1=2. With two PGD modes the error

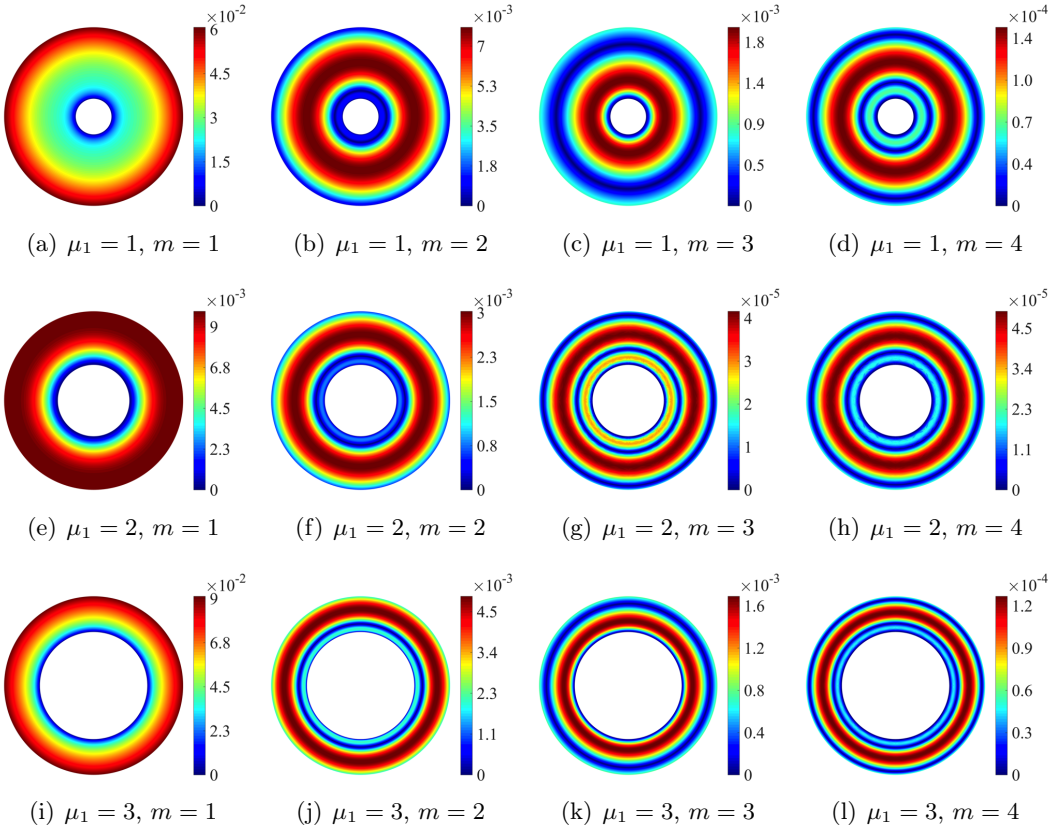

FIGURE 3.5: Coaxial Couette flow: Absolute value of the error of the velocity magnitude using n PGD modes and for different values of the geometric parameter μ_1. A quartic approximation is used for all variables in the second mesh of figure 3.1.

drops substantially, being less than 7×10^{-3} in all cases, and with only PGD modes the error is below 2×10^{-4} for the three configurations considered.

To further illustrate the accuracy of the proposed HDG-PGD approach, the relative error in the $\mathcal{L}_2(\Omega \times \boldsymbol{\mathcal{I}})$ norm, defined as

$$\varepsilon_{\texttt{PGD}} = \left(\frac{\int_{\mathcal{I}_1} \int_{\Omega} (\boldsymbol{u}_{\texttt{PGD}} - \boldsymbol{u}) \cdot (\boldsymbol{u}_{\texttt{PGD}} - \boldsymbol{u}) d\Omega \, d\mu}{\int_{\mathcal{I}_1} \int_{\Omega} \boldsymbol{u} \cdot \boldsymbol{u} \, d\Omega \, d\mu} \right)^{1/2}, \tag{3.66}$$

is studied and compared to the error of the full order HDG approach.

Figure 3.6 shows the evolution of $\varepsilon_{\texttt{PGD}}$, for all the variables, as the number of PGD modes is increased, for different meshes using a quadratic degree of approximation. The discontinuous lines show the relative error of the full order HDG method, measured in the $\mathcal{L}_2(\Omega \times \boldsymbol{\mathcal{I}})$ norm. It is worth noting that the computation of the error for the full order approach requires the computation of a large number of solutions. More precisely, the number of HDG solutions required is equal to the number of elements in the parametric space multiplied by number of integrations points in each element.

The results show that the error of the proposed ROM converges monotonically to

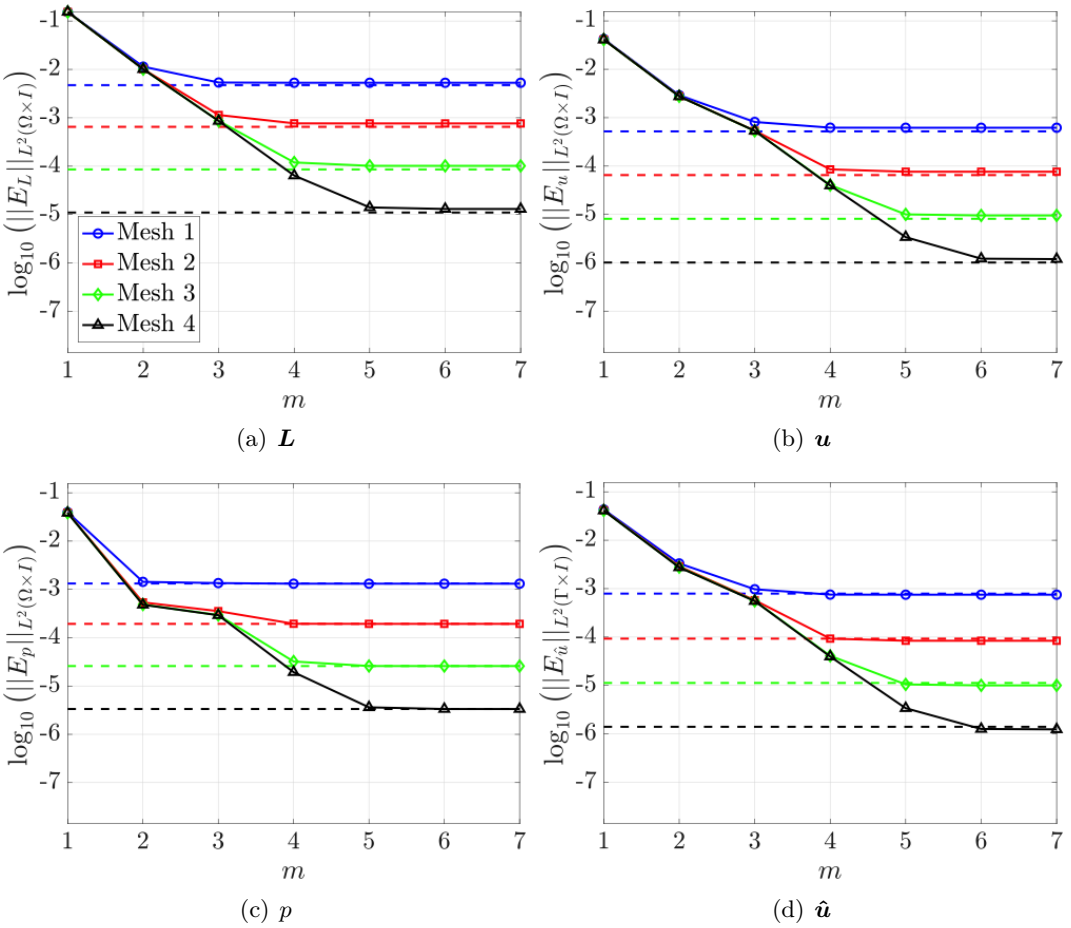

(a) $\boldsymbol{L}$ (b) $\boldsymbol{u}$

(c) p (d) $\hat{\boldsymbol{u}}$

FIGURE 3.6: Coaxial Couette flow: convergence of the $\mathcal{L}_2$ norm of the error for $\boldsymbol{L}$, $\boldsymbol{u}$, p and $\hat{\boldsymbol{u}}$ as the number of PGD modes is increased. A quadratic approximation is used for all the variables.

the error of the full order approach with as the number of modes is increased. In all cases the number of PGD modes required to reach the maximum accuracy on a given mesh is lower than six. Furthermore, the results in figure 3.6 illustrate the increased level of accuracy obtained as the spatial and parametric discretisations are refined. Analogous results, not reported here for brevity, are obtained for lower and higher orders of approximation.

Next, the optimal approximation properties of the proposed HDG-PDG method are studied by performing a mesh convergent study.

Figure 3.7 shows the evolution of the relative error in the $\mathcal{L}_2(\Omega\times\boldsymbol{\mathcal{I}})$ norm as a function of the characteristic element size, h, for different orders of approximation and for all the variables of the HDG formulation. The optimal rate of convergence, equal to h^{k+1}, is approximately observed for all the variables. In each case, the minimum number of PGD modes required to achieve the accuracy of the full order method is selected, as previously discussed when presenting the results of figure 3.6.

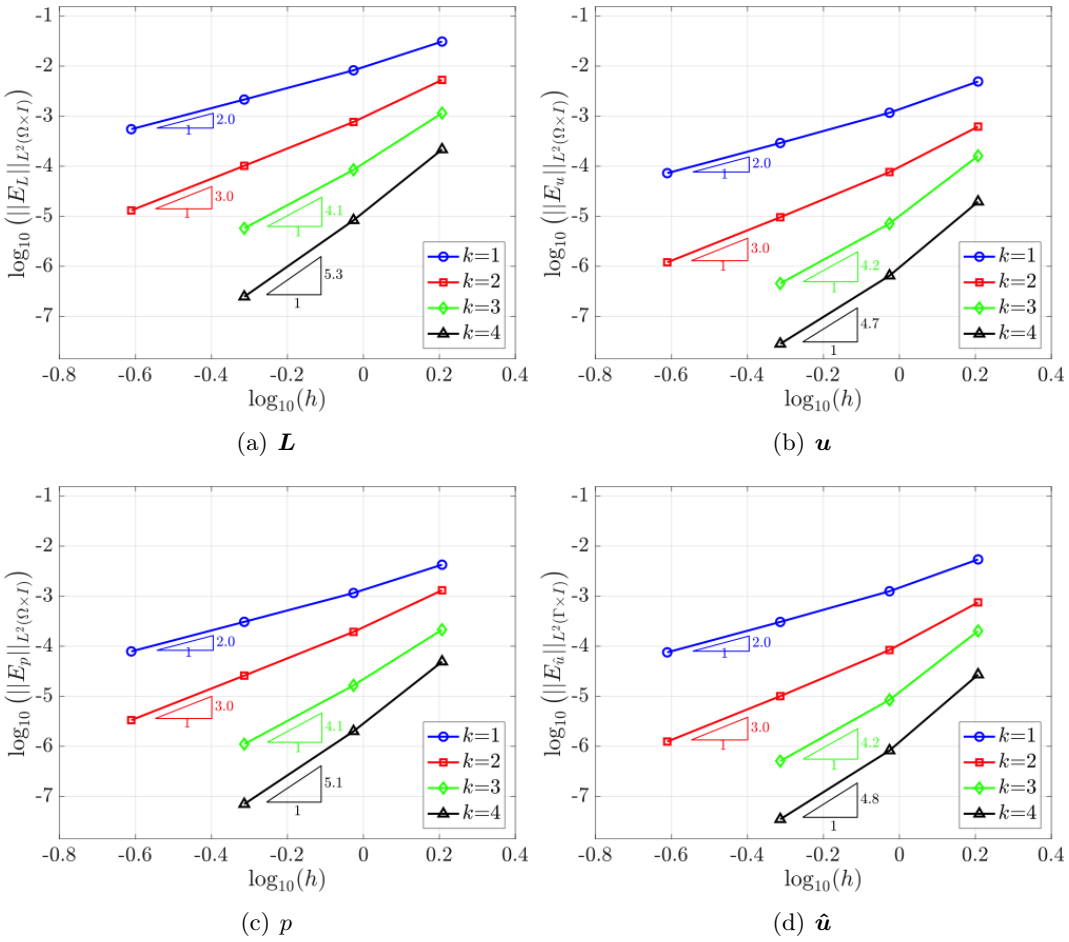

(a) $\boldsymbol{L}$ (b) $\boldsymbol{u}$

(c) p (d) $\hat{\boldsymbol{u}}$

FIGURE 3.7: Coaxial Couette flow: mesh convergence of the $\mathcal{L}_2$ norm of the error for $\boldsymbol{L}$, $\boldsymbol{u}$, p and $\hat{\boldsymbol{u}}$.

Finally, it is worth mentioning the differences between the proposed HDG-PGD approach presented here and the recently proposed PGD approach for geometrically parametrised domains in Sevilla et al., (2020b) using standard finite elements for the spatial discretisation. First, the current approach does not require the higher order PGD projection to separate the inverse of the determinant of the Jacobian, given the first-order character of the problem solved with HDG. Second, the current approach enables the use of the same degree of approximation for velocity and pressure, contrary to the standard FE approach where specific choices are required to satisfy the LBB condition. In the context of geometrically parametrised domains with curved boundaries this implies that the current approach enables the use of isoparametric elements whereas super-parametric or sub-parametric elements are required in the FE context. Third, the weak imposition of the Dirichlet boundary conditions, as usually done in a DG context, facilitates the construction of the generalised solution without the need for specific choices for the modes that satisfy the Dirichlet boundary conditions, as required by other approaches. Finally, the results in figure 3.7 can be compared to the results in Sevilla et al., (2020b).

3.4.2 Axisymmetric Stokes flow past a sphere

The second example considers the Stokes flow past a sphere, a typical test case for axisymmetric Stokes flow solvers. The domain of interest is selected as the region confined by two concentric spheres with radius R_{in} and R_{out} respectively, with $R_{\text{in}}{<}R_{\text{out}}$. This problem also has analytical solution, given, in polar coordinates, by the following velocity and pressure fields

$$\begin{aligned} u_\rho &= \frac{v_\infty}{2\rho^3}\left(2\rho^3 - 3R_{\text{in}}\rho^2 + R_{\text{in}}^3\right)\cos\phi, \\ u_\theta &= 0, \\ u_\phi &= -\frac{v_\infty}{4\rho^3}\left(4\rho^3 - 3R_{\text{in}}\rho^2 + R_{\text{in}}^3\right)\sin\phi, \\ p &= p_\infty - \frac{3}{2\rho^2}\nu v_\infty R_{\text{in}}\cos\phi, \end{aligned} \tag{3.67}$$

where v_∞ and p_∞ are the magnitude of the velocity and the pressure of the undisturbed flow, far away from the obstacle and $\rho{=}\sqrt{r^2+z^2}$ (see (2.59) for velocity and pressure fields in cylindrical coordinates). A typical quantity of interest in this problem is the drag force, whose exact value is given by $F_D{=}6\pi\nu v_\infty R_{\text{in}}$.

For the numerical experiments in this section, four triangular meshes of the reference domain are generated, as shown in figure 3.8. A no-slip boundary condition is imposed

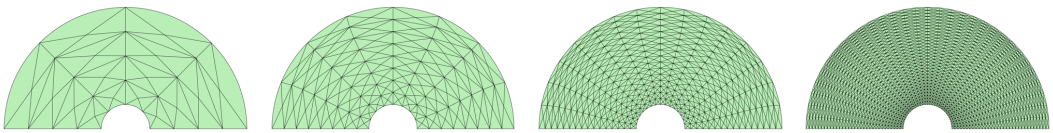

(a) Mesh 1 (b) Mesh 2 (c) Mesh 3 (d) Mesh 4

FIGURE 3.8: Axisymmetric flow past a sphere: Four triangular meshes of the reference domain.

on the inner sphere, a Dirichlet boundary condition corresponding to the exact solution on the outer boundary and axial symmetry is imposed on the rest of the boundary. The axial symmetry is imposed by selecting $\alpha{=}\beta{=}0$ in the matrices $\boldsymbol{D}^{\boldsymbol{\mu}}$ and $\boldsymbol{E}^{\boldsymbol{\mu}}$ in equation (3.1). As mentioned earlier, in Remark 5, the portion of the boundary where the axial symmetry is imposed depends on the geometric parameter, but the normal and tangent to the boundary are independent on the geometric changes. Therefore, the matrices $\boldsymbol{D}$ and $\boldsymbol{E}$ do not depend upon the geometric parameters.

Geometric mapping Similar to the previous example, the geometric parameter considered here is the radius of the inner sphere. The parametric domain considers the axial symmetry of the problem is defined as $\Omega^\mu{=}\{\boldsymbol{r}^{\boldsymbol{\mu}} \in \mathbb{R}^2 \mid r^\mu \geq 0 \text{ and } \mu_1 \leq \rho^\mu \leq R_{\text{out}}\}$, with $bR{=}(z,r)$, $R_{\text{out}}{=}5$ and $\mu_1 \in \boldsymbol{\mathcal{I}}{=}\mathcal{I}^1{=}[1,3]$. The reference domain is chosen to be $\Omega{=}\{\boldsymbol{r} \in \mathbb{R}^2 \mid r \geq 0 \text{ and } 1 \leq \rho \leq R_{\text{out}}\}$.

The mapping between the reference and the geometrically parametrised domains is analogous to the one utilised in the previous example, but considering an axisymmetric domain

$$\begin{aligned} \mathbf{M}^1(\boldsymbol{r}) &= \frac{1}{\rho}\boldsymbol{r} \qquad & \psi^1(\mu) &= \frac{R_{\text{out}}(\mu-1)}{R_{\text{out}}-1}, \\ \mathbf{M}^2(\boldsymbol{r}) &= \boldsymbol{r} \qquad & \psi^2(\mu) &= \frac{R_{\text{out}}-\mu}{R_{\text{out}}-1}. \end{aligned} \tag{3.68}$$

The Jacobian of the mapping is also written in the general separated form of equation (3.23), with

$$\mathbf{J}^1(\boldsymbol{r}) = \frac{1}{\rho^3}\begin{bmatrix} r^2 & -zr \\ -zr & z^2 \end{bmatrix}, \qquad \mathbf{J}^2(\boldsymbol{r}) = \mathbf{I}_2. \tag{3.69}$$

Off-line phase The proposed ROM is used to obtain the generalised solution of the parametric axisymmetric Stokes problem. The computation was performed using the second mesh with a degree of approximation $k = 4$ for all the variables and with a mesh of 1,000 elements in the parametric dimension with also $k = 4$.

The first four normalised modes of the magnitude of the velocity field and the pressure are shown in figures 3.9 and 3.10.

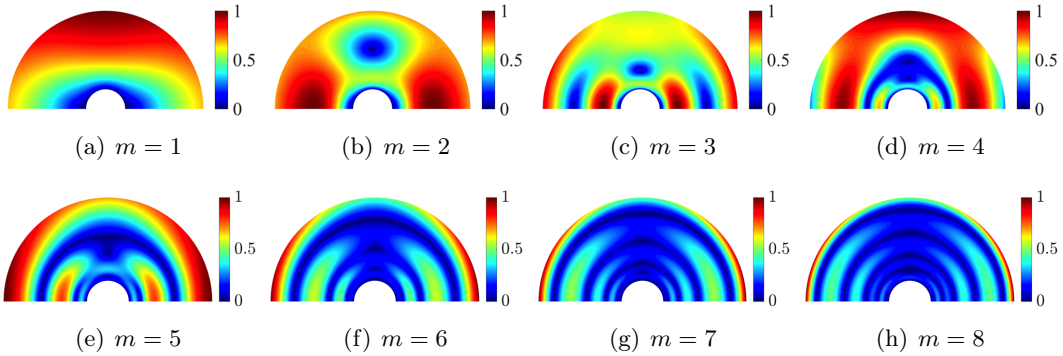

(a) $m = 1$ (b) $m = 2$ (c) $m = 3$ (d) $m = 4$

(e) $m = 5$ (f) $m = 6$ (g) $m = 7$ (h) $m = 8$

FIGURE 3.9: Axisymmetric flow past a sphere: First eight normalised spatial modes of the norm of the velocity field.

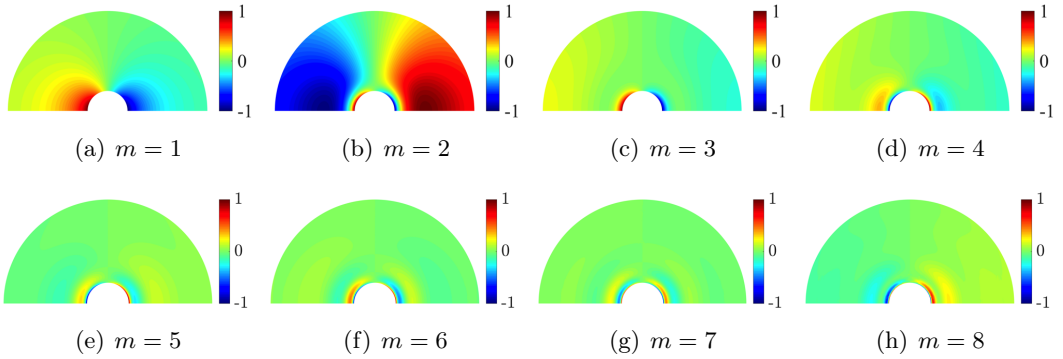

(a) $m = 1$ (b) $m = 2$ (c) $m = 3$ (d) $m = 4$

(e) $m = 5$ (f) $m = 6$ (g) $m = 7$ (h) $m = 8$

FIGURE 3.10: Axisymmetric flow past a sphere: First eight normalised spatial modes of the pressure field.

Figure 3.11 shows the first eight normalised parametric modes computed. It is worth

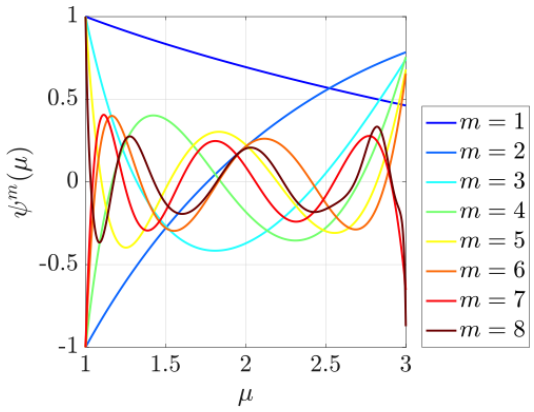

FIGURE 3.11: Axisymmetric flow past a sphere: First eight normalised parametric modes.

noting that despite the different nature of the flow and the axisymmetric boundary condition, the parametric modes have a similar behaviour when compared to the modes obtained in the previous example. This is mainly attributed to the geometric parameter describing an analogous variation of the computational domain.

As in the previous example, the evolution of the relative amplitude of the modes is shown in 3.12. The rapid decrease shows that it is possible to compute a generalised

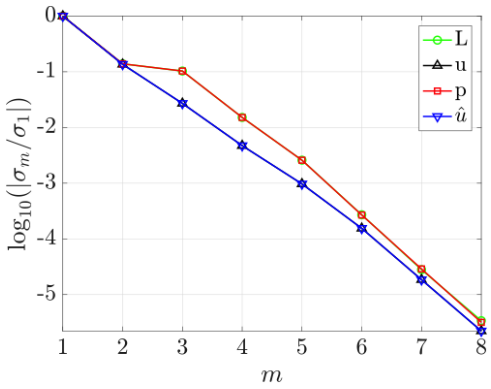

FIGURE 3.12: Axisymmetric flow past a sphere: Convergence of the mode amplitudes.

solution to this problem with a very small number of modes. With eight modes the relative amplitude is already below 10^{-5}.

On-line phase Once the generalised solution is computed, it is of interest to quantify its accuracy.

Figure 3.13 and figure 3.14 shows the absolute value of the error of the velocity magnitude and pressure using as the number of modes is increased for three relevant configurations corresponding to the parameter μ_1=1, μ_1=2 and μ_1=3.

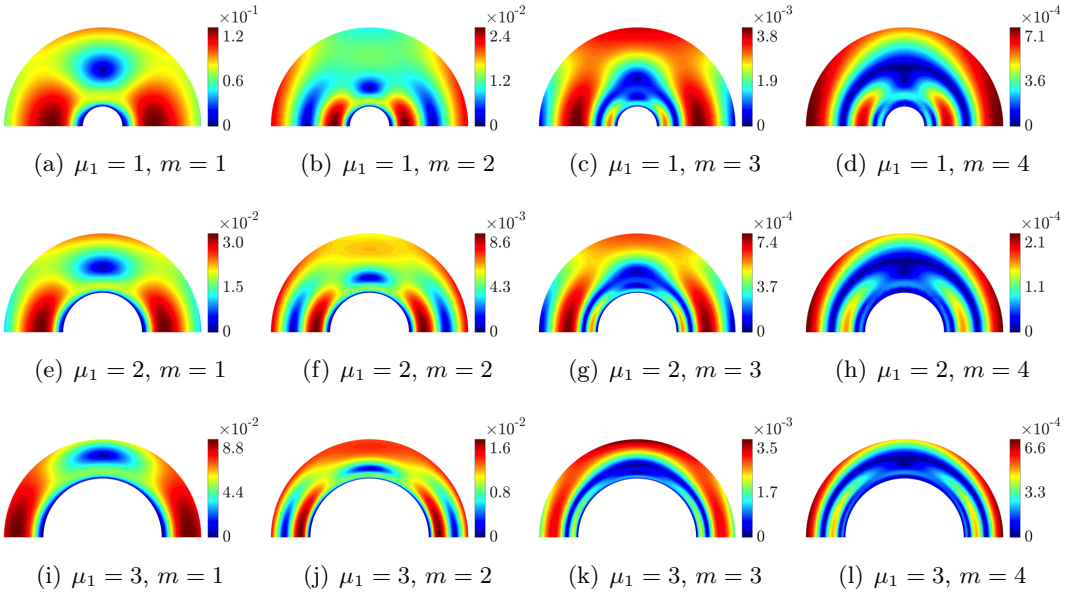

FIGURE 3.13: Axisymmetric flow past a sphere: Absolute value of the error of the velocity magnitude using n PGD modes and for different values of the geometric parameter μ_1. A quartic approximation is used for all variables in the second mesh of figure 3.8.

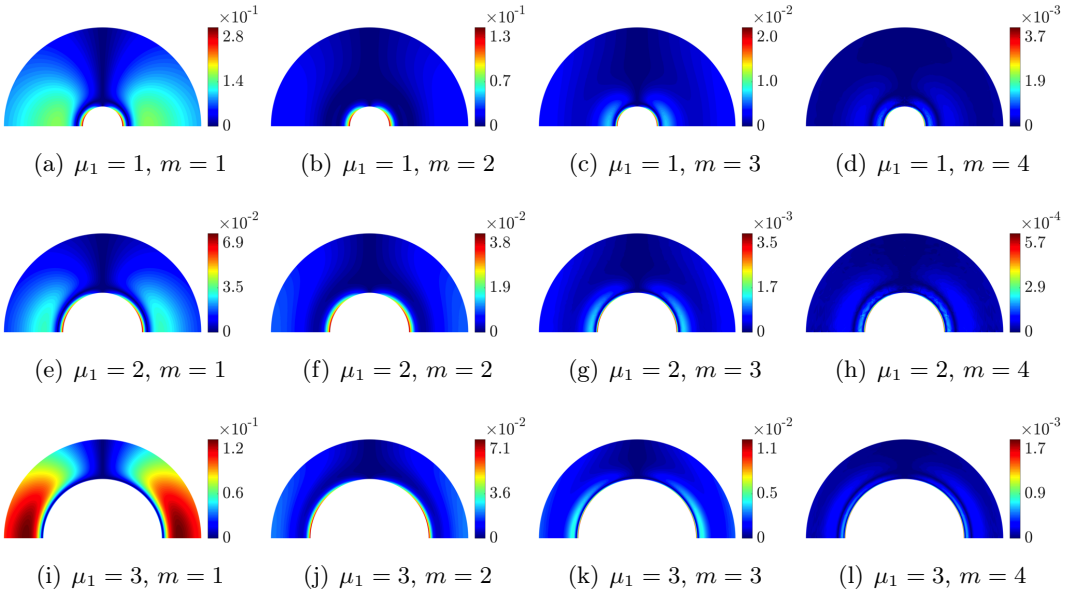

FIGURE 3.14: Axisymmetric flow past a sphere: Absolute value of the pressure magnitude using n PGD modes and for different values of the geometric parameter μ_1. A quartic approximation is used for all variables in the second mesh of figure 3.8.

The results show that with only one PGD mode an absolute error of the order of 10^{-1} or below is already obtained for all three configurations for both velocity and pressure. Analogously to the previous example more accurate results are obtained for the case with μ_1=2. The error drops substantially, being less than 3.8×10^{-3}, in all cases with three and four modes for velocity and pressure, respectively.

To further illustrate the accuracy of the proposed HDG-PGD approach, the relative error in the $\mathcal{L}_2(\Omega \times \boldsymbol{\mathcal{I}})$ norm, defined in (3.66) is studied and compared to the error of the full order HDG approach.

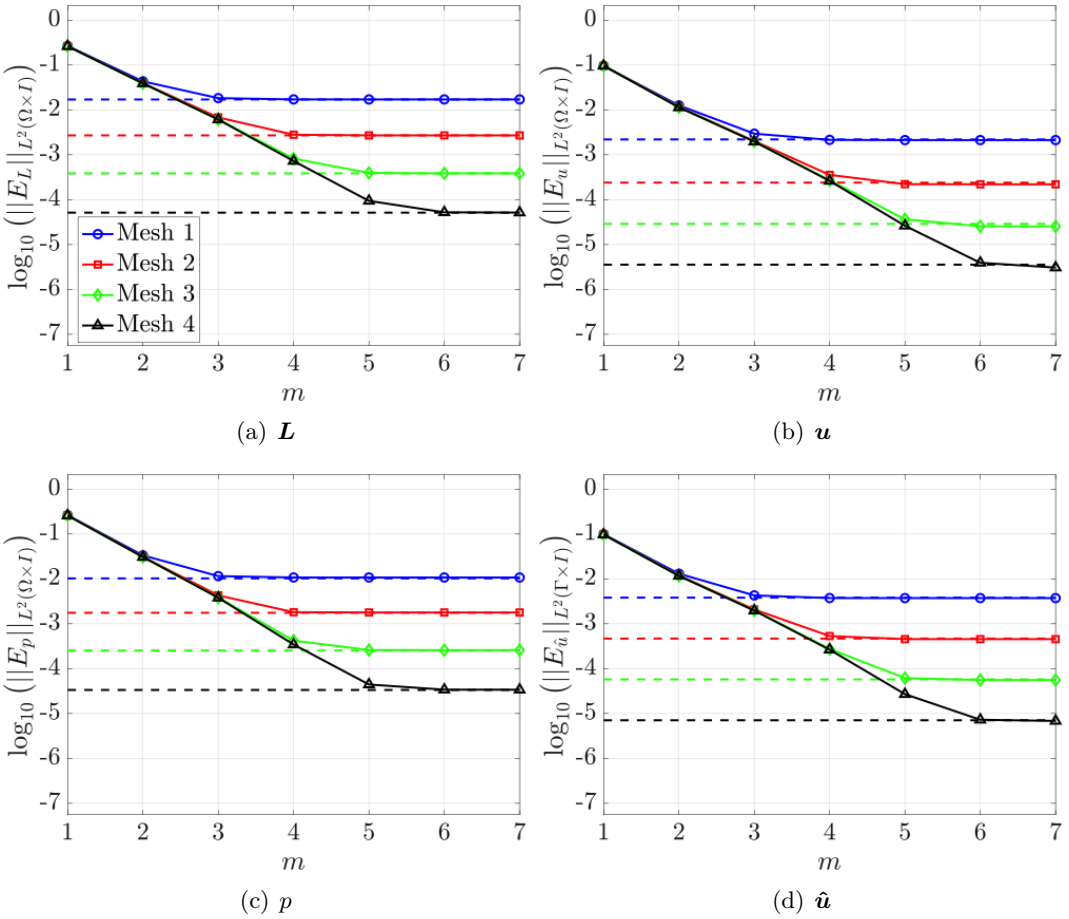

(a) $\boldsymbol{L}$ (b) $\boldsymbol{u}$

(c) p (d) $\hat{\boldsymbol{u}}$

FIGURE 3.15: Axisymmetric flow past a sphere: convergence of the $\mathcal{L}_2$ norm of the error for $\boldsymbol{L}$, $\boldsymbol{u}$, p and $\hat{\boldsymbol{u}}$ as the number of PGD modes is increased. A quadratic approximation is used for all the variables.

Figure 3.15 shows the evolution of $\varepsilon_{\texttt{PGD}}$, for all the variables, as the number of PGD modes is increased, for different meshes using a quadratic degree of approximation. The discontinuous lines in figure 3.15 show the relative error of the full order HDG method, measured in the $\mathcal{L}_2(\Omega \times \boldsymbol{\mathcal{I}})$ norm.

Next, similarly with the previous example, the optimal approximation properties of the proposed HDG-PGD method are studied by performing a mesh convergent study.

Figure 3.16 shows the evolution of the relative error in the $\mathcal{L}_2(\Omega \times \boldsymbol{\mathcal{I}})$ norm as a function of the characteristic element size, h, for different orders of approximation and for all the variables of the HDG formulation. The optimal rate of convergence, equal to h^{k+1}, is approximately observed for all the variables.

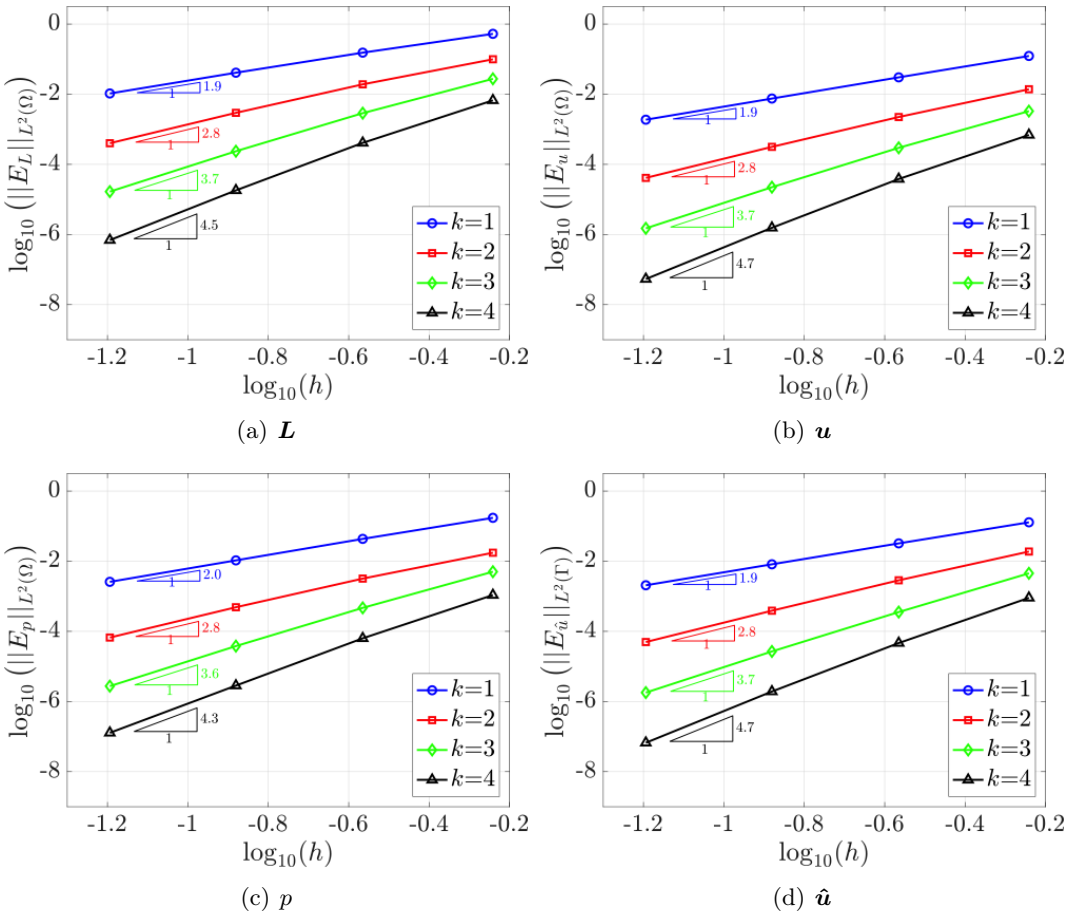

(a) $\boldsymbol{L}$ (b) $\boldsymbol{u}$

(c) p (d) $\hat{\boldsymbol{u}}$

FIGURE 3.16: Axisymmetric flow past a sphere: mesh convergence of the $\mathcal{L}_2$ norm of the error for $\boldsymbol{L}$, $\boldsymbol{u}$, p and $\hat{\boldsymbol{u}}$.

Finally, the accuracy of the HDG-PGD approach on the drag force is studied for three different configurations corresponding to μ_1=1, μ_1=2 and μ_1=3. Figure 3.17 shows evolution of the error in the drag force as the number of of degrees of freedom is increased for the three different geometric configurations and for different orders of approximation. The number of degrees of freedom refers to the size of the HDG global problem as this is the most time consuming part of the spatial iteration. The

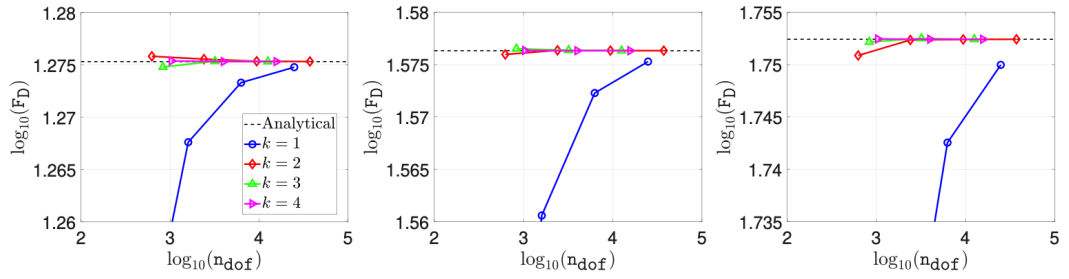

(a) $\mu_1 = 1$ (b) $\mu_1 = 2$ (c) $\mu_1 = 3$

FIGURE 3.17: Axisymmetric flow past a sphere: evolution of the error in the drag force as the number of modes is increased for three different geometric configurations.

results show the variation of the drag force induced by the variation of the geometric parameter and how the generalised solution produces accurate results for any value of the geometric parameter. In all cases, convergence to exact value is observed, and the superiority of using high-order approximations is clearly appreciated. For the first configuration, the results in figure 3.17(a) show that with a linear approximation requires the solution of a global problem with 24,832 degrees of freedom to obtain relative error in the drag force of 0.0181. In contrast , using a quartic approximation, the error in the first mesh is 0.0021, solving a global problem with only 416 degrees of freedom, that is an error one order of magnitude lower with almost 20 times less degrees of freedom. The results also show that for higher values of the geometric parameter the solution is slightly more difficult to capture and the number of degrees of freedom required is slightly higher. In fact, the advantages of high-order approximations are more noticeable for the case of μ_1=3.

3.4.3 Stokes flow past a sphere

The third example considers as well the Stokes flow past a sphere, but contrary from the previous one, in a 3D fashion.

The domain of interest is again selected as the region confined by two concentric spheres with radius R_{in} and R_{out} respectively, with $R_{\text{in}}<R_{\text{out}}$. The analytical solution (3.67), in Cartesian coordinates, is given by the following velocity and pressure fields

$$\begin{aligned} u_x &= v_\infty + v_\infty \frac{R_{\text{in}}^3}{4r^3}\left(\frac{3x^2}{r^2}-1\right) - v_\infty \frac{3R_{\text{in}}}{4r}\left(\frac{x^2}{r^2}+1\right), \\ u_y &= v_\infty \frac{3R_{\text{in}}xy}{4r^3}\left(\frac{R_{\text{in}}^2}{r^2}-1\right), \\ u_z &= v_\infty \frac{3R_{\text{in}}xz}{4r^3}\left(\frac{R_{\text{in}}^2}{r^2}-1\right), \\ p &= p_\infty - \frac{3}{2r^3}\nu v_\infty R_{\text{in}} x, \end{aligned} \tag{3.70}$$

with $r=\sqrt{x^2+y^2+z^2}$ where v_∞ and p_∞ are the magnitude of the velocity in the x-direction and the pressure of the undisturbed flow, far away from the obstacle.

The geometry of the reference domain, corresponding to μ_1=1, is shown in figure 3.18(a). A no-slip boundary condition is imposed on the inner sphere, a Dirichlet boundary condition corresponding to the exact solution on the outer boundary. Given the symmetric nature of the problem, to reduce its computational cost, only one forth of the domain is considered introducing a free slip boundary condition on the two interfaces of symmetry (shown in figure 3.18(b)).

Also in this case, as mentioned in Remark 5, the portion of the boundary where the symmetry is imposed depends on the geometric parameter, but the normal and

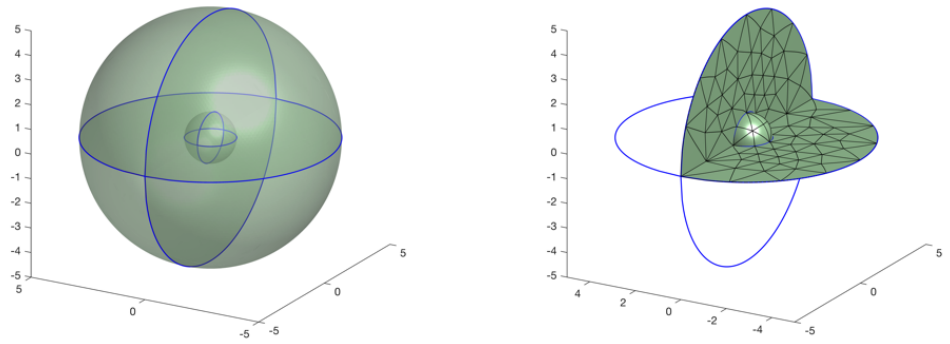

(a) Geometry (b) Mesh

FIGURE 3.18: Flow past a sphere: Geometry of the domain and computational mesh of a quarter of the domain.

tangent to the boundary are independent on the geometric changes. Therefore, the matrices $\boldsymbol{D}$ and $\boldsymbol{E}$ do not depend upon the geometric parameters.

Remark 9. *The assumption that matrices $\boldsymbol{D}$ and $\boldsymbol{E}$ do not depend upon the geometric parameters because of the orthogonality between the vector $\boldsymbol{n}$ and the surface of symmetry is crucial to obtain a converging algorithm when a symmetrical surface is used, moreover in a three dimensional framework. During the development of this thesis, has been noticed that it is critical to ensure that all the points of the computational mesh belonging to a symmetric surface lye exactly on that surface (with almost no margin of error).*

Geometric mapping The mapping between the reference and the geometrically parametrised domains is analogous to the mapping utilised in the previous example, given by the two terms in equation (3.64), but for a three dimensional Cartesian domain. The separated mapping is

$$\begin{aligned} \mathbf{M}^1(\boldsymbol{x}) &= \frac{1}{r}\boldsymbol{x} \qquad & \psi^1(\mu) &= \frac{R_{\text{out}}(\mu-1)}{R_{\text{out}}-1}, \\ \mathbf{M}^2(\boldsymbol{x}) &= \boldsymbol{x} \qquad & \psi^2(\mu) &= \frac{R_{\text{out}}-\mu}{R_{\text{out}}-1}. \end{aligned} \tag{3.71}$$

and the Jacobian of the mapping written in the general separated form of equation (3.23) results

$$\mathbf{J}^1(\boldsymbol{x}) = \frac{1}{r^3}\begin{bmatrix} y^2+z^2 & -xy & -xz \\ -xy & x^2+z^2 & -yz \\ -xz & -yz & x^2+y^2 \end{bmatrix}, \qquad \mathbf{J}^2(\boldsymbol{x}) = \mathbf{I}_3, \tag{3.72}$$

where $r{=}\sqrt{x^2+y^2+z^2}$.

Off-line phase The proposed ROM is used to obtain the generalised solution of the parametric Stokes problem.

The computation was performed using the second mesh with a degree of approximation k=4 for all the variables and with a mesh of 1,000 elements in the parametric dimension with also k=4.

The first eight normalised modes of the magnitude of the velocity field and the pressure are shown in figures 3.19 and 3.20.

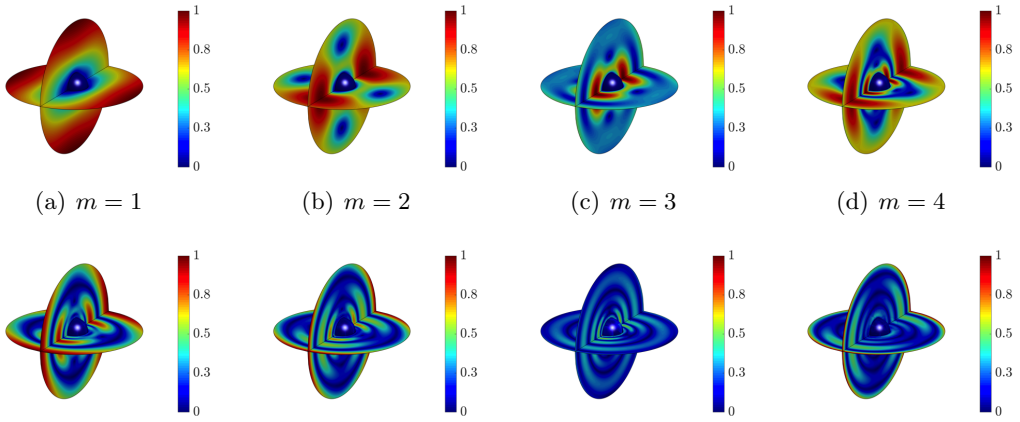

(a) $m = 1$ (b) $m = 2$ (c) $m = 3$ (d) $m = 4$

(e) $m = 5$ (f) $m = 6$ (g) $m = 7$ (h) $m = 8$

FIGURE 3.19: Flow past a sphere: First eight normalised spatial modes of the norm of the velocity field.

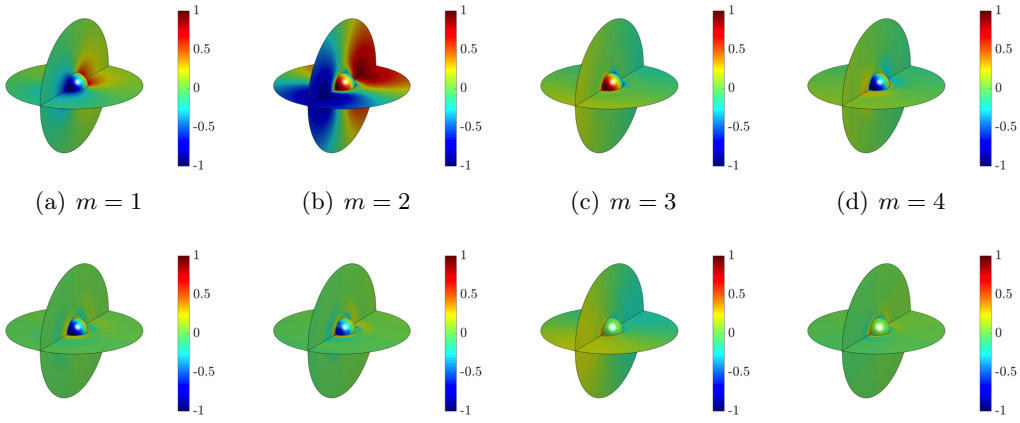

(a) $m = 1$ (b) $m = 2$ (c) $m = 3$ (d) $m = 4$

(e) $m = 5$ (f) $m = 6$ (g) $m = 7$ (h) $m = 8$

FIGURE 3.20: Flow past a sphere: First eight normalised spatial modes of the pressure field.

Figure 3.21 shows the first eight normalised parametric modes computed. It is worth noting the expected similarity between the majority of the spatial modes represented in figures 3.9 and 3.19, 3.10 and 3.20 and parametric ones shown in figures3.11 and 3.21 respectively.

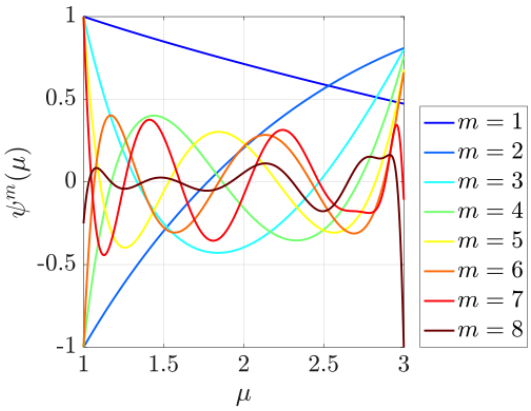

FIGURE 3.21: Flow past a sphere: First eight normalised parametric modes.

As in the previous example, the evolution of the relative amplitude of the modes is shown in 3.22. The rapid decrease shows that it is possible to compute a generalised solution to this problem with a very small number of modes. With nine modes the relative amplitude is already below 10^{-5}.

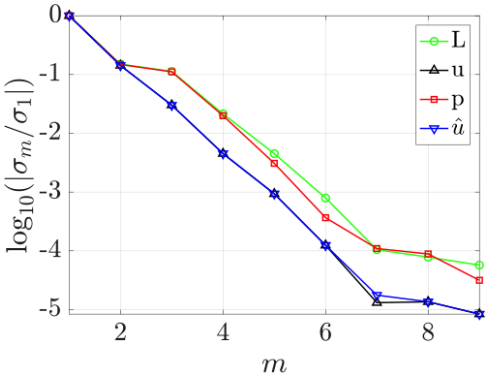

FIGURE 3.22: Flow past a sphere: Convergence of the mode amplitudes.

On-line phase Once the generalised solution is computed, it is of interest to quantify its accuracy.

Figure 3.22 and figure 3.23 shows the absolute value of the error of the velocity magnitude and pressure using as the number of modes is increased for three relevant configurations corresponding to the parameter μ_1=1, μ_1=2 and μ_1=3.

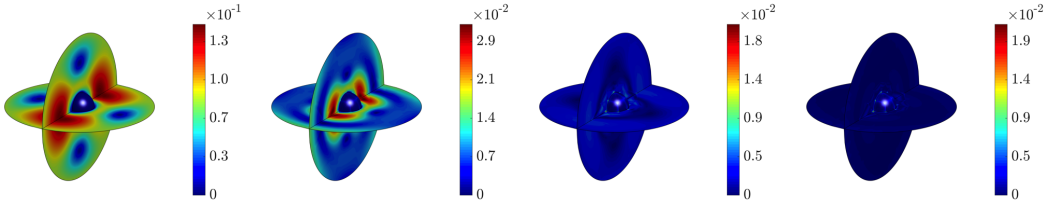

(a) $\mu_1 = 1$, $m = 1$ (b) $\mu_1 = 1$, $m = 2$ (c) $\mu_1 = 1$, $m = 3$ (d) $\mu_1 = 1$, $m = 4$

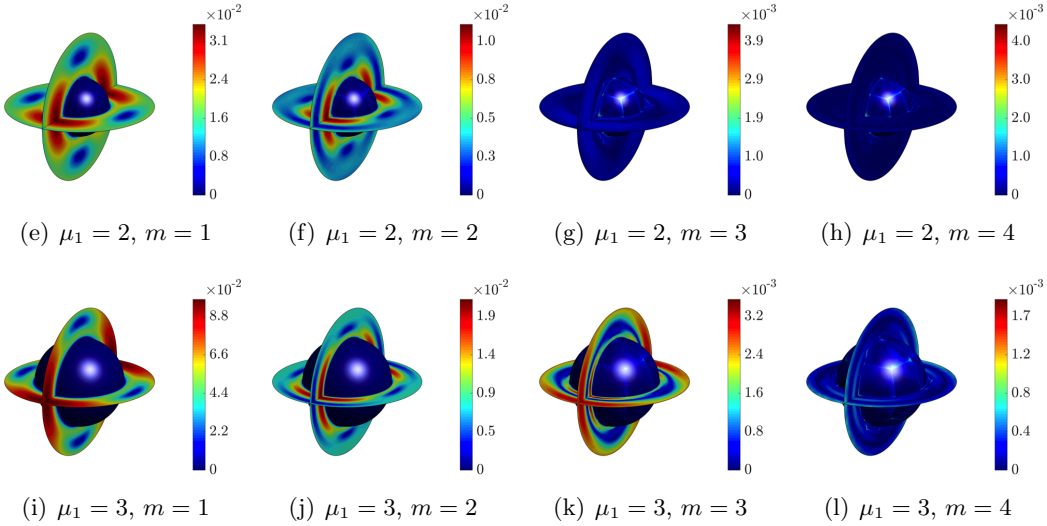

(e) $\mu_1 = 2$, $m = 1$ (f) $\mu_1 = 2$, $m = 2$ (g) $\mu_1 = 2$, $m = 3$ (h) $\mu_1 = 2$, $m = 4$

(i) $\mu_1 = 3$, $m = 1$ (j) $\mu_1 = 3$, $m = 2$ (k) $\mu_1 = 3$, $m = 3$ (l) $\mu_1 = 3$, $m = 4$

FIGURE 3.22: Stokes flow past a sphere: Absolute value of the error of the velocity magnitude using n PGD modes and for different values of the geometric parameter μ_1. A quartic approximation is used for all variables in the mesh of figure 3.18.

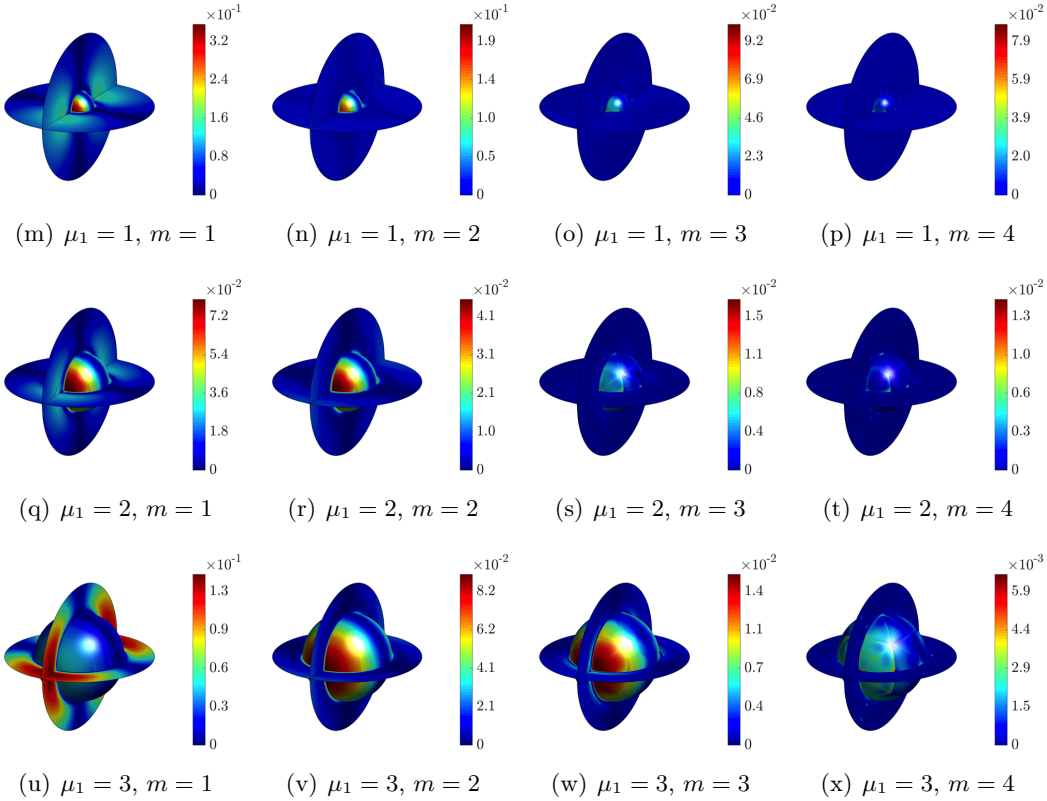

(m) $\mu_1 = 1$, $m = 1$ (n) $\mu_1 = 1$, $m = 2$ (o) $\mu_1 = 1$, $m = 3$ (p) $\mu_1 = 1$, $m = 4$

(q) $\mu_1 = 2$, $m = 1$ (r) $\mu_1 = 2$, $m = 2$ (s) $\mu_1 = 2$, $m = 3$ (t) $\mu_1 = 2$, $m = 4$

(u) $\mu_1 = 3$, $m = 1$ (v) $\mu_1 = 3$, $m = 2$ (w) $\mu_1 = 3$, $m = 3$ (x) $\mu_1 = 3$, $m = 4$

FIGURE 3.23: Stokes flow past a sphere: Absolute value of the pressure magnitude using n PGD modes and for different values of the geometric parameter μ_1. A quartic approximation is used for all variables in the mesh of figure 3.18.

Similarly to results shown in figures 3.13 and 3.13 with only one PGD mode an absolute error of the order of 10^{-1} or below is already obtained for all three configurations for both velocity and pressure. The more accurate results are obtained in agreement with previous results for the case with μ_1=2. From 3 to 4 modes the error saturates for the given mesh, for both velocity and pressure, showing improvements of the accuracy of the solution only for μ_1=3. This is in agreement with next results.

To further illustrate the accuracy of the proposed HDG-PGD approach, the relative error in the $\mathcal{L}_2(\Omega \times \boldsymbol{\mathcal{I}})$ norm, defined in (3.66) is studied and compared to the error of the full order HDG approach.

Figure 3.15 shows the evolution of $\varepsilon_{\texttt{PGD}}$, for all the variables, as the number of PGD modes is increased, for different degree of approximation and mesh drawn in Figure 3.18. The discontinuous lines in figure 3.24 show the relative error of the full order HDG method, measured in the $\mathcal{L}_2(\Omega \times \boldsymbol{\mathcal{I}})$ norm.

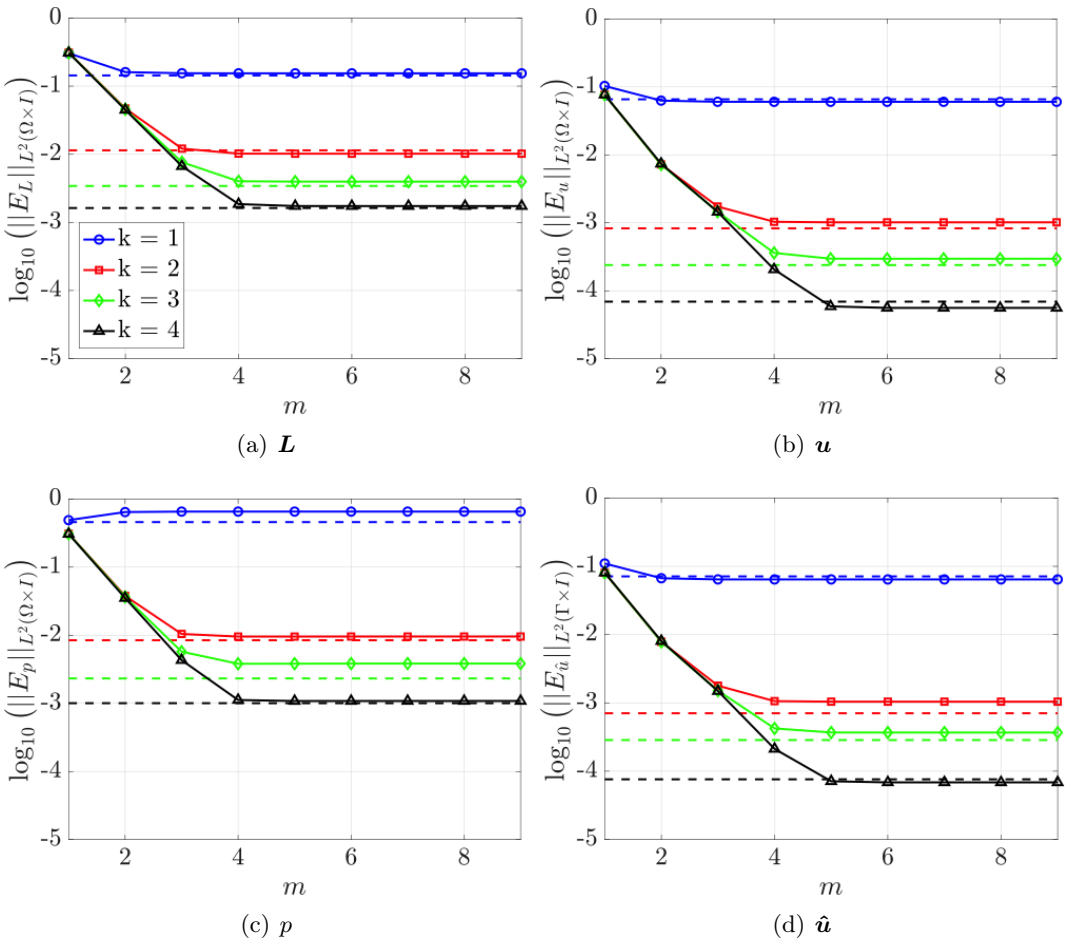

FIGURE 3.24: Flow past a sphere: convergence of the $\mathcal{L}_2$ norm of the error for $\boldsymbol{L}$, $\boldsymbol{u}$, p and $\hat{\boldsymbol{u}}$ as the number of PGD modes is increased for linear to quartic approximations.

Also in this case excellent agreement between the two errors is observed.

Finally, the accuracy of the HDG-PGD approach on the drag force is studied for three different configurations corresponding to μ_1=1, μ_1=2 and μ_1=3.

Figure 3.25 shows evolution of the drag force for different orders of approximation and mesh of Figure 3.18(b). The number of degrees of freedom refers to the size of the HDG global problem as this is the most time consuming part of the spatial iteration.

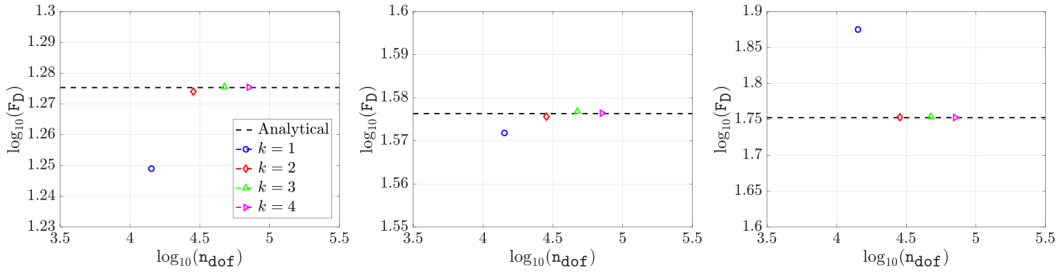

(a) $\mu_1 = 1$ (b) $\mu_1 = 2$ (c) $\mu_1 = 3$

FIGURE 3.25: Flow past a sphere: evolution of the error in the drag force as the number of modes is increased for three different geometric configurations.

Figure 3.26 shows evolution of the error of the drag force associated to Figure 3.18(b) compared with the analogous error computed with axisymmetric strategy for different orders of approximation on the first mesh of Figure 3.8.

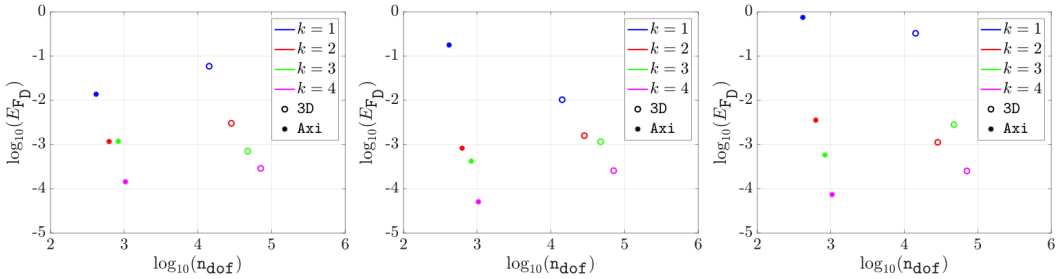

(a) $\mu_1 = 1$ (b) $\mu_1 = 2$ (c) $\mu_1 = 3$

FIGURE 3.26: Flow past a sphere: comparison between the error in the drag force for three different geometric configurations obtained with a 3D and axisymmetric strategy in function of the number of degrees of freedom used.

For all parameters, convergence to exact value is observed, and the superiority of using high-order approximations is clearly appreciated. Moreover, it is visible the saving on in terms of degrees of freedom that an axisymmetric strategy provides.

3.4.4 Stokes flow around two cylinders

The next example is taken from Sevilla et al., (2020b) and considers the Stokes flow around two cylinders. The problem consists of two circles that can change their mutual distance and individual area, whilst maintaining the total area of the two objects. The two cylinders are placed in a rectangular channel of length L and width D.

Two geometric parameters are considered in this example. The first one, $\mu_1 \in \mathcal{I}_1{=}[-1,1]$, controls the radius of the two circles in such a way that the total area is maintained. The second parameter, $\mu_2 \in \mathcal{I}_2{=}[-1,1]$, controls the distance between the centre of the two cylinders. The value of $\mu_1 = -1$ corresponds to the configuration where the radius of the first sphere is $R_1{=}1.0733$ and the radius of the second sphere is $R_2{=}0.3578$, whereas the value of $\mu{=}1$ corresponds to the opposite situation, with $R_1{=}0.3578$ and $R_2{=}1.0733$. Both configurations correspond to the cases where the area of one of the circles is 90% and 10% respectively of the total area occupied by both circles. The value of $\mu_2{=}-1$ corresponds to the case where the distance between the spheres is maximum, with the centres of the spheres placed at $(-7.75, 0)$ and $(7.75, 0)$ respectively. The value of $\mu_2{=}1$ corresponds to the case where the distance between the spheres is minimum, with the centres of the spheres placed at $(-6.25, 0)$ and $(6.25, 0)$ respectively.

The reference domain shown in figure 3.27 is chosen as the bi-dimensional rectangle $\Omega{=}([-L,L]\times[-H,H])\backslash(\mathcal{B}^+\cup\mathcal{B}^-)$, with $L{=}20$, $H{=}7$, $\boldsymbol{x}_0{=}(7,0)$, $R_{\text{ref}}{=}0.8$ and where

$$\mathcal{B}^{\pm} = \{\boldsymbol{x}\in\mathbb{R}^2 \mid \|\boldsymbol{x}\pm\boldsymbol{x}_0\|\leq R_{\text{ref}}\}. \tag{3.73}$$

Analogously to the example presented in section 3.4.3, to reduce the computational costs of the problem, only on half of the domain is considered introducing a slip boundary condition. On the left part of the boundary a Dirichlet boundary condition, corresponding to a horizontal velocity of magnitude one, is imposed. On the right part of the boundary a homogeneous Neumann boundary condition is imposed. On

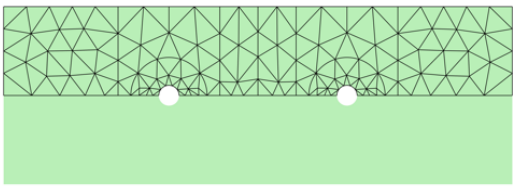

FIGURE 3.27: Stokes flow around two cylinders: Domain and computational mesh.

the surface of the two spheres a no-slip boundary condition is enforced and on the upper part of the boundary a slip boundary condition is imposed. The computational triangular mesh used to solve the problem is highlighted in figure 3.27. The mesh has 208 elements, leading to a system in the HDG global problem of 3500 equations for a degree of approximation $k{=}4$.

Geometric mapping The mapping used in the example involving the flow around two cylinders is designed as the composition of two mappings. The first mapping, $\boldsymbol{\mathcal{M}}_{\mu_1}$, is defined to account for the change of radius of the two circles and it is written in the general separable expression of equation (3.22) with

$$
\begin{aligned}
\mathbf{M}_1^1(\boldsymbol{x}) &= \begin{cases} \frac{1}{r}\boldsymbol{x}_0^- & \text{if } \|\boldsymbol{x}_0^-\| \leq R_{\text{out}} \\ 0 & \text{otherwise} \end{cases} && \psi_1^1(\mu_1) = A(R^+(\mu_1)), \\
\mathbf{M}_1^2(\boldsymbol{x}) &= \begin{cases} \boldsymbol{x}_0^- & \text{if } \|\boldsymbol{x}_0^-\| \leq R_{\text{out}} \\ 0 & \text{otherwise} \end{cases} && \psi_1^2(\mu_1) = B(R^+(\mu_1)), \\
\mathbf{M}_1^3(\boldsymbol{x}) &= \begin{cases} r\boldsymbol{x}_0^- & \text{if } \|\boldsymbol{x}_0^-\| \leq R_{\text{out}} \\ 0 & \text{otherwise} \end{cases} && \psi_1^3(\mu_1) = C(R^+(\mu_1)), \\
\mathbf{M}_1^4(\boldsymbol{x}) &= \begin{cases} r^2\boldsymbol{x}_0^- & \text{if } \|\boldsymbol{x}_0^-\| \leq R_{\text{out}} \\ 0 & \text{otherwise} \end{cases} && \psi_1^4(\mu_1) = D(R^+(\mu_1)), \\
\mathbf{M}_1^5(\boldsymbol{x}) &= \begin{cases} \boldsymbol{x}_0 & \text{if } \|\boldsymbol{x}_0^-\| \leq R_{\text{out}} \\ 0 & \text{otherwise} \end{cases} && \psi_1^5(\mu_1) = 1, \\
\mathbf{M}_1^6(\boldsymbol{x}) &= \begin{cases} \frac{1}{r}\boldsymbol{x}_0^+ & \text{if } \|\boldsymbol{x}_0^+\| \leq R_{\text{out}} \\ 0 & \text{otherwise} \end{cases} && \psi_1^6(\mu_1) = A(R^-(\mu_1)), \\
\mathbf{M}_1^7(\boldsymbol{x}) &= \begin{cases} \boldsymbol{x}_0^+ & \text{if } \|\boldsymbol{x}_0^+\| \leq R_{\text{out}} \\ 0 & \text{otherwise} \end{cases} && \psi_1^7(\mu_1) = B(R^-(\mu_1)), \\
\mathbf{M}_1^8(\boldsymbol{x}) &= \begin{cases} r\boldsymbol{x}_0^+ & \text{if } \|\boldsymbol{x}_0^+\| \leq R_{\text{out}} \\ 0 & \text{otherwise} \end{cases} && \psi_1^8(\mu_1) = C(R^-(\mu_1)),, \\
\mathbf{M}_1^9(\boldsymbol{x}) &= \begin{cases} r^2\boldsymbol{x}_0^+ & \text{if } \|\boldsymbol{x}_0^+\| \leq R_{\text{out}} \\ 0 & \text{otherwise} \end{cases} && \psi_1^9(\mu_1) = D(R^-(\mu_1)), \\
\mathbf{M}_1^{10}(\boldsymbol{x}) &= \begin{cases} -\boldsymbol{x}_0 & \text{if } \|\boldsymbol{x}_0^+\| \leq R_{\text{out}} \\ 0 & \text{otherwise} \end{cases} && \psi_1^{10}(\mu_1) = 1,
\end{aligned}
\tag{3.74}
$$

where $\boldsymbol{x}_0^{\pm}=\boldsymbol{x}\pm\boldsymbol{x}_0$, $R_{\text{out}}=3$ and, as detailed in section 3.4.4, $\boldsymbol{x}_0=(7,0)$ and $R_{\text{ref}}=0.8$. The radius of the sphere centred at $\boldsymbol{x}_0$ is defined as $R^+(\mu_1)=-0.0845\mu_1^2+0.3578\mu_1+0.8$ so that it takes value 0.3578 for $\mu_1=-1$, 0.8 for $\mu_1=0$ and 1.0733 for $\mu_1=1$. The radius of the sphere centred at $-\boldsymbol{x}_0$ is defined in terms of $R^+(\mu_1)$ in such a way that the total area of the two spheres is maintained, namely $(R^+)^2+(R^-)^2=32/25$.

The piecewise nature of the mapping is illustrated in figure 3.28, in the vicinity of one of the spheres. Notice that the number of terms composing the mapping are chosen arbitrarily depending on the required regularity. Imposing properly conditions on the smoothness of both the mapping and its derivatives, the parametric modes can be particularized.

A linear mapping can be devised imposing its continuity in the inner and outer radius. The parametric modes are particularised by

$$\begin{aligned} A(R) &= \frac{R_{\text{out}}(R-R_{\text{ref}})}{R_{\text{out}}-R_{\text{ref}}}, \qquad & B(R) &= \frac{R_{\text{out}}-R}{R_{\text{out}}-R_{\text{ref}}}, \\ C(R) &= 0, & D(R) &= 0. \end{aligned} \tag{3.75}$$

A quadratic mapping can be devised imposing its continuity in the inner and outer radius and the continuity of the first derivative in the outer radius. The parametric modes are particularised by

$$\begin{aligned} A(R) &= \frac{R_{\text{out}}^2(R-R_{\text{ref}})}{(R_{\text{out}}-R_{\text{ref}})^2}, \qquad & B(R) &= \frac{(R_{\text{out}}^2-2RR_{\text{out}}+R_{\text{ref}}^2)}{(R_{\text{out}}-R_{\text{ref}})^2}, \\ C(R) &= \frac{(R-R_{\text{ref}}))}{(R_{\text{out}}-R_{\text{ref}})^2}, & D(R) &= 0. \end{aligned} \tag{3.76}$$

A cubic mapping can be devised imposing its continuity and the continuity of the first derivative in the inner and outer radius. The parametric modes are particularised by

$$\begin{aligned} A(R) &= \frac{R_{\text{out}}^2(R_{\text{out}}-3R_{\text{ref}})(R-R_{\text{ref}}))}{(R_{\text{out}}-R_{\text{ref}})^3}, \\ B(R) &= \frac{R_{\text{out}}^3-3R_{\text{out}}^2R_{\text{ref}}-3R_{\text{out}}R_{\text{ref}}^2+6RR_{\text{out}}R_{\text{ref}}-R_{\text{ref}}^3}{(R_{\text{out}}-R_{\text{ref}})^3}, \\ C(R) &= \frac{3(R_{\text{out}}+R_{\text{ref}})(R_{\text{ref}}-R)}{(R_{\text{out}}-R_{\text{ref}})^3}, \\ D(R) &= \frac{2(R-R_{\text{ref}})}{(R_{\text{out}}-R_{\text{ref}})^3}. \end{aligned} \tag{3.77}$$

The second mapping, $\boldsymbol{\mathcal{M}}_{\mu_2}$, is defined to account for the change of distance between the spheres and it is written in the general separable expression of equation (3.22) with

$$\begin{aligned} \mathbf{M}_2^1(\boldsymbol{x}) &= \begin{Bmatrix} d(x) \\ 0 \end{Bmatrix} \qquad & \psi_2^1(\mu_2) &= -\mu_2/2, \\ \mathbf{M}_2^2(\boldsymbol{x}) &= \boldsymbol{x} & \psi_2^2(\mu_2) &= 1, \end{aligned} \tag{3.78}$$

where the function $d(x)$ is given by

$$d(x) := \begin{cases} \zeta+\xi x+\psi x^2 & \text{if } x \in [-L, -x_0-R_{\text{int}}] \\ -1 & \text{if } x \in [-x_0-R_{\text{int}}, -x_0+R_{\text{int}}] \\ \alpha+\beta x+\gamma x^2+\delta x^3 & \text{if } x \in [-x_0+R_{\text{int}}, x_0-R_{\text{int}}] \\ 1 & \text{if } x \in [x_0-R_{\text{int}}, x_0+R_{\text{int}}] \\ -\zeta+\xi x-\psi x^2 & \text{if } x \in [x_0+R_{\text{int}}, L] \end{cases}, \tag{3.79}$$

with R_{int}=4 and L=20.

Analogously with the first mapping, linear piecewise or smoother mappings can be obtained particularising properly constants $\alpha, \beta, \gamma, \delta, \zeta, \xi, \psi$.

A piecewise linear mapping can be devised imposing its continuity. In this fashion constants results

$$\begin{aligned} &\alpha = 0, && \beta = \frac{1}{x_0 - R_{\text{int}}}, \\ &\gamma = 0, && \delta = 0, \\ &\zeta = \frac{L}{x_0 + R_{\text{int}} - L}, && \xi = \frac{1}{x_0 + R_{\text{int}} - L}, \\ &\psi = 0. \end{aligned} \tag{3.80}$$

A piecewise quadratic and cubic mapping can be devised imposing its continuity and the continuity of its first derivative. In this fashion constants results

$$\begin{aligned} &\alpha = 0, && \beta = \frac{3}{2(x_0 - R_{\text{int}})}, \\ &\gamma = 0, && \delta = -\frac{1}{2(x_0 - R_{\text{int}})^3}, \\ &\zeta = -\frac{L(2R_{\text{int}} + 2x_0 - L)}{(R_{\text{int}} + x_0 - L)^2}, && \xi = \frac{2(R_{\text{int}} + x_0)}{(R_{\text{int}} + x_0 - L)^2}, \\ &\psi = -\frac{1}{(R_{\text{int}} + x_0 - L)^2}. \end{aligned} \tag{3.81}$$

As illustrated in figure 3.28 both mappings are defined in a piecewise form. It is

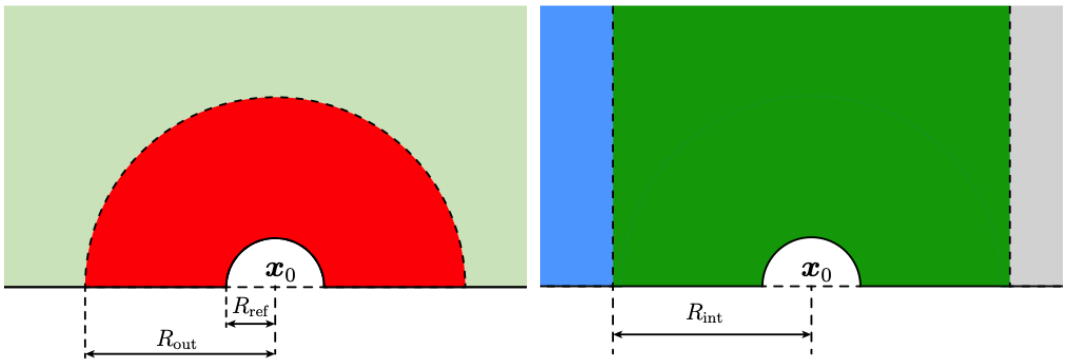

(a) $\boldsymbol{\mathcal{M}}_{\mu_1}$ (b) $\boldsymbol{\mathcal{M}}_{\mu_2}$

FIGURE 3.28: Illustration of the piecewise nature of the mappings $\boldsymbol{\mathcal{M}}_{\mu_1}$ and $\boldsymbol{\mathcal{M}}_{\mu_2}$ detailed in equations (3.74) and (3.78) respectively in the vicinity of the sphere centred at $\boldsymbol{x}_0$.

worth noting that the use of smoother mappings, allows to impose the continuity of its derivatives, in that way the requirement of a conforming mesh given the piecewise nature of the mapping decays. This represents a great advantage in terms of freedom in generating the mesh but on the other hand it has several numerical drawbacks. First, if compared with the use of a linear mapping, a higher number of integration

points are required to ensure that errors due to the numerical integration are lower than the interpolation error. Second, the terms of the separable approximation, for the first mapping, increase and with them the computational complexity of the problem. For that reasons, the mappings selected are only $\mathcal{C}^0$ on the artificial interfaces denoted by discontinuous lines in figure 3.28. Therefore, to facilitate the numerical integration of the terms involving the Jacobian and the adjoint of the mapping, the computational meshes selected are conforming with these interfaces, as it can be observed in the mesh displayed in figure 3.27.

Off-line phase The computation was performed using the mesh of figure 3.27 with a degree of approximation k=4 for all the variables and with a mesh of 50 elements in each parametric dimension with also k=4. The first six spatial modes for the velocity and pressure computed with the proposed HDG-PGD technique are shown in figures 3.29 and 3.30.

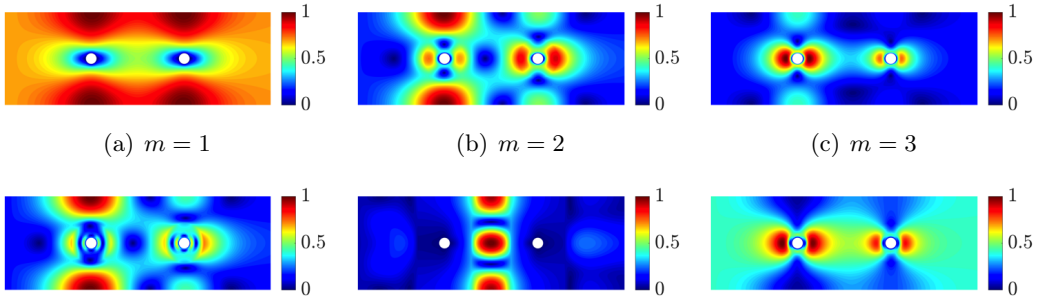

(a) $m = 1$ (b) $m = 2$ (c) $m = 3$

(d) $m = 4$ (e) $m = 5$ (f) $m = 6$

FIGURE 3.29: Stokes flow around two cylinders: First six normalised spatial modes of the velocity field.

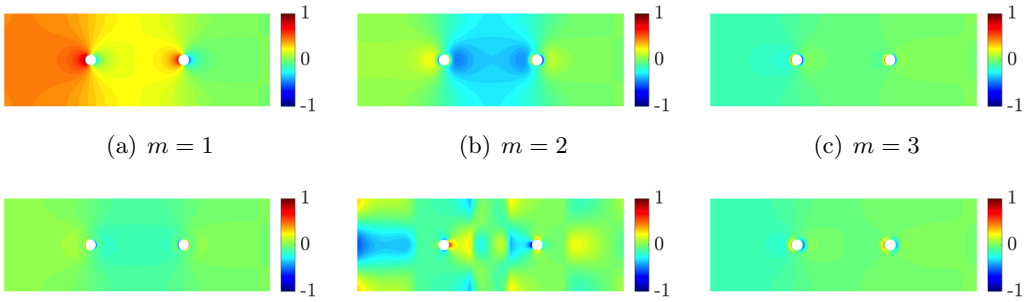

(a) $m = 1$ (b) $m = 2$ (c) $m = 3$

(d) $m = 4$ (e) $m = 5$ (f) $m = 6$

FIGURE 3.30: Stokes flow around two cylinders: First six normalised spatial modes of the pressure field.

Figure 3.31 shows the first six normalised parametric modes computed. In this example there are more parametric modes that have an important influence over the whole range of values for both μ_1 and μ_2. Moreover it is observable that the majority of the parametric modes associated to μ_1 are symmetric,this implies that the two spheres

for the given range of μ_2 behave at the same way. On the other hand, the first six parametric modes associated to the distance have a normalised value near one for the whole range of values of μ_2. This implies that μ_1 has a more relevant effect on the solution while μ_2 begins to affect the computations from mode 7.

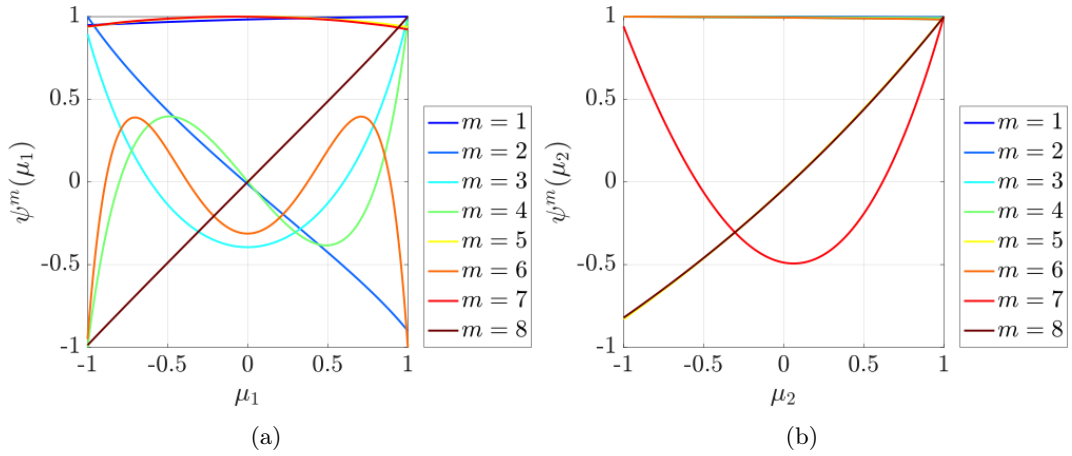

(a) (b)

FIGURE 3.31: Stokes flow around two cylinders: First eight normalised parametric modes.

The evolution of the relative amplitude of the modes is displayed in figure 3.32. The results show that with 9 modes the relative amplitude of the hybrid variable, used to check convergence, is below 10^{-3}, with 16 modes is below 10^{-5} while with 20 modes is below 10^{-6}.

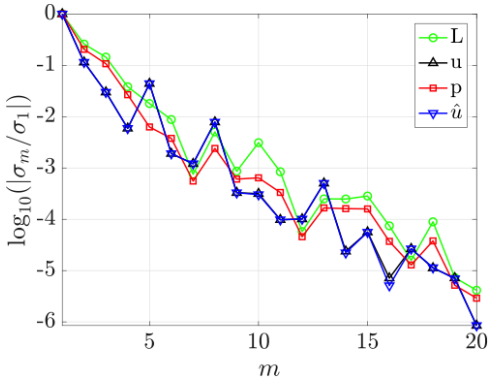

FIGURE 3.32: Stokes flow around two cylinders: Convergence of the mode amplitudes.

On-line phase To illustrate the variation in the geometry induced by the parameters as well as the different flow features that are induced by the geometric changes, figure 3.33 shows the magnitude of the velocity and the pressure fields in the three dimensional domain for three different configurations. The first configuration, shown in figures 3.33(a) and 3.33(d), corresponds to the case where the distance between the spheres is maximum and the sphere closer to the inflow boundary has maximum

radius. The opposite scenario, with the distance between spheres is minimum and the sphere closer to the inflow boundary has minimum radius in shown in figures 3.33(c) and 3.33(f). Finally, the configuration displayed in figures 3.33(b) and 3.33(e) corresponds to the case when the distance between the spheres is half the maximum value and the radius of both spheres is the same.

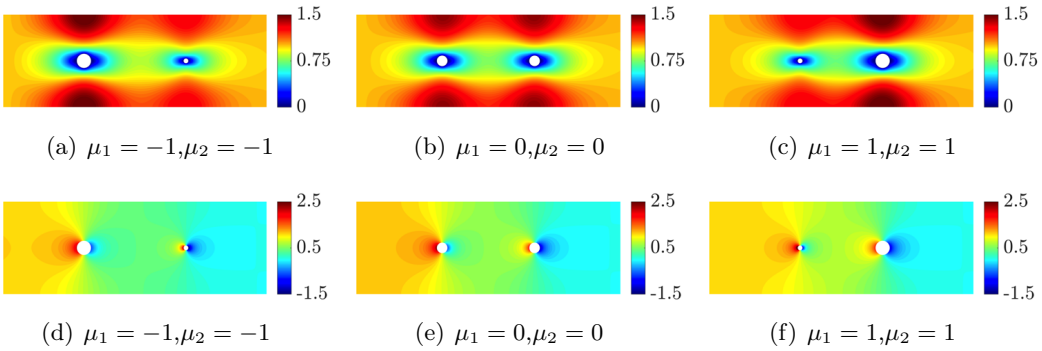

(a) $\mu_1 = -1, \mu_2 = -1$ (b) $\mu_1 = 0, \mu_2 = 0$ (c) $\mu_1 = 1, \mu_2 = 1$

(d) $\mu_1 = -1, \mu_2 = -1$ (e) $\mu_1 = 0, \mu_2 = 0$ (f) $\mu_1 = 1, \mu_2 = 1$

FIGURE 3.33: Stokes flow around two cylinders: Velocity (top) and pressure (bottom) fields for three different geometric configurations.

Once the on-line solution is obtained, in order to verify its accuracy with respect the full order solution computed on the same mesh, the relative value of the error (i.e. the absolute value divided by the norm of the maximum of the field) of the velocity magnitude and pressure is computed.

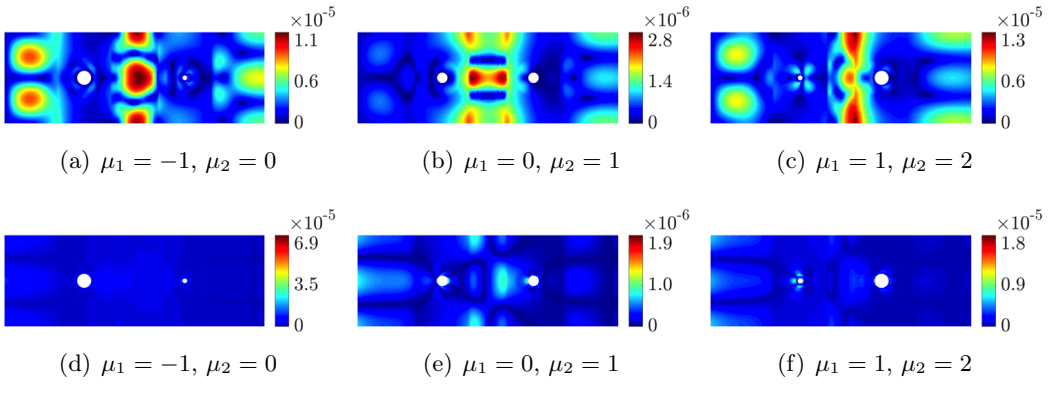

(a) $\mu_1 = -1,\ \mu_2 = 0$ (b) $\mu_1 = 0,\ \mu_2 = 1$ (c) $\mu_1 = 1,\ \mu_2 = 2$

(d) $\mu_1 = -1,\ \mu_2 = 0$ (e) $\mu_1 = 0,\ \mu_2 = 1$ (f) $\mu_1 = 1,\ \mu_2 = 2$

FIGURE 3.34: Stokes flow around two cylinders: Relative value of the error of the velocity magnitude (top) and pressure (bottom) fields for three different geometric configurations.

Finally, to further illustrate the general accuracy of the proposed HDG-PGD solution, in absence of an analytical solution, the relative error between the reduced and the full order solution in the $\mathcal{L}_2(\Omega \times \boldsymbol{\mathcal{I}})$ norm, defined as

$$\varepsilon_{\texttt{PGD-HDG}} = \left(\frac{\int_{\mathcal{I}_1} \int_{\Omega} (\boldsymbol{u}_{\texttt{PGD}} - \boldsymbol{u}_{\texttt{HDG}}) \cdot (\boldsymbol{u}_{\texttt{PGD}} - \boldsymbol{u}_{\texttt{HDG}}) d\Omega \, d\mu}{\int_{\mathcal{I}_1} \int_{\Omega} \boldsymbol{u}_{\texttt{HDG}} \cdot \boldsymbol{u}_{\texttt{HDG}} \, d\Omega \, d\mu} \right)^{1/2}, \tag{3.82}$$

is computed for different discretisations of the parametric space accounting of different number of elements and a quadratic degree of approximation. Figure 3.35 shows the evolution of $\varepsilon_{\texttt{PGD-HDG}}$, for all the variables, as the number of PGD modes is increased. It is worth observing how $\varepsilon_{\texttt{PGD-HDG}}$ saturates when an enough number of modes is

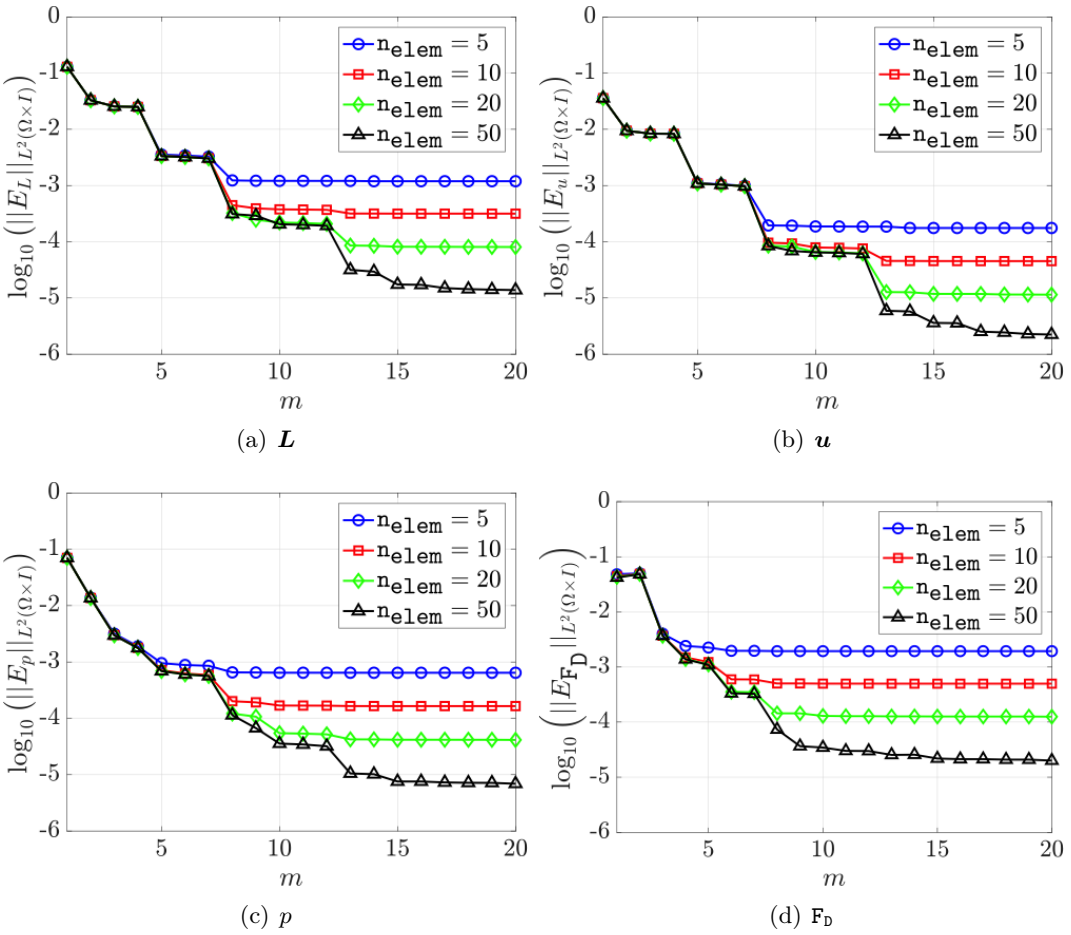

(a) $\boldsymbol{L}$ (b) $\boldsymbol{u}$

(c) p (d) $\mathtt{F_D}$

FIGURE 3.35: Flow past a sphere: $\mathcal{L}_2$ norm of the error for $\boldsymbol{L}$, $\boldsymbol{u}$, p and $\mathtt{F_D}$.

considered, and how the saturation error decreases refining the parametric mesh. As known, this operation is computationally inexpensive as each parametric direction consists of a 1D problem.

3.4.5 Axisymmetric Stokes flow around two microswimmers

The next example considers the Stokes flow around the so-called *push-me-push-you microswimmer*, proposed in Avron et al., (2005). This swimmer consists of two spherical bladders that have the ability to change their mutual distance and individual volume, whilst maintaining the total volume of the two spheres. The swimmer is placed in a cylindrical channel of length L and diameter D.

Two geometric parameters are considered in this example according with the study developed in Alouges et al., (2009). The first one, $\mu_1 \in \mathcal{I}_1=[-1,1]$, controls the radius of the two spheres in such a way that the total volume of the two spheres is maintained. The second parameter, $\mu_2 \in \mathcal{I}_2=[-3,2]$, controls the distance between the centre of the two spheres. The value of $\mu_1=-1$ corresponds to the configuration where the radius of the first sphere is R_1=0.3096 and the radius of the second sphere is R_2=0.116, whereas the value of μ=1 corresponds to the opposite situation, with R_1=0.116 and R_2=0.3096. The value of $\mu_2=-3$ corresponds to the case where the distance between the spheres is maximum, with the centres of the spheres placed at $(-3,0)$ and $(3,0)$ respectively. The value of μ_2=2 corresponds to the case where the distance between the spheres is minimum, with the centres of the spheres placed at $(-0.5,0)$ and $(0.5,0)$ respectively.

Using the axial symmetry of the problem, the computational reference domain is chosen as $\Omega=([-L,L]\times[0,H])\setminus(\mathcal{B}^+\cup\mathcal{B}^-)$, where

$$\mathcal{B}^{\pm}=\{\boldsymbol{r}\in\mathbb{R}^2 \mid \|\boldsymbol{r}\pm\boldsymbol{r}_0\|\leq R_{\text{ref}}\}, \tag{3.83}$$

where L=6, H=2, $\boldsymbol{r}_0$=(1.5, 0) and R_{ref}=0.116. Figure 3.36 shows the triangular mesh of the reference domain used for this numerical example. The mesh has 1,426 elements, leading to a system in the HDG global problem of 22,260 equations for a degree of approximation k=4. On the left part of the boundary a Dirichlet boundary condition, corresponding to a horizontal velocity of magnitude one, is imposed. On the right part of the boundary a homogeneous Neumann boundary condition is imposed. On the surface of the two spheres a no-slip boundary condition is enforced and on the rest of the boundary a slip boundary condition is imposed.

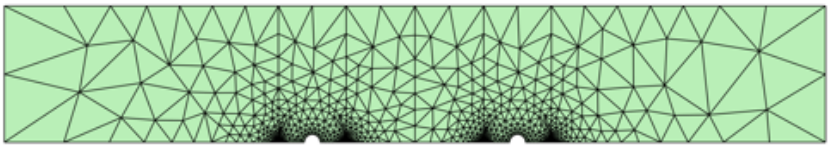

FIGURE 3.36: Axisymmetric flow around two microswimmers: Computational mesh.

It is worth to comment the visible difference between the meshes shown in figures 3.27 and 3.36. The two meshes refer to a comparable problem, and, as the next paragraph shows, are also associated with a similar mapping. By the way, while in the former the reference configurations correspond to a possible configuration, in the latter it does not. This computational mesh is the results of numerous numerical experiments where the influence of the reference configuration on the PGD approximation has been studied. While changes in the value of $\boldsymbol{r}_0$, i.e. the position of the spheres, has not brought significant variations in the reduced solution, changes in the ratio $R_{\text{out}}/R_{\text{ref}}$ and the value of R_{int} did. The most suitable configuration would be a value R_{ref} large

enough to include all the particularities of the flow around each sphere. Due to the piecewise definition of the mapping, the value of R_{out} is limited by the value of R_{int}, which itself is limited by the second value of the range $\mathcal{I}_2$ considered. As the spheres in this example can get much closer respect the cylinders of the previous one, the design of the reference mesh complicates. A good compromise has been considering a similar value for the ratio $R_{\text{out}}/R_{\text{ref}}$, in this case, resulting in $R_{\text{out}}/R_{\text{ref}}$=3.8793 while for the previous example in $R_{\text{out}}/R_{\text{ref}}$=3.75. Being R_{out} limited, the only option available was decreasing R_{ref}. This issue can be avoided through a smoother deforming mapping, as done for instance in Sevilla et al., (2020b) where the geometric mapping is built solving a solid mechanics problem (Persson et al., 2009; Poya et al., 2016; Xie et al., 2013).

Geometric mapping The mapping used in the example involving the flow around two microswimmers is analogous to the one defined for the previous example, but with a different parametric setting and coordinates system. For analogous reasons, the mappings selected are only $\mathcal{C}^0$ on the artificial interfaces denoted by discontinuous lines in figure 3.28. The first mapping, $\boldsymbol{\mathcal{M}}_{\mu_1}$, is defined to account for the change of radius of the two spheres and it is written in the general separable expression of equation (3.22) with

$$
\begin{aligned}
\mathbf{M}_1^1(\boldsymbol{r}) &= \begin{cases} \dfrac{1}{\rho}\boldsymbol{r}_0^- & \text{if } \|\boldsymbol{r}_0^-\| \leq R_{\text{out}} \\ 0 & \text{otherwise} \end{cases} & \psi_1^1(\mu_1) &= \frac{R_{\text{out}}(R^+(\mu_1) - R_{\text{ref}})}{R_{\text{out}} - R_{\text{ref}}}, \\
\mathbf{M}_1^2(\boldsymbol{r}) &= \begin{cases} \boldsymbol{r}_0^- & \text{if } \|\boldsymbol{r}_0^-\| \leq R_{\text{out}} \\ 0 & \text{otherwise} \end{cases} & \psi_1^2(\mu_1) &= \frac{R_{\text{out}} - R^+(\mu_1)}{R_{\text{out}} - R_{\text{ref}}}, \\
\mathbf{M}_1^3(\boldsymbol{r}) &= \begin{cases} \boldsymbol{r}_0 & \text{if } \|\boldsymbol{r}_0^-\| \leq R_{\text{out}} \\ 0 & \text{otherwise} \end{cases} & \psi_1^3(\mu_1) &= 1, \\
\mathbf{M}_1^4(\boldsymbol{r}) &= \begin{cases} \dfrac{1}{\rho}\boldsymbol{r}_0^+ & \text{if } \|\boldsymbol{r}_0^+\| \leq R_{\text{out}} \\ 0 & \text{otherwise} \end{cases} & \psi_1^4(\mu_1) &= \frac{R_{\text{out}}(R^-(\mu_1) - R_{\text{ref}})}{R_{\text{out}} - R_{\text{ref}}}, \\
\mathbf{M}_1^5(\boldsymbol{r}) &= \begin{cases} \boldsymbol{r}_0^+ & \text{if } \|\boldsymbol{r}_0^+\| \leq R_{\text{out}} \\ 0 & \text{otherwise} \end{cases} & \psi_1^5(\mu_1) &= \frac{R_{\text{out}} - R^-(\mu_1)}{R_{\text{out}} - R_{\text{ref}}}, \\
\mathbf{M}_1^6(\boldsymbol{r}) &= \begin{cases} -\boldsymbol{r}_0 & \text{if } \|\boldsymbol{r}_0^+\| \leq R_{\text{out}} \\ 0 & \text{otherwise} \end{cases} & \psi_1^6(\mu_1) &= 1,
\end{aligned}
\tag{3.84}
$$

where $\boldsymbol{r}_0^{\pm}=\boldsymbol{r}\pm\boldsymbol{r}_0$, R_{out}=0.45 and, as detailed in section 3.4.5, $\boldsymbol{r}_0$=(1.5, 0) and R_{ref}=0.116. The radius of the sphere centred at $\boldsymbol{r}_0$ is defined as $R^+(\mu_1)=-0.0372\mu_1^2+0.0968\mu_1+0.25$ so that it takes value 0.116 for $\mu_1=-1$, 0.25 for $\mu_1=0$ and 0.3096 for $\mu_1=1$. The radius of the sphere centred at $-\boldsymbol{r}_0$ is defined in terms of $R^+(\mu_1)$ in such a way that the total volume of the two spheres is maintained, namely $(R^+)^3+(R^-)^3=1/32$. The piecewise nature of the mapping is illustrated in figure 3.28, in the vicinity of one of the spheres.

The second mapping, $\boldsymbol{\mathcal{M}}_{\mu_2}$, is defined to account for the change of distance between the spheres and it is written in the general separable expression of equation (3.22) with

$$\begin{aligned} \mathbf{M}_2^1(\boldsymbol{r}) &= \begin{Bmatrix} d(z) \\ 0 \end{Bmatrix} & \psi_2^1(\mu_2) &= -\mu_2/2, \\ \mathbf{M}_2^2(\boldsymbol{r}) &= \boldsymbol{r} & \psi_2^2(\mu_2) &= 1, \end{aligned} \tag{3.85}$$

where the function $d(z)$ is given by

$$d(z) := \begin{cases} \dfrac{z+L}{z_0+R_{\text{int}}-L} & \text{if } z \in [-L, -z_0-R_{\text{int}}] \\ -1 & \text{if } z \in [-z_0-R_{\text{int}}, -z_0+R_{\text{int}}] \\ \dfrac{z}{z_0-R_{\text{int}}} & \text{if } z \in [-z_0+R_{\text{int}}, z_0-R_{\text{int}}] \\ 1 & \text{if } z \in [z_0-R_{\text{int}}, z_0+R_{\text{int}}] \\ \dfrac{z-L}{z_0+R_{\text{int}}-L} & \text{if } z \in [z_0+R_{\text{int}}, L] \end{cases}, \tag{3.86}$$

with R_{int}=0.47 and, as detailed in section 3.4.5, L=6.

Off-line phase The first four spatial modes for the velocity and pressure computed with the proposed HDG-PGD are shown in figures 3.37 and 3.38. The computation

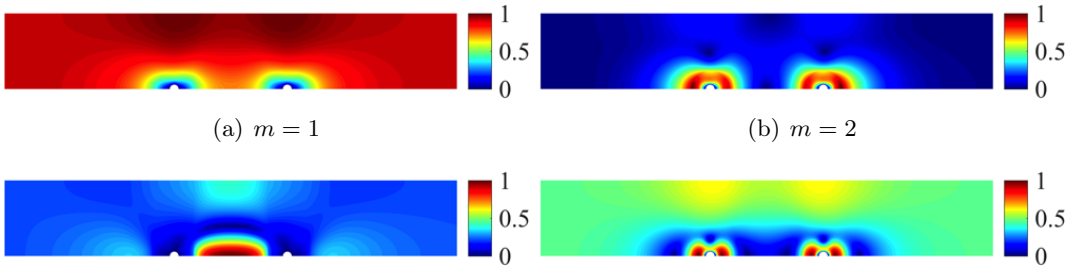

(a) $m = 1$ (b) $m = 2$

(c) $m = 3$ (d) $m = 4$

FIGURE 3.37: Axisymmetric flow around two microswimmers: First four normalised spatial modes of the velocity field.

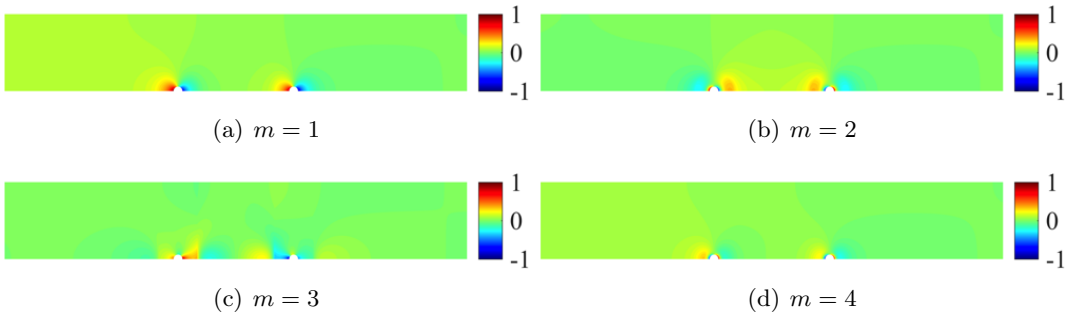

(a) $m = 1$ (b) $m = 2$

(c) $m = 3$ (d) $m = 4$

FIGURE 3.38: Axisymmetric flow around two microswimmers: First four normalised spatial modes of the pressure field.

was performed using the mesh of figure 3.36 with a degree of approximation k=4 for all the variables and with a mesh of 10,000 elements in each parametric dimension with also k=4. It is worth noting that the cost of the one-dimensional parametric problems is negligible when compared to the cost of the spatial iteration. Therefore, a large number of elements is used in the parametric dimension to ensure that the variation induced by the geometric parameters are captured with no a priori knowledge of the solution.

Figure 3.39 shows the first eight normalised parametric modes computed. As in pre-

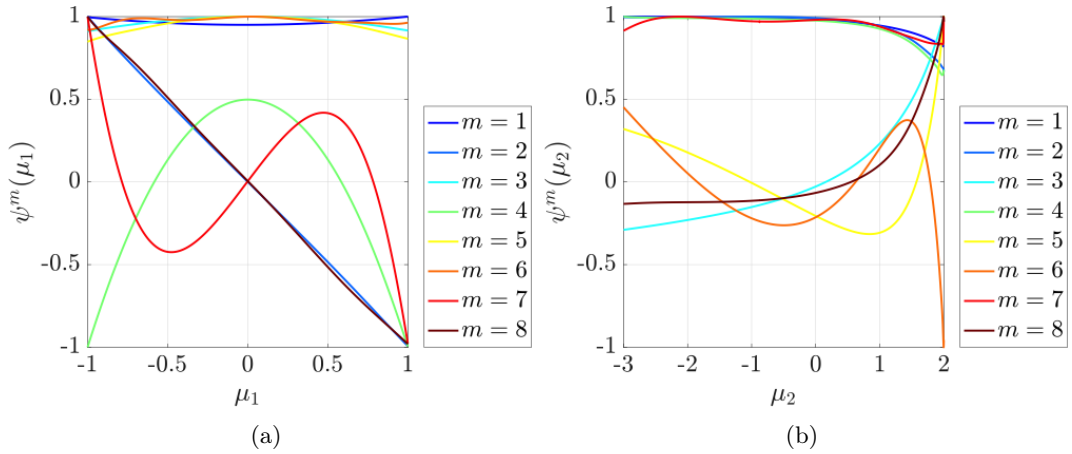

(a) (b)

FIGURE 3.39: Axisymmetric flow around two microswimmers: First eight normalised parametric modes.

vious example, in this example there are more parametric modes that have an important influence over the whole range of values for both μ_1 and μ_2. For instance, in figure 3.39(a) the first, third, fifth and six parametric modes have a normalised value near one for the whole range of values of μ_1. A similar behaviour is observed for the second parameter μ_2. In addition, the second parameter, corresponding to the distance between the spheres it can be observed that many of the modes have a much more relevant influence near μ_2=2. This is expected as this configuration corresponds to the case where the distance between the spheres is minimum and therefore induces an important variation in the flow field because the first sphere will influence the flow that is reaching the second sphere.

The evolution of the relative amplitude of the modes is displayed in figure 3.40. The results show that with 24 modes all the relative amplitude of the hybrid variable, used to check convergence, is below 10^{-3}. A slower decrease of the relative amplitudes when compared with the previous examples can be observed. This is attributed to two factors. First, this problem considers two geometric parameters and, second, the range of variation of the distance is relatively high when compared to the minimum radius of the spheres.

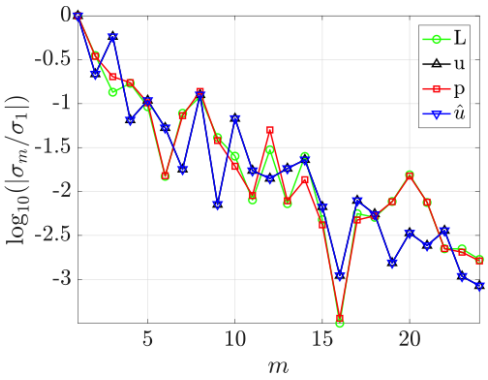

FIGURE 3.40: Axisymmetric flow around two microswimmers: Convergence of the mode amplitudes.

On-line phase To illustrate the variation in the geometry induced by the parameters as well as the different flow features that are induced by the geometric changes, figure 3.41 shows the magnitude of the velocity and the pressure fields in the three dimensional domain for three different configurations.

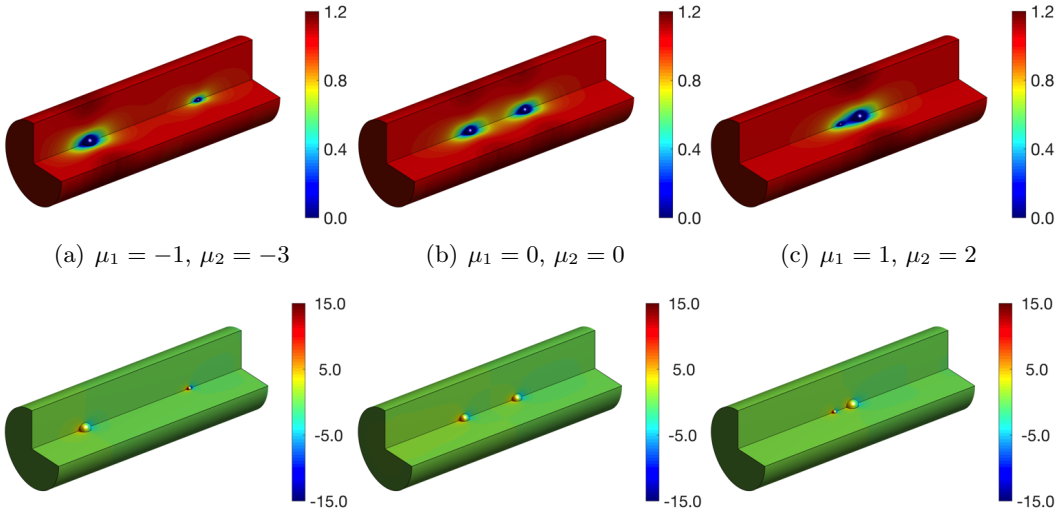

(a) $\mu_1 = -1$, $\mu_2 = -3$ (b) $\mu_1 = 0$, $\mu_2 = 0$ (c) $\mu_1 = 1$, $\mu_2 = 2$

(d) $\mu_1 = -1$, $\mu_2 = -3$ (e) $\mu_1 = 0$, $\mu_2 = 0$ (f) $\mu_1 = 1$, $\mu_2 = 2$

FIGURE 3.41: Axisymmetric flow around two microswimmers: Velocity (top) and pressure (bottom) fields for three different geometric configurations.

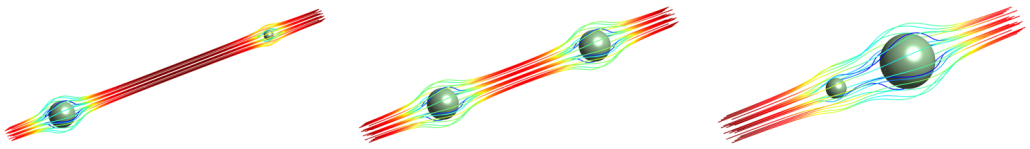

(a) $\mu_1 = -1$, $\mu_2 = -3$ (b) $\mu_1 = 0$, $\mu_2 = 0$ (c) $\mu_1 = 1$, $\mu_2 = 2$

FIGURE 3.42: Axisymmetric flow around two microswimmer: Velocity streamlines associated to velocity fields of figures 3.41(a)-3.41(c) for three different geometric configurations.

The first configuration, shown in figures 3.41(a) and 3.41(d), corresponds to the case where the distance between the spheres is maximum and the sphere closer to the inflow boundary has maximum radius. The opposite scenario, with the distance between spheres is minimum and the sphere closer to the inflow boundary has minimum radius in shown in figures 3.41(c) and 3.41(f). Finally, the configuration displayed in figures 3.41(b) and 3.41(e) corresponds to the case when the distance between the spheres is half the maximum value and the radius of both spheres is the same.

Once the on-line solution is obtained, as done for the previous example in order to verify its accuracy with respect the full order solution computed on the same mesh, the relative value of the error of the velocity magnitude and pressure is computed. The results show that a relative error of the order of 3.1×10^{-3} or below is obtained

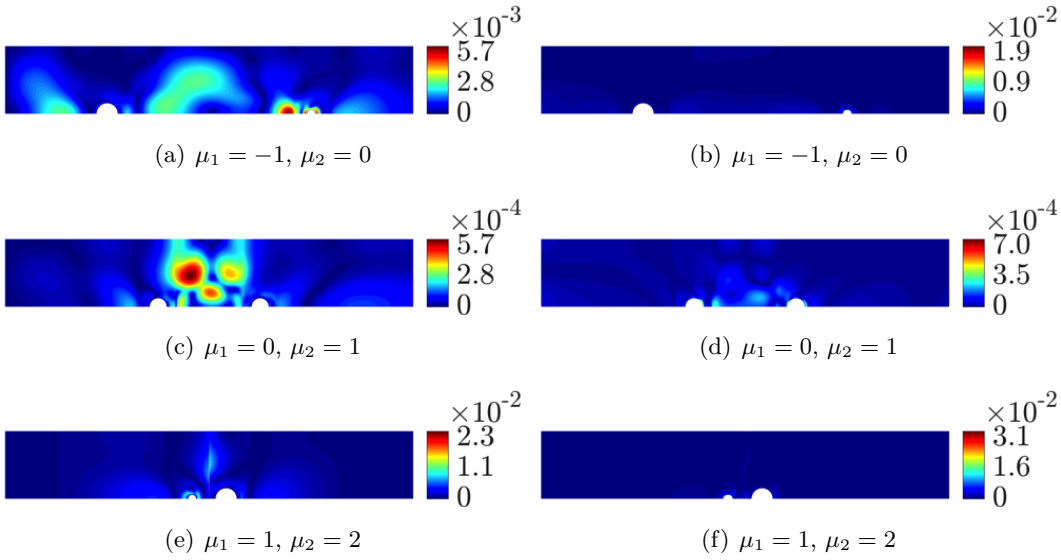

(a) $\mu_1 = -1$, $\mu_2 = 0$ (b) $\mu_1 = -1$, $\mu_2 = 0$

(c) $\mu_1 = 0$, $\mu_2 = 1$ (d) $\mu_1 = 0$, $\mu_2 = 1$

(e) $\mu_1 = 1$, $\mu_2 = 2$ (f) $\mu_1 = 1$, $\mu_2 = 2$

FIGURE 3.43: Axisymmetric flow around two microswimmer: Relative value of the error of the velocity magnitude (left) and pressure (tight) fields for three different geometric configurations.

for all three configurations for both velocity and pressure. The more accurate results are obtained for the case with μ_1=0 and μ_2=0. It is worth to specify that this is not related with the choice of the reference configuration but mainly with the choice of the parametric domains. Results obtained with different reference configurations, not reported in this document, shown in fact analogous results.

To analyse the accuracy of the proposed approach, figure 3.44 compares the drag force on the two spheres as a function of the μ_2, controlling the distance between the spheres, and for three different configurations of the μ_1, controlling the radius of both spheres. The results obtained with the HDG-PGD approach are compared to the results of the standard HDG method on a reference mesh. Both solutions show an excellent agreement in all cases, with an overlap between the symbols used to plot the results of the standard HDG method and the discontinuous line used to plot the results of the proposed PGD approach.

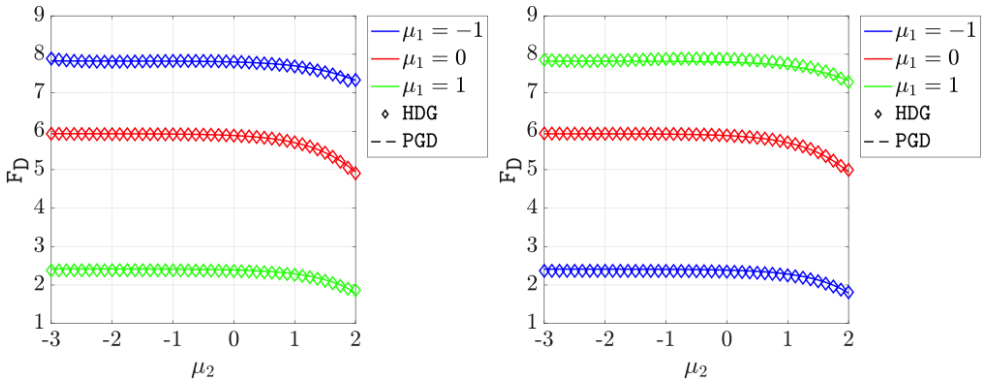

(a) First sphere (b) Second sphere

FIGURE 3.44: Axisymmetric flow around two microswimmer: Comparison of the drag computed on the first and second sphere with the proposed HDG-PGD approach against a reference solution for different configurations.

Finally, to stress the potential of the proposed approach, figure 3.45 shows the drag force on the two spheres and the total drag as a function of both geometric parameters. This figure shows that generalised solution computed with the HDG-PGD approach

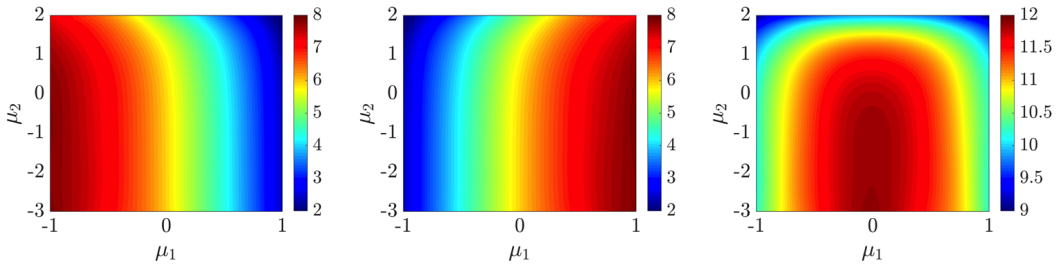

(a) First sphere (b) Second sphere (c) Total

FIGURE 3.45: Axisymmetric flow around two microswimmer: Drag force on the individual spheres and the total drag over the two spheres.

can be used to rapidly explore the whole space of parameters and used to find optimal strokes, of interest in many applications (Alouges et al., 2009).

3.4.6 Stokes flow around a sphere in a corrugated channel

The last example, inspired from the studies in Vieira et al., (2020) and Yang et al., (2017), considers the flow past a sphere placed in a corrugated channel.

The corrugated channel has a height of 1μm and the undulatory profile is defined by the expression

$$y = \begin{cases} \frac{1}{2}\left(f_\omega + f_n\right) + \frac{1}{2}\left(f_\omega - f_n\right)\cos\left(\frac{16\pi x}{7L}\right) & \text{if} \quad |x| < \frac{7}{16}L, \\ f_n & \text{if} \quad \frac{7}{16}L \leq |x| \leq \frac{1}{2}L, \end{cases} \tag{3.87}$$

where L=12.5μm, f_ω=2μm and the value of f_n controls the oscillation of the boundary. A sphere of radius R, centred at the origin, is placed inside the corrugated channel. A Dirichlet boundary condition is imposed at one end of the channel, given by $\boldsymbol{u}_D(\boldsymbol{x})=\left\{64(y^2-1/4)(z^2-1/4),0,0\right\}^T$, and a homogeneous Neumann boundary condition is imposed at the other end. A homogeneous Dirichlet boundary condition is on the rest of the boundary of the domain, corresponding to material walls.

To demonstrate the applicability and potential of the proposed methodology in three dimensions, two geometric parameters are considered. The first parameter $\mu_1 \in [-1,1]$ is used to control the radius of the sphere, defined as $R(\mu_1)=(\mu_1+2)/10$. The second parameter $\mu_2 \in [0,2]$ controls the amplitude of the corrugated channel, given by $f_n=1/2+\mu_2$. The geometry of the reference domain, corresponding to $\mu_1=\mu_2=0$, is shown in figure 3.46(a). Exploiting the symmetry of the problem, a mesh of a

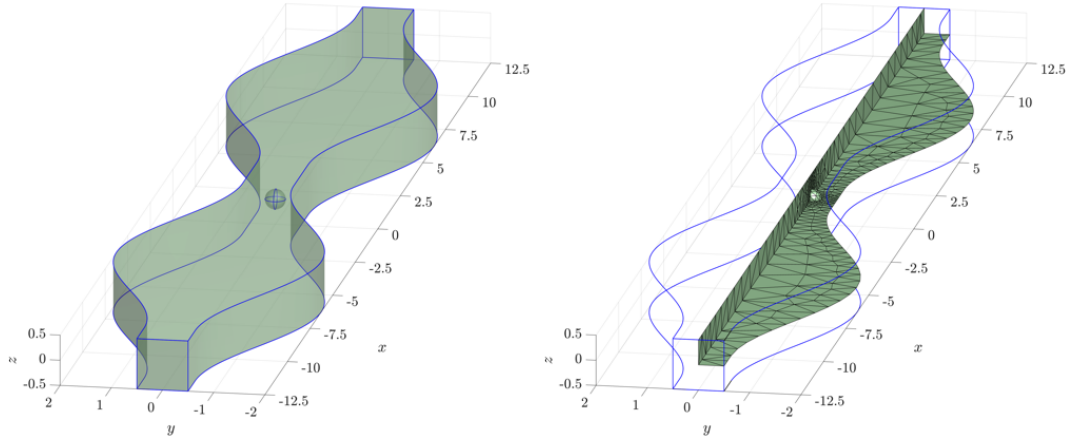

(a) Geometry (b) Mesh

FIGURE 3.46: Flow around a sphere in a corrugated channel: Geometry of the domain and computational mesh of a quarter of the domain.

quarter of the domain is considered, with 2,191 tetrahedral elements, as depicted in figure 3.46(b).

Geometric mapping Similarly to the previous example, the mapping used in the example involving the flow around a sphere in a corrugated channel is designed as the composition of two mappings.

The first mapping, $\boldsymbol{\mathcal{M}}_{\mu_1}$, is defined to account for the change of radius of the sphere and it is written in the general separable expression of equation (3.22) with

$$\begin{aligned}
\mathbf{M}_1^1(\boldsymbol{x}) &= \begin{cases} \dfrac{1}{r}\boldsymbol{x} & \text{if } \|\boldsymbol{x}\| \leq R_{\text{out}} \\ 0 & \text{otherwise} \end{cases} & \psi_1^1(\mu_1) &= \frac{R_{\text{out}}(R(\mu_1) - R_{\text{ref}})}{R_{\text{out}} - R_{\text{ref}}}, \\
\mathbf{M}_1^2(\boldsymbol{x}) &= \begin{cases} \boldsymbol{x} & \text{if } \|\boldsymbol{x}\| \leq R_{\text{out}} \\ 0 & \text{otherwise} \end{cases} & \psi_1^2(\mu_1) &= \frac{R_{\text{out}} - R(\mu_1)}{R_{\text{out}} - R_{\text{ref}}}, \\
\mathbf{M}_1^3(\boldsymbol{x}) &= \begin{cases} \boldsymbol{x} & \text{if } \|\boldsymbol{x}\| > R_{\text{out}} \\ 0 & \text{otherwise} \end{cases} & \psi_1^3(\mu_1) &= 1,
\end{aligned} \tag{3.88}$$

where R_{out}=0.4 and R_{ref}=0.2 and the radius of the sphere, centred at the origin, is defined as $R(\mu_1)$=$(\mu_1+2)/10$. The associated spatial modes of the Jacobian of the mapping result

$$\mathbf{J}_1^1(\boldsymbol{x}) = \frac{1}{r^3}\begin{bmatrix} y^2+z^2 & -xy & -xz \\ -xy & x^2+z^2 & -yz \\ -xz & -yz & x^2+y^2 \end{bmatrix}, \qquad \mathbf{J}_1^2(\boldsymbol{x}) = \mathbf{J}_1^3(\boldsymbol{x}) = \mathbf{I}_3. \tag{3.89}$$

The second mapping, $\boldsymbol{\mathcal{M}}_{\mu_2}$, is defined to account for the change of amplitude in the undulatory part of the channel. It only affects the y coordinate and, more precisely, only the definition of f_n in equation (3.87). More precisely, the profile of the channel is given by equation (3.87) with f_n=$1/2+\mu_2$ so that the mapping results

$$\begin{aligned}
\mathbf{M}_2^1(\boldsymbol{x}) &= \begin{cases} \boldsymbol{x} & \text{if } \|\boldsymbol{x}\| \leq f_\omega/4 \\ 0 & \text{otherwise} \end{cases} & \psi_1^1(\mu_2) &= 1, \\
\mathbf{M}_2^2(\boldsymbol{x}) &= \begin{cases} \boldsymbol{h}(\boldsymbol{x}) & \text{if } \|\boldsymbol{x}\| > f_\omega/4 \\ 0 & \text{otherwise} \end{cases} & \psi_1^2(\mu_2) &= \mu_2,
\end{aligned} \tag{3.90}$$

where $\boldsymbol{h}(\boldsymbol{x}) = (x, 4/9y^2+5/9y+1/9, z)$. The associated spatial modes of the Jacobian are

$$\mathbf{J}_2^1(\boldsymbol{x}) = \mathbf{I}_3, \qquad \mathbf{J}_2^2(\boldsymbol{x}) = \begin{bmatrix} 1 & 0 & 0 \\ 0 & 8/9y+5/9 & 0 \\ 0 & 0 & 1 \end{bmatrix}. \tag{3.91}$$

Remark 10. *It is worth to note that for this example a quadratic mapping has been applied. The imposed constraints are the continuity of both the mapping and its derivative in* $\boldsymbol{x}$=$(0, f_\omega/4, 0)$. *For that reason the use of a computational mesh conforming with the mapping is not required.*

Off-line phase The computation was performed using the mesh of figure 3.46(a) with a degree of approximation k=3 for all the variables and with a mesh of 10,000 elements in each parametric dimension with also k=3.

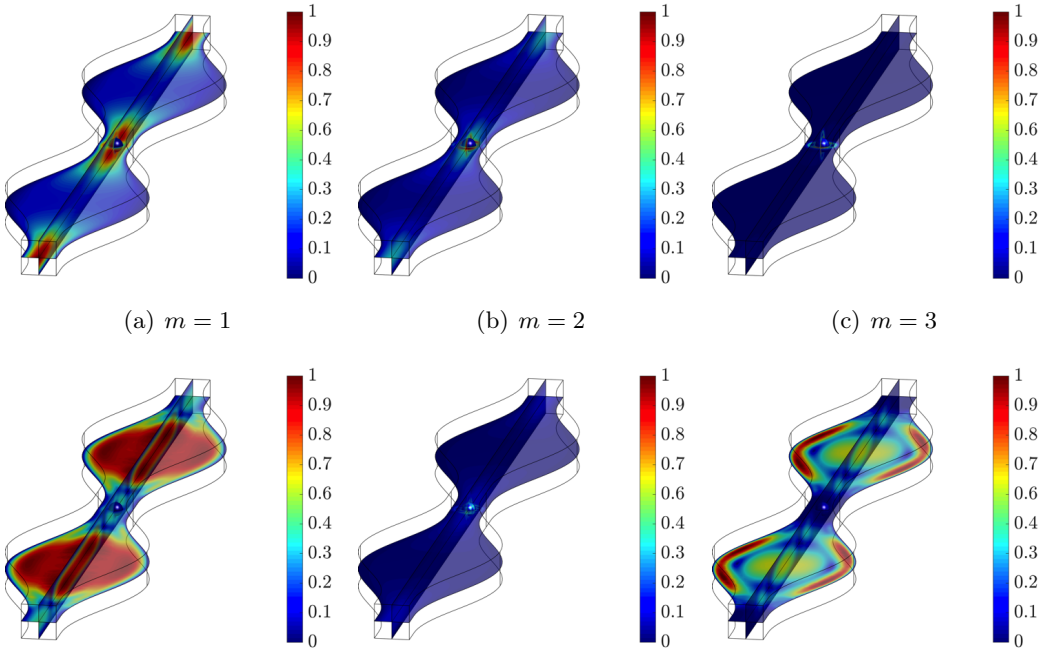

(a) $m = 1$ (b) $m = 2$ (c) $m = 3$

(d) $m = 4$ (e) $m = 5$ (f) $m = 6$

FIGURE 3.47: Flow around a sphere in a corrugated channel: First six normalised spatial modes of the velocity field.

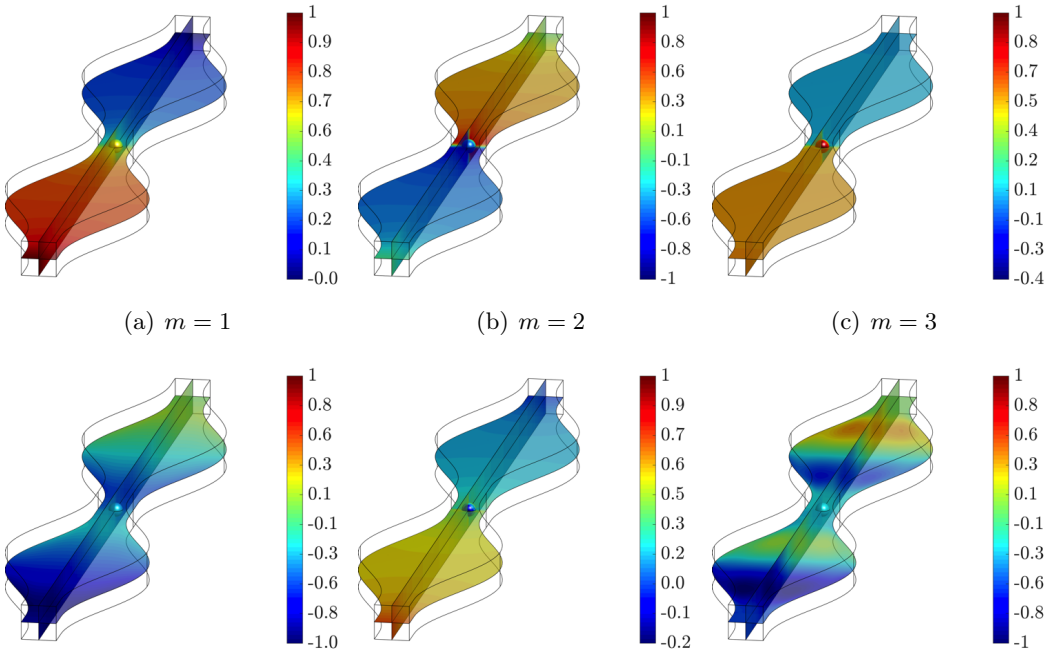

(a) $m = 1$ (b) $m = 2$ (c) $m = 3$

(d) $m = 4$ (e) $m = 5$ (f) $m = 6$

FIGURE 3.48: Flow around a sphere in a corrugated channel: First six normalised spatial modes of the pressure field.

The first four spatial modes for the velocity and pressure computed with the proposed HDG-PGD are shown in figures 3.47 and 3.48.

Figure 3.49 shows the first six normalised parametric modes computed. Compared to

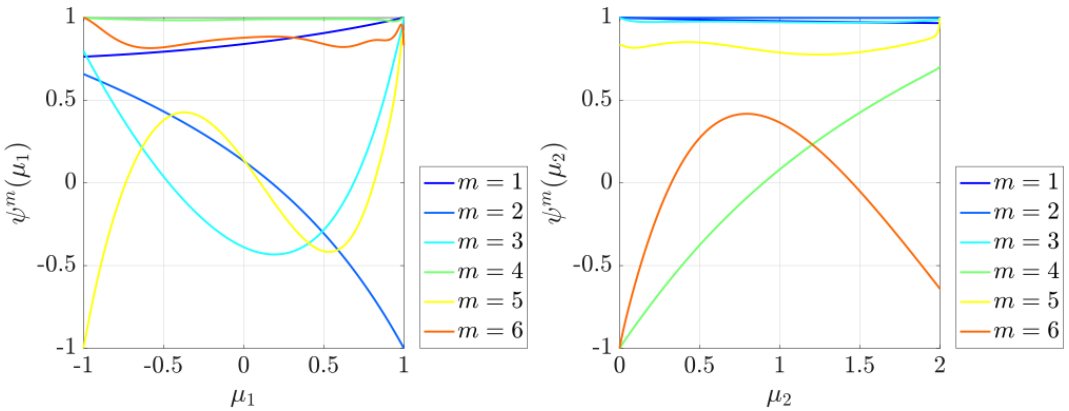

(a) (b)

FIGURE 3.49: Flow around a sphere in a corrugated channels: First six normalised parametric modes.

previous examples, the results show that more modes have an influence over the whole range of parameters, illustrating the more complex nature of this three dimensional example.

The evolution of the relative amplitude of the modes is displayed in figure 3.50. In

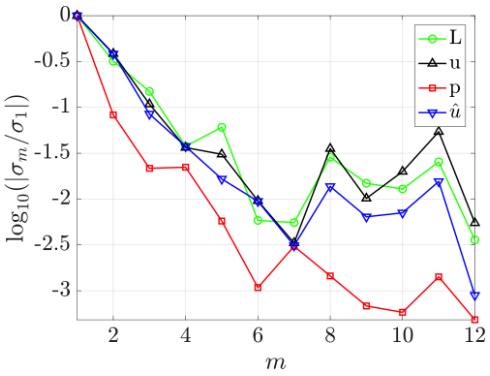

FIGURE 3.50: Flow around a sphere in a corrugated channel: Convergence of the mode amplitudes.

this example, 12 modes are required to ensure the relative amplitude of the hybrid variable, used to check convergence, is below 10^{-3}.

On-line phase Figure 3.51 shows the magnitude of the velocity and the pressure fields in the channel for three different configurations.

The results illustrate the variation in the velocity and pressure fields as the amplitude of the channel and the radius of the sphere is increased.

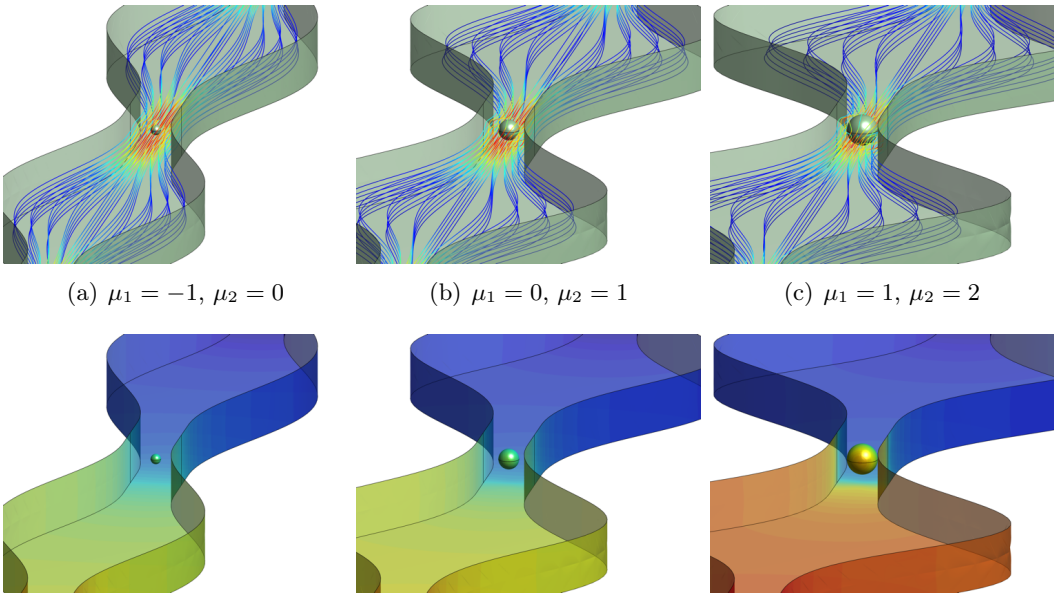

(a) $\mu_1 = -1$, $\mu_2 = 0$ (b) $\mu_1 = 0$, $\mu_2 = 1$ (c) $\mu_1 = 1$, $\mu_2 = 2$

(d) $\mu_1 = -1$, $\mu_2 = 0$ (e) $\mu_1 = 0$, $\mu_2 = 1$ (f) $\mu_1 = 1$, $\mu_2 = 2$

FIGURE 3.51: Flow around a sphere in a corrugated channel: Velocity (top) and pressure (bottom) fields for three different geometric configurations.

Once the on-line solution is obtained, in order to verify its accuracy with respect the full order solution computed on the same mesh, the relative value of the error of the velocity magnitude and pressure is computed. The results show that a relative error

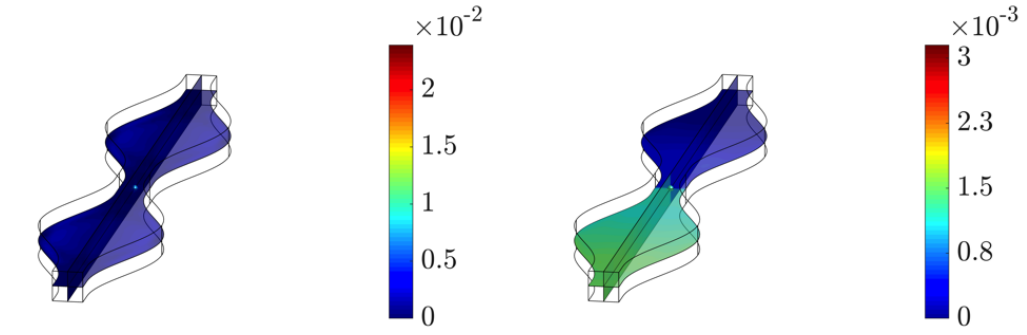

(a) $\mu_1 = -1$, $\mu_2 = 0$ (b) $\mu_1 = -1$, $\mu_2 = 0$

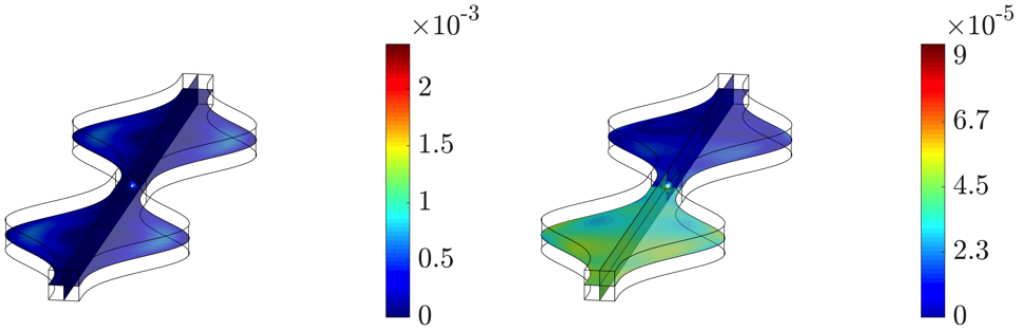

(c) $\mu_1 = 0$, $\mu_2 = 1$ (d) $\mu_1 = 0$, $\mu_2 = 1$

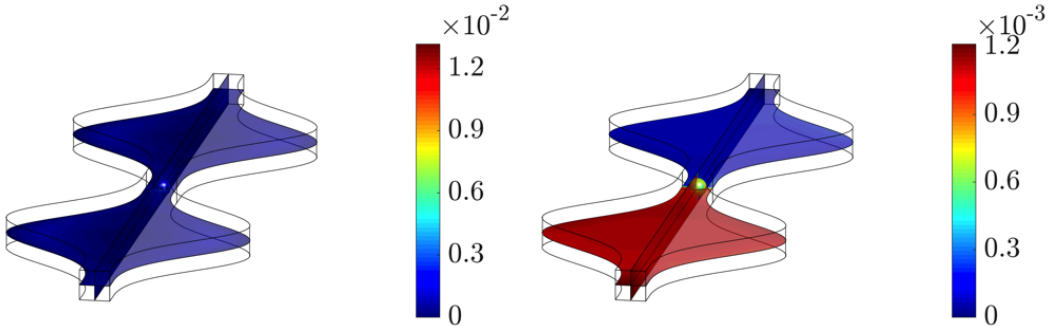

(e) $\mu_1 = 1$, $\mu_2 = 2$ (f) $\mu_1 = 1$, $\mu_2 = 2$

FIGURE 3.51: Flow around a sphere in a corrugated channel: Relative value of the error of the velocity magnitude (left) and pressure (right) fields for three different geometric configurations.

of the order of 2.5×10^{-2} or below is obtained for all three configurations for both velocity and pressure. The more accurate results are obtained for the case with μ_1=0 and μ_2=1.

To assess the accuracy of the computed generalised solution computed with the proposed approach, a reference solution is computed for the three configurations displayed in figure 3.51. The reference solutions are computed on a much finer mesh with a standard HDG solver. As a quantity of interest, the drag on the sphere is measured. Figure 3.52 shows the evolution of the error of the drag force as the number of PGD modes is increased. To further analyse the accuracy of the computed generalised

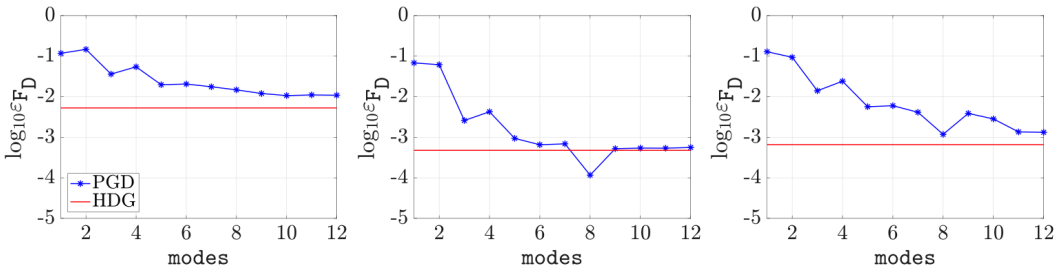

(g) $\mu_1 = -1$, $\mu_2 = 0$ (h) $\mu_1 = 0$, $\mu_2 = 1$ (i) $\mu_1 = 1$, $\mu_2 = 2$

FIGURE 3.52: Flow around a sphere in a corrugated channel: Evolution of the error on the drag force as the number of PGD modes is increased. The horizontal line denotes the reference error computed on a finer mesh with the standard HDG method.

solution, the error of an HDG solution, computed in each configuration using the same spatial resolution as the one used in the HDG-PGD formulation is considered. The results show that the error of the HDG-PGD approach tends to the error of the HDG solution computed for each configuration, showing the ability of the proposed approach to accurately capture the solution for different geometric configurations.

As mentioned in the previous example, the proposed approach provides a generalised solution that can be used to perform fast queries of different quantities of interest. To

illustrate the potential of the developed HDG-PGD approach, figure 3.53 shows the drag force on the sphere and the pressure drop, measured as the difference between the pressure at the inlet and outlet, as a function of the geometric parameters μ_1 and μ_2.

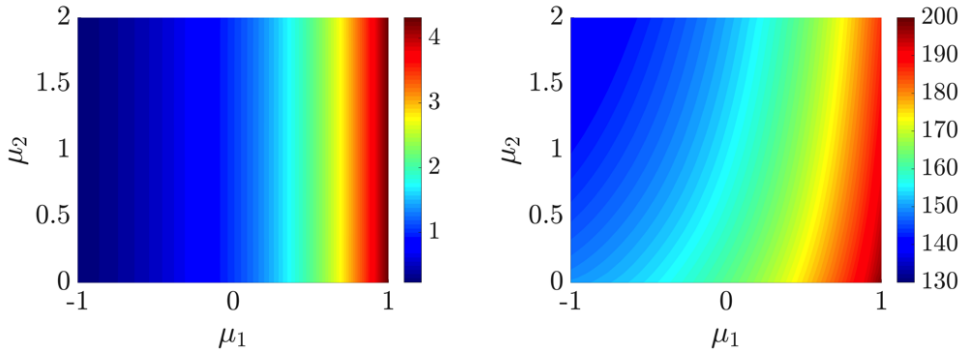

(a) Drag (b) Pressure drop

FIGURE 3.53: Flow around a sphere in a corrugated channel: Drag force on the sphere and difference between the pressure at the inlet and the outlet.

The results show that the drag force is not sensitive to the variation of the amplitude of the channel oscillation but very dependent on the radius of the sphere. In contrast, the pressure drop shows a dependency on both geometric parameters.

Chapter 4

Comparison of a priori and a posteriori PGD algorithms

In this chapter[1]the parametric problem (3.4), whose resolution needs to be efficiently computed for a large number of configurations, is solved through two PGD-based strategies. The a priori HDG-PGD technique and the a posteriori PGD described in section 1.3. That allows constructing response surfaces for the real-time evaluation of quantities of interest in terms of separated functions.

4.1 The a priori PGD algorithm

The a priori PGD algorithm introduced in section 3.3.6 of the previous chapter is here recalled.

Algorithm 2 The a priori PGD algorithm

Require: For the greedy enrichment loop, the value $\eta^\star$ of the tolerance. For the AD loop, the number of iterations $\mathtt{n_i}$.

Set $m \leftarrow 1$ and initialise the amplitude of the spatial mode $\sigma_{\hat{u}}^1 \leftarrow 1$.
while $\sigma_{\hat{u}}^m / \sigma_{\hat{u}}^1 > \eta^\star$ **do**
  Set $q \leftarrow 1$ and initialise the parametric prediction.
  Solve the HDG global and local problems to compute the spatial prediction.
  while $q < \mathtt{n_i}$ **do**
    Solve the parametric linear system to compute the parametric correction.
    Update the parametric prediction with the correction.
    Solve the HDG global and local problems to compute the spatial correction.
    Update the spatial prediction with the correction.
    Increase the counter of the AD iterations $q \leftarrow q + 1$.
  end while
  Increase the mode counter $m \leftarrow m + 1$.
end while

[1]This chapter is a modified version of the submitted article "Separated response surfaces for flows in parametrised domains: comparison of a priori and a posteriori PGD algorithms" (Giacomini, Borchini, Sevilla, and Huerta, 2020b).

Given a guess for the prediction of the parametric mode, the loop for the PGD enrichment first determines a prediction of the spatial mode by solving the HDG global and local problems (Algorithm 2 - Step 4). Then, the AD scheme computes the parametric (Algorithm 2 - Steps 6-7) and spatial (Algorithm 2 - Steps 8-9) corrections solving a parametric linear system and the HDG global and local problems, respectively. The procedure in the AD scheme is then repeated until the maximum number of iterations $\mathtt{n_i}$ is achieved. Finally, the greedy iterations stop when the ratio of the amplitude of the current mode to the one of the first mode is negligible (Algorithm 2 - Step 2). The resulting a priori PGD strategy is reported in algorithm 2.

4.2 A posteriori proper generalised decomposition

Contrary to the a priori PGD, the a posteriori framework relies on constructing a reduced basis starting from a series of snapshots. Each snapshot is defined as a vector

$$\mathbf{U}_s^T := \left[\hat{\mathbf{u}}^T,\ \boldsymbol{\rho}^T,\ \mathbf{u}^T,\ \mathbf{p}^T,\ \mathbf{L}^T\right]_s \quad , \quad s = 1, \dots, \mathtt{n_s}, \tag{4.1}$$

where $\hat{\mathbf{u}}$, $\boldsymbol{\rho}$, $\mathbf{u}$, $\mathbf{p}$ and $\mathbf{L}$ denote the vectors of nodal values of the unknowns of problem (3.4), computed using the full-order HDG spatial solver for a given set of the parameters. Hence, the size of each snapshot vector is equal to the number of degrees of freedom of the HDG global and local problems. The $\mathtt{n_s}$ snapshots are thus gathered in a multidimensional tensor structure $\mathbf{G}$. For the case of a unique parameter, this is given by a tensor of order 2, that is, a matrix

$$\mathbf{G} = \left[\mathbf{U}_1, \quad \mathbf{U}_2, \quad \dots, \quad \mathbf{U}_{\mathtt{n_s}}\right], \tag{4.2}$$

where the lines correspond to the degrees of freedom of the HDG spatial discretisation and the columns are associated with the snapshots in the parametric interval. In case more than one parameter is considered, a matrix of the form in equation (4.2) is constructed in each parametric direction. The resulting structure is thus a multidimensional tensor of order $\mathtt{n_{pa}}$+1, with one dimension for each parameter plus one dimension for the space.

The a posteriori PGD, also known as PGD separation or least-squares PGD (Díez et al., 2018, 2019; Modesto et al., 2015), computes the separated approximation of $\mathbf{G}$ in the form of product of rank-one approximations (3.32) using a greedy approach, that is, given $m-1$ modes, the m-th term in the PGD expansion is computed as

$$\left(\mathbf{f}_{\mathrm{U}}^m, \boldsymbol{\psi}_1^m, \dots, \boldsymbol{\psi}_{\mathtt{n_{pa}}}^m\right) = \arg\min \left\| \mathbf{G} - \mathbf{G}_{\mathtt{PGD}}^{m-1} - \sigma_{\mathrm{U}}^m \tilde{\mathbf{f}}_{\mathrm{U}}^m \otimes \widetilde{\boldsymbol{\psi}}_1^m \otimes \cdots \otimes \widetilde{\boldsymbol{\psi}}_{\mathtt{n_{pa}}}^m \right\|_2, \tag{4.3}$$

where each vector $\tilde{\mathbf{f}}_{\mathrm{U}}^m, \widetilde{\boldsymbol{\psi}}_1^m, \dots, \widetilde{\boldsymbol{\psi}}_{\mathtt{n_{pa}}}^m$ is sought in a subspace of $\mathbb{R}^d$ of appropriate dimension, namely the sizes of $\tilde{\mathbf{f}}_{\mathrm{U}}^m$ and $\widetilde{\boldsymbol{\psi}}_j^m$, j=$1, \dots, \mathtt{n_{pa}}$ being the number of degrees

of freedom of the HDG spatial solution $\mathbf{U}$ and of the parametric discretisations in the directions $\mathcal{I}_j,\ j{=}1,\dots,\mathtt{n_{pa}}$, respectively.

From a practical point of view, the nonlinear problem (4.3) is solved using an AD scheme. It is worth noticing that in this context, both spatial and parametric iterations are determined as rank-one approximations on a purely algebraic level and they do not require any information on the underlying multidimensional HDG discretisation. Hence, their computation relies on elementary tensorial operations, i.e. products and sums of separated objects (Díez et al., 2019), and the resulting cost is proportional to the size of the vectors of spatial and parametric modes. The resulting a posteriori PGD strategy is reported in algorithm 3. First, a set of $\mathtt{n_s}$ snapshots is constructed using the full-order HDG spatial solver (Algorithm 3 - Step 1). Then, in each PGD enrichment iteration, the parametric mode is initialised with a user-defined guess and the AD loop alternately computes the spatial (Algorithm 3 - Step 6) and parametric (Algorithm 3 - Step 7) modes solving two rank-one problems at the algebraic level. The above routine is repeated until a convergence criterion (Algorithm 3 - Step 8) is fulfilled or the maximum number of iterations $\mathtt{n_i}$ is achieved. Similarly to the a priori PGD algorithm, the greedy enrichment loop stops when the ratio of the amplitude of the current mode to the one of the first mode is negligible (Algorithm 3 - Step 3).

Algorithm 3 The a posteriori PGD algorithm

Require: For the greedy enrichment loop, the value $\eta^\star$ of the tolerance. For the AD loop, the value η_σ of the tolerance on the amplitude variation and the maximum number of iterations $\mathtt{n_i}$.

1: Compute $\mathtt{n_s}$ snapshots solving the HDG global and local problems.
2: Set $m \leftarrow 1$ and initialise the amplitude of the spatial mode $\sigma_{\hat{u}}^1 \leftarrow 1$.
3: **while** $\sigma_{\hat{u}}^m/\sigma_{\hat{u}}^1 > \eta^\star$ **do**
4: Set $q \leftarrow 1$ and initialise the parametric mode.
5: **while** $\varepsilon_\sigma > \eta_\sigma$ or $q < \mathtt{n_i}$ **do**
6: Compute the rank-one spatial mode.
7: Compute the rank-one parametric mode.
8: Update the stopping criterion $\varepsilon_\sigma = (\sigma_{\hat{u}}^{m,q} - \sigma_{\hat{u}}^{m-1})/\sigma_{\hat{u}}^{m,q}$.
9: Increase the counter of the AD iterations $q \leftarrow q + 1$.
10: **end while**
11: Increase the mode counter $m \leftarrow m + 1$.
12: **end while**

4.3 Devising separated response surfaces

Once the reduced solution is computed for all the variables using either the a priori or the a posteriori algorithms presented above, parametric response surfaces can be easily devised as a postprocess of the separated PGD solutions. More precisely, separated response surfaces are obtained as explicit functions of the parameters of interest. For the case of the drag force on an object of surface $\mathcal{B}$, the rank-m separated

approximation is given by

$$\begin{aligned} \mathtt{F}^m_{\mathtt{D}_{\mathtt{PGD}}}(\boldsymbol{\mu}) &= \int_{\mathcal{B}} \left(-p^m_{\mathtt{PGD}}(\boldsymbol{x},\boldsymbol{\mu})\mathbf{I}_{\mathtt{n_{sd}}} - (\boldsymbol{L}^m_{\mathtt{PGD}}(\boldsymbol{x},\boldsymbol{\mu}) + \boldsymbol{L}^m_{\mathtt{PGD}}(\boldsymbol{x},\boldsymbol{\mu})^T)\right)\boldsymbol{n}\ d\Gamma \\ &= \sum_{j=1}^{m} \mathtt{D}^j \psi^j(\boldsymbol{\mu}) \end{aligned} \tag{4.4}$$

where the $\mathtt{D}^j$ corresponds to the drag coefficient of the j-th spatial mode and is obtained as

$$\mathtt{D}^j := \int_{\mathcal{B}} \left(-\sigma^j_p f^j_p(\boldsymbol{x})\mathbf{I}_{\mathtt{n_{sd}}} - \sigma^j_L(\boldsymbol{F}^j_L(\boldsymbol{x}) + \boldsymbol{F}^j_L(\boldsymbol{x})^T)\right)\boldsymbol{n}\ d\Gamma. \tag{4.5}$$

It is worth noticing that the accuracy of the separated response surface of a quantity of interest directly depends upon the precision achieved by the PGD approximation of the variables utilised for its computation (e.g. pressure and gradient of velocity in the case of the drag). In this context, the HDG method used as full-order solver allows to achieve optimal convergence of order k+1 for both the pressure and the mixed variable representing the gradient of velocity (Giacomini et al., 2018; Sevilla et al., 2020a). Thus, it provides additional accuracy in the approximation of the viscous part of the drag with respect to classical primal finite element formulations, in which this is obtained as a postprocess of the computed velocity field. To construct separated approximations assessing the accuracy in a given quantity of interest, interested readers are referred to García-Blanco et al., (2017, 2018), where PGD algorithms with goal-oriented error control were investigated.

4.4 Critical comparison of a priori and a posteriori PGD algorithms

Both the a priori and a posteriori approach introduced above have attractive properties and their performance differs depending upon the problem under analysis and the parameters of interest. As it is not possible to know which of the two methodologies will perform better for a given problem, this section offers a critical comparison of the two approaches, highlighting the main advantages and disadvantages of each method. It is worth noticing that geometric parameters are one of the more challenging problems to consider in the context of parametric PDEs as the changes induced by such parameters not only have an influence on the discretised equations but also on the computational spatial domain.

The main drawback of the a posteriori PGD approach is that the user is required to select of a set of snapshots, corresponding to the simulations of the full-order problem, for a given set of values of the parameters. In order to provide a comparison of the cost of a priori and a posteriori PGD in terms of full-order solves, in this work no problem-specific sampling is considered and the snapshots are computed in

correspondence of the nodes of the parametric intervals used by the a priori algorithm. Although more advanced sampling techniques have been proposed, see chapter 1, the selected points are expected to produce accurate representations of the solution in the parametric domain inheriting the good approximation properties of the utilised Fekete nodal distributions. Despite the vast literature on sampling methods, it is not possible to initially know the number of snapshots the a posteriori ROM will require to capture the multidimensional solution accurately. In contrast, the a priori PGD approach requires no previous knowledge of the solution and no snapshots need to be selected by the user. Instead, a set of modes is automatically constructed in the enrichment process and the required number of terms is automatically determined by the greedy algorithm according to a user-defined tolerance. An important advantage of the a posteriori approach is that the snapshots can be computed in parallel as they are completely independent of each other. In contrast, the a priori approach computes the modes sequentially within the enrichment process. The computation of each mode involves several calls to the spatial solver in order to obtain the solution of the nonlinear problem by using the AD scheme.

The main drawback of the a priori PGD approach is that its standard implementation is generally intrusive with respect to the spatial solver (Sevilla et al., 2020a,b). This means that access to the code is required to devise the PGD algorithm starting from the spatial solver. Despite some recent advances towards non-intrusive implementations of the a priori PGD (Courard et al., 2016; Tsiolakis et al., 2020a; Zou et al., 2018), this aspect still represents an important challenge for the application of the methodology in an industrial context, where the use of commercial software is preferred. On the contrary, the a posteriori approach does not require access to the code sources as it simply relies on a set of snapshots, which can be obtained using any computational code.

Concerning the two types of separated approximations introduced in section 3.3.4, it is worth mentioning that equation (3.32) and (3.33) are equivalent. In the latter, the computation of each new mode is split into a prediction and a correction step. This approach is fostered for the a priori PGD as it allows to refine the stopping criterion of the AD scheme (Algorithm 2 - Step 5) by introducing an additional check to end the iteration loop when the amplitude of the correction is negligible with respect to the amplitude of the current mode, see Sevilla et al., (2020a). This test has been omitted in the present work to perform a more transparent comparison with the a posteriori PGD algorithm in which no information is provided a priori to reduce the number of computed snapshots.

The points previously discussed are general for any parametric problem, but a crucial aspect specific to geometrically parametrised problems concerns the mesh generation process. In the a priori PGD framework, a reference configuration is used, see Ammar et al., (2014), Sevilla et al., (2020a,b), and Zlotnik et al., (2015). Hence, only one mesh is required to obtain the solution for any geometric configuration of interest. In

contrast, the a posteriori PGD approach requires a different mesh for each snapshot. In addition, it is worth noticing that the different meshes need to have the same number of nodes and connectivity matrix. A common approach is thus to generate one mesh and morph it to obtain the mesh corresponding to each geometric configuration of interest. In this context, special attention need to be paid to the morphing algorithm, especially in a high-order framework, as the deformation can induce a significant decrease in the quality of the meshes.

4.5 Numerical results

This section presents a set of numerical examples to investigate the performance of a priori and a posteriori PGD approaches in the context of Stokes flows in geometrically parametrised domains. The problem of interest is the so-called PMPY microswimmer, studied in section 3.4.5. The swimmer consists of two bladders of spherical shape that can change their volume and mutual distance, with the constraint that the total volume of the two bladders is kept constant. Several test cases involving one and two geometric parameters, with different ranges of values, are investigated in the remaining parts of this section.

4.5.1 Problem setup and comparison criteria

The computational domain and the computational mesh for the PMPY microswimmer are identical to those considered in 3.4.5. The interval for the first parameter is $\mathcal{I}^1$=$[-1, 1]$. For μ_1=-1, the radius of the two spheres are R_1=0.3096 and R_2=0.116 respectively, whereas for μ_1=1 the radii of the two spheres are R_1=0.116 and R_2=0.3096, respectively. For the second parameter, two different intervals are considered in order to study the influence of the variability introduced by geometric parameters on the accuracy of both the a priori and the a posteriori PGD algorithms. The first interval is $\mathcal{I}^2$=$[-2, -1]$ and it induces a maximum and minimum distance between the bladders equal to D_{max}=5 and D_{min}=4, respectively. The second interval considered is $\mathcal{I}^2$=$[-3, 2]$ and it induces a maximum and minimum distance between the bladders equal to D_{max}=6 and D_{min}=1, respectively.

For the a priori PGD approach, 10 elements are used to discretise the parametric domain $\mathcal{I}^1$, whereas 20 and 100 elements are employed for the intervals $\mathcal{I}^2$=$[-2, -1]$ and $\mathcal{I}^2$=$[-3, 2]$, respectively. The different number of elements in each parametric interval has been selected after observing that the variation in the flow induced by the first parameter is weaker than the variation induced by the second one (Sevilla et al., 2020a,b). It is worth noticing that the set of nodes used to discretise the second parametric dimension in the first case, $\mathcal{I}^2$=$[-2, -1]$, is a subset of the nodes selected for the second case, where $\mathcal{I}^2$=$[-3, 2]$. In all the numerical tests, a degree of approximation k=4 is utilised for both the spatial and the parametric discretisations

and non-uniform Fekete nodal distributions are employed. For the a posteriori PGD algorithm, the snapshots are computed in correspondance of the position of the nodes in the parametric space utilised for the a priori approach.

To compare the accuracy of the a priori and the a posteriori PGD algorithms, two error measures are considered.

First, a multidimensional $\mathcal{L}_2(\Omega \times \boldsymbol{\mathcal{I}})$ error is defined for each variable, namely velocity, pressure and gradient of the velocity, by using a reference solution. For instance, the multidimensional $\mathcal{L}_2(\Omega \times \boldsymbol{\mathcal{I}})$ error measure for the velocity field is given by

$$E_u := \left(\frac{\int_{\boldsymbol{\mathcal{I}}} \int_{\Omega} (\boldsymbol{u}_{\text{PGD}}(\boldsymbol{x}, \boldsymbol{\mu}) - \boldsymbol{u}_{\text{REF}}(\boldsymbol{x}, \boldsymbol{\mu})) \cdot (\boldsymbol{u}_{\text{PGD}}(\boldsymbol{x}, \boldsymbol{\mu}) - \boldsymbol{u}_{\text{REF}}(\boldsymbol{x}, \boldsymbol{\mu})) d\Omega \, d\mu}{\int_{\boldsymbol{\mathcal{I}}} \int_{\Omega} \boldsymbol{u}_{\text{REF}}(\boldsymbol{x}, \boldsymbol{\mu}) \cdot \boldsymbol{u}_{\text{REF}}(\boldsymbol{x}, \boldsymbol{\mu}) \, d\Omega \, d\mu} \right)^{1/2}. \tag{4.6}$$

It is worth noticing that the evaluation of the multidimensional error in equation (4.6) requires a reference solution for each integration point of the parametric space. This is done by generating a new mesh and performing a new full-order computation for each geometric configuration described by an integration point in the parametric space. Each reference solution is computed via HDG with a higher order polynomial approximation and a finer mesh to ensure that the difference between the numerical PGD solutions and the reference solution provides an accurate description of the error of the reduction strategy. For the example with $\mathcal{I}^1$=$[-1, 1]$ and $\mathcal{I}^2$=$[-3, 2]$, a total of 25,000 reference solutions were required to compute this error measure, since five integration points in each parametric element are utilised for k=4.

Second, the separated response surface for the drag force $\mathtt{F_D}$ and its error are considered to assess the accuracy of the PGD-based strategies analysed. More precisely, the $\mathcal{L}_2(\boldsymbol{\mathcal{I}})$ error measure for the drag force in the parametric space is defined as

$$E_D = \left(\frac{\int_{\boldsymbol{\mathcal{I}}} (\mathtt{F}_{\mathtt{D}_{\text{PGD}}}(\boldsymbol{\mu}) - \mathtt{F}_{\mathtt{D}_{\text{REF}}}(\boldsymbol{\mu}))^2 \, d\mu}{\int_{\boldsymbol{\mathcal{I}}} \mathtt{F}_{\mathtt{D}_{\text{REF}}}(\boldsymbol{\mu})^2 \, d\mu} \right)^{1/2}, \tag{4.7a}$$

whereas the error in the quantity of interest $\mathtt{F_D}$ as a function of the parameters is given by

$$\varepsilon_D(\boldsymbol{\mu}) = \frac{|\mathtt{F}_{\mathtt{D}_{\text{PGD}}}(\boldsymbol{\mu}) - \mathtt{F}_{\mathtt{D}_{\text{REF}}}(\boldsymbol{\mu})|}{|\mathtt{F}_{\mathtt{D}_{\text{REF}}}(\boldsymbol{\mu})|}. \tag{4.7b}$$

4.5.2 One geometric parameter

In this section, two geometric mappings, affecting independently the radius of the spherical bladders and their distance, are considered. An extensive comparison of accuracy and computational cost of the a priori and the a posteriori PGD approaches is presented for these two cases and special attention is devoted to the PGD-based separated response surfaces for the drag force.

Varying the radius of the spherical bladders

The first example involves the simulation of the Stokes flow past the PMPY microswimmer when the domain is parametrised using μ_1 and the distance between the centres of the two spheres is fixed and equal to 3. To evaluate the influence of the number of nonlinear iterations in the AD scheme of the a priori PGD, different numbers of iterations are considered, namely $\mathtt{n_i}$=1, 2, 3, 5. In addition, to evaluate the influence of the number of snapshots used in the a posteriori PGD approach, different numbers of snapshots are employed, namely $\mathtt{n_s}$=11, 21, 41.

First, the effect of the geometric mapping on the quality of the meshes is investigated. Figure 4.1 displays the mesh quality, measured as the scaled Jacobian of the isoparametric mapping (Poya et al., 2016; Xie et al., 2013), of two deformed configurations with the radius of the bladders as geometric parameter. The mesh quality map shows

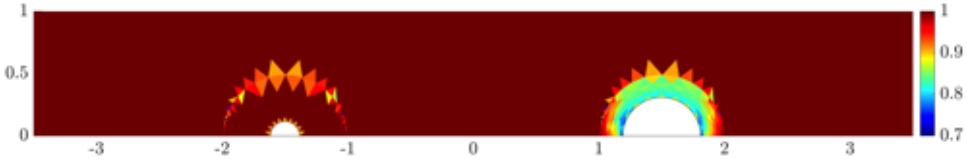

(a) $\mu_1 = -1$

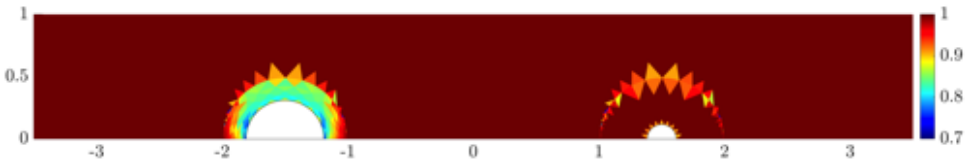

(b) $\mu_1 = 1$

FIGURE 4.1: Mesh quality of two deformed configurations for the mapping with μ_1 as a geometric parameter.

that for the sphere with minimum radius, 0.116, the quality is lower than one only in the elements with an edge on the boundary or on the interior interface used to define the piecewise geometric mapping described in Sevilla et al., (2020a). This is due to the use of the mesh generation technique described in Poya et al., (2016) and Xie et al., (2013), where only the elements in contact with curved entities are represented with high-order polynomials. In contrast, for the sphere with maximum radius, 0.3096, all the elements in the region where the mapping is different from the identity are deformed.

Figure 4.2 shows the evolution of the $\mathcal{L}_2(\Omega \times \mathcal{I}^1)$ error measure for velocity and pressure as a function of the number of modes, m, for both the a priori and the a posteriori PGD approaches. The results in figure 4.2(a) show that the a posteriori approach is able to provide highly accurate results, with an error below 10^{-3}, with only five modes and using 11 snapshots. If a higher accuracy is required, the experiments show that increasing the number of snapshots to 21 is not sufficient and this number need to be increased to 41 in order to be able to reduce the error below 10^{-4}.

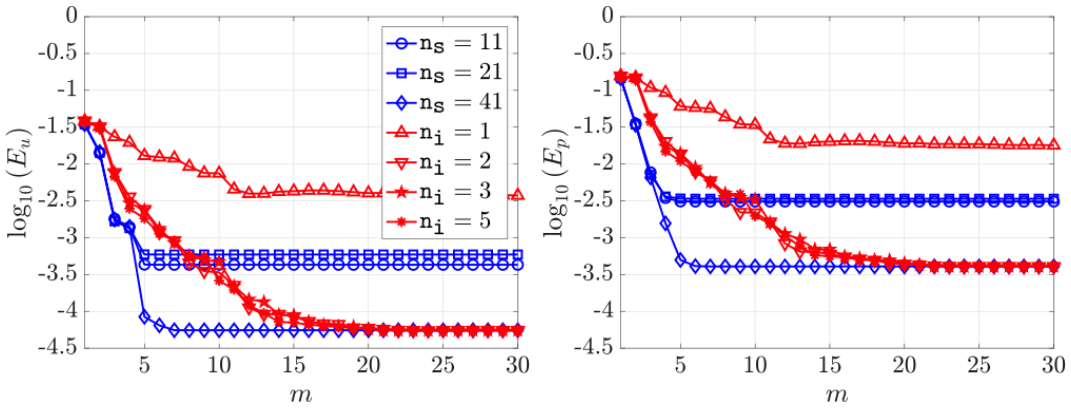

(a) $\boldsymbol{u}$ (b) p

FIGURE 4.2: Evolution of the $\mathcal{L}_2(\Omega \times \mathcal{I}^1)$ error for (a) velocity and (b) pressure as a function of the number of PGD modes for the problem with one geometric parameter controlling the radius of the spherical bladders. The legend details the number $\mathtt{n_s}$ of snapshots used by the a posteriori PGD approach (blue) and the number $\mathtt{n_i}$ of nonlinear AD iterations used by the a priori PGD approach (red).

For the a priori approach, the results show that with only one iteration in the AD scheme, the accuracy of the computed modes is limited and the error stagnates at a level almost two orders of magnitude higher than the corresponding results obtained performing two iterations. In addition, this example also shows that two iterations is the optimal value as higher values, for instance three or five iterations, provide results with almost the same accuracy but they require additional solutions of the spatial problem. With two iterations in the AD scheme, the a priori PGD approach requires up to 20 modes to reach an accuracy that is comparable to the accuracy obtained by the a posteriori approach with five modes and 41 snapshots.

To further analyse the accuracy of the two PGD approaches, the evolution of the $\mathcal{L}_2(\Omega \times \mathcal{I}^1)$ error for the gradient of velocity and the $\mathcal{L}_2(\mathcal{I}^1)$ error for the drag force on the two spherical bladders is computed as a function of the number of modes (Fig. 4.3). It can be observed that the results for the gradient of velocity are very similar, qualitatively and quantitatively, to the ones presented in figure 4.2(b) for the pressure field. This is due to the extra accuracy provided by the HDG formulation in the gradient of velocity, compared to other approaches based on primal formulations. Furthermore, this example also confirms that the accuracy that is obtained in the drag force is similar to the accuracy obtained in the pressure and in the gradient of velocity, from which it is computed. In all cases, the a posteriori PGD approach requires five modes and 41 snapshots to construct a solution with an error in the drag force below 10^{-3}, whereas the a priori approach achieves a similar level of accuracy using two iterations and 15 modes. Hence, the results show that the two PGD approaches require a similar computational cost to reach an error in the drag force below 10^{-3}. The a priori approach requires the solution of 45 spatial problems (i.e. 15 modes, each computed with two iterations of the AD scheme plus the initial solve to perform the

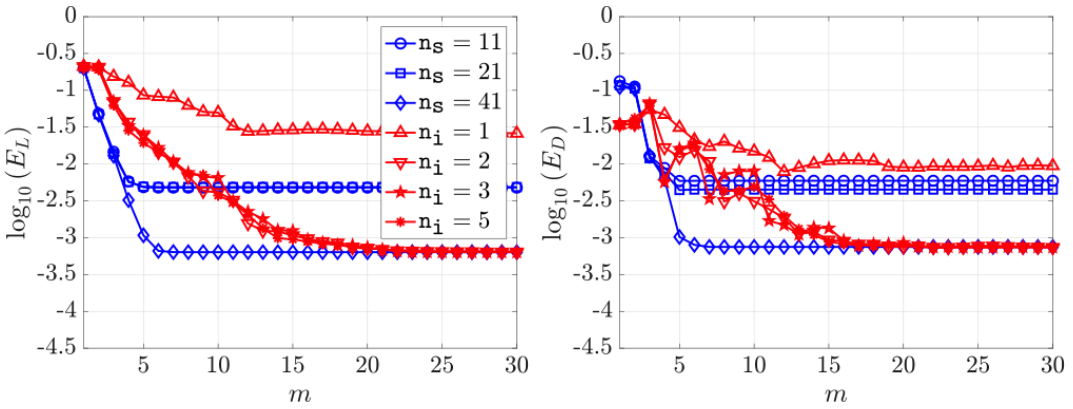

(a) $\boldsymbol{L}$ (b) $\mathtt{F_D}$

FIGURE 4.3: Evolution of (a) the $\mathcal{L}_2(\Omega \times \mathcal{I}^1)$ error for the gradient of velocity and (b) the $\mathcal{L}_2(\mathcal{I}^1)$ error for the drag force as a function of the number of PGD modes for the problem with one geometric parameter controlling the radius of the spherical bladders. The legend details the number $\mathtt{n_s}$ of snapshots used by the a posteriori PGD approach (blue) and the number $\mathtt{n_i}$ of nonlinear AD iterations used by the a priori PGD approach (red).

prediction of the mode, see algorithm 2), whereas the a posteriori approach utilises 41 snapshots to reach the same level of accuracy.

It is very important to emphasise that no compression of the modes obtained in the a priori approach, see Modesto et al., (2015), has been performed to enable the reader to clearly see the number of calls to the spatial solver required. However, the number of modes computed by the two approaches is expected to be the same when the PGD compression is performed. It is also worth noticing that both the a priori and the a posteriori algorithms stagnate at the same level of error as this is the error induced by the hypothesis of separability of the exact solution of the problem.

In a similar fashion, separated response surfaces for quantities of interest can be devised as explicit functions of the parameter. Figure 4.4 reports the response surface of the drag force as a function of the radius of the two spherical bladders, computed using the a priori PGD. As expected, the drag is maximum on the first sphere when its radius is maximum (i.e. μ_1=−1) and it decreases monotonically until reaching the configuration of minimum radius for μ_1=1. An analogous behaviour is observed for the second sphere, with the drag force spanning from its minimum value at μ_1=−1 to its maximum at μ_1=1. Moreover, the forces on the two spheres are equal for the geometric configuration of μ_1=0, that is, when the two bladders have the same volume (Fig. 4.4(a)). For the sake of completeness, figure 4.4(b) displays the total drag on the two spheres as a function of the geometric parameter μ_1. The results obtained with the a posteriori PGD are qualitatively and quantitatively similar, whence they are omitted for the sake of brevity. A detailed comparison of the accuracy of the two approaches is presented in section 4.5.2.

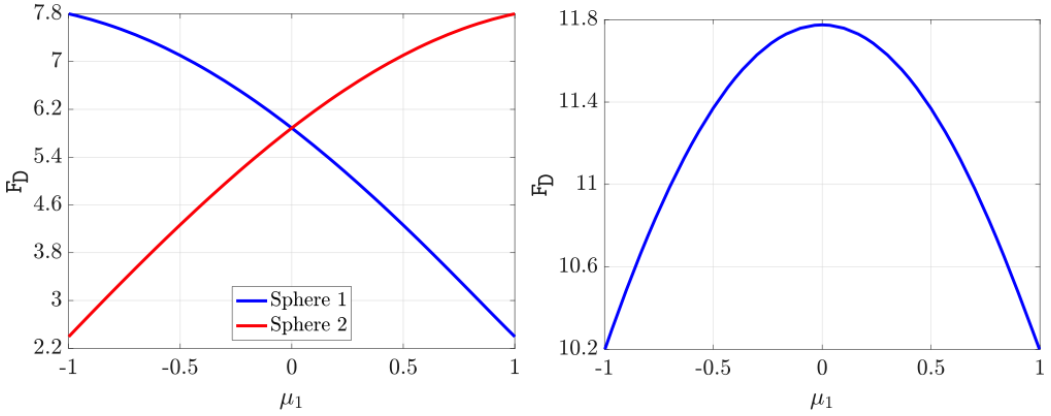

(a) Drag force on each sphere

(b) Total drag force

FIGURE 4.4: Response surfaces of the drag force as a function of the radius μ_1 of the first sphere.

Varying the distance between the spherical bladders

The second example considers a geometrically parametrised problem, where the parameter controls the distance between two equal spherical bladders with radius 0.25. It is worth recalling that the reference geometry in figure 3.36 is characterised by two equal spheres of radius R_{ref}=0.116. Hence, for the cases studied in this section, the geometric mapping accounts for both a parameter-dependent variation of the distance between the two bladders and an expansion of the spheres, independent of the parameter.

Two intervals $\mathcal{I}^2$ are considered to analyse the sensitivity of the PGD solutions to the range of variations of the parameter.

The first interval is taken as $\mathcal{I}^2$=$[-2,-1]$ and figure 4.5 reports the evolution of the $\mathcal{L}_2(\Omega \times \mathcal{I}^2)$ error for velocity, pressure and gradient of velocity and the $\mathcal{L}_2(\mathcal{I}^2)$ error for the drag force as a function of the number m of modes. The results show that with only four modes, the a posteriori PGD approach is able to produce the most accurate results for all the variables, including the drag force computed from the pressure and the gradient of velocity. It is worth noticing that in this example the accuracy of the a posteriori approach in the drag force does not improve when increasing the number of snapshots and 21 snapshots are sufficient to provide a drag force with an error below 10^{-5}. For the a priori approach, five modes computed with two AD iterations are required to obtain the maximum accuracy in all the variables. With one iteration, the error in the drag force is more than one order of magnitude higher than the one obtained with two iterations. Furthermore, a higher number of iterations does not produce any gain in accuracy despite the increased computational cost. In this case, the two PGD approaches show similar performance as the a priori algorithm provides an error in the drag force below 10^{-5} with 12 solutions of the spatial problem (i.e. four modes, each computed with two iterations of the AD scheme plus the initial

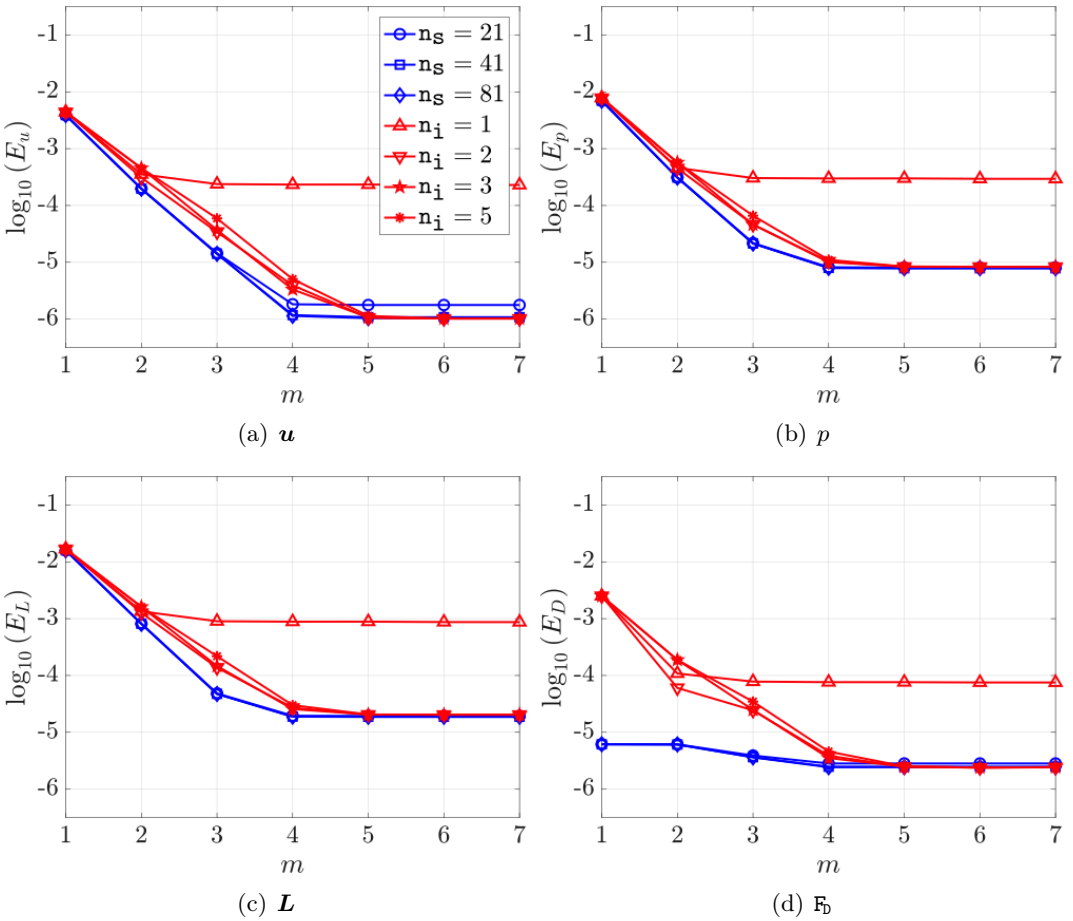

(a) $\boldsymbol{u}$ (b) p

(c) $\boldsymbol{L}$ (d) $\mathtt{F_D}$

FIGURE 4.5: Evolution of (a-c) the $\mathcal{L}_2(\Omega \times \mathcal{I}^2)$ error for velocity, pressure and gradient of velocity and (d) the $\mathcal{L}_2(\mathcal{I}^2)$ error for the drag force as a function of the number of PGD modes for the problem with one geometric parameter controlling the distance between the spherical bladders and $\mathcal{I}^2$=$[-2,-1]$. The legend details the number $\mathtt{n_s}$ of snapshots used by the a posteriori PGD approach (blue) and the number $\mathtt{n_i}$ of nonlinear AD iterations used by the a priori PGD approach (red).

solve to perform the prediction of the mode, see algorithm 2), whereas the a posteriori approach requires 21 snapshots for a similar level of accuracy.

Second, the parametric interval is extended to $\mathcal{I}^2$=$[-3,2]$. Figure 4.6 displays the mesh quality, measured as the scaled Jacobian of the isoparametric mapping, of two deformed configurations with the distance between the bladders as geometric parameter. The results report that the mesh quality is not affected by the mapping considered as the change in distance is piecewise linear and the lower mesh quality only concentrates in the vicinity of the spheres. This is due to the deformation required to transform the reference mesh with radius 0.116 into the geometric configuration under analysis, associated with the bladders of equal volume, in which the radius achieve the value 0.25.

Figure 4.7 shows the evolution of the $\mathcal{L}_2(\Omega \times \mathcal{I}^2)$ error for velocity, pressure and

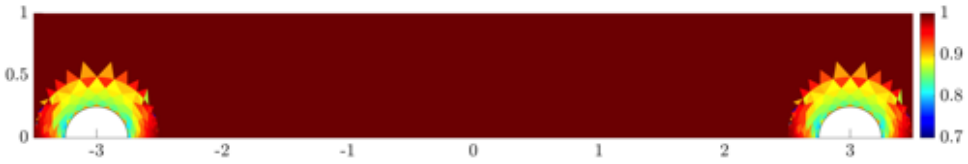

(a) $\mu_2 = -3$

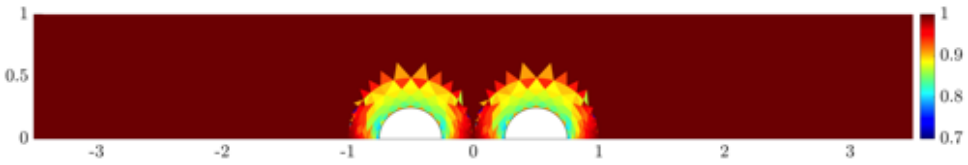

(b) $\mu_2 = 2$

FIGURE 4.6: Mesh quality of two deformed configurations for the mapping with μ_2 as a geometric parameter.

gradient of velocity and the $\mathcal{L}_2(\mathcal{I}^2)$ error for the drag force as a function of the number m of modes. It is worth empasising that a simple visual comparison of the results in figures 4.5 and 4.7 clearly illustrates the challenge that a larger interval of variation of the geometric parameter induces for both PGD approaches.

The results show that the a posteriori approach requires 10 modes in order to reach the maximum accuracy for velocity, pressure and gradient of velocity. In addition, it can be observed that the a posteriori algorithm requires eight modes and 201 snapshots to provide an error in the drag force below 10^{-5}. A higher number of snapshots does not lead to a further reduction in the error, whereas a lower number of snapshots, 101, is responsible for a slight increase in the error. Concerning the a priori PGD, the AD scheme with one iteration leads to a stagnated error that is several orders of magnitude higher than the one obtained with two or more iterations. For two iterations, the number of modes required to reach the maximum accuracy is 15 and for three or five iterations the number of modes required varies between 10 and 12. When the drag force is considered, the a priori approach shows that an accuracy below 10^{-5} can be obtained with two iterations and 14 modes, three iterations and 10 modes or five iterations and 10 modes. The most efficient alternative thus consists of computing 10 modes with three AD iterations for a total of 40 spatial solves, requiring a marginally lower cost than the computation of 14 modes with two AD iterations, that is, 42 calls to the HDG spatial solver.

Comparing the performance of the a priori and a posteriori approaches for this more challenging problem, it is clear that the a priori approach is capable of producing the same accuracy as the a posteriori approach with a significant lower computational cost. For instance, to reach an accuracy in the drag force below 10^{-5}, the a priori approach requires 40 solutions of the spatial problem whereas the same level of accuracy cannot be reached by the a posteriori approach with 101 snapshots. In this case the a posteriori approach requires 201 snapshots, which is five times more than the a

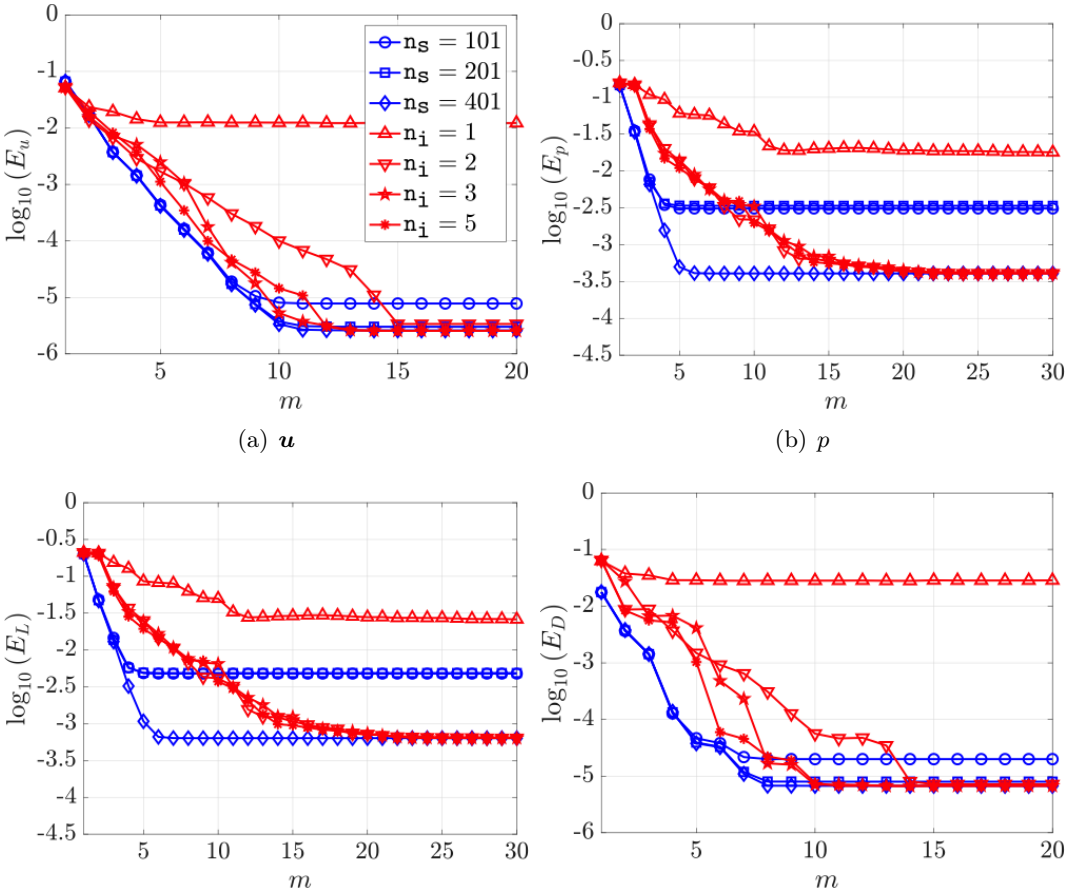

(a) $\boldsymbol{u}$ (b) p

(c) $\boldsymbol{L}$ (d) $\mathtt{F_D}$

FIGURE 4.7: Evolution of (a-c) the $\mathcal{L}_2(\Omega \times \mathcal{I}^2)$ error for velocity, pressure and gradient of velocity and (d) the $\mathcal{L}_2(\mathcal{I}^2)$ error for the drag force as a function of the number of PGD modes for the problem with one geometric parameter controlling the distance between the spherical bladders and $\mathcal{I}^2$=$[-3, 2]$. The legend details the number $\mathtt{n_s}$ of snapshots used by the a posteriori PGD approach (blue) and the number $\mathtt{n_i}$ of nonlinear AD iterations used by the a priori PGD approach (red).

priori method. Although this may seem a clear disadvantage of the a posteriori PGD, it is worth recalling that the 201 snapshots could be computed in parallel whereas the solution of the spatial problems in the a priori approach needs to be performed sequentially. In addition, different sampling methods could be considered for the a posteriori approach in order to potentially reduce the number of snapshots required, but this is out of the scope of the current work.

As in the previous example, the separated response surface of the total drag force on the two spheres is computed using the a priori PGD algorithm. It is worth noticing that the range of values of μ_2 considered in figure 4.8(a) is a subinterval of the one analysed in figure 4.8(b). The scales of the two figures confirm the higher variability of the flow quantities when larger parametric intervals are considered and the consequent additional difficulties faced by the PGD-ROM strategies to cope with the sensitivity

to the range of values considered.

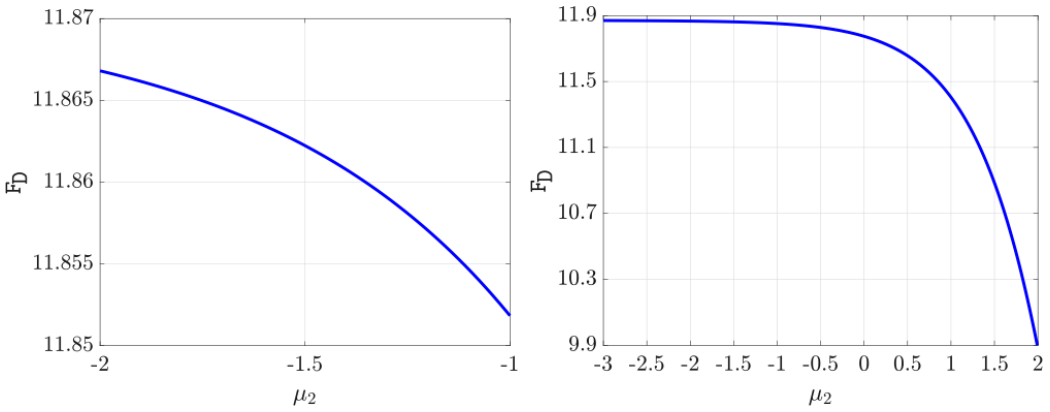

(a) $\mathcal{I}^2 = [-2, -1]$ (b) $\mathcal{I}^2 = [-3, 2]$

FIGURE 4.8: Response surfaces of the total drag force as a function of the distance μ_2 between the two spheres, for two different ranges of values of the parameter.

Accuracy of a priori and a posteriori response surfaces

The previous examples with one geometric parameter have shown that, when the error in equation (4.7a) is considered, the computational cost of the a priori PGD is as competitive as the a posteriori one and outperforms it for a larger range of the parametric interval. However, this quantity measures the average accuracy over the whole parametric domain, without considering the worst case scenarios, that is, the cases where the maximum error is observed. To further compare the two approaches, figure 4.9 displays the value of the error in equation (4.7b) in the drag force, as a function of the parameter μ_1 for the first example with one geometric parameter controlling the radius of the spherical bladders. The minima observed for both the

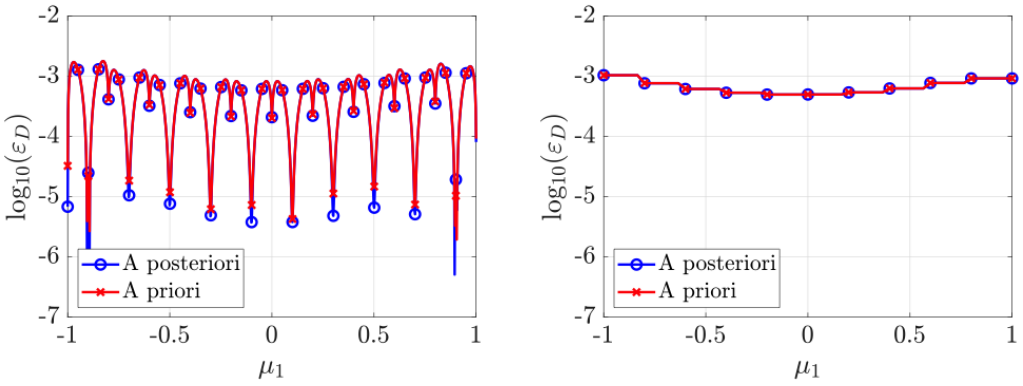

(a) Error measure (b) Smoothed error measure

FIGURE 4.9: Error in the drag, defined in equation (4.7b), as a function of the parameter μ_1.

a priori and the a posteriori approaches in figure 4.9(a) coincide with the midpoints of the elements $\mathcal{I}_e^1$, $e{=}1,\ldots,\mathtt{n_{el}^1}$ as these locations correspond to both a high-order node and an integration point for the fourth-order polynomial approximation used in each element of the parametric space. More importantly, the results show that the accuracy of the a priori and the a posteriori approaches is almost identical, not only when measured in the $\mathcal{L}_2(\mathcal{I}^1)$ norm (Fig. 4.3(b)), but also when the pointwise error in the drag force is displayed for every configuration in $\mathcal{I}^1$. To capture the qualitative behaviour of the error as a function of μ_1, a smoothing is displayed in figure 4.9(b). The results clearly show that the error is slightly higher near the boundary of the parametric interval. The smoothing is performed by considering a single value for the error in each element, obtained as the average of the error at all integration points.

Similarly, figure 4.10 compares the value of the smoothed error measure in the drag force as a function of the parameter μ_2 for the second example, with one geometric parameter controlling the distance between the spherical bladders. Both cases previ-

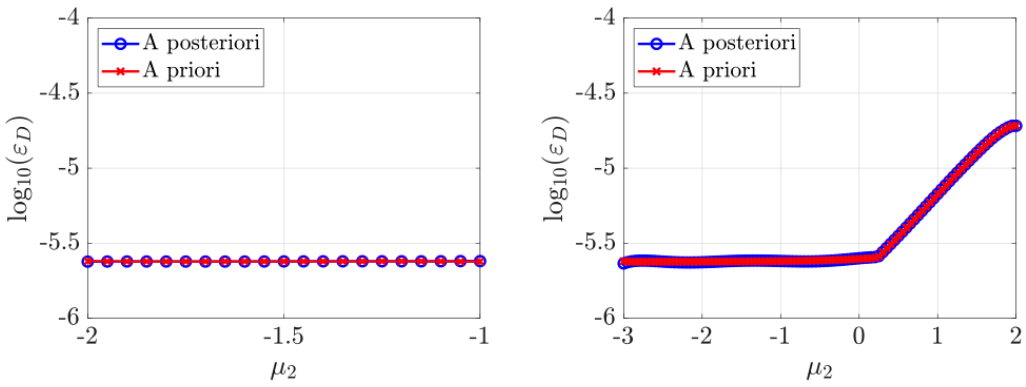

(a) $\mathcal{I}^2 = [-2, -1]$ (b) $\mathcal{I}^2 = [-3, 2]$

FIGURE 4.10: Smoothed error measure in the drag force, defined in equation (4.7b), as a function of the parameter μ_2.

ously studied, with $\mathcal{I}^2{=}[-2,-1]$ and $\mathcal{I}^2{=}[-3,2]$ are displayed, showing the increased difficulty of computing an accurate response surface as the range of values in the parametric space increases. For $\mathcal{I}^2{=}[-2,-1]$, the accuracy is almost independent of the value of the parameter, whereas for $\mathcal{I}^2{=}[-3,2]$ a more significant dependence is observed, especially near $\mu_2{=}2$, that is, when the distance between the spherical bladders is minimum. It is clear that for large values of μ_2, there is a strong influence in the flow impinging onto the second sphere caused by its proximity to the first sphere.

Finally, the comparison of the results in figures 4.9 and 4.10 clearly illustrates the rationale behind the choice of the resolution for the discretisation of the intervals $\mathcal{I}^1$ and $\mathcal{I}^2$. Given the limited variation of the solution in figure 4.9(b), only 10 elements were considered in the first parametric dimension, whereas the discretisation of the second parametric dimension contains 20 elements for the interval $\mathcal{I}^2{=}[-2,-1]$ and 100 elements for the case of $\mathcal{I}^2{=}[-3,2]$.

4.5.3 Two geometric parameters

In this section, the two geometric parameters studied separately in the previous examples are considered in a unique simulation.

First, the interval for the parameter that controls the distance is set to $\mathcal{I}^2$=$[-2,-1]$. Figure 4.11 shows the evolution of the $\mathcal{L}_2(\Omega \times \boldsymbol{\mathcal{I}})$ error for velocity, pressure and gradient of velocity and the $\mathcal{L}_2(\boldsymbol{\mathcal{I}})$ error for the drag force as a function of the number m of modes. The results reveal that the a posteriori approach provides almost identical

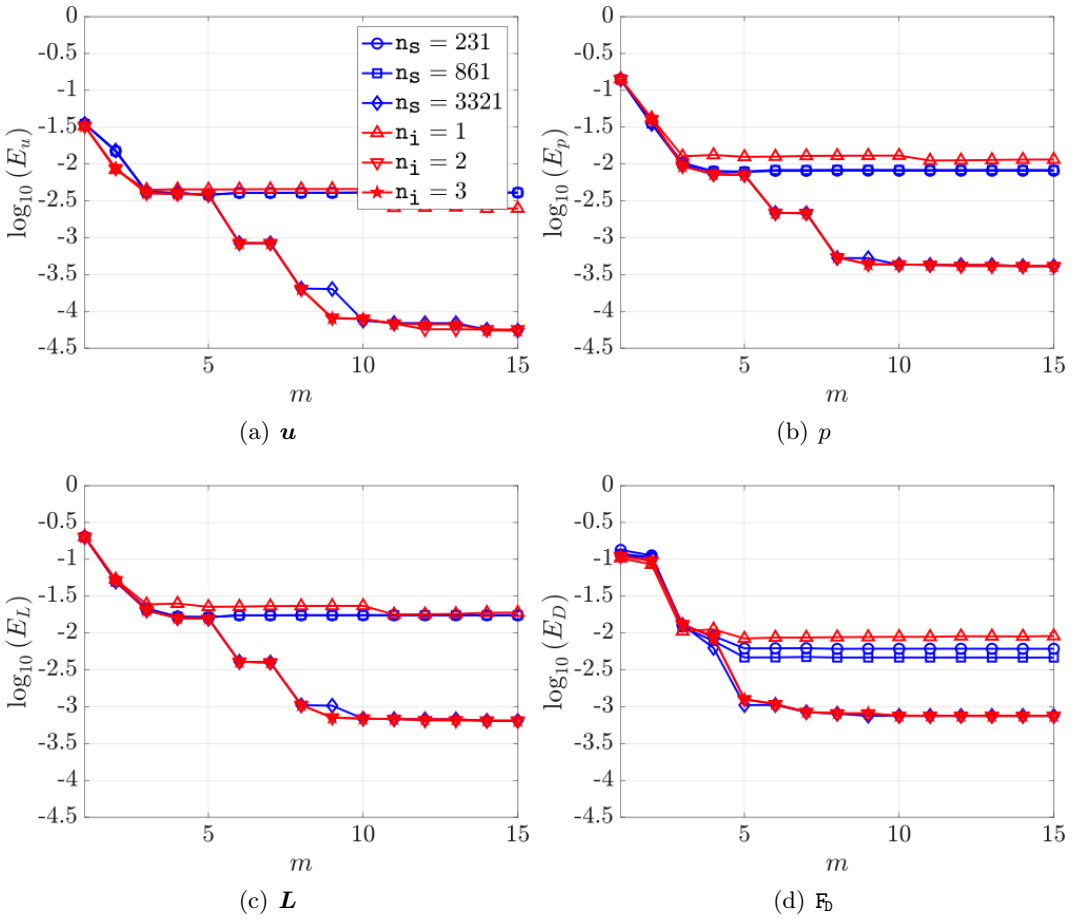

(a) $\boldsymbol{u}$ (b) p

(c) $\boldsymbol{L}$ (d) $\mathtt{F_D}$

FIGURE 4.11: Evolution of (a-c) the $\mathcal{L}_2(\Omega \times \boldsymbol{\mathcal{I}})$ error for velocity, pressure and gradient of velocity and (d) the $\mathcal{L}_2(\boldsymbol{\mathcal{I}})$ error for the drag force as a function of the number of PGD modes for the problem with two geometric parameters and $\mathcal{I}^2$=$[-2,-1]$. The legend details the number $\mathtt{n_s}$ of snapshots used by the a posteriori PGD approach (blue) and the number $\mathtt{n_i}$ of nonlinear iterations used by the a priori PGD approach (red).

accuracy using 231 and 861 snapshots. The errors in velocity and pressure are below 10^{-2} and the error in the gradient of velocity is almost 10^{-2}. In this case, four modes are sufficient to obtain the maximum accuracy in velocity, pressure and gradient of velocity, whereas an additional mode is required to achieve the most accurate results in the drag force. Using 3,321 snapshots, the a posteriori PGD computes 10 modes

and provides much more accurate results, with an error one order of magnitude lower, compared to the computation with 861 snapshots. To obtain an error in the drag force below 10^{-2}, the a posteriori approach requires four modes and 231 snapshots, whereas seven modes and 3,321 snapshots are required to achieve an error below 10^{-3}. When the a priori PGD algorithm is employed, one nonlinear iteration in the AD scheme is sufficient to obtain an accuracy almost identical to the one provided by the a posteriori approach with 231 and 861 snapshots. In addition, by considering only two nonlinear iterations, the a priori approach is capable of producing the same accuracy as the a posteriori PGD with 3,321 snapshots. In both cases, the number of modes required by the a priori and the a posteriori approaches to obtain the maximum accuracy is the same.

For this example, the a priori approach is therefore extremely competitive as, for an error in the drag force below 10^{-2}, it only requires the solution of 10 spatial problems (i.e. five modes, each computed with one iteration of the AD scheme plus the initial solve to perform the prediction of the mode, see algorithm 2), whereas the a posteriori approach needs 231 snapshots. For higher accuracy, namely for an error in the drag force below 10^{-3}, the a priori approach requires the solution of 21 spatial problems (i.e. seven modes, each computed with two iterations of the AD scheme plus the initial solve to perform the prediction of the mode, see algorithm 2), whereas 3,321 snapshots are needed by the a posteriori approach. As mentioned in section 4.2, the a posteriori approach benefits from the possibility to compute the snapshots in parallel, but this example shows that the number of calls to the spatial solver required is significantly larger than the ones performed using the a priori algorithm. In addition, the results suggest that the higher the accuracy requested by the user, the more competitive the a priori approach is. In this example, for an error in the drag force below 10^{-2}, the a priori approach requires less than 5% of the number of calls to the HDG solver performed by the a posteriori PGD algorithm, whereas for an error in the drag force below 10^{-3}, the number of spatial solutions required by the a priori approach is less than 1% of the corresponding a posteriori approximation.

The last example considers the more challenging scenario with two geometric parameters and with the interval for the distance between the bladders equal to $\mathcal{I}^2=[-3,2]$. Figure 4.12 reports the evolution of the $\mathcal{L}_2(\Omega\times\boldsymbol{\mathcal{I}})$ error for velocity, pressure and gradient of velocity and the $\mathcal{L}_2(\boldsymbol{\mathcal{I}})$ error for the drag force as a function of the number m of modes. The results are qualitatively similar to the previous example but the number of snapshots and modes required by the a posteriori and a priori PGD approaches changes significantly. The a posteriori approach with 1,111 and 4,221 snapshots provide almost identical accuracy in all the variables. In this case, 15 modes are sufficient to provide the maximum accuracy in velocity, pressure and gradient of velocity. One order of magnitude more accurate results are obtained if the number of snapshots is increased to 16,441. In terms of the drag force, with 1,111 snapshots and 10 modes the a posteriori approach is able to provide an accuray below 10^{-2}. To obtain an accuracy

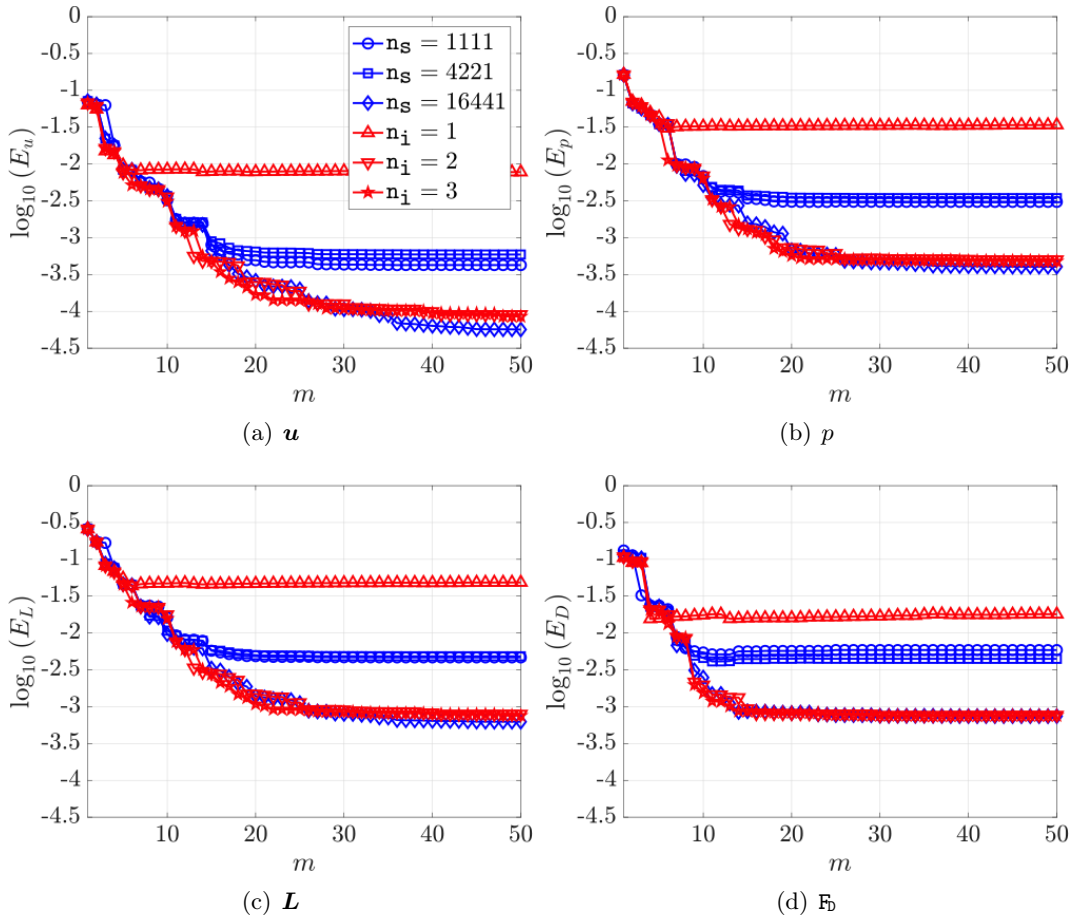

(a) $\boldsymbol{u}$ (b) p

(c) $\boldsymbol{L}$ (d) $\mathbb{F}_D$

FIGURE 4.12: Evolution of (a-c) the $\mathcal{L}_2(\Omega \times \boldsymbol{\mathcal{I}})$ error for velocity, pressure and gradient of velocity and (d) the $\mathcal{L}_2(\boldsymbol{\mathcal{I}})$ error for the drag force as a function of the number of PGD modes for the problem with two geometric parameters and $\mathcal{I}^2$=$[-3, 2]$. The legend details the number n_s of snapshots used by the a posteriori PGD approach (blue) and the number n_i of nonlinear iterations used by the a priori PGD approach (red).

below 10^{-3}, the a posteriori approach requires 16,441 snapshots and 13 modes. In this example, the a priori approach with only one nonlinear AD iteration is not able to produce results with an error in the drag force below 10^{-2}. It is worth noticing that, despite an accurate velocity field is obtained, the error in both pressure and gradient of velocity is higher than 10^{-2}. However, by performing only two nonlinear iterations in the AD scheme and computing enough modes, the error in the velocity field drops of two orders of magnitude and accurate results are obtained for both pressure and gradient of velocity, with an error below 10^{-3}.

The a priori approach with 14 modes and two nonlinear iterations provides a solution with an error in the drag force below 10^{-3}. To obtain the same accuracy, the a posteriori approach also requires 14 modes but the number of snapshots needed for this challenging problem is 16,441. This means that the a posteriori approach requires 391 times extra spatial solutions to provide the same error as the a priori approach.

The results illustrate again that the higher the accuracy required and the higher the variability in the solution introduced by the geometric parameters, the more beneficial is the use of the a priori approach.

Accuracy of a priori and a posteriori response surfaces

The separated response surfaces for the total drag force on the spheres computed using the a priori PGD are presented in figure 4.13, as a function of the parameters μ_1 and μ_2. The results confirm the increased sensitivity of the quantity of interest to

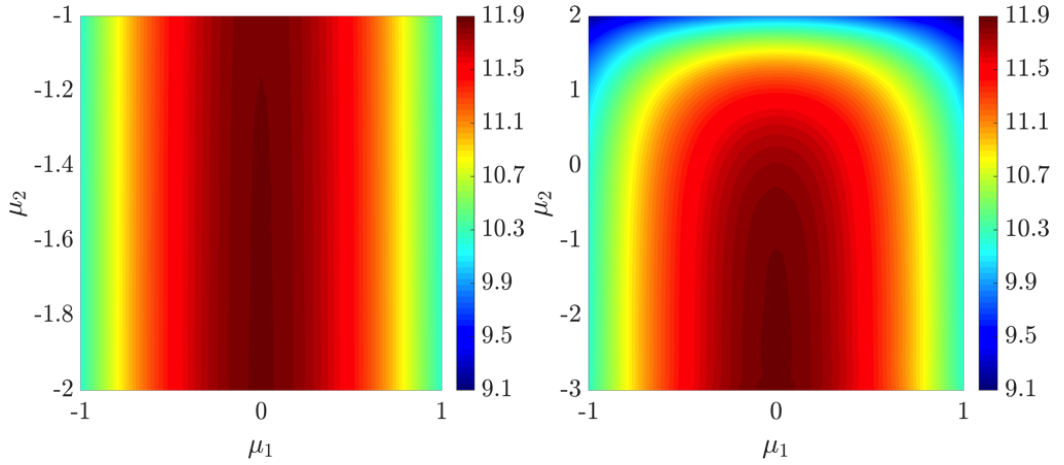

(a) $\mathcal{I}^2 = [-2, -1]$ (b) $\mathcal{I}^2 = [-3, 2]$

FIGURE 4.13: Response surfaces of the total drag force as a function of the radius μ_1 of the first sphere and the distance μ_2 between the two bladders, for two different ranges of values of the parameter μ_2.

the extended range of the parameter μ_2, as already observed in figure 4.8, with the appearence of localised variations of the drag force in the vicinity of the value μ_2=2 (Fig. 4.13(b)).

The previous two examples with two geometric parameters have shown that the a priori PGD approach is competitive when the multidimensional error measure in equation (4.7a) is considered. To further analyse the performance of both PGD approaches, figure 4.14 reports the smoothed pointwise error of the drag force as a function of the two parameters μ_1 and μ_2 for the first example in this section, when the second parameter belongs to the interval $\mathcal{I}^2$=$[-2, -1]$. The results show that both the a priori and the a posteriori approaches produce almost identical results for each value of the two geometric parameters. The behaviour is very similar to the one observed for the solution with only one parameter, as reported in figures 4.9(b) and 4.10(a). A slightly higher error is observed for the a priori PGD near the left and right boundaries of the parametric domain, corresponding to the maximum and minimum radius of the first sphere, respectively. In addition, the accuracy obtained is almost independent on the value of the second parameter. This is attributed to the fact that, with the interval

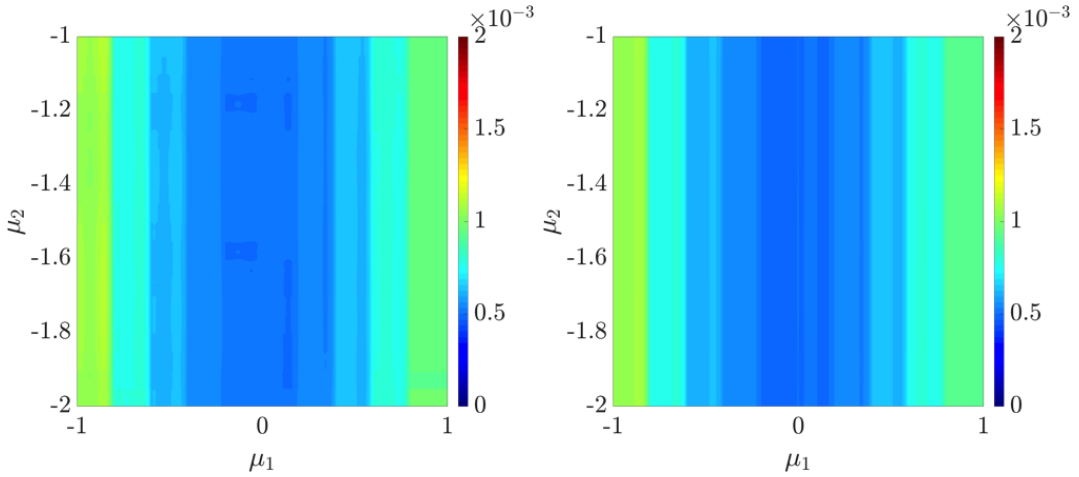

(a) ε_D, a priori PGD (b) ε_D, a posteriori PGD

FIGURE 4.14: Error map for the drag force as a function of the two parameters $\mu_1 \in [-1, 1]$ and $\mu_2 \in [-2, -1]$.

$\mathcal{I}^2$=$[-2, -1]$ considered here, the minimum distance between the spheres does not induce a significant variation of the flow impinging onto the second sphere.

The same study is repated for the case of $\mathcal{I}^2$=$[-3, 2]$. Figure 4.15 shows the smoothed error of the drag force as a function of the two parameters μ_1 and μ_2 for the second example, with $\mu_2 \in [-3, 2]$. Despite the $\mathcal{L}_2(\boldsymbol{\mathcal{I}})$ error measure is almost identical

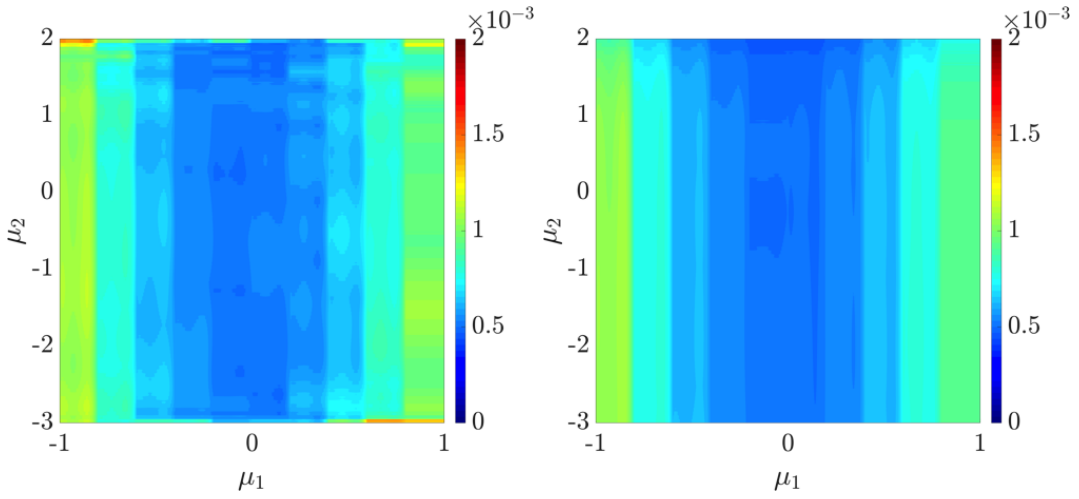

(a) ε_D, a priori PGD (b) ε_D, a posteriori PGD

FIGURE 4.15: Error map for the drag force as a function of the two parameters $\mu_1 \in [-1, 1]$ and $\mu_2 \in [-3, 2]$.

for the a priori and the a posteriori PGD approaches (Fig. 4.12(d)), the error map displays important differences between the two methods. More precisely, the error map of the a priori approach reveals higher error in the vicinity of the boundary of $\boldsymbol{\mathcal{I}}$, whereas the error of the a posteriori PGD does not show such increase near the boundary. It is worth noticing that the higher errors observed in the a priori approach

are very localised and therefore they are not observed when the $\mathcal{L}_2(\boldsymbol{\mathcal{I}})$ error measure is computed. In addition, the higher errors are not only observed for the maximum value of the parameter μ_2 but also for lower values of μ_2.

This result reveals the increased difficulty in addressing problems with more than one geometric parameter with the a priori approach. Furthermore, the study shows that the conclusions of independent studies with only one geometric parameter do not extend to problems with the same parameters considered in a single simulation.

Chapter 5

Conclusions and future developments

5.1 Summary and contributions

In the following, the more relevant contributions of this thesis are summarised.

Chapter 2 devised the HDG formulation for axisymmetric Stokes flow problems. The more challenging case, where the axis of symmetry intersects the computational domain, was considered, which to the best of the author's knowledge, had never been formulated in the context of HDG. The proposed formulation shows that in this scenario, the boundary condition imposed in the axis of symmetry is a slip condition. The formulation developed shows that this boundary condition only influences the global problem of the HDG formulation and not the element-by-element local problems. Next, under the additional hypothesis of non-rotative flow u_θ=0, the three-dimensional axisymmetric problem was reduced to a bi-dimensional problem with one extra unknown, Λ representing the fifth nonzero component of the mixed variable, corresponding to the gradient of the velocity tensor. The proposed formulation allows re-using completely a bi-dimensional HDG implementation accounting of some extra-terms arising from the hypothesis of axisymmetry. The numerical results demonstrated the optimal rates of convergence for all variables, including the new variable Λ. Finally, a comparison between axisymmetric and three-dimensional formulations for the same physical problem of the flow past a sphere was presented. The results showed the significant saving in terms of degrees of freedom that an axisymmetric strategy provides for a given accuracy in a quantity of interest analysed, e.g. the drag force.

Chapter 3 proposed the HDG-PGD methodology for geometrically parametrised Stokes flows. Considering the Stokes equation in a domain $\Omega^{\boldsymbol{\mu}}$, where the superindex $^{\boldsymbol{\mu}}$ denotes the parametric dependence of the spatial domain Ω, the multidimensional geometrically parametrised Stokes equation was stated. The HDG strong and weak forms were obtained for both local and global problems in a multidimensional framework, explicitly stating the bilinear and linear forms appearing. The adoption of an

HDG formulation enables the use of equal order of approximation for all the variables circumventing the LBB condition. That is advantageous in the context of geometrically parametrised problems in complex domains as it enables the use of standard isoparametric formulations. Finally, the use of an HDG formulation implies that no special treatment of the Dirichlet boundary conditions is required. Given the multidimensional nature of the problem, a reduced order model framework, based on the PGD, was introduced. Analogously to other ROMs for parametric PDEs (Patera et al., 2007; Rozza, 2014), HDG local and global weak forms were defined on a parameter-independent reference domain for which a single mesh was generated. That was possible introducing a proper affine dependence of the domain on the parameters $\boldsymbol{\mu}$ whose separated representation, in this case, was assumed to be given analytically. Also, the separated description of the determinant and the adjoint of the Jacobian of the mapping were obtained using the Leibniz formula and the Leverrier's algorithm, respectively. The use of a method such HDG was shown to be crucial in achieving the separability of all the terms appearing in the forms arisen from the introduction of the mapping. Each term, or mode, of the PDG approximation was computed solving a non-linear problem exploiting an alternate direction algorithm (ADA). The HDG-PGD algorithm was implemented following a predictor-corrector PGD rationale, presented in Tsiolakis et al., (2020a). The HDG local postprocess used to devise a superconvergence solution is analysed in geometrically parametrised frameworks showing the necessity of the high-order PGD projection to obtain a reduced basis for the postprocessed velocity. The applicability and potential of the proposed HDG-PGD technique is demonstrated using several numerical examples. Academic test cases with analytical solutions are used to demonstrate the optimal approximation properties of the developed HDG-PGD approach. More complex examples in two and thee dimensions involving two geometric parameters are used to show the potential of the proposed ROM. The application examples, relevant to the microfluidics community, show the flow around a microswimmer and the flow in a corrugated channel with a spherical obstacle. In both cases the ability of the proposed ROM to compute parametric solutions and response surfaces is demonstrated.

Chapter 4 presented a comparison of a priori and a posteriori PGD algorithms for the solution of geometrically parametrised Stokes flow problems. The a priori PGD is used in combination with the high-order HDG solver. For both methods, separated response surfaces of a quantity of interest in microfluidics applications are devised. Extensive numerical experiments are performed to test the sensitivity of the two PGD approaches to the range of the parametric intervals and the number of parameters considered. For problems with a unique geometric parameter inducing limited variations in the flow, accuracy and performance of the two approaches are comparable. When the range of variation of the parameters is extended, the a priori approach requires a significantly lower computational cost, measured in terms of the number of full-order HDG solves, with respect to the a posteriori PGD.

Appendix A presented the HDG-PGD method for viscosity parametrised Oseen flow. This chapter intended to apply the HDG-PGD technique to a problem whose parametric nature was concealed not in the geometry, as done for previous cases, but in some physical proprieties, e.g. material proprieties or boundary conditions. As Stokes problems scale linearly with the variation of the viscosity and boundary conditions, the Oseen equation was considered. Separability of both viscosity and convective term were discussed showing the less complexity of a problem affected by material parameters with respect geometrical ones. The reduced basis of the postprocessed velocity could be devised without the need of extra computations. Focusing on a viscosity parametrised Oseen flow, an academic example commonly used for validation purposes was proposed (Kovasznay, 1948). A range for the viscosity accounting of both convected-dominated and diffusion-dominated representations of the Kovasznay flow was studied. Results of the off-line phase and on-line phase are presented. With only a few terms of the PGD approximation, the reduced solver could reproduce almost identically the results given by a full-order solver.

5.2 Future developments

The multitude of fields where HDG method was already applied and the potentiality of PGD framework to solve parametric problems makes the HDG-PGD methodology easily extendible to several applications in various contexts. The possible developments strictly related to this work are the following.

1. **Integration of NEFEM within the HDG-PGD framework.** Following the work done by Sevilla et al., (2018b), the NURBS-enhanced finite element method (NEFEM) can combine with a hybridisable discontinuous Galerkin (HDG) framework. That allows eliminating the uncertainty induced by a polynomial approximation of curved boundaries that is common within an isoparametric approach. The parameters controlling the geometry consists of the control points characterising the NURBS curves or surfaces. Merging the two works and the one proposed in this thesis a resulting HDG-PGD methodology involving geometry integrated with computer-aided design can be developed. Besides the removal of the geometric error, this description helps in the definition of the affine mapping required for the resolution of geometrically parametrised problems, which sometimes can not be defined analytically. Moreover, this framework would also remove the necessity of conforming meshes due to the polynomial piecewise nature of the mappings.

2. **Development and implementation of HDG-PGD formulation for incompressible Navier-Stokes equations.** A second possible development follows from the application of the proposed HDG-PGD methodology to the parametrised Oseen flow shown in Appendix A. It consists of an extension

to nonlinear problems following the rationale presented in Dumon et al., 2011 and Tsiolakis et al., 2020a. This formulation would allow solving Navier-Stokes problems for parametric viscosity, thus parametric Reynolds number, considering the many phenomena characterising convected dominated flows which at low Reynolds number do not appear. The PGD framework has been for the first time applied to incompressible Navier-Stokes equations in the turbulent regime using the Spalart-Allmaras turbulence model by Tsiolakis et al., 2020b to solve parametric flow control problems. All these problems could be extended to a geometrically parametrised framework. To that purpose, it is worth to note that the implementation of the HDG-PGD algorithm for the Oseen flow with parametric viscosity already accounts of possible variations of the geometry. Consequently, the integration of the geometrically parametrised framework for Navier-Stokes problems is direct.

3. **Development and implementation of HDG-PGD formulation for compressible Navier-Stokes equations** A further development of this methodology could be the numerical resolution of the compressible Navier-Stokes equations accounting of the geometric design variables as extra parameters. Similarly to microfluidics context, the importance of fast and accurate evaluations of drag and aerodynamic noise around vehicles for aero-acoustics in today's industry is crucial because of its impact in the overall design time. The application of hybrid discretisation techniques to compressible flow problems firstly appeared in Peraire et al., (2010) and more recently in Williams, (2018) with a consequent development of shock-capturing techniques (Persson, 2013; Vila-Pérez et al., 2019). The technique developed in this thesis could be implemented in a compressible context for the simulation of aerospace flows.

Appendix A

Proper generalised decomposition for material parameters

A.1 Problem statement

This chapter is dedicated to the formulation of the HDG-PGD methodology for flow problems where the parametric dependence is not concealed in the geometry, but in some physical properties (e.g. material proprieties, boundary conditions). As Stokes' equations scale linearly with a variation of the viscosity or a variation of boundaries conditions, a more complex problem is introduced. For that purpose, a linearisation of the steady Navier–Stokes equations, known as Oseen equations, is considered.

A.1.1 The multi-dimensional parametric Oseen problem

Inspired by the work done in Giacomini et al., (2020c) to develop HDG formulation for Oseen equations, following the approach defined in Section 3.1 it is possible to write a multi-dimensional parametric Oseen problem. Let us consider a domain $\Omega \subset \mathbb{R}^{\mathtt{n_{sd}}}$, where $\mathtt{n_{sd}}$ is the number of spatial dimensions and $\boldsymbol{\mu} \in \boldsymbol{\mathcal{I}} \subset \mathbb{R}^{\mathtt{n_{pa}}}$ is a set of material parameters that controls some material proprieties of the problem (e.g. viscosity ν) or boundary conditions with $\mathtt{n_{pa}}$ being the number of parameters. For any set of parameters $\boldsymbol{\mu}$, the goal is to find the parametric velocity, $\boldsymbol{u}(\boldsymbol{x}, \boldsymbol{\mu})$, and pressure, $p(\boldsymbol{x}, \boldsymbol{\mu})$. The multi-dimensional parametric Oseen problem reads

$$
\begin{cases}
-\boldsymbol{\nabla}\cdot\left(\nu\boldsymbol{\nabla}\boldsymbol{u} - p\mathbf{I}_{\mathtt{n_{sd}}} - \boldsymbol{u}\otimes\boldsymbol{a}\right) = \boldsymbol{s} & \text{in } \Omega\times\boldsymbol{\mathcal{I}}, \\
\boldsymbol{\nabla}\cdot\boldsymbol{u} = 0 & \text{in } \Omega\times\boldsymbol{\mathcal{I}}, \\
\boldsymbol{u} = \boldsymbol{u}_D & \text{on } \Gamma_D\times\boldsymbol{\mathcal{I}}, \\
\boldsymbol{n}\cdot\left(\nu\boldsymbol{\nabla}\boldsymbol{u} - p\mathbf{I}_{\mathtt{n_{sd}}} - \boldsymbol{u}\otimes\boldsymbol{a}\right) = \boldsymbol{g}_N & \text{on } \Gamma_N\times\boldsymbol{\mathcal{I}}, \\
\boldsymbol{u}\cdot\boldsymbol{D} + \boldsymbol{n}\cdot\left(\nu\boldsymbol{\nabla}\boldsymbol{u} - p\mathbf{I}_{\mathtt{n_{sd}}} - \boldsymbol{u}\otimes\boldsymbol{a}\right)\boldsymbol{E} = \mathbf{0} & \text{on } \Gamma_S\times\boldsymbol{\mathcal{I}}.
\end{cases}
\tag{A.1}
$$

where $\boldsymbol{a}$ is a solenoidal field. Compatibility conditions and the additional constraint to avoid the indeterminacy of the pressure, required when $\Gamma_N{=}\emptyset$, are identical to those defined in (3.5) and (3.6).

A.1.2 Strong form of the local and global problems

Following section 3.2 let us consider a subdivision of the domain Ω in $\mathtt{n_{el}}$ disjoint subdomains Ω_e and the union of the interior boundaries of the subdomains which defines the mesh skeleton or internal interface Γ as in (3.8). Introducing the so-called *mixed variable* $\boldsymbol{L}{=}-\nu\boldsymbol{\nabla}\boldsymbol{u}$, the Oseen problem can be written as a first-order system of equations in the broken computational domain, namely

$$\begin{cases} \boldsymbol{L}_e+\nu\boldsymbol{\nabla}\boldsymbol{u}_e=\boldsymbol{0} & \text{in } \Omega_e\times\boldsymbol{\mathcal{I}},\\ \boldsymbol{\nabla}\cdot\big(\boldsymbol{L}_e+p_e\mathbf{I}_{\mathtt{n_{sd}}}+\boldsymbol{u}\otimes\boldsymbol{a}\big)=\boldsymbol{s} & \text{in } \Omega_e\times\boldsymbol{\mathcal{I}},\\ \boldsymbol{\nabla}\cdot\boldsymbol{u}_e=0 & \text{in } \Omega_e\times\boldsymbol{\mathcal{I}},\\ \boldsymbol{u}_e=\boldsymbol{u}_D & \text{on } (\partial\Omega_e\cap\Gamma_D)\times\boldsymbol{\mathcal{I}},\\ \boldsymbol{n}\cdot\big(\boldsymbol{L}_e+p_e\mathbf{I}_{\mathtt{n_{sd}}}\big)=-\boldsymbol{g}_N & \text{on } (\partial\Omega_e\cap\Gamma_N)\times\boldsymbol{\mathcal{I}},\\ \boldsymbol{u}_e\cdot\boldsymbol{D}-\boldsymbol{n}\cdot\big(\boldsymbol{L}_e+p_e\mathbf{I}_{\mathtt{n_{sd}}}+\boldsymbol{u}_e\otimes\boldsymbol{a}\big)\boldsymbol{E}=\boldsymbol{0} & \text{on } (\partial\Omega_e\cap\Gamma_S)\times\boldsymbol{\mathcal{I}},\\ [\![\boldsymbol{u}\otimes\boldsymbol{n}]\!]=\boldsymbol{0} & \text{on } (\partial\Omega_e\cap\Gamma)\times\boldsymbol{\mathcal{I}},\\ [\![\boldsymbol{n}\cdot\big(\boldsymbol{L}+p\mathbf{I}_{\mathtt{n_{sd}}}+\boldsymbol{u}\otimes\boldsymbol{a}\big)]\!]=\boldsymbol{0} & \text{on } (\partial\Omega_e\cap\Gamma)\times\boldsymbol{\mathcal{I}}. \end{cases} \tag{A.2}$$

for $e{=}1,\ldots,\mathtt{n_{el}}$. It is worth to notice that here normal flux is composed not only by a diffusive part as happened in (3.10) but also by a convective part.

From (A.2) following the classical HDG approach, first the so–called *local problems* are obtained

$$\begin{cases} \boldsymbol{L}_e+\nu\boldsymbol{\nabla}\boldsymbol{u}_e=\boldsymbol{0} & \text{in } \Omega_e\times\boldsymbol{\mathcal{I}}, \text{ and for } e=1,\ldots,\mathtt{n_{el}},\\ \boldsymbol{\nabla}\cdot\big(\boldsymbol{L}_e+p_e\mathbf{I}_{\mathtt{n_{sd}}}+\boldsymbol{u}_e\otimes\boldsymbol{a}\big)=\boldsymbol{s} & \text{in } \Omega_e\times\boldsymbol{\mathcal{I}}, \text{ and for } e=1,\ldots,\mathtt{n_{el}},\\ \boldsymbol{\nabla}\cdot\boldsymbol{u}_e=0 & \text{in } \Omega_e\times\boldsymbol{\mathcal{I}}, \text{ and for } e=1,\ldots,\mathtt{n_{el}},\\ \boldsymbol{u}_e=\boldsymbol{u}_D & \text{on } (\partial\Omega_e\cap\Gamma_D)\times\boldsymbol{\mathcal{I}},\\ \boldsymbol{u}_e=\hat{\boldsymbol{u}} & \text{on } (\partial\Omega_e\setminus\Gamma_D)\times\boldsymbol{\mathcal{I}},\\ \Big\langle\dfrac{1}{|\partial\Omega_e|}p_e,1\Big\rangle_{\partial\Omega_e\times\boldsymbol{\mathcal{I}}}=\rho_e, & \text{for } e=1,\ldots,\mathtt{n_{el}}, \end{cases} \tag{A.3}$$

and second, the so-called *global problem*

$$\begin{cases} [\![\boldsymbol{n}\cdot\big(\boldsymbol{L}+p\mathbf{I}_{\mathtt{n_{sd}}}+\boldsymbol{u}\otimes\boldsymbol{a}\big)]\!]=\boldsymbol{0} & \text{on } \Gamma\times\boldsymbol{\mathcal{I}},\\ \boldsymbol{n}\cdot\big(\boldsymbol{L}_e+p_e\mathbf{I}_{\mathtt{n_{sd}}}+\boldsymbol{u}_e\otimes\boldsymbol{a}\big)=-\boldsymbol{g}_N & \text{on } (\partial\Omega_e\cap\Gamma_N)\times\boldsymbol{\mathcal{I}},\\ \boldsymbol{u}_e\cdot\boldsymbol{D}-\boldsymbol{n}\cdot\big(\boldsymbol{L}_e+p_e\mathbf{I}_{\mathtt{n_{sd}}}+\boldsymbol{u}_e\otimes\boldsymbol{a}\big)\boldsymbol{E}=\boldsymbol{0} & \text{on } (\partial\Omega_e\cap\Gamma_S)\times\boldsymbol{\mathcal{I}}. \end{cases} \tag{A.4}$$

The constraint of equation (3.5), induced by the incompressibility condition, is also considered in the global problem and written in terms of the hybrid variable as

$$\langle 1, \boldsymbol{u}_D \cdot \boldsymbol{n} \rangle_{\Gamma_D \times \boldsymbol{\mathcal{I}}} + \langle 1, \hat{\boldsymbol{u}} \cdot \boldsymbol{n} \rangle_{(\partial\Omega \setminus \Gamma_D) \times \boldsymbol{\mathcal{I}}} = 0. \tag{A.5}$$

A.1.3 Weak form of the local and global problems

Proceeding analogously to section 3.2.3, the following discrete functional spaces are introduced:

$$\begin{aligned}
\mathcal{V}^h(\Omega) &:= \{v \in \mathcal{L}_2(\Omega) : v|_{\Omega_e} \in \mathcal{P}^k(\Omega_e)\ \forall \Omega_e\,,\ e = 1, \dots, \mathtt{n_{el}}\},\\
\widehat{\mathcal{V}}^h(S) &:= \{\hat{v} \in \mathcal{L}_2(S) : \hat{v}|_{\Gamma_i} \in \mathcal{P}^k(\Gamma_i)\ \forall \Gamma_i \subset S \subseteq \Gamma \cup \partial\Omega\},\\
\mathcal{L}^h(\mathcal{I}^j) &:= \{v \in \mathcal{L}_2(\mathcal{I}^j) : v|_{\mathcal{I}^j_e} \in \mathcal{P}^k(\mathcal{I}^j_e)\ \forall \mathcal{I}^j_e\,,\ e = 1, \dots, \mathtt{n}^j_{\mathtt{el}}\},\\
\boldsymbol{\mathcal{L}}^h(\boldsymbol{\mathcal{I}}) &:= \mathcal{L}^h(\mathcal{I}^1) \otimes \cdots \otimes \mathcal{L}^h(\mathcal{I}^{\mathtt{n_{pa}}}),\\
\mathcal{V}^h_{\boldsymbol{\mu}} &:= \mathcal{V}^h(\Omega) \otimes \boldsymbol{\mathcal{L}}^h(\boldsymbol{\mathcal{I}}),\\
\widehat{\mathcal{V}}^h_{\boldsymbol{\mu}} &:= \left[\widehat{\mathcal{V}}^h(\Gamma \cup \Gamma_N \cup \Gamma_S) \otimes \boldsymbol{\mathcal{L}}^h(\boldsymbol{\mathcal{I}})\right]^{\mathtt{n_{sd}}},\\
\boldsymbol{\mathcal{V}}^h_{\boldsymbol{\mu}} &:= \left[\mathcal{V}^h(\Omega) \otimes \boldsymbol{\mathcal{L}}^h(\boldsymbol{\mathcal{I}})\right]^{\mathtt{n_{sd}}},\\
\boldsymbol{\mathcal{W}}^h_{\boldsymbol{\mu}} &:= \left[\mathcal{V}^h(\Omega) \otimes \boldsymbol{\mathcal{L}}^h(\boldsymbol{\mathcal{I}})\right]^{\mathtt{n_{sd}} \times \mathtt{n_{sd}}},
\end{aligned}$$

where $\mathcal{P}^k(\Omega_e)$, $\mathcal{P}^k(\Gamma_i)$ and $\mathcal{P}^k(\mathcal{I}^j_e)$ stand for the spaces of polynomial functions of complete degree at most k in Ω_e, on Γ_i and in $\mathcal{I}^j_e$ respectively.

The weak form of the local problems, for $e = 1, \dots, \mathtt{n_{el}}$, reads: given $\boldsymbol{u}_D$ on Γ_D and $\hat{\boldsymbol{u}}^h$ on $\Gamma \cup \Gamma_N \cup \Gamma_S$, find $(\boldsymbol{L}^h_e, \boldsymbol{u}^h_e, p^h_e) \in \boldsymbol{\mathcal{W}}^h_{\boldsymbol{\mu}} \times \boldsymbol{\mathcal{V}}^h_{\boldsymbol{\mu}} \times \mathcal{V}^h_{\boldsymbol{\mu}}$ that satisfy

$$\begin{aligned}
A_{LL}(\boldsymbol{W}, \boldsymbol{L}^h_e) + A_{Lu}(\boldsymbol{W}, \boldsymbol{u}^h_e) &= L_L(\boldsymbol{W}) + A_{L\hat{u}}(\boldsymbol{W}, \hat{\boldsymbol{u}}^h),\\
A_{uL}(\boldsymbol{v}, \boldsymbol{L}^h_e) + A_{uu}(\boldsymbol{v}, \boldsymbol{u}^h_e) + A_{up}(\boldsymbol{v}, p^h_e) &= L_u(\boldsymbol{v}) + A_{u\hat{u}}(\boldsymbol{v}, \hat{\boldsymbol{u}}^h),\\
A_{pu}(v, \boldsymbol{u}^h_e) &= L_p(v) + A_{p\hat{u}}(v, \hat{\boldsymbol{u}}^h),\\
A_{\rho p}(1, p^h_e) &= A_{\rho\rho}(1, \rho^h_e),
\end{aligned} \tag{A.6}$$

for all $(\boldsymbol{W}, \boldsymbol{v}, v) \in \boldsymbol{\mathcal{W}}_{\boldsymbol{\mu}}^h \times \boldsymbol{\mathcal{V}}_{\boldsymbol{\mu}}^h \times \mathcal{V}_{\boldsymbol{\mu}}^h$, where the multi-dimensional bilinear and linear forms of the local problem are given by

$$\begin{aligned}
A_{LL}(\boldsymbol{W}, \boldsymbol{L}) &:= -\big(\boldsymbol{W}, \nu^{-1}\boldsymbol{L}\big)_{\Omega_e \times \boldsymbol{\mathcal{I}}}, \\
A_{Lu}(\boldsymbol{W}, \boldsymbol{u}) &:= \big(\boldsymbol{\nabla}\cdot \boldsymbol{W}, \boldsymbol{u}\big)_{\Omega_e \times \boldsymbol{\mathcal{I}}}, \\
A_{L\hat{u}}(\boldsymbol{W}, \hat{\boldsymbol{u}}) &:= \langle \boldsymbol{n}\cdot \boldsymbol{W}, \hat{\boldsymbol{u}}\rangle_{(\partial\Omega_e \setminus \Gamma_D)\times \boldsymbol{\mathcal{I}}}, \\
A_{uL}(\boldsymbol{v}, \boldsymbol{L}) &:= \big(\boldsymbol{v}, \boldsymbol{\nabla}\cdot \boldsymbol{L}\big)_{\Omega_e \times \boldsymbol{\mathcal{I}}}, \\
A_{uu}(\boldsymbol{v}, \boldsymbol{u}) &:= \langle \boldsymbol{v}, \boldsymbol{\tau}\boldsymbol{u}\rangle_{\partial\Omega_e \times \boldsymbol{\mathcal{I}}} - \big(\boldsymbol{\nabla}\boldsymbol{v}, \boldsymbol{u}\otimes \boldsymbol{a}\big)_{\Omega_e \times \boldsymbol{\mathcal{I}}}, \\
A_{up}(\boldsymbol{v}, p) &:= \big(\boldsymbol{v}, \boldsymbol{\nabla} p\big)_{\Omega_e \times \boldsymbol{\mathcal{I}}}, \\
A_{u\hat{u}}(\boldsymbol{v}, \hat{\boldsymbol{u}}) &:= \langle \boldsymbol{v}, (\boldsymbol{\tau} - (\boldsymbol{a}\cdot \boldsymbol{n})\,\mathbf{I}_{\mathtt{n_{sd}}})\hat{\boldsymbol{u}}\rangle_{(\partial\Omega_e \setminus \Gamma_D)\times \boldsymbol{\mathcal{I}}}, \\
A_{pu}(v, \boldsymbol{u}) &:= \big(\boldsymbol{\nabla} v, \boldsymbol{u}\big)_{\Omega_e \times \boldsymbol{\mathcal{I}}}, \\
A_{p\hat{u}}(v, \hat{\boldsymbol{u}}) &:= \langle v, \hat{\boldsymbol{u}}\cdot \boldsymbol{n}\rangle_{(\partial\Omega_e \setminus \Gamma_D)\times \boldsymbol{\mathcal{I}}}, \\
A_{\rho p}(w, p) &:= \langle w, |\partial\Omega_e|^{-1} p\rangle_{\partial\Omega_e \times \boldsymbol{\mathcal{I}}}, \\
A_{\rho\rho}(w, \rho) &:= \big(w, \rho\big)_{\boldsymbol{\mathcal{I}}},
\end{aligned} \tag{A.7}$$

and

$$\begin{aligned}
L_L(\boldsymbol{W}) &:= \langle \boldsymbol{n}\cdot \boldsymbol{W}, \boldsymbol{u}_D\rangle_{(\partial\Omega_e \cap \Gamma_D)\times \boldsymbol{\mathcal{I}}}, \\
L_u(\boldsymbol{v}) &:= \big(\boldsymbol{v}, \boldsymbol{s}\big)_{\Omega_e \times \boldsymbol{\mathcal{I}}} + \langle \boldsymbol{v}, (\boldsymbol{\tau} - (\boldsymbol{a}\cdot \boldsymbol{n})\,\mathbf{I}_{\mathtt{n_{sd}}})\boldsymbol{u}_D\rangle_{(\partial\Omega_e \cap \Gamma_D)\times \boldsymbol{\mathcal{I}}}, \\
L_p(v) &:= \langle v, \boldsymbol{u}_D\cdot \boldsymbol{n}\rangle_{(\partial\Omega_e \cap \Gamma_D)\times \boldsymbol{\mathcal{I}}},
\end{aligned} \tag{A.8}$$

respectively. Similarly, the weak form of the global problem is: find $\hat{\boldsymbol{u}}^h \in \widehat{\boldsymbol{\mathcal{V}}}_{\boldsymbol{\mu}}^h$ and $\rho^h \in \mathbb{R}^{\mathtt{n_{el}}} \otimes \boldsymbol{\mathcal{L}}^h(\boldsymbol{\mathcal{I}})$ that satisfies

$$\begin{aligned}
\sum_{e=1}^{\mathtt{n_{el}}} \{\, A_{\hat{u}L}(\hat{\boldsymbol{v}}, \boldsymbol{L}_e^h) + A_{\hat{u}u}(\hat{\boldsymbol{v}}, \boldsymbol{u}_e^h) + A_{\hat{u}p}(\hat{\boldsymbol{v}}, p_e^h) + A_{\hat{u}\hat{u}}(\hat{\boldsymbol{v}}, \hat{\boldsymbol{u}}^h) \,\} &= \sum_{e=1}^{\mathtt{n_{el}}} \{L_{\hat{u}}(\hat{\boldsymbol{v}})\}\,, \\
A_{p\hat{u}}(1, \hat{\boldsymbol{u}}^h) &= -L_p(1),
\end{aligned} \tag{A.9}$$

for all $\hat{\boldsymbol{v}} \in \widehat{\boldsymbol{\mathcal{V}}}_{\boldsymbol{\mu}}^h$, where the multi-dimensional bilinear and linear forms of the global problem are given by

$$\begin{aligned}
A_{\hat{u}L}(\hat{\boldsymbol{v}}, \boldsymbol{L}) :=& \langle \hat{\boldsymbol{v}}, \boldsymbol{n}\cdot \boldsymbol{L}\rangle_{(\partial\Omega_e \setminus (\Gamma_D \cup \Gamma_S))\times \boldsymbol{\mathcal{I}}} - \langle \hat{\boldsymbol{v}}, \boldsymbol{n}\cdot \boldsymbol{L}\boldsymbol{E}\rangle_{(\partial\Omega_e \cap \Gamma_S)\times \boldsymbol{\mathcal{I}}} \\
A_{\hat{u}u}(\hat{\boldsymbol{v}}, \boldsymbol{u}) :=& \langle \hat{\boldsymbol{v}}, \boldsymbol{\tau}\boldsymbol{u}\rangle_{(\partial\Omega_e \setminus (\Gamma_D \cup \Gamma_S))\times \boldsymbol{\mathcal{I}}} - \langle \hat{\boldsymbol{v}}, (\boldsymbol{\tau}\boldsymbol{u})\cdot \boldsymbol{E}\rangle_{(\partial\Omega_e \cap \Gamma_S)\times \boldsymbol{\mathcal{I}}} \\
A_{\hat{u}p}(\hat{\boldsymbol{v}}, p) :=& \langle \hat{\boldsymbol{v}}, p\boldsymbol{n}\rangle_{(\partial\Omega_e \setminus (\Gamma_D \cup \Gamma_S))\times \boldsymbol{\mathcal{I}}} \\
A_{\hat{u}\hat{u}}(\hat{\boldsymbol{v}}, \hat{\boldsymbol{u}}) :=& - \langle \hat{\boldsymbol{v}}, (\boldsymbol{\tau} - (\boldsymbol{a}\cdot \boldsymbol{n})\,\mathbf{I}_{\mathtt{n_{sd}}})\hat{\boldsymbol{u}}\rangle_{(\partial\Omega_e \setminus (\Gamma_D \cup \Gamma_S))\times \boldsymbol{\mathcal{I}}} \\
&+ \langle \hat{\boldsymbol{v}}, \hat{\boldsymbol{u}}\cdot \boldsymbol{D} + ((\boldsymbol{\tau} - (\boldsymbol{a}\cdot \boldsymbol{n})\,\mathbf{I}_{\mathtt{n_{sd}}})\hat{\boldsymbol{u}})\cdot \boldsymbol{E}\rangle_{(\partial\Omega_e \cap \Gamma_S)\times \boldsymbol{\mathcal{I}}}
\end{aligned} \tag{A.10}$$

and

$$L_{\hat{u}}(\hat{\boldsymbol{v}}) := -\langle \hat{\boldsymbol{v}}, \boldsymbol{g}_N\rangle_{(\partial\Omega_e \cap \Gamma_N)\times \boldsymbol{\mathcal{I}}}, \tag{A.11}$$

respectively.

Remark 11. *Compared to the stabilisation tensor $\boldsymbol{\tau}$ defined in equations* (3.16) *and* (3.19) *for the purely diffusive case (i.e. Stokes), in this case, stabilization of the convective term has also to be considered. It has been proved (Cesmelioglu et al., 2013) that a non-optimal choice of these parameters can bring to a gradual loss of optimal convergence as the Reynold number increases (e.g. convection dominated problems). For a more detailed analysis on the choice of the stabilization, parameters see Giacomini et al., (2020c).*

A.2 The proper generalised decomposition

A.2.1 Separated representation

As detailed in section 3.3, to apply a proper generalised decomposition framework to a problem of dimension $\mathtt{n_{sd}}+\mathtt{n_{pa}}$ it is required that the bilinear and linear forms in the weak form can be expressed, or well approximated, by a sum of products of parametric functions and operators that are parameter-independent.

Similarly to section 3.3.3, data is assumed to be given in separated form. For Oseen equations beside boundary conditions and the source term which also appear for Stokes's in (3.31) two additional terms are needed

$$\begin{aligned} \nu^{-1} &= \sum_{k=1}^{\mathtt{n}_\nu} N^k(\boldsymbol{x})\mathcal{N}^k(\boldsymbol{\mu}), \\ \boldsymbol{a} &= \sum_{k=1}^{\mathtt{nc}} \boldsymbol{C}^k(\boldsymbol{x})\mathcal{C}^k(\boldsymbol{\mu}). \end{aligned} \tag{A.12}$$

Remark 12. *It is worth to observe that as a consequence of the definition of the mixed variable, the required term to be written in a separable form is the inverse of the viscosity and not the viscosity itself. In a general framework when a function is separable, its inverse is not. This signifies the necessity of some extra computations (e.g. higher order PGD projection, see Díez et al., 2018) to obtain the required separable approximation. Anyway in the particular case of an Oseen problem with parametrised viscosity, follows $\mathtt{n}_\nu$=1, $N^1(\boldsymbol{x})$=1 and $\mathcal{N}^1(\boldsymbol{\mu})$=$\nu$ thus the separable approximation of ν^{-1} is immediate and exact.*

Following section 3.3.4 each variable of the HDG formulation, is written as a rank-m separable approximation such as (3.32) and (3.33) under the assumption of *single-parameter* approach (Remark 7). Moreover a proper tangent manifold is also considered for each variable.

A.2.2 Alternating direction scheme

With the separated structure of the PGD approximations, using the same strategy proposed in section 3.3.5 it is possible to solve the high-dimensional problem with an affordable cost.

The spatial iteration

Introducing the expression of the PGD approximations and the weighting functions in the weak form of the HDG local problems, the following weak form of the local problem for the spatial iteration is obtained: find $(\sigma_L^m \Delta \boldsymbol{F}_L, \sigma_u^m \Delta \boldsymbol{f}_u, \sigma_p^m \Delta f_p) \in \boldsymbol{\mathcal{W}}^h \times \boldsymbol{\mathcal{V}}^h \times \mathcal{V}^h$ for all $(\delta \boldsymbol{F}_L, \delta \boldsymbol{f}_u, \delta f_p) \in \boldsymbol{\mathcal{W}}^h \times \boldsymbol{\mathcal{V}}^h \times \mathcal{V}^h$ that satisfy

$$
\begin{aligned}
\sum_{k=1}^{\mathtt{n}_\nu} \beta_\nu^k \mathcal{A}_{LL}^k(\delta \boldsymbol{F}_L, \sigma_L^m \Delta \boldsymbol{F}_L) + \beta \mathcal{A}_{Lu}(\delta \boldsymbol{F}_L, \sigma_u^m \Delta \boldsymbol{f}_u) & \\
= \mathcal{R}_L^m(\delta \boldsymbol{F}_L \psi^m) + \beta \mathcal{A}_{L\hat{u}}(\delta \boldsymbol{F}_L, \sigma_{\hat{u}}^m \Delta \boldsymbol{f}_{\hat{u}}), & \\
\beta \mathcal{A}_{uL}(\delta \boldsymbol{f}_u, \sigma_L^m \Delta \boldsymbol{F}_L) + \sum_{k=1}^{\mathtt{n}_C} \beta_C^k \mathcal{A}_{uu}^k(\delta \boldsymbol{f}_u, \sigma_u^m \Delta \boldsymbol{f}_u) + \beta \mathcal{A}_{uu}(\delta \boldsymbol{f}_u, \sigma_u^m \Delta \boldsymbol{f}_u) & \\
+ \beta \mathcal{A}_{up}(\delta \boldsymbol{f}_u, \sigma_p^m \Delta f_p) = \mathcal{R}_u^m(\delta \boldsymbol{f}_u \psi^m) + \sum_{k=1}^{\mathtt{n}_C} \beta_C^k \mathcal{A}_{u\hat{u}}^k(\delta \boldsymbol{f}_u, \sigma_{\hat{u}}^m \Delta \boldsymbol{f}_{\hat{u}}) & \\
+ \beta \mathcal{A}_{u\hat{u}}(\delta \boldsymbol{f}_u, \sigma_{\hat{u}}^m \Delta \boldsymbol{f}_{\hat{u}}), & \\
\beta \mathcal{A}_{pu}(\delta f_p, \sigma_u^m \Delta \boldsymbol{f}_u) = \mathcal{R}_p^m(\delta f_p \psi^m) + \beta \mathcal{A}_{p\hat{u}}(\delta f_p, \sigma_{\hat{u}}^m \Delta \boldsymbol{f}_{\hat{u}}) & \\
\beta \mathcal{A}_{\rho p}(1, \sigma_p^m \Delta f_p) = \mathcal{R}_{\overline{p}}^m(\psi^m) + \beta \mathcal{A}_{\rho\rho}(1, \sigma_\rho^m \Delta f_\rho). &
\end{aligned}
\tag{A.13}
$$

The bilinear and linear forms of the local problem are detailed in equation (A.14)

$$
\begin{aligned}
\mathcal{A}_{LL}^k(\delta \boldsymbol{F}_L, \boldsymbol{F}_L) &:= -\big(\delta \boldsymbol{F}_L, N^k \boldsymbol{F}_L\big)_{\Omega_e}, \\
\mathcal{A}_{Lu}(\delta \boldsymbol{F}_L, \boldsymbol{f}_u) &:= \big(\boldsymbol{\nabla}\cdot \delta \boldsymbol{F}_L, \boldsymbol{f}_u\big)_{\Omega_e}, \\
\mathcal{A}_{L\hat{u}}(\delta \boldsymbol{F}_L, \boldsymbol{f}_{\hat{u}}) &:= \langle \boldsymbol{n} \cdot \delta \boldsymbol{F}_L, \boldsymbol{f}_{\hat{u}} \rangle_{\partial\Omega_e \setminus \Gamma_D}, \\
\mathcal{A}_{uL}(\delta \boldsymbol{f}_u, \boldsymbol{F}_L) &:= \big(\delta \boldsymbol{f}_u, \boldsymbol{\nabla}\cdot \boldsymbol{F}_L\big)_{\Omega_e}, \\
\mathcal{A}_{uu}(\delta \boldsymbol{f}_u, \boldsymbol{f}_u) &:= \langle \delta \boldsymbol{f}_u, \boldsymbol{\tau} \boldsymbol{f}_u \rangle_{\partial\Omega_e}, \\
\mathcal{A}_{uu}^k(\delta \boldsymbol{f}_u, \boldsymbol{f}_u) &:= -\big(\boldsymbol{\nabla} \delta \boldsymbol{f}_u, \boldsymbol{f}_u \otimes \boldsymbol{C}^k\big)_{\Omega_e}, \\
\mathcal{A}_{up}(\delta \boldsymbol{f}_u, f_p) &:= \big(\delta \boldsymbol{f}_u, \boldsymbol{\nabla} f_p\big)_{\Omega_e}, \\
\mathcal{A}_{u\hat{u}}(\delta \boldsymbol{f}_u, \boldsymbol{f}_{\hat{u}}) &:= \langle \delta \boldsymbol{f}_u, \boldsymbol{\tau} \boldsymbol{f}_{\hat{u}} \rangle_{\partial\Omega_e \setminus \Gamma_D} \\
\mathcal{A}_{u\hat{u}}^k(\delta \boldsymbol{f}_u, \boldsymbol{f}_{\hat{u}}) &:= -\langle \delta \boldsymbol{f}_u, (\boldsymbol{C}^k \cdot \boldsymbol{n}) \boldsymbol{f}_{\hat{u}} \rangle_{\partial\Omega_e \setminus \Gamma_D} \\
\mathcal{A}_{pu}(\delta f_p, \boldsymbol{f}_u) &:= \big(\boldsymbol{\nabla} \delta f_p, \boldsymbol{f}_u\big)_{\Omega_e}, \\
\mathcal{A}_{p\hat{u}}(\delta f_p, \boldsymbol{f}_{\hat{u}}) &:= \langle \delta f_p, \boldsymbol{f}_{\hat{u}} \cdot \boldsymbol{n} \rangle_{\partial\Omega_e \setminus \Gamma_D}, \\
\mathcal{A}_{\rho p}(\delta f_\rho, f_p) &:= \langle \delta f_\rho, |\partial\Omega_e|^{-1} f_p \rangle_{\partial\Omega_e}, \\
\mathcal{A}_{\rho\rho}(\delta f_\rho, f_\rho) &:= \delta f_\rho \, f_\rho,
\end{aligned}
\tag{A.14}
$$

and equation (A.15), respectively

$$
\begin{aligned}
\mathcal{R}_L^m(\delta \boldsymbol{F}_L \psi) := & \sum_{l=1}^{\mathtt{n_D}} \langle \boldsymbol{n} \cdot \delta \boldsymbol{F}_L, \boldsymbol{g}_D^l \rangle_{\partial\Omega_e \cap \Gamma_D} \mathcal{A}(\psi, \lambda_D^l) \\
& - \sum_{i=1}^{m} \sum_{k=1}^{\mathtt{n_\nu}} \mathcal{A}_{LL}^k(\delta \boldsymbol{F}_L, \sigma_L^i \boldsymbol{F}_L^i) \mathcal{A}_\nu^k(\psi, \psi^i) \\
& - \sum_{i=1}^{m} \left\{ \mathcal{A}_{Lu}^k(\delta \boldsymbol{F}_L, \sigma_u^i \boldsymbol{f}_u^i) - \mathcal{A}_{L\hat{u}}(\delta \boldsymbol{F}_L, \sigma_{\hat{u}}^i \boldsymbol{f}_{\hat{u}}^i) \right\} \mathcal{A}(\psi, \psi^i) \\
\mathcal{R}_u^m(\delta \boldsymbol{f}_u \psi) := & \sum_{l=1}^{\mathtt{n_S}} \left(\delta \boldsymbol{f}_u, \boldsymbol{g}_S^l \right)_{\Omega_e} \mathcal{A}(\psi, \lambda_S^l) \\
& + \sum_{l=1}^{\mathtt{n_D}} \langle \delta \boldsymbol{f}_u, \boldsymbol{\tau} \boldsymbol{g}_D^l \rangle_{\partial\Omega_e \cap \Gamma_D} \mathcal{A}(\psi, \lambda_D^l) \\
& - \sum_{k=1}^{\mathtt{n_C}} \sum_{l=1}^{\mathtt{n_D}} \langle \delta \boldsymbol{f}_u, (\boldsymbol{C}^k \cdot \boldsymbol{n}) \boldsymbol{g}_D^l \rangle_{\partial\Omega_e \cap \Gamma_D} \mathcal{A}_C^k(\psi, \lambda_D^l) \\
& - \sum_{i=1}^{m} \{ \mathcal{A}_{uL}(\delta \boldsymbol{f}_u, \sigma_L^i \boldsymbol{F}_L^i) + \mathcal{A}_{uu}(\delta \boldsymbol{f}_u, \sigma_u^i \boldsymbol{f}_u^i) \\
& \qquad + \mathcal{A}_{up}(\delta \boldsymbol{f}_u, \sigma_p^i f_p^i) - \mathcal{A}_{u\hat{u}}(\delta \boldsymbol{f}_u, \sigma_{\hat{u}}^i \boldsymbol{f}_{\hat{u}}^i) \} \mathcal{A}(\psi, \psi^i) \\
& - \sum_{i=1}^{m} \sum_{k=1}^{\mathtt{n_C}} \left\{ \mathcal{A}_{uu}(\delta \boldsymbol{f}_u, \sigma_u^i \boldsymbol{f}_u^i) - \mathcal{A}_{u\hat{u}}(\delta \boldsymbol{f}_u, \sigma_{\hat{u}}^i \boldsymbol{f}_{\hat{u}}^i) \right\} \mathcal{A}_C^k(\psi, \psi^i) \\
\mathcal{R}_p^m(\delta f_p \psi) := & \sum_{l=1}^{\mathtt{n_D}} \langle \delta f_p, \boldsymbol{g}_D^l \cdot \boldsymbol{n} \rangle_{\partial\Omega_e \cap \Gamma_D} \mathcal{A}(\psi, \lambda_D^l) \\
& - \sum_{i=1}^{m} \sum_{k=1}^{\mathtt{n_a}} \left\{ \mathcal{A}_{pu}^k(\delta f_p, \sigma_u^i \boldsymbol{f}_u^i) - \mathcal{A}_{p\hat{u}}^k(\delta f_p, \sigma_{\hat{u}}^i \boldsymbol{f}_{\hat{u}}^i) \right\} \mathcal{A}(\psi, \psi^i) \\
\mathcal{R}_{\overline{p}}^m(\delta f_\rho \psi) := & - \sum_{i=1}^{m} \left\{ \mathcal{A}_{\rho p}(\delta f_\rho, \sigma_p^i f_p^i) - \mathcal{A}_{\rho\rho}(\delta f_\rho, \sigma_\rho^i f_\rho^i) \right\} \mathcal{A}(\psi, \psi^i).
\end{aligned}
\tag{A.15}
$$

The constants in equation (A.13) are given by

$$
\beta_\nu^k := \mathcal{A}_\nu^k(\psi^m, \psi^m) \qquad \beta_C^k := \mathcal{A}_C^k(\psi^m, \psi^m), \qquad \beta := \mathcal{A}(\psi^m, \psi^m), \tag{A.16}
$$

where the bilinear forms involved in the definitions of these constants are introduced in equation (A.17)

$$
\begin{aligned}
\mathcal{A}_\nu^k(\delta\psi, \psi) &:= \left(\delta\psi, \mathcal{N}^k \psi \right)_{\boldsymbol{\mathcal{I}}}, \\
\mathcal{A}_C^k(\delta\psi, \psi) &:= \left(\delta\psi, \mathcal{C}^k \psi \right)_{\boldsymbol{\mathcal{I}}}, \\
\mathcal{A}(\delta\psi, \psi) &:= \left(\delta\psi, \psi \right)_{\boldsymbol{\mathcal{I}}}.
\end{aligned}
\tag{A.17}
$$

Similarly, the weak form of the global problem is: find $\sigma_{\hat{u}}^m \Delta \boldsymbol{f}_{\hat{u}} \in \widehat{\boldsymbol{\mathcal{V}}}^h$ and $\sigma_{\rho}^m \Delta f_{\rho} \in \mathbb{R}^{\mathtt{n_{el}}}$ that satisfy

$$\begin{aligned}\sum_{e=1}^{\mathtt{n_{el}}} \Bigg\{ & \beta \mathcal{A}_{\hat{u}L}(\delta \boldsymbol{f}_{\hat{u}}, \sigma_L^m \Delta \boldsymbol{F}_L) + \beta \mathcal{A}_{\hat{u}u}(\delta \boldsymbol{f}_{\hat{u}}, \sigma_u^m \Delta \boldsymbol{f}_u) \\ & + \beta \mathcal{A}_{\hat{u}p}(\delta \boldsymbol{f}_{\hat{u}}, \sigma_p^m \Delta f_p) + \beta \mathcal{A}_{\hat{u}\hat{u}}(\delta \boldsymbol{f}_{\hat{u}}, \sigma_{\hat{u}}^m \Delta \boldsymbol{f}_{\hat{u}}) \\ & + \sum_{k=1}^{\mathtt{n_C}} \beta_C^k \mathcal{A}_{\hat{u}\hat{u}}^k(\delta \boldsymbol{f}_{\hat{u}}, \sigma_{\hat{u}}^m \Delta \boldsymbol{f}_{\hat{u}}) \Bigg\} = \sum_{e=1}^{\mathtt{n_{el}}} \mathcal{R}_{\hat{u}}^m(\delta \boldsymbol{f}_{\hat{u}} \psi^m),\end{aligned} \tag{A.18a}$$

for all $\delta \boldsymbol{f}_{\hat{u}} \in \widehat{\boldsymbol{\mathcal{V}}}^h$, with the incompressibility constraint

$$\beta \mathcal{A}_{p\hat{u}}^k(1, \sigma_{\hat{u}}^m \Delta \boldsymbol{f}_{\hat{u}}) = \mathcal{R}_{\rho}^m(\psi^m), \quad e = 1, \ldots, \mathtt{n_{el}}. \tag{A.18b}$$

The bilinear and linear forms of the local problem are detailed in equation (A.19)

$$\begin{aligned}\mathcal{A}_{\hat{u}L}(\delta \boldsymbol{f}_{\hat{u}}, \boldsymbol{F}_L) &:= \langle \delta \boldsymbol{f}_{\hat{u}}, \boldsymbol{n} \cdot \boldsymbol{F}_L \rangle_{\partial\Omega_e \setminus (\Gamma_D \cup \Gamma_S)} - \langle \delta \boldsymbol{f}_{\hat{u}}, (\boldsymbol{n} \cdot \boldsymbol{F}_L) \boldsymbol{E} \rangle_{\partial\Omega_e \cap \Gamma_S}, \\ \mathcal{A}_{\hat{u}u}(\delta \boldsymbol{f}_{\hat{u}}, \boldsymbol{f}_u) &:= \langle \delta \boldsymbol{f}_{\hat{u}}, \boldsymbol{\tau} \boldsymbol{f}_u \rangle_{\partial\Omega_e \setminus (\Gamma_D \cup \Gamma_S)} - \langle \delta \boldsymbol{f}_{\hat{u}}, (\boldsymbol{\tau} \boldsymbol{f}_u) \cdot \boldsymbol{E} \rangle_{\partial\Omega_e \cap \Gamma_S}, \\ \mathcal{A}_{\hat{u}p}(\delta \boldsymbol{f}_{\hat{u}}, f_p) &:= \langle \delta \boldsymbol{f}_{\hat{u}}, f_p \boldsymbol{n} \rangle_{\partial\Omega_e \setminus (\Gamma_D \cup \Gamma_S)}, \\ \mathcal{A}_{\hat{u}\hat{u}}(\delta \boldsymbol{f}_{\hat{u}}, \boldsymbol{f}_{\hat{u}}) &:= \langle \delta \boldsymbol{f}_{\hat{u}}, \boldsymbol{f}_{\hat{u}} \cdot (\boldsymbol{D} + \boldsymbol{\tau} \cdot \boldsymbol{E} \rangle_{\partial\Omega_e \cap \Gamma_S} - \langle \delta \boldsymbol{f}_{\hat{u}}, \boldsymbol{\tau} \boldsymbol{f}_{\hat{u}} \rangle_{\partial\Omega_e \setminus (\Gamma_D \cup \Gamma_S)}, \\ \mathcal{A}_{\hat{u}\hat{u}}^k(\delta \boldsymbol{f}_{\hat{u}}, \boldsymbol{f}_{\hat{u}}) &:= -\langle \delta \boldsymbol{f}_{\hat{u}}, \boldsymbol{f}_{\hat{u}} \cdot (\boldsymbol{C}^k \cdot \boldsymbol{n}) \cdot \boldsymbol{E} \rangle_{\partial\Omega_e \cap \Gamma_S} \\ &\qquad + \langle \delta \boldsymbol{f}_{\hat{u}}, (\boldsymbol{C}^k \cdot \boldsymbol{n}) \boldsymbol{f}_{\hat{u}} \rangle_{\partial\Omega_e \setminus (\Gamma_D \cup \Gamma_S)},\end{aligned} \tag{A.19}$$

and equation (A.20), respectively

$$\begin{aligned}\mathcal{R}_{\hat{u}}^m(\delta \boldsymbol{f}_{\hat{u}} \psi) := & - \sum_{l=1}^{\mathtt{n_N}} \langle \delta \boldsymbol{f}_{\hat{u}}, \boldsymbol{g}_N^l \rangle_{\partial\Omega_e \cap \Gamma_N} \mathcal{A}(\psi, \lambda_N^l) \\ & - \sum_{i=1}^{m} \{ \mathcal{A}_{\hat{u}L}(\delta \boldsymbol{f}_{\hat{u}}, \sigma_L^i \boldsymbol{F}_L^i) + \mathcal{A}_{\hat{u}u}(\delta \boldsymbol{f}_{\hat{u}}, \sigma_u^i \boldsymbol{f}_u^i) \\ & \qquad + \mathcal{A}_{\hat{u}p}(\delta \boldsymbol{f}_{\hat{u}}, \sigma_p^i f_p^i) + \mathcal{A}_{\hat{u}\hat{u}}(\delta \boldsymbol{f}_{\hat{u}}, \sigma_{\hat{u}}^i \boldsymbol{f}_{\hat{u}}^i) \} \mathcal{A}(\psi, \psi^i) \\ & - \sum_{i=1}^{m} \sum_{k=1}^{\mathtt{n_C}} \mathcal{A}_{\hat{u}\hat{u}}^k(\delta \boldsymbol{f}_{\hat{u}}, \sigma_{\hat{u}}^i \boldsymbol{f}_{\hat{u}}^i) \mathcal{A}_C^k(\psi, \psi^i), \\ \mathcal{R}_{\rho}^m(\delta f_{\rho} \psi) := & - \sum_{l=1}^{\mathtt{n_D}} \langle \delta f_{\rho}, \boldsymbol{g}_D^l \cdot \boldsymbol{n} \rangle_{\partial\Omega_e \cap \Gamma_D} \mathcal{A}(\psi, \lambda_D^l) \\ & - \sum_{i=1}^{m} \mathcal{A}_{p\hat{u}}(\delta f_{\rho}, \sigma_{\hat{u}}^i \boldsymbol{f}_{\hat{u}}^i) \mathcal{A}(\psi, \psi^i).\end{aligned} \tag{A.20}$$

A.2.3 The parametric iteration

After computing the spatial corrections following the procedure described in Section 3.3.5, the spatial modes are updated and the parametric iteration is solved.

Introducing the expression of the PGD approximations and the weighting functions in the weak form of the HDG local problems, the following weak form of the local problem for the parametric iteration is obtained: find $\Delta\psi \in \boldsymbol{\mathcal{L}}^h(\boldsymbol{\mathcal{I}})$ such that

$$\begin{aligned}
\sum_{k=1}^{\mathtt{n}_\nu} \gamma_{LL}^k \mathcal{A}_\nu^k(\delta\psi, \Delta\psi) + \gamma_{Lu}\mathcal{A}(\delta\psi, \Delta\psi) & \\
= \mathcal{R}_L^m(\sigma_L^m \boldsymbol{F}_L^m \delta\psi) + \gamma_{L\hat{u}}\mathcal{A}(\delta\psi, \Delta\psi), & \\
\gamma_{uL}\mathcal{A}(\delta\psi, \Delta\psi) + \sum_{k=1}^{\mathtt{n}_\mathtt{C}} \gamma_{uu}^k \mathcal{A}_C^k(\delta\psi, \Delta\psi) + \gamma_{uu}\mathcal{A}(\delta\psi, \Delta\psi) + \gamma_{up}\mathcal{A}(\delta\psi, \Delta\psi) & \\
= \mathcal{R}_u^m(\sigma_u^m \boldsymbol{f}_u^m \delta\psi) + \sum_{k=1}^{\mathtt{n}_\mathtt{C}} \gamma_{u\hat{u}}^k \mathcal{A}_C^k(\delta\psi, \Delta\psi) + \gamma_{u\hat{u}}\mathcal{A}(\delta\psi, \Delta\psi), & \\
\gamma_{pu}\mathcal{A}(\delta\psi, \Delta\psi) = \mathcal{R}_p^m(\sigma_p^m f_p^m \delta\psi) + \gamma_{p\hat{u}}\mathcal{A}(\delta\psi, \Delta\psi), & \\
\gamma_{\rho p}\mathcal{A}(\delta\psi, \Delta\psi) = \mathcal{R}_{\overline{p}}^m(\delta\psi) + \gamma_{\rho\rho}\mathcal{A}(\delta\psi, \Delta\psi), &
\end{aligned} \tag{A.21}$$

for all $\delta\psi \in \boldsymbol{\mathcal{L}}^h(\boldsymbol{\mathcal{I}})$.

Similarly, the weak form of the global problem is: find $\Delta\psi \in \boldsymbol{\mathcal{L}}^h(\boldsymbol{\mathcal{I}})$ that satisfies

$$\begin{aligned}
\sum_{e=1}^{\mathtt{n}_\mathtt{el}} \Bigg\{ \gamma_{\hat{u}L}\mathcal{A}(\delta\psi, \Delta\psi) + \gamma_{\hat{u}u}\mathcal{A}(\delta\psi, \Delta\psi) + \gamma_{\hat{u}p}\mathcal{A}(\delta\psi, \Delta\psi) & \\
+ \sum_{k=1}^{\mathtt{n}_\mathtt{C}} \gamma_{\hat{u}\hat{u}}^k \mathcal{A}_C^k(\delta\psi, \Delta\psi) + \gamma_{\hat{u}\hat{u}}\mathcal{A}(\delta\psi, \Delta\psi) \Bigg\} = \sum_{e=1}^{\mathtt{n}_\mathtt{el}} \mathcal{R}_{\hat{u}}^m(\sigma_{\hat{u}}^m \boldsymbol{f}_{\hat{u}}^m \delta\psi), & \\
\gamma_{\rho\hat{u}}\mathcal{A}(\delta\psi, \psi^m) = \mathcal{R}_\rho^m(\delta\psi), &
\end{aligned} \tag{A.22}$$

for all $\delta\psi \in \boldsymbol{\mathcal{L}}^h(\boldsymbol{\mathcal{I}})$.

The constants in equations (A.21) and (A.22) are defined as

$$\begin{aligned}
\gamma_{LL}^k &:= \mathcal{A}_{LL}^k(\sigma_L^m \boldsymbol{F}_L^m, \sigma_L^m \boldsymbol{F}_L^m), & \gamma_{Lu} &:= \mathcal{A}_{Lu}(\sigma_L^m \boldsymbol{F}_L^m, \sigma_u^m \boldsymbol{f}_u^m), \\
\gamma_{L\hat{u}} &:= \mathcal{A}_{L\hat{u}}(\sigma_L^m \boldsymbol{F}_L^m, \sigma_{\hat{u}}^m \boldsymbol{f}_{\hat{u}}^m), & \gamma_{uL} &:= \mathcal{A}_{uL}(\sigma_u^m \boldsymbol{f}_u^m, \sigma_L^m \boldsymbol{F}_L^m), \\
\gamma_{uu}^k &:= \mathcal{A}_{uu}^k(\sigma_u^m \boldsymbol{f}_u^m, \sigma_u^m \boldsymbol{f}_u^m), & \gamma_{uu} &:= \mathcal{A}_{uu}(\sigma_u^m \boldsymbol{f}_u^m, \sigma_u^m \boldsymbol{f}_u^m), \\
\gamma_{up} &:= \mathcal{A}_{up}(\sigma_u^m \boldsymbol{f}_u^m, \sigma_p^m f_p^m), & \gamma_{u\hat{u}}^k &:= \mathcal{A}_{u\hat{u}}^k(\sigma_u^m \boldsymbol{f}_u^m, \sigma_{\hat{u}}^m \boldsymbol{f}_{\hat{u}}^m), \\
\gamma_{u\hat{u}} &:= \mathcal{A}_{u\hat{u}}(\sigma_u^m \boldsymbol{f}_u^m, \sigma_{\hat{u}}^m \boldsymbol{f}_{\hat{u}}^m), & \gamma_{pu} &:= \mathcal{A}_{pu}(\sigma_p^m f_p^m, \sigma_u^m \boldsymbol{f}_u^m), \\
\gamma_{p\hat{u}} &:= \mathcal{A}_{p\hat{u}}(\sigma_p^m f_p^m, \sigma_{\hat{u}}^m \boldsymbol{f}_{\hat{u}}^m), & \gamma_{\rho p} &:= \mathcal{A}_{\rho p}(1, \sigma_p^m f_p^m), \\
\gamma_{\rho\rho} &:= \mathcal{A}_{\rho\rho}(1, \sigma_\rho^m f_\rho^m), & & \\
\gamma_{\hat{u}L}^k &:= \mathcal{A}_{\hat{u}L}^k(\sigma_{\hat{u}}^m \boldsymbol{f}_{\hat{u}}^m, \sigma_L^m \boldsymbol{F}_L^m), & \gamma_{\hat{u}u} &:= \mathcal{A}_{\hat{u}u}(\sigma_{\hat{u}}^m \boldsymbol{f}_{\hat{u}}^m, \sigma_u^m \boldsymbol{f}_u^m), \\
\gamma_{\hat{u}p} &:= \mathcal{A}_{\hat{u}p}^k(\sigma_{\hat{u}}^m \boldsymbol{f}_{\hat{u}}^m, \sigma_p^m f_p^m), & \gamma_{\hat{u}\hat{u}}^k &:= \mathcal{A}_{\hat{u}\hat{u}}^k(\sigma_{\hat{u}}^m \boldsymbol{f}_{\hat{u}}^m, \sigma_{\hat{u}}^m \boldsymbol{f}_{\hat{u}}^m), \\
\gamma_{\hat{u}\hat{u}} &:= \mathcal{A}_{\hat{u}\hat{u}}(\sigma_{\hat{u}}^m \boldsymbol{f}_{\hat{u}}^m, \sigma_{\hat{u}}^m \boldsymbol{f}_{\hat{u}}^m), & \gamma_{\rho\hat{u}} &:= \mathcal{A}_{p\hat{u}}^k(1, \sigma_{\hat{u}}^m \boldsymbol{f}_{\hat{u}}^m).
\end{aligned} \tag{A.23}$$

The choice of a single parameter approximation implies that we can combine equations (A.21) and (A.22) to obtain the following parametric problem: find $\Delta\psi \in \boldsymbol{\mathcal{L}}^h(\boldsymbol{\mathcal{I}})$

that satisfies

$$\sum_{k=1}^{\mathtt{n}_\nu} \gamma_{LL}^k \mathcal{A}_\nu^k(\delta\psi, \Delta\psi) + \sum_{k=1}^{\mathtt{n}_\mathtt{C}} \gamma_C^k \mathcal{A}_C^k(\delta\psi, \Delta\psi) + \gamma\mathcal{A}(\delta\psi, \Delta\psi) = \mathcal{R}^m(\delta\psi), \tag{A.24}$$

for all $\delta\psi \in \boldsymbol{\mathcal{L}}^h(\boldsymbol{\mathcal{I}})$, where

$$\begin{aligned}
\gamma_C^k :=& \gamma_{uu}^k - \gamma_{u\hat{u}}^k + \gamma_{\hat{u}\hat{u}}^k, \\
\gamma :=& \gamma_{Lu} - \gamma_{L\hat{u}} + \gamma_{uL} + \gamma_{uu} + \gamma_{up} - \gamma_{u\hat{u}} + \gamma_{\rho p} - \gamma_{\rho\rho} \\
&+ \gamma_{\hat{u}L} + \gamma_{\hat{u}u} + \gamma_{\hat{u}p} + \gamma_{\hat{u}\hat{u}}, \\
\mathcal{R}^m(\delta\psi) :=& \mathcal{R}_L^m(\sigma_L^m \boldsymbol{F}_L^m \delta\psi) + \mathcal{R}_u^m(\sigma_u^m \boldsymbol{f}_u^m \delta\psi) + \mathcal{R}_p^m(\sigma_p^m f_p^m \delta\psi) \\
&+ \mathcal{R}_{\overline{p}}^m(\delta\psi) + \mathcal{R}_{\hat{u}}^m(\sigma_{\hat{u}}^m \boldsymbol{f}_{\hat{u}}^m \delta\psi) + \mathcal{R}_\rho^m(\delta\psi).
\end{aligned} \tag{A.25}$$

A.2.4 Local postprocess of the primal variable

For a multi-dimensional problem, the local postprocess necessary to obtain the superconvergent solution $\boldsymbol{u}^*$ analogous to system of equations (2.22) reads: given $\boldsymbol{u} \in \boldsymbol{\mathcal{V}}_{\boldsymbol{\mu}}^h$ and $\boldsymbol{L} \in \boldsymbol{\mathcal{W}}_{\boldsymbol{\mu}}^h$ find $\boldsymbol{u}^* \in \boldsymbol{\mathcal{U}}_{\boldsymbol{\mu}}^h$ that satisfies

$$\begin{aligned}
\big(\boldsymbol{\nabla v}, \boldsymbol{\nabla u}^*\big)_{\Omega_e \times \boldsymbol{\mathcal{I}}} &= -\big(\boldsymbol{\nabla v}, \nu^{-1}\boldsymbol{L}\big)_{\Omega_e \times \boldsymbol{\mathcal{I}}} \\
\big(w, \boldsymbol{u}^*\big)_{\Omega_e \times \boldsymbol{\mathcal{I}}} &= -\big(w, \boldsymbol{u}\big)_{\Omega_e \times \boldsymbol{\mathcal{I}}},
\end{aligned} \tag{A.26}$$

where the tangent manifolds for $\boldsymbol{u}$ is equal to $\boldsymbol{v} \in \boldsymbol{\mathcal{U}}_{\boldsymbol{\mu}}^h$, defined as

$$\begin{aligned}
\mathcal{U}^h(\Omega) &:= \{v \in \mathcal{L}_2(\Omega) : v|_{\Omega_e} \in \mathcal{P}^{k+1}(\Omega_e)\ \forall \Omega_e\,,\ e = 1, \ldots, \mathtt{n_{el}}\}, \\
\boldsymbol{\mathcal{U}}^h &:= \Big[\mathcal{U}^h(\Omega)\Big]^{\mathtt{n_{sd}}}, \\
\boldsymbol{\mathcal{U}}_{\boldsymbol{\mu}}^h &:= \Big[\mathcal{U}^h(\Omega) \otimes \boldsymbol{\mathcal{L}}^h(\boldsymbol{\mathcal{I}})\Big]^{\mathtt{n_{sd}}},
\end{aligned}$$

and $w \in \boldsymbol{\mathcal{L}}^h(\boldsymbol{\mathcal{I}})$, with $\boldsymbol{\mathcal{L}}^h(\boldsymbol{\mathcal{I}})$ defined in sectionA.1.3.

Analogously with section 3.3.7, a rank-m separable approximation is assumed for $\boldsymbol{u}^*$, namely

$$\boldsymbol{u}_{\mathtt{PGD}}^{*,m}(\boldsymbol{x}, \boldsymbol{\mu}) = \sigma_u^{*,m} \boldsymbol{f}_u^{*,m}(\boldsymbol{x})\, \psi^m(\boldsymbol{\mu}) + \boldsymbol{u}_{\mathtt{PGD}}^{*,m-1}(\boldsymbol{x}, \boldsymbol{\mu}). \tag{A.27}$$

where the corresponding correction terms have been omitted because unnecessary. Introducing equation A.27 in (A.26) and solving the system for the m-th mode, it is obtained

$$\begin{aligned}
\big(\boldsymbol{\nabla v}, \boldsymbol{\nabla} \sigma_u^{*,m} \boldsymbol{f}_u^{*,m} \psi^m\big)_{\Omega_e \times \boldsymbol{\mathcal{I}}} &= -\big(\boldsymbol{\nabla v}, \nu^{-1} \sigma_L^m \boldsymbol{F}_L^m \psi^m\big)_{\Omega_e \times \boldsymbol{\mathcal{I}}} \\
\big(\sigma_u^{*,m} \boldsymbol{f}_u^{*,m} \psi^m, \psi^m\big)_{\Omega_e \times \boldsymbol{\mathcal{I}}} &= -\big(\sigma_u^m \boldsymbol{f}_u^m \psi^m, \psi^m\big)_{\Omega_e \times \boldsymbol{\mathcal{I}}},
\end{aligned} \tag{A.28}$$

with tangent manifolds for $\boldsymbol{u}$ similar to the one defined in (3.36), but considering only the spatial variation and neglecting the parametric ones, namely $\boldsymbol{v} = \delta\boldsymbol{f}_u \psi^m$ with $\delta\boldsymbol{f}_u \in \boldsymbol{\mathcal{U}}^h$.

Thanks to the separable form of ν^{-1} system (A.28) can be simplified introducing proper constants defined in (A.16). The weak form reads: given $\sigma_u^m \boldsymbol{f}_u^m \in \boldsymbol{\mathcal{V}}^h$ and $\sigma_L^m \boldsymbol{F}_L^m \in \boldsymbol{\mathcal{W}}^h$ find $\sigma_u^{*,m} \boldsymbol{f}_u^{*,m} \in \boldsymbol{\mathcal{U}}^h$ that satisfies

$$\begin{aligned} \beta\big(\boldsymbol{\nabla}\delta\boldsymbol{f}_u, \boldsymbol{\nabla}\sigma_u^{*,m}\boldsymbol{f}_u^{*,m}\big)_{\Omega_e} &= -\sum_{k=1}^{\mathtt{n}_\nu} \beta_N^k\big(\boldsymbol{\nabla}\delta\boldsymbol{f}_u, N^k\sigma_L^m\boldsymbol{F}_L^m\big)_{\Omega_e} \\ \beta\big(\sigma_u^{*,m}\boldsymbol{f}_u^{*,m}, 1\big)_{\Omega_e} &= -\beta\big(\sigma_u^m\boldsymbol{f}_u^m, 1\big)_{\Omega_e}, \end{aligned} \tag{A.29}$$

for $\delta\boldsymbol{f}_u \in \boldsymbol{\mathcal{U}}^h$. Solving spatial problem (A.29) for each m-mode computed allows constructing a PGD vademecum also for the postprocessed solution which, analogously to those computed for local and global variables, can be particularized in the on-line phase.

A.3 Numerical example: Kovazsnay flow with parametrised viscosity

To validate the proposed technique the Kovasznay flow is introduced. Obtained in Kovasznay, (1948), Kovasznay flow is a solution of the Oseen problem with $\boldsymbol{a}$=$\boldsymbol{u}$.

A multi-dimensional parametrised version of this problem can be created assuming viscosity as an extra-variable and looking for a solution depending on it. This problem has a known analytical solution (shown in figures A.1 and A.2) given by

$$\begin{aligned} u_x(\boldsymbol{x},\boldsymbol{\mu}) &= 1 - \exp(2\lambda x)\cos(2\pi(2y-0.5)), \\ u_y(\boldsymbol{x},\boldsymbol{\mu}) &= \lambda/2\pi\exp(2\lambda x)\sin(2\pi(2y-0.5)), \\ p(\boldsymbol{x},\boldsymbol{\mu}) &= -1/2\exp(4\lambda x) + C. \end{aligned} \tag{A.30}$$

where

$$\begin{aligned} \lambda &= \mathrm{Re}/2 - \sqrt{\mathrm{Re}^2/4 + 4\pi^2}, \\ C &= [1 + \exp(4\lambda) - (1/2\lambda)(1 - \exp(4\lambda))]. \end{aligned} \tag{A.31}$$

The purpose of this section, is to solve the parametrised Kovasznay for all $(\boldsymbol{x},\boldsymbol{\mu})$ in the higher dimensional domain $\Omega\times\boldsymbol{\mathcal{I}}$, where Ω=$[0,0.5]\times[0,1] \subset \mathbb{R}^2$ and $\boldsymbol{\mathcal{I}}$=$\mathcal{I}^1$=$[0.001,1]$. On $\partial\Omega$ pure Dirichlet boundary conditions are imposed, thus $\partial\Omega$=Γ_D.

A.3.1 Separated representation of the data

Following the theory, as explained in Section A.2.1, a separated representation of the data is required. It is worth to notice that for Kovasznay flow, the convective field is chosen equal to the velocity $\boldsymbol{u}$, thus the same separable approximation obtained for $\boldsymbol{a}$ holds also for the Dirichlet datum $\boldsymbol{u}_D$ that is immediate, unlike the source term $\boldsymbol{s}$ which requires few more efforts. Finally observing, that the problem is a pure

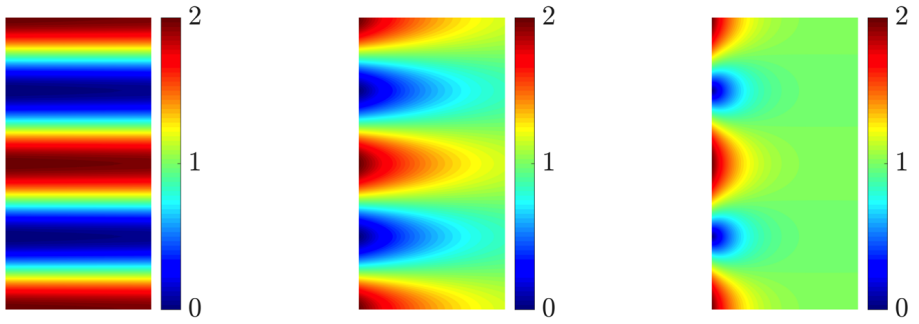

(a) $\mu = 10^{-3}$ (b) $\mu = 0.05$ (c) $\mu = 1$

FIGURE A.1: Kovasznay flow: Analytical solution of the norm of the velocity field for different values of μ.

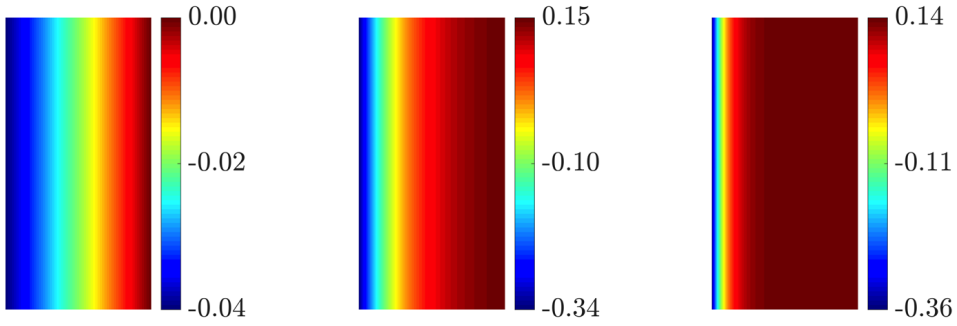

(a) $\mu = 10^{-3}$ (b) $\mu = 0.05$ (c) $\mu = 1$

FIGURE A.2: Kovasznay flow: Analytical solution of the pressure field for different values of μ.

Dirichlet problem, a separable approximation of the pressure is also required to impose the extra condition used to remove its indeterminacy.

While the separated form of the inverse of the viscosity is exact and immediate ($\mathtt{n}_\nu$=1, $N^1(\boldsymbol{x})$=1 and $\mathcal{N}^1(\boldsymbol{\mu})$=$\mu$ being $\mu = \nu$), the exponential appearing in the analytical form of the solution makes an exact separation impossible for velocity and pressure. To circumvent this obstacle an HO-SVD can be applied, or else a more scholastic Taylor expansion.

To reduce as much as possible the approximation error, both exponential functions appearing in (A.30) have been Taylor expanded by mean of an approximation of 25 terms centred in $\mathtt{x}_0$=1/4. With just a few extra calculations, the analytical source term can be computed and approximated by mean of the same technique. The expanded forms of analytical solutions read

$$\boldsymbol{u}(\boldsymbol{x},\boldsymbol{\mu}) = \begin{cases} 1 - \ T^1_{25}(\boldsymbol{x},\boldsymbol{\mu}) \ \cos(2\pi(2y-0.5)) \\ (\lambda(\boldsymbol{\mu})/2\pi) \ \mathcal{T}^1_{25}(\boldsymbol{x},\boldsymbol{\mu}) \ \sin(2\pi(2y-0.5)) \end{cases} \tag{A.32}$$

$$p(\boldsymbol{x},\boldsymbol{\mu}) = -1/2 \ \mathcal{T}^2_{25}(\boldsymbol{x},\boldsymbol{\mu}) \ + C(\boldsymbol{\mu}),$$

where

$$\begin{aligned} \exp(2\lambda x) &\approx \mathcal{T}^1_{25}(\boldsymbol{x}, \boldsymbol{\mu}) = \sum_{n=0}^{25} \frac{(2\lambda x - 1/4)^n}{n!} \\ \exp(4\lambda x) &\approx \mathcal{T}^2_{25}(\boldsymbol{x}, \boldsymbol{\mu}) = \sum_{n=0}^{25} \frac{(4\lambda x - 1/4)^n}{n!}. \end{aligned} \tag{A.33}$$

which being separable transmit their separability to all their spatial derivatives, included the source term, which is a linear combination of them.

A.3.2 Off-line phase

The proposed ROM is used to obtain the generalised solution of the parametric Oseen problem. For the numerical experiment a uniform triangular mesh with 64 elements is generated. The computation was performed using a degree of approximation k=5 for all the variables and with a mesh of 500 elements in the parametric dimension with also k=5.

The first eight normalised modes of the magnitude of the velocity field and the pressure are shown in figures A.3 and figure A.4, respectively.

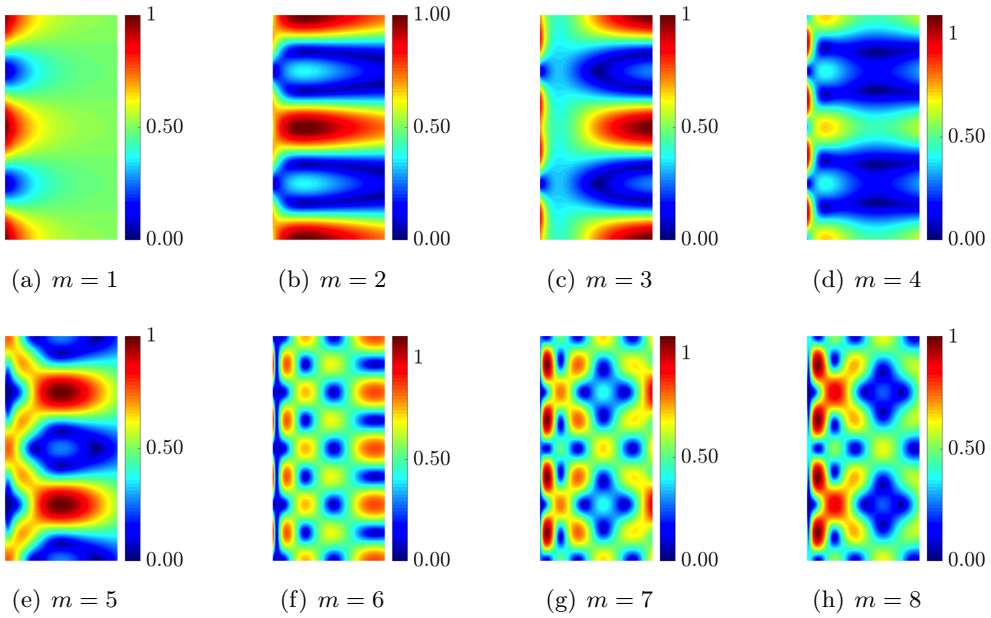

(a) $m = 1$ (b) $m = 2$ (c) $m = 3$ (d) $m = 4$

(e) $m = 5$ (f) $m = 6$ (g) $m = 7$ (h) $m = 8$

FIGURE A.3: Kovasznay flow: First eight normalised spatial modes of the norm of the velocity field.

The first eight normalised parametric modes are shown in figure A.5. It is worth noting the increase of amplitude and frequency of parametric modes by increasing the number of modes and approaching to the left extreme of the parametric interval. This is mainly attributed to the scale at which the convective term becomes more dominant.

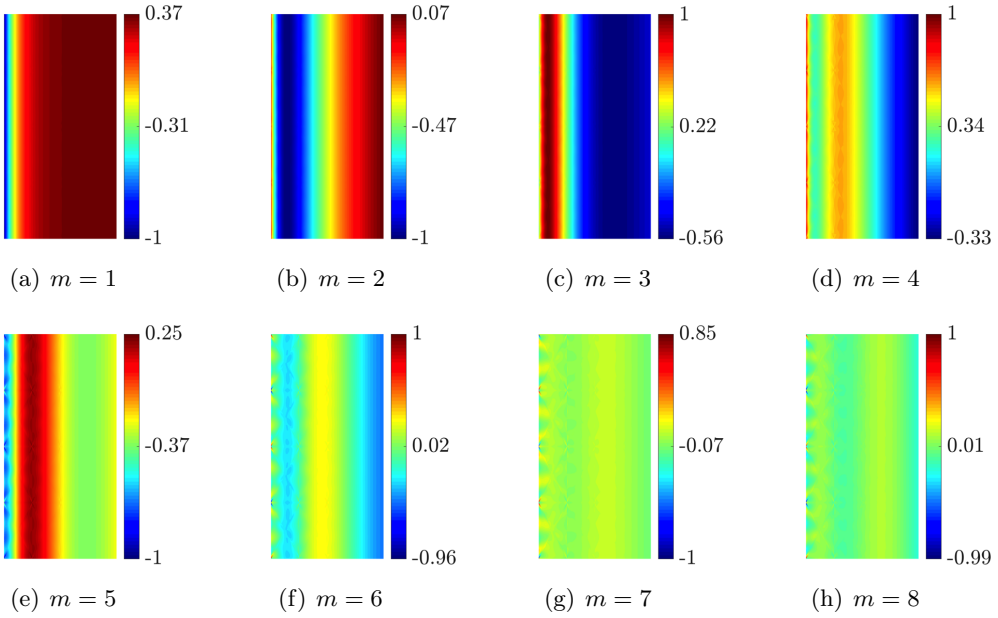

(a) $m = 1$ (b) $m = 2$ (c) $m = 3$ (d) $m = 4$

(e) $m = 5$ (f) $m = 6$ (g) $m = 7$ (h) $m = 8$

FIGURE A.4: Kovasznay flow: First eight normalised spatial modes of the pressure field.

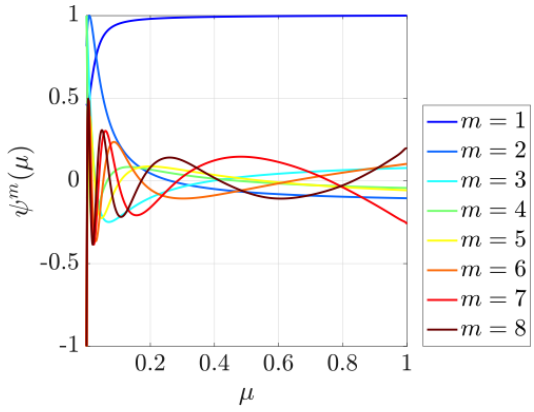

FIGURE A.5: Kovasznay flow: First eight normalised parametric modes.

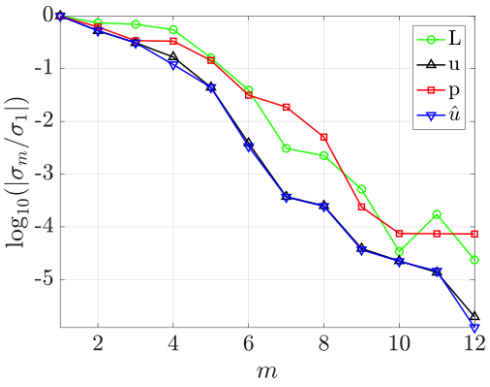

FIGURE A.6: Kovasznay flow: Convergence of the mode amplitudes.

The evolution of the relative amplitude of the modes is shown in A.6. The rapid decrease shows that it is possible to compute a generalised solution to this problem

with a very small number of modes. With twelve compressed modes the relative amplitude is already below 10^{-5}. This off-line solution has been obtained computing a total of 156 modes reaching a maximum of 10 iterations in the alternating direction algorithm for each enrichment.

A.3.3 On-line phase

Once the generalised solution is computed, it is of interest to quantify its accuracy.

Figures A.7 and A.8 shows the absolute value of the error of the velocity magnitude and pressure using as the number of modes is increased for three relevant configurations corresponding to the parameter values μ_1=$\{0.001, 0.05, 1\}$ associated to Reynolds numbers $R_e = \{1000, 20, 1\}$. It is worth noting that the configurations analysed include both convection-dominated and diffusion-dominated flow regimes.

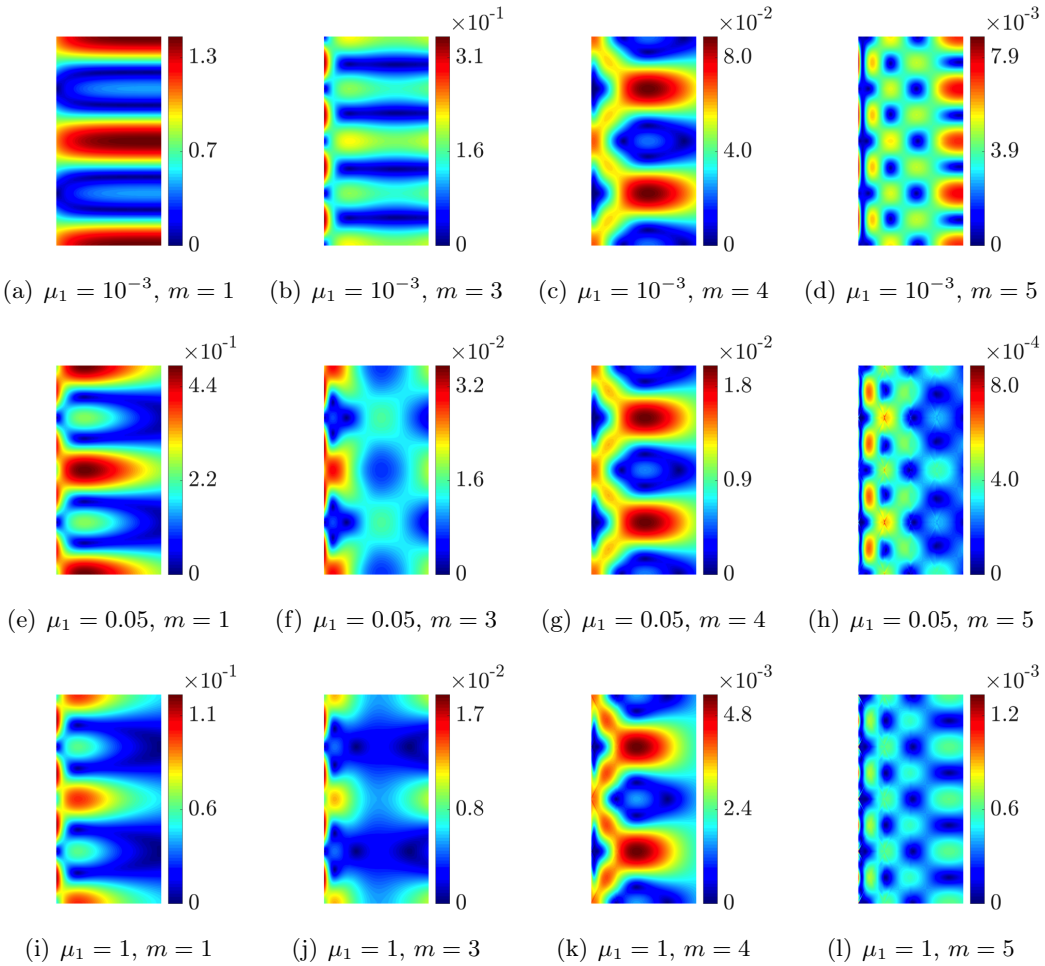

(a) $\mu_1 = 10^{-3}$, $m = 1$ (b) $\mu_1 = 10^{-3}$, $m = 3$ (c) $\mu_1 = 10^{-3}$, $m = 4$ (d) $\mu_1 = 10^{-3}$, $m = 5$

(e) $\mu_1 = 0.05$, $m = 1$ (f) $\mu_1 = 0.05$, $m = 3$ (g) $\mu_1 = 0.05$, $m = 4$ (h) $\mu_1 = 0.05$, $m = 5$

(i) $\mu_1 = 1$, $m = 1$ (j) $\mu_1 = 1$, $m = 3$ (k) $\mu_1 = 1$, $m = 4$ (l) $\mu_1 = 1$, $m = 5$

FIGURE A.7: Kovasznay flow: Absolute value of the error of the velocity magnitude using m PGD modes and for different values of the material parameter μ_1. An approximation of degree $k = 5$ is used for all variables.

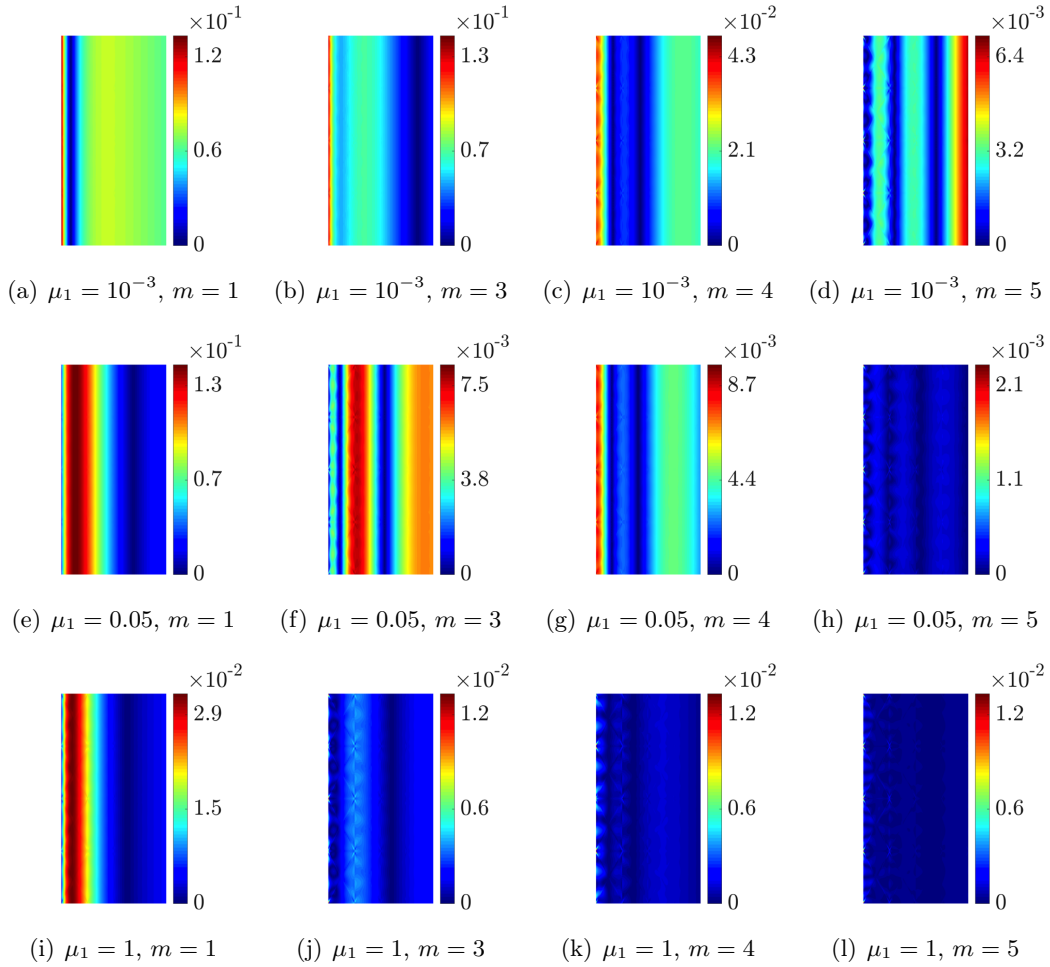

(a) $\mu_1 = 10^{-3}$, $m = 1$ (b) $\mu_1 = 10^{-3}$, $m = 3$ (c) $\mu_1 = 10^{-3}$, $m = 4$ (d) $\mu_1 = 10^{-3}$, $m = 5$

(e) $\mu_1 = 0.05$, $m = 1$ (f) $\mu_1 = 0.05$, $m = 3$ (g) $\mu_1 = 0.05$, $m = 4$ (h) $\mu_1 = 0.05$, $m = 5$

(i) $\mu_1 = 1$, $m = 1$ (j) $\mu_1 = 1$, $m = 3$ (k) $\mu_1 = 1$, $m = 4$ (l) $\mu_1 = 1$, $m = 5$

FIGURE A.8: Kovasznay flow: Absolute value of the error of the pressure field using m PGD modes and for different values of the material parameter μ_1. An approximation of degree $k = 5$ is used for all variables.

The results show that with few PGD modes the absolute error is still quite large, particularly for the case with μ_1=0.001 which is the configuration representing the convection dominated solution. With five PGD modes, the error drops substantially, being less than 8×10^{-3} for the velocity and less than 2.2×10^{-2} for the pressure.

To further illustrate the accuracy of the proposed HDG-PGD approach, the relative error in the $\mathcal{L}_2(\Omega \times \boldsymbol{\mathcal{I}})$ norm, defined in equation (3.66) is studied and compared to the error of the full order HDG approach. Figure A.9 shows the evolution of $\varepsilon_{\texttt{PGD}}$ as the number of PGD modes is increased for all local variables, global variable $\hat{\boldsymbol{u}}$ and the postprocess velocity $\boldsymbol{u}^*$ to whom is dedicated next section. The discontinuous

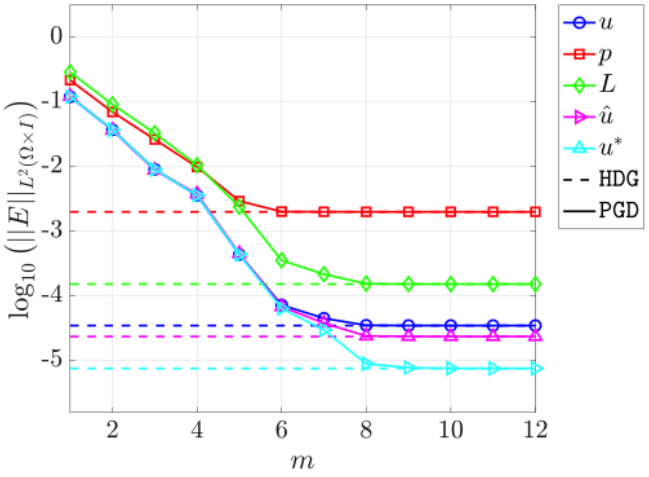

(a)

FIGURE A.9: Kovasznay flow: $\mathcal{L}_2$ norm of the error for $\boldsymbol{L}$, $\boldsymbol{u}$, p and $\hat{\boldsymbol{u}}$ as the number of PGD modes is increased. An approximation of degree $k = 5$ is used for all the variables.

lines in figure A.9 show the relative error of the full order HDG method, measured in the $\mathcal{L}_2(\Omega \times \boldsymbol{\mathcal{I}})$ norm. The results show that the error of the proposed ROM converges monotonically to the error of the full order approach with as the number of modes is increased. In all cases, the number of PGD modes required to reach the maximum accuracy for each variable on the given mesh is equal or lower than eight.

Bibliography

Allaire, Grégoire and Marc Schoenauer (2007). *Conception optimale de structures*. Vol. 58. Springer.

Alouges, F, A DeSimone, and A Lefebvre (2009). "Optimal strokes for axisymmetric microswimmers". In: *The European Physical Journal E: Soft Matter and Biological Physics* 28.3, pp. 279–284.

Ammar, Amine, Béchir Mokdad, Francisco Chinesta, and Roland Keunings (2006). "A new family of solvers for some classes of multidimensional partial differential equations encountered in kinetic theory modeling of complex fluids". In: *Journal of Non-Newtonian Fluid Mechanics* 139.3, pp. 153–176.

– (2007). "A new family of solvers for some classes of multidimensional partial differential equations encountered in kinetic theory modelling of complex fluids: Part II: Transient simulation using space-time separated representations". In: *Journal of non-newtonian fluid mechanics* 144.2-3, pp. 98–121.

Ammar, Amine, Antonio Huerta, Francisco Chinesta, Elías Cueto, and Adrien Leygue (2014). "Parametric solutions involving geometry: a step towards efficient shape optimization". In: *Computer Methods in Applied Mechanics and Engineering* 268, pp. 178–193.

Amsallem, David and Charbel Farhat (2008). "Interpolation method for adapting reduced-order models and application to aeroelasticity". In: *AIAA journal* 46.7, pp. 1803–1813.

Araya, Rodolfo, Manuel Solano, and Patrick Vega (2019). "A posteriori error analysis of an HDG method for the Oseen problem". In: *Applied Numerical Mathematics* 146, pp. 291–308.

Arnold, Douglas N (1982). "An interior penalty finite element method with discontinuous elements". In: *SIAM journal on numerical analysis* 19.4, pp. 742–760.

Arnold, Douglas N, Franco Brezzi, Bernardo Cockburn, and L Donatella Marini (2002). "Unified analysis of discontinuous Galerkin methods for elliptic problems". In: *SIAM journal on numerical analysis* 39.5, pp. 1749–1779.

Arroyo, Marino, Luca Heltai, Daniel Millán, and Antonio DeSimone (2012). "Reverse engineering the euglenoid movement". In: *Proceedings of the National Academy of Sciences* 109.44, pp. 17874–17879.

Ashraf, Muhammad Waseem, Shahzadi Tayyaba, and Nitin Afzulpurkar (2011). "Micro electromechanical systems (MEMS) based microfluidic devices for biomedical applications". In: *International journal of molecular sciences* 12.6, pp. 3648–3704.

Avron, JE, O Kenneth, and DH Oaknin (2005). "Pushmepullyou: an efficient micro-swimmer". In: *New Journal of Physics* 7.1, p. 234.

Avron, Joseph E and Oren Raz (2008). "A geometric theory of swimming: Purcell's swimmer and its symmetrized cousin". In: *New Journal of Physics* 10.6, p. 063016.

Baiges, Joan, Ramon Codina, and Sergio Idelsohn (2013). "Explicit reduced-order models for the stabilized finite element approximation of the incompressible Navier–Stokes equations". In: *International Journal for Numerical Methods in Fluids* 72.12, pp. 1219–1243.

Ballarin, Francesco, Andrea Manzoni, Alfio Quarteroni, and Gianluigi Rozza (2015). "Supremizer stabilization of POD–Galerkin approximation of parametrized steady incompressible Navier–Stokes equations". In: *International Journal for Numerical Methods in Engineering* 102.5, pp. 1136–1161.

Ballarin, Francesco, Elena Faggiano, Sonia Ippolito, Andrea Manzoni, Alfio Quarteroni, Gianluigi Rozza, and Roberto Scrofani (2016a). "Fast simulations of patient-specific haemodynamics of coronary artery bypass grafts based on a POD–Galerkin method and a vascular shape parametrization". In: *Journal of Computational Physics* 315, pp. 609–628.

Ballarin, Francesco and Gianluigi Rozza (2016b). "POD–Galerkin monolithic reduced order models for parametrized fluid-structure interaction problems". In: *International Journal for Numerical Methods in Fluids* 82.12, pp. 1010–1034.

Ballarin, Francesco, Elena Faggiano, Andrea Manzoni, Alfio Quarteroni, Gianluigi Rozza, Sonia Ippolito, Carlo Antona, and Roberto Scrofani (2017). "Numerical modeling of hemodynamics scenarios of patient-specific coronary artery bypass grafts". In: *Biomechanics and modeling in mechanobiology* 16.4, pp. 1373–1399.

Ballarin, Francesco, Alessandro D'Amario, Simona Perotto, and Gianluigi Rozza (2019). "A POD-selective inverse distance weighting method for fast parametrized shape morphing". In: *International Journal for Numerical Methods in Engineering* 117.8, pp. 860–884.

Baroli, Davide, Cristina Maria Cova, Simona Perotto, Lorenzo Sala, and Alessandro Veneziani (2017). "Hi-POD solution of parametrized fluid dynamics problems: preliminary results". In: *Model Reduction of Parametrized Systems*. Springer, pp. 235–254.

Barroso, Guillem, Antonio J Gil, Paul D Ledger, Mike Mallett, and Antonio Huerta (2020a). "A regularised-adaptive Proper Generalised Decomposition implementation for coupled magneto-mechanical problems with application to MRI scanners". In: *Computer Methods in Applied Mechanics and Engineering* 358, p. 112640.

Barroso, Guillem, Marcos Seoane, Antonio J Gil, Paul D Ledger, Mike Mallett, and Antonio Huerta (2020b). "A staggered high-dimensional Proper Generalised Decomposition for coupled magneto-mechanical problems with application to MRI scanners". In: *Computer Methods in Applied Mechanics and Engineering* 370, p. 113271.

Bassi, Francesco and Stefano Rebay (1997). "A high-order accurate discontinuous finite element method for the numerical solution of the compressible Navier–Stokes equations". In: *Journal of computational physics* 131.2, pp. 267–279.

Bassi, Francesco, L Botti, Alessandro Colombo, Andrea Crivellini, Antonio Ghidoni, and F Massa (2016). "On the development of an implicit high-order discontinuous Galerkin method for DNS and implicit LES of turbulent flows". In: *European Journal of Mechanics-B/Fluids* 55, pp. 367–379.

Beck, Andrea D, Thomas Bolemann, David Flad, Hannes Frank, Gregor J Gassner, Florian Hindenlang, and Claus-Dieter Munz (2014). "High-order discontinuous Galerkin spectral element methods for transitional and turbulent flow simulations". In: *International Journal for Numerical Methods in Fluids* 76.8, pp. 522–548.

Becker, Leif E, Stephan A Koehler, and Howard A Stone (2003). "On self-propulsion of micro-machines at low Reynolds number: Purcell's three-link swimmer". In: *Journal of fluid mechanics* 490, pp. 15–35.

Berg, Howard C (1993). *Random walks in biology*. Princeton University Press.

Biswas, Rupak, Karen D Devine, and Joseph E Flaherty (1994). "Parallel, adaptive finite element methods for conservation laws". In: *Applied Numerical Mathematics* 14.1-3, pp. 255–283.

Bognet, Brice, Felipe Bordeu, Francisco Chinesta, Adrien Leygue, and Arnaud Poitou (2012). "Advanced simulation of models defined in plate geometries: 3D solutions with 2D computational complexity". In: *Computer Methods in Applied Mechanics and Engineering* 201, pp. 1–12.

Brezzi, Franco, Jim Douglas, and L Donatella Marini (1985). "Two families of mixed finite elements for second order elliptic problems". In: *Numerische Mathematik* 47.2, pp. 217–235.

Brezzi, Franco, Gianmarco Manzini, Donatella Marini, Paola Pietra, and Alessandro Russo (2000). "Discontinuous Galerkin approximations for elliptic problems". In: *Numerical Methods for Partial Differential Equations: An International Journal* 16.4, pp. 365–378.

Bui-Thanh, Tan, Karen Willcox, and Omar Ghattas (2008). "Model reduction for large-scale systems with high-dimensional parametric input space". In: *SIAM Journal on Scientific Computing* 30.6, pp. 3270–3288.

Cesmelioglu, Aycil, Bernardo Cockburn, Ngoc Cuong Nguyen, and Jaume Peraire (2013). "Analysis of HDG methods for Oseen equations". In: *Journal of Scientific Computing* 55.2, pp. 392–431.

Chamoin, Ludovic and HP Thai (2019). "Certified real-time shape optimization using isogeometric analysis, PGD model reduction, and a posteriori error estimation". In: *International Journal for Numerical Methods in Engineering* 119.3, pp. 151–176.

Chapelier, J-B, M De La Llave Plata, F Renac, and E Lamballais (2014). "Evaluation of a high-order discontinuous Galerkin method for the DNS of turbulent flows". In: *Computers & Fluids* 95, pp. 210–226.

Chapelle, Dominique, Asven Gariah, Philippe Moireau, and Jacques Sainte-Marie (2013). "A Galerkin strategy with Proper Orthogonal Decomposition for parameter-dependent problems-Analysis, assessments and applications to parameter estimation". In: *ESAIM: Mathematical Modelling and Numerical Analysis-Modélisation Mathématique et Analyse Numérique* 47.6, pp. 1821–1843.

Childress, Stephen (1981). *Mechanics of swimming and flying*. Vol. 2. Cambridge University Press.

Childs, Peter RN (2010). *Rotating flow*. Elsevier.

Chinesta, F., A. Huerta, G. Rozza, and K. Willcox (2017). "Model Reduction Methods". In: *Encyclopedia of Computational Mechanics Second Edition*. Ed. by Erwin Stein, Rene de Borst, and Thomas J. R. Hughes. Vol. Part 1 Solids and Structures. Chichester: John Wiley & Sons, Ltd. Chap. 3, pp. 1–36.

Chinesta, Francisco, Amine Ammar, Adrien Leygue, and Roland Keunings (2011). "An overview of the proper generalized decomposition with applications in computational rheology". In: *Journal of Non-Newtonian Fluid Mechanics* 166.11, pp. 578–592.

Chinesta, Francisco, Adrien Leygue, Felipe Bordeu, Jose Vicente Aguado, Elías Cueto, David González, Iciar Alfaro, Amine Ammar, and Antonio Huerta (2013a). "PGD-based computational vademecum for efficient design, optimization and control". In: *Archives of Computational Methods in Engineering* 20.1, pp. 31–59.

Chinesta, Francisco, Roland Keunings, and Adrien Leygue (2013b). *The proper generalized decomposition for advanced numerical simulations: a primer*. Springer Science & Business Media.

Chinesta, Francisco, Elias Cueto, and Antonio Huerta (2014). "PGD for solving multi-dimensional and parametric models". In: *Separated representations and PGD-based model reduction*. Springer, pp. 27–89.

Chinesta, Francisco, Elias Cueto, Emmanuelle Abisset-Chavanne, Jean Louis Duval, and Fouad El Khaldi (2020). "Virtual, digital and hybrid twins: a new paradigm in data-based engineering and engineered data". In: *Archives of computational methods in engineering* 27.1, pp. 105–134.

Cockburn, Bernardo (2016). "Static condensation, hybridization, and the devising of the HDG methods". In: *Building bridges: connections and challenges in modern approaches to numerical partial differential equations*. Springer, pp. 129–177.

Cockburn, Bernardo, San-Yih Lin, and Chi-Wang Shu (1988). "TVB Runge-Kutta local projection discontinuous Galerkin finite element method for conservation laws III: one dimensional systems". In:

Cockburn, Bernardo and Chi-Wang Shu (1989). "TVB Runge-Kutta local projection discontinuous Galerkin finite element method for conservation laws. II. General framework". In: *Mathematics of computation* 52.186, pp. 411–435.

Cockburn, Bernardo, Suchung Hou, and Chi-Wang Shu (1990). "The Runge-Kutta local projection discontinuous Galerkin finite element method for conservation laws.

IV. The multidimensional case". In: *Mathematics of Computation* 54.190, pp. 545–581.

Cockburn, Bernardo and Chi-Wang Shu (1998). "The local discontinuous Galerkin method for time-dependent convection-diffusion systems". In: *SIAM Journal on Numerical Analysis* 35.6, pp. 2440–2463.

Cockburn, Bernardo, George E Karniadakis, and Chi-Wang Shu (2000). "The development of discontinuous Galerkin methods". In: *Discontinuous Galerkin Methods*. Springer, pp. 3–50.

Cockburn, Bernardo, Guido Kanschat, Dominik Schötzau, and Christoph Schwab (2002). "Local discontinuous Galerkin methods for the Stokes system". In: *SIAM Journal on Numerical Analysis* 40.1, pp. 319–343.

Cockburn, Bernardo and Jayadeep Gopalakrishnan (2004a). "A characterization of hybridized mixed methods for second order elliptic problems". In: *SIAM Journal on Numerical Analysis* 42.1, pp. 283–301.

Cockburn, Bernardo, Guido Kanschat, and Dominik SchÃķtzau (2004b). "The local discontinuous Galerkin method for the Oseen equations". In: *Mathematics of Computation* 73.246, pp. 569–593.

Cockburn, Bernardo, Bo Dong, and Johnny Guzmán (2008). "A superconvergent LDG-hybridizable Galerkin method for second-order elliptic problems". In: *Mathematics of Computation* 77.264, pp. 1887–1916.

Cockburn, Bernardo, Johnny Guzmán, and Haiying Wang (2009a). "Superconvergent discontinuous Galerkin methods for second-order elliptic problems". In: *Mathematics of Computation* 78.265, pp. 1–24.

Cockburn, Bernardo and Jayadeep Gopalakrishnan (2009b). "The derivation of hybridizable discontinuous Galerkin methods for Stokes flow". In: *SIAM Journal on Numerical Analysis* 47.2, pp. 1092–1125.

Cockburn, Bernardo, Jayadeep Gopalakrishnan, and Raytcho Lazarov (2009c). "Unified hybridization of discontinuous Galerkin, mixed, and continuous Galerkin methods for second order elliptic problems". In: *SIAM Journal on Numerical Analysis* 47.2, pp. 1319–1365.

– (2009d). "Unified hybridization of discontinuous Galerkin, mixed, and continuous Galerkin methods for second order elliptic problems". In: *SIAM Journal on Numerical Analysis* 47.2, pp. 1319–1365.

Cockburn, Bernardo, Ngoc Cuong Nguyen, and Jaume Peraire (2010). "A comparison of HDG methods for Stokes flow". In: *Journal of Scientific Computing* 45.1-3, pp. 215–237.

Cockburn, Bernardo, Jayadeep Gopalakrishnan, Ngoc Nguyen, Jaume Peraire, and Francisco-Javier Sayas (2011). "Analysis of HDG methods for Stokes flow". In: *Mathematics of Computation* 80.274, pp. 723–760.

Cockburn, Bernardo, Weifeng Qiu, and Ke Shi (2012). "Conditions for superconvergence of HDG methods for second-order elliptic problems". In: *Mathematics of Computation* 81.279, pp. 1327–1353.

Cockburn, Bernardo and Ke Shi (2014). "Devising HDG methods for Stokes flow: an overview". In: *Computers & Fluids* 98, pp. 221–229.

Cockburn, Bernardo, Daniele A Di Pietro, and Alexandre Ern (2016). "Bridging the hybrid high-order and hybridizable discontinuous Galerkin methods". In: *ESAIM: Mathematical Modelling and Numerical Analysis* 50.3, pp. 635–650.

Cockburn, Bernardo, Guosheng Fu, and Weifeng Qiu (2017). "A note on the devising of superconvergent HDG methods for Stokes flow by M-decompositions". In: *IMA Journal of Numerical Analysis* 37.2, pp. 730–749.

Courard, Amaury, David Néron, Pierre Ladevèze, and Ludovic Ballere (2016). "Integration of PGD-virtual charts into an engineering design process". In: *Computational Mechanics* 57.4, pp. 637–651.

Dacles-Mariani, Jennifer, Gregory G Zilliac, Jim S Chow, and Peter Bradshaw (1995). "Numerical/experimental study of a wingtip vortex in the near field". In: *AIAA journal* 33.9, pp. 1561–1568.

Di Pietro, Daniele A, Alexandre Ern, and Simon Lemaire (2014). "An arbitrary-order and compact-stencil discretization of diffusion on general meshes based on local reconstruction operators". In: *Computational Methods in Applied Mathematics* 14.4, pp. 461–472.

Di Pietro, Daniele A and Alexandre Ern (2015). "A hybrid high-order locking-free method for linear elasticity on general meshes". In: *Computer Methods in Applied Mechanics and Engineering* 283, pp. 1–21.

Di Pietro, Daniele Antonio and Roberta Tittarelli (2018). "An introduction to hybrid high-order methods". In: *Numerical methods for PDEs*. Springer, pp. 75–128.

Díez, Pedro, Sergio Zlotnik, and Antonio Huerta (2017). "Generalized parametric solutions in Stokes flow". In: *Computer Methods in Applied Mechanics and Engineering* 326, pp. 223–240.

Díez, Pedro, Sergio Zlotnik, Alberto García-González, and Antonio Huerta (2018). "Algebraic PGD for tensor separation and compression: an algorithmic approach". In: *Comptes Rendus Mécanique* 346.7, pp. 501–514.

– (2019). "Encapsulated PGD algebraic toolbox operating with high-dimensional data". In: *Archives of computational methods in engineering*, pp. 1–16.

Donea, J. and A. Huerta (2003). *Finite Element Methods for Flow Problems*. John Wiley & Sons.

Douglas, Jim and Jun Ping Wang (1989). "An absolutely stabilized finite element method for the Stokes problem". In: *Mathematics of computation* 52.186, pp. 495–508.

Dreyfus, Rémi, Jean Baudry, Marcus L Roper, Marc Fermigier, Howard A Stone, and Jérôme Bibette (2005). "Microscopic artificial swimmers". In: *Nature* 437.7060, pp. 862–865.

Du, Qiang, Vance Faber, and Max Gunzburger (1999). "Centroidal Voronoi tessellations: Applications and algorithms". In: *SIAM review* 41.4, pp. 637–676.

Dumon, Antoine, Cyrille Allery, and Amine Ammar (2011). "Proper general decomposition (PGD) for the resolution of Navier–Stokes equations". In: *Journal of Computational Physics* 230.4, pp. 1387–1407.

Egger, Herbert and Joachim Schöberl (2010). "A hybrid mixed discontinuous Galerkin finite-element method for convection–diffusion problems". In: *IMA Journal of Numerical Analysis* 30.4, pp. 1206–1234.

Ekaterinaris, John A (2005). "High-order accurate, low numerical diffusion methods for aerodynamics". In: *Progress in Aerospace Sciences* 41.3-4, pp. 192–300.

Elgeti, Jens, Roland G Winkler, and Gerhard Gompper (2015). "Physics of microswimmers—single particle motion and collective behavior: a review". In: *Reports on progress in physics* 78.5, p. 056601.

Feynman, Richard P (1960). "There's plenty of room at the bottom". In: *California Institute of Technology, Engineering and Science magazine*.

Fonda, Enrico and Katepalli R Sreenivasan (2017). "Unmixing demonstration with a twist: A photochromic Taylor-Couette device". In: *American Journal of Physics* 85.10, pp. 796–800.

Fortin, Michel and Franco Brezzi (1991). *Mixed and hybrid finite element methods*. New York: Springer-Verlag.

García-Blanco, Raquel, Domenico Borzacchiello, Francisco Chinesta, and Pedro Diez (2017). "Monitoring a PGD solver for parametric power flow problems with goal-oriented error assessment". In: *International Journal for Numerical Methods in Engineering* 111.6, pp. 529–552.

García-Blanco, Raquel, Pedro Díez, Domenico Borzacchiello, and Francisco Chinesta (2018). "Algebraic and parametric solvers for the power flow problem: towards real-time and accuracy-guaranteed simulation of electric systems". In: *Archives of Computational Methods in Engineering* 25.4, pp. 1003–1026.

Garikapati, Hasini, Sergio Zlotnik, Pedro Díez, Clemens V Verhoosel, and E Harald van Brummelen (2020). "A Proper Generalized Decomposition (PGD) approach to crack propagation in brittle materials: with application to random field material properties". In: *Computational Mechanics* 65.2, pp. 451–473.

Gassner, Gregor J and Andrea D Beck (2013). "On the accuracy of high-order discretizations for underresolved turbulence simulations". In: *Theoretical and Computational Fluid Dynamics* 27.3-4, pp. 221–237.

Gauger, Erik and Holger Stark (2006). "Numerical study of a microscopic artificial swimmer". In: *Physical Review E* 74.2, p. 021907.

Giacomini, Matteo, Alexandros Karkoulias, Ruben Sevilla, and Antonio Huerta (2018). "A superconvergent HDG method for Stokes flow with strongly enforced symmetry of the stress tensor". In: *Journal of Scientific Computing* 77.3, pp. 1679–1702.

Giacomini, Matteo and Ruben Sevilla (2020a). "A second-order face-centred finite volume method on general meshes with automatic mesh adaptation". In: *arXiv preprint arXiv:2005.01663*.

Giacomini, Matteo, Luca Borchini, Ruben Sevilla, and Antonio Huerta (2020b). "Separated response surfaces for flows in parametrised domains: comparison of a priori and a posteriori PGD algorithms". In: *arXiv preprint arXiv:2009.02176*.

Giacomini, Matteo, Ruben Sevilla, and Antonio Huerta (2020c). "Tutorial on Hybridizable Discontinuous Galerkin (HDG) Formulation for Incompressible Flow Problems". In: *Modeling in Engineering Using Innovative Numerical Methods for Solids and Fluids*. Springer, pp. 163–201.

Giorgiani, Giorgio, Sonia Fernández Méndez, and Antonio Huerta (2012). "Hybridizable discontinuous Galerkin p-adaptivity for wave problems". In: *Proceedings of the First ECCOMAS young investigators conference on computational methods in applied sciences. Aveiro (Portugal), 24-27 April 2012*, pp. 1–10.

– (2014). "Hybridizable discontinuous Galerkin with degree adaptivity for the incompressible Navier–Stokes equations". In: *Computers & Fluids* 98, pp. 196–208.

Giraldi, Loïc, Dishi Liu, Hermann G Matthies, and Anthony Nouy (2015). "To be or not to be intrusive? The solution of parametric and stochastic equations—Proper Generalized Decomposition". In: *SIAM Journal on Scientific Computing* 37.1, A347–A368.

González, David, José Vicente Aguado, E Cueto, E Abisset-Chavanne, and F Chinesta (2018). "kPCA-based parametric solutions within the PGD framework". In: *Archives of Computational Methods in Engineering* 25.1, pp. 69–86.

Grepl, Martin A and Anthony T Patera (2005). "A posteriori error bounds for reduced-basis approximations of parametrized parabolic partial differential equations". In: *ESAIM: Mathematical Modelling and Numerical Analysis* 39.1, pp. 157–181.

Guyan, Robert J (1965). "Reduction of stiffness and mass matrices". In: *AIAA journal* 3.2, pp. 380–380.

Hartmann, Ralf and Paul Houston (2003). "Adaptive discontinuous Galerkin finite element methods for nonlinear hyperbolic conservation laws". In: *SIAM Journal on Scientific Computing* 24.3, pp. 979–1004.

Heller, John P (1960). "An unmixing demonstration". In: *American Journal of Physics* 28.4, pp. 348–353.

Hesthaven, Jan S, Gianluigi Rozza, Benjamin Stamm, et al. (2016). *Certified reduced basis methods for parametrized partial differential equations*. Vol. 590. Springer.

Heuzé, Thomas, Adrien Leygue, and Guillaume Racineux (2016). "Parametric modeling of an electromagnetic compression device with the proper generalized decomposition". In: *International Journal of Material Forming* 9.1, pp. 101–113.

Huerta, Antonio, Aleksandar Angeloski, Xevi Roca, and Jaime Peraire (2013). "Efficiency of high-order elements for continuous and discontinuous Galerkin methods". In: *International Journal for numerical methods in Engineering* 96.9, pp. 529–560.

Hughes, Thomas JR (1979). "A multidimentional upwind scheme with no crosswind diffusion". In: *Finite Element Methods for Convection Dominated Flows, AMD 34*.

Hughes, Thomas JR, Leopoldo P Franca, and Marc Balestra (1986). "A new finite element formulation for computational fluid dynamics: V. Circumventing the Babuška-Brezzi condition: A stable Petrov-Galerkin formulation of the Stokes problem accommodating equal-order interpolations". In: *Computer Methods in Applied Mechanics and Engineering* 59.1, pp. 85–99.

Ibañez, Ruben, Domenico Borzacchiello, Jose Vicente Aguado, Emmanuelle Abisset-Chavanne, Elías Cueto, Pierre Ladevèze, and Francisco Chinesta (2017). "Data-driven non-linear elasticity: constitutive manifold construction and problem discretization". In: *Computational Mechanics* 60.5, pp. 813–826.

Ibanez, Rubén, Emmanuelle Abisset-Chavanne, Jose Vicente Aguado, David Gonzalez, Elias Cueto, and Francisco Chinesta (2018). "A manifold learning approach to data-driven computational elasticity and inelasticity". In: *Archives of Computational Methods in Engineering* 25.1, pp. 47–57.

Ibáñez, Rubén, Emmanuelle Abisset-Chavanne, Amine Ammar, David González, Elías Cueto, Antonio Huerta, Jean Louis Duval, and Francisco Chinesta (2018). "A multidimensional data-driven sparse identification technique: the sparse proper generalized decomposition". In: *Complexity* 2018.

Johnson, Claes and Juhani Pitkäranta (1986). "An analysis of the discontinuous Galerkin method for a scalar hyperbolic equation". In: *Mathematics of computation* 46.173, pp. 1–26.

Keaveny, Eric E, Shawn W Walker, and Michael J Shelley (2013). "Optimization of chiral structures for microscale propulsion". In: *Nano letters* 13.2, pp. 531–537.

Kirby, Robert M, Spencer J Sherwin, and Bernardo Cockburn (2012). "To CG or to HDG: a comparative study". In: *Journal of Scientific Computing* 51.1, pp. 183–212.

Kovasznay, LIG (1948). "Laminar flow behind a two-dimensional grid". In: *Mathematical Proceedings of the Cambridge Philosophical Society*. Vol. 44. 1. Cambridge University Press, pp. 58–62.

Kroll, Norbert, Charles Hirsch, Francesco Bassi, Craig Johnston, and Koen Hillewaert (2015). *IDIHOM: Industrialization of High-Order Methods-A Top-Down Approach: Results of a Collaborative Research Project Funded by the European Union, 2010-2014*. Vol. 128. Springer.

Ladevèze, P (1991). "New advances in the large time increment method". In: *New advances in computational structural mechanics. Elsevier, Amsterdam*, pp. 3–21.

Ladevèze, Pierre (1999). *Nonlinear Computational Structural Mechanics*. Springer.

Lauga, Eric (2011). "Life around the scallop theorem". In: *Soft Matter* 7.7, pp. 3060–3065.

Lê, T-H, J-M Le Gouez, and E Garnier (2011). "High accuracy flow simulations: Advances and challenges for future needs in aeronautics". In: *Computers & fluids* 43.1, pp. 90–97.

Leander, BS (2008). "Euglenida: Euglenids or euglenoids." In: *The Tree of Life Web Project, http://tolweb. org. http://tolweb. org/Euglenida/97461/2008.09* 11.

Lederer, Philip L, Christoph Lehrenfeld, and Joachim Schöberl (2018). "Hybrid discontinuous Galerkin methods with relaxed H (div)-conformity for incompressible flows. Part I". In: *SIAM Journal on Numerical Analysis* 56.4, pp. 2070–2094.

– (2019). "Hybrid Discontinuous Galerkin methods with relaxed H (div)-conformity for incompressible flows. Part II". In: *ESAIM: Mathematical Modelling and Numerical Analysis* 53.2, pp. 503–522.

Lesaint, Pierre and Pierre-Arnaud Raviart (1974). "On a finite element method for solving the neutron transport equation". In: *Publications mathématiques et informatique de Rennes* S4, pp. 1–40.

Leshansky, AM and Oded Kenneth (2008). "Surface tank treading: Propulsion of Purcell's toroidal swimmer". In: *Physics of fluids* 20.6, p. 063104.

LeVeque, Randall J et al. (2002). *Finite volume methods for hyperbolic problems*. Vol. 31. Cambridge university press.

Leygue, Adrien and Erwan Verron (2010). "A first step towards the use of proper general decomposition method for structural optimization". In: *Archives of Computational Methods in Engineering* 17.4, pp. 465–472.

Lighthill, Sir James (1975). *Mathematical biofluiddynamics*. SIAM.

Lumley, John Leask (1967). "The structure of inhomogeneous turbulent flows". In: *Atmospheric turbulence and radio wave propagation*.

Manzoni, Andrea (2014). "An efficient computational framework for reduced basis approximation and a posteriori error estimation of parametrized Navier–Stokes flows". In: *ESAIM: Mathematical Modelling and Numerical Analysis* 48.4, pp. 1199–1226.

Manzoni, Andrea, Alfio Quarteroni, and Gianluigi Rozza (2012a). "Model reduction techniques for fast blood flow simulation in parametrized geometries". In: *International journal for numerical methods in biomedical engineering* 28.6-7, pp. 604–625.

– (2012b). "Shape optimization for viscous flows by reduced basis methods and free-form deformation". In: *International Journal for Numerical Methods in Fluids* 70.5, pp. 646–670.

Manzoni, Andrea and Federico Negri (2017). "Efficient reduction of PDEs defined on domains with variable shape". In: *Model Reduction of Parametrized Systems*. Springer, pp. 183–199.

McKay, Michael D, Richard J Beckman, and William J Conover (2000). "A comparison of three methods for selecting values of input variables in the analysis of output from a computer code". In: *Technometrics* 42.1, pp. 55–61.

Millán, Daniel and Marino Arroyo (2013). "Nonlinear manifold learning for model reduction in finite elastodynamics". In: *Computer Methods in Applied Mechanics and Engineering* 261, pp. 118–131.

Modesto, David, Sergio Zlotnik, and Antonio Huerta (2015). "Proper Generalized Decomposition for parameterized Helmholtz problems in heterogeneous and unbounded domains: application to harbor agitation". In: *Computer Methods in Applied Mechanics and Engineering* 295, pp. 127–149.

Modesto, David, Boyi Ye, Sergio Zlotnik, and Antonio Huerta (2020). "Fast solution of elliptic harbor agitation problems under frequency-direction input spectra by model order reduction and NURBS-enhanced FEM". In: *Coastal Engineering* 156, p. 103618.

Montlaur, A, Sonia Fernandez-Mendez, and Antonio Huerta (2008). "Discontinuous Galerkin methods for the Stokes equations using divergence-free approximations". In: *International journal for numerical methods in fluids* 57.9, pp. 1071–1092.

Moran, Jeffrey L and Jonathan D Posner (2019). "Microswimmers with no moving parts". In: *Physics today* 72.5, pp. 44–52.

Nagarajan, Santhanam, Sanjiva K Lele, and Joel H Ferziger (2003). "A robust high-order compact method for large eddy simulation". In: *Journal of Computational Physics* 191.2, pp. 392–419.

Najafi, Ali and Ramin Golestanian (2004). "Simple swimmer at low Reynolds number: Three linked spheres". In: *Physical Review E* 69.6, p. 062901.

Negri, Federico, Gianluigi Rozza, Andrea Manzoni, and Alfio Quarteroni (2013). "Reduced basis method for parametrized elliptic optimal control problems". In: *SIAM Journal on Scientific Computing* 35.5, A2316–A2340.

Negri, Federico, Andrea Manzoni, and Gianluigi Rozza (2015). "Reduced basis approximation of parametrized optimal flow control problems for the Stokes equations". In: *Computers & Mathematics with Applications* 69.4, pp. 319–336.

Nguyen, Cuong and Jaime Peraire (2011a). "An adaptive shock-capturing HDG method for compressible flows". In: *20th AIAA Computational Fluid Dynamics Conference*, p. 3060.

Nguyen, N. C., J. Peraire, and B. Cockburn (2009a). "An implicit high-order hybridizable discontinuous Galerkin method for linear convection-diffusion equations". In: *Journal of Computational Physics* 228.9, pp. 3232–3254.

– (2009b). "An implicit high-order hybridizable discontinuous Galerkin method for nonlinear convection-diffusion equations". In: *Journal of Computational Physics* 228.23, pp. 8841–8855.

Nguyen, Nam-Trung, Steven T Wereley, and Seyed Ali Mousavi Shaegh (2019). *Fundamentals and applications of microfluidics*. Artech house.

Nguyen, N.C., J. Peraire, and B. Cockburn (2010a). "A hybridizable discontinuous Galerkin method for Stokes flow". In: *Computer Methods in Applied Mechanics and Engineering* 199.9-12, pp. 582–597.

Nguyen, Ngoc Cuong, Jaume Peraire, and Bernardo Cockburn (2009c). "An implicit high-order hybridizable discontinuous Galerkin method for linear convection–diffusion equations". In: *Journal of Computational Physics* 228.9, pp. 3232–3254.

– (2009d). "An implicit high-order hybridizable discontinuous Galerkin method for nonlinear convection–diffusion equations". In: *Journal of Computational Physics* 228.23, pp. 8841–8855.

Nguyen, Ngoc Cuong, Jaime Peraire, and Bernardo Cockburn (2010b). "A hybridizable discontinuous Galerkin method for Stokes flow". In: *Computer Methods in Applied Mechanics and Engineering* 199.9-12, pp. 582–597.

Nguyen, Ngoc Cuong, Jaume Peraire, and Bernardo Cockburn (2011b). "An implicit high-order hybridizable discontinuous Galerkin method for the incompressible Navier–Stokes equations". In: *Journal of Computational Physics* 230.4, pp. 1147–1170.

Nouy, Anthony (2010). "Proper generalized decompositions and separated representations for the numerical solution of high dimensional stochastic problems". In: *Archives of Computational Methods in Engineering* 17.4, pp. 403–434.

Pasquetti, Richard (2005). "High-order LES modeling of turbulent incompressible flow". In: *Comptes Rendus Mécanique* 333.1, pp. 39–49.

Patera, Anthony T, Gianluigi Rozza, et al. (2007). *Reduced basis approximation and a posteriori error estimation for parametrized partial differential equations.*

Peherstorfer, Benjamin, Karen Willcox, and Max Gunzburger (2018). "Survey of multifidelity methods in uncertainty propagation, inference, and optimization". In: *Siam Review* 60.3, pp. 550–591.

Peraire, Jaime and P-O Persson (2008). "The compact discontinuous Galerkin (CDG) method for elliptic problems". In: *SIAM Journal on Scientific Computing* 30.4, pp. 1806–1824.

Peraire, Jaime, Ngoc Nguyen, and Bernardo Cockburn (2010). "A hybridizable discontinuous Galerkin method for the compressible Euler and Navier-Stokes equations". In: *48th AIAA aerospace sciences meeting including the new horizons forum and aerospace exposition*, p. 363.

Perotto, Simona (2014). "A survey of hierarchical model (Hi-Mod) reduction methods for elliptic problems". In: *Numerical simulations of coupled problems in engineering.* Springer, pp. 217–241.

Perotto, Simona, Alexandre Ern, and Alessandro Veneziani (2010). "Hierarchical local model reduction for elliptic problems: a domain decomposition approach". In: *Multiscale Modeling & Simulation* 8.4, pp. 1102–1127.

Perotto, Simona, Michele Giuliano Carlino, and Francesco Ballarin (2018). "Model reduction by separation of variables: a comparison between Hierarchical Model reduction and Proper Generalized Decomposition". In: *arXiv preprint arXiv:1811.11486.*

Persson, P.-O. and J. Peraire (2009). "Curved Mesh Generation and Mesh Refinement using Lagrangian Solid Mechanics". In: *Proceedings of the 47th AIAA Aerospace Sciences Meeting and Exhibit.* AIAA.

Persson, Per-Olof (2013). "Shock capturing for high-order discontinuous Galerkin simulation of transient flow problems". In: *21st AIAA Computational Fluid Dynamics Conference*, p. 3061.

Peterson, Janet S (1989). "The reduced basis method for incompressible viscous flow calculations". In: *SIAM Journal on Scientific and Statistical Computing* 10.4, pp. 777–786.

Phalippou, P, S Bouabdallah, P Breitkopf, P Villon, and M Zarroug (2020). "'On-the-fly'snapshots selection for Proper Orthogonal Decomposition with application to nonlinear dynamics". In: *Computer Methods in Applied Mechanics and Engineering* 367, p. 113120.

Poya, Roman, Ruben Sevilla, and Antonio J Gil (2016). "A unified approach for a posteriori high-order curved mesh generation using solid mechanics". In: *Computational Mechanics* 58.3, pp. 457–490.

Purcell, Edward M (1977). "Life at low Reynolds number". In: *American journal of physics* 45.1, pp. 3–11.

– (1997). "The efficiency of propulsion by a rotating flagellum". In: *Proceedings of the National Academy of Sciences* 94.21, pp. 11307–11311.

Qiu, Weifeng and Ke Shi (2016). "A superconvergent HDG method for the incompressible Navier–Stokes equations on general polyhedral meshes". In: *IMA Journal of Numerical Analysis* 36.4, pp. 1943–1967.

Quaranta, Giacomo, Mustapha Ziane, Simó Masqué Barri, Carlos Terres Aboitiz, Anne Chambard, Jean Louis Duval, Elias Cueto, and Francisco Chinesta (2020). "From Component Reduced Models to Reduced Modelling of Multi-Component Systems". In: *Procedia Manufacturing* 47, pp. 696–701.

Quarteroni, Alfio and Gianluigi Rozza (2007). "Numerical solution of parametrized Navier–Stokes equations by reduced basis methods". In: *Numerical Methods for Partial Differential Equations: An International Journal* 23.4, pp. 923–948.

Quarteroni, Alfio, Gianluigi Rozza, and Andrea Manzoni (2011). "Certified reduced basis approximation for parametrized partial differential equations and applications". In: *Journal of Mathematics in Industry* 1.1, p. 3.

Quarteroni, Alfio, Andrea Manzoni, and Federico Negri (2015). *Reduced basis methods for partial differential equations: an introduction*. Vol. 92. Springer.

Raviart, Pierre-Arnaud and Jean-Marie Thomas (1977). "A mixed finite element method for 2-nd order elliptic problems". In: *Mathematical aspects of finite element methods*. Springer, pp. 292–315.

Reed, William H and TR Hill (1973). *Triangular mesh methods for the neutron transport equation*. Tech. rep. Los Alamos Scientific Lab., N. Mex.(USA).

Rozza, Gianluigi (2011). "Reduced basis approximation and error bounds for potential flows in parametrized geometries". In: *Communications in Computational Physics* 9.1, pp. 1–48.

– (2014). "Fundamentals of reduced basis method for problems governed by parametrized PDEs and applications". In: *Separated representations and PGD-based model reduction*. Springer, pp. 153–227.

Rozza, Gianluigi, Dinh Bao Phuong Huynh, and Anthony T Patera (2007). "Reduced basis approximation and a posteriori error estimation for affinely parametrized elliptic coercive partial differential equations". In: *Archives of Computational Methods in Engineering* 15.3, p. 1.

Rozza, Gianluigi, DB Phuong Huynh, and Andrea Manzoni (2013). "Reduced basis approximation and a posteriori error estimation for Stokes flows in parametrized geometries: roles of the inf-sup stability constants". In: *Numerische Mathematik* 125.1, pp. 115–152.

Ryckelynck, David (2005). "A priori hyperreduction method: an adaptive approach". In: *Journal of computational physics* 202.1, pp. 346–366.

Sánchez-Vizuet, Tonatiuh and Manuel E Solano (2019). "A hybridizable discontinuous Galerkin solver for the Grad–Shafranov equation". In: *Computer Physics Communications* 235, pp. 120–132.

Sevilla, Ruben and Antonio Huerta (2016a). "Tutorial on Hybridizable Discontinuous Galerkin (HDG) for second-order elliptic problems". In: *Advanced Finite Element Technologies*. Ed. by J. Schröder and P. Wriggers. Vol. 566. CISM International Centre for Mechanical Sciences. Springer International Publishing, pp. 105–129.

– (2016b). "Tutorial on Hybridizable Discontinuous Galerkin (HDG) for second-order elliptic problems". In: *Advanced Finite Element Technologies*. Ed. by J. Schröder and P. Wriggers. Vol. 566. CISM International Centre for Mechanical Sciences. Springer International Publishing, pp. 105–129.

Sevilla, Ruben, Matteo Giacomini, Alexandros Karkoulias, and Antonio Huerta (2018a). "A superconvergent hybridisable discontinuous Galerkin method for linear elasticity". In: *International Journal for Numerical Methods in Engineering* 116.2, pp. 91–116.

Sevilla, Ruben and Antonio Huerta (2018b). "HDG-NEFEM with degree adaptivity for Stokes flows". In: *Journal of Scientific Computing* 77.3, pp. 1953–1980.

Sevilla, Ruben, Luca Borchini, Matteo Giacomini, and Antonio Huerta (2020a). "Hybridisable discontinuous Galerkin solution of geometrically parametrised Stokes flows". In: *Computer Methods in Applied Mechanics and Engineering* 372, p. 113397.

Sevilla, Ruben, Sergio Zlotnik, and Antonio Huerta (2020b). "Solution of geometrically parametrised problems within a CAD environment via model order reduction". In: *Computer Methods in Applied Mechanics and Engineering* 358, p. 112631.

Shen, Jiguang, John R Singler, and Yangwen Zhang (2019). "HDG–POD reduced order model of the heat equation". In: *Journal of Computational and Applied Mathematics* 362, pp. 663–679.

Shu, Chi-Wang (2003). "High-order finite difference and finite volume WENO schemes and discontinuous Galerkin methods for CFD". In: *International Journal of Computational Fluid Dynamics* 17.2, pp. 107–118.

Sibileau, Alberto, Alberto García-González, Ferdinando Auricchio, Simone Morganti, and Pedro Díez (2018). "Explicit parametric solutions of lattice structures with proper generalized decomposition (PGD)". In: *Computational Mechanics* 62.4, pp. 871–891.

Silverberg, Oliver, Ebru Demir, Grant Mishler, Brent Hosoume, Nikhil Rupal Trivedi, Connor Tisch, Daniel Plascencia, On Shun Pak, and Ismail Emre Araci (2020).

"Realization of a Push-Me-Pull-You swimmer at low Reynolds numbers". In: *Bioinspiration & Biomimetics*.

Solano, Manuel and Felipe Vargas (2019). "A high order HDG method for Stokes flow in curved domains". In: *Journal of Scientific Computing* 79.3, pp. 1505–1533.

Stone, Howard A and Aravinthan DT Samuel (1996). "Propulsion of microorganisms by surface distortions". In: *Physical Review Letters* 77.19, p. 4102.

Strawn, Roger and Jasim Ahmad (2000). "Computational modeling of hovering rotors and wakes". In: *38th Aerospace Sciences Meeting and Exhibit*, p. 110.

Tabeling, Patrick (2005). *Introduction to microfluidics*. OUP Oxford.

Tam, Daniel and Annete E Hosoi (2007). "Optimal stroke patterns for Purcell's three-link swimmer". In: *Physical Review Letters* 98.6, p. 068105.

Taylor, Geoffrey Ingram (1952). "The action of waving cylindrical tails in propelling microscopic organisms". In: *Proceedings of the Royal Society of London. Series A. Mathematical and Physical Sciences* 211.1105, pp. 225–239.

Teh, Shia-Yen, Robert Lin, Lung-Hsin Hung, and Abraham P Lee (2008). "Droplet microfluidics". In: *Lab on a Chip* 8.2, pp. 198–220.

Tsiolakis, Vasileios, Matteo Giacomini, Ruben Sevilla, Carsten Othmer, and Antonio Huerta (2020a). "Nonintrusive proper generalised decomposition for parametrised incompressible flow problems in OpenFOAM". In: *Computer physics communications* 249, p. 107013.

– (2020b). "Parametric solutions of turbulent incompressible flows in OpenFOAM via the proper generalised decomposition". In: *arXiv preprint arXiv:2006.07073*.

Veroy, K and AT Patera (2005). "Certified real-time solution of the parametrized steady incompressible Navier–Stokes equations: rigorous reduced-basis a posteriori error bounds". In: *International Journal for Numerical Methods in Fluids* 47.8-9, pp. 773–788.

Veubeke, Baudouin Fraeijs de (1965). "Displacement and equilibrium models in the finite element method". In: *Stress analysis*, chapter–9.

Vieira, Luan M, Matteo Giacomini, Ruben Sevilla, and Antonio Huerta (2020). "A second-order face-centred finite volume method for elliptic problems". In: *Computer Methods in Applied Mechanics and Engineering* 358, p. 112655.

Vila-Pérez, Jordi, Matteo Giacomini, Ruben Sevilla, and Antonio Huerta (2019). "An HLL Riemann solver for the hybridised discontinuous Galerkin formulation of compressible flows". In: *arXiv preprint arXiv:1912.00044*.

Volkwein, Stefan (2011). "Model reduction using proper orthogonal decomposition". In: *Lecture Notes, Institute of Mathematics and Scientific Computing, University of Graz. see http://www. uni-graz. at/imawww/volkwein/POD. pdf* 1025.

Wagner, Claus, Thomas Hüttl, and Pierre Sagaut (2007). *Large-eddy simulation for acoustics*. Vol. 20. Cambridge University Press.

Wang, CY (1991). "Exact solutions of the steady-state Navier-Stokes equations". In: *Annual Review of Fluid Mechanics* 23.1, pp. 159–177.

Wang, Zhi Jian (2007). "High-order methods for the Euler and Navier–Stokes equations on unstructured grids". In: *Progress in Aerospace Sciences* 43.1-3, pp. 1–41.

Wang, Zhijian J, Krzysztof Fidkowski, Rémi Abgrall, Francesco Bassi, Doru Caraeni, Andrew Cary, Herman Deconinck, Ralf Hartmann, Koen Hillewaert, Hung T Huynh, et al. (2013). "High-order CFD methods: current status and perspective". In: *International Journal for Numerical Methods in Fluids* 72.8, pp. 811–845.

White, Frank M and Isla Corfield (2006). *Viscous fluid flow*. Vol. 3. McGraw-Hill New York.

Whitesides, George M (2006). "The origins and the future of microfluidics". In: *Nature* 442.7101, pp. 368–373.

Williams, D (2018). "An entropy stable, hybridizable discontinuous Galerkin method for the compressible Navier-Stokes equations". In: *Mathematics of Computation* 87.309, pp. 95–121.

Xie, Zhong Q, Ruben Sevilla, Oubay Hassan, and Kenneth Morgan (2013). "The generation of arbitrary order curved meshes for 3D finite element analysis". In: *Computational Mechanics* 51.3, pp. 361–374.

Yang, Xiang, Chang Liu, Yunyun Li, Fabio Marchesoni, Peter Hänggi, and HP Zhang (2017). "Hydrodynamic and entropic effects on colloidal diffusion in corrugated channels". In: *Proceedings of the National Academy of Sciences* 114.36, pp. 9564–9569.

Zienkiewicz, OC and YK Cheung (1967). "Finite element methods in structural and continuum mechanics". In: *McGrawhill Publication*.

Zlotnik, Sergio, Pedro Díez, David Modesto, and Antonio Huerta (2015). "Proper generalized decomposition of a geometrically parametrized heat problem with geophysical applications". In: *International Journal for Numerical Methods in Engineering* 103.10, pp. 737–758.

Zou, Xi, Michele Conti, Pedro Díez, and Ferdinando Auricchio (2018). "A nonintrusive proper generalized decomposition scheme with application in biomechanics". In: *International Journal for Numerical Methods in Engineering* 113.2, pp. 230–251.